EVALUATION OF HYPERVELOCITY GOLD NANOPARTICLES FOR NANOVOLUME SURFACE MASS SPECTROMETRY

A Dissertation

by

JOHN DANIEL DEBORD

Submitted to the Office of Graduate Studies of
Texas A&M University
in partial fulfillment of the requirements for the degree of

DOCTOR OF PHILOSOPHY

Approved by:

Chair of Committee,	Emile Schweikert
Committee Members,	David Russell
	Gyula Vigh
	Andreas Holzenburg
Head of Department,	David Russell

December 2012

Major Subject: Chemistry

ABSTRACT

Impacts of high kinetic energy massive gold clusters (~ 500 keV Au_{400}^{+4}) exhibit significantly enhanced secondary ion yields relative to traditional atomic or polyatomic primary ions (e.g. Au_3 and C_{60}). The one-of-a-kind instrument used to generate these hypervelocity nanoparticles (~2 nm diameter, ~30 km/s) and monitor emissions from their impacts (SIMS) is described in detail for the first time.

The projectile range of 520 keV Au_{400}^{+4} is measured to be ~20 nm in amorphous carbon and projectile disintegration is observed at the exit of carbon foils as thin as 5 nm. These experiments were performed by monitoring carbon cluster ions emitted from both sides of a foil impacted by the projectile. Surprisingly, clusters emitted in the forward direction are larger than those emitted backward. The composition of the mass spectra is shown to depend on both the thickness of the foil and the size of the projectile.

Secondary ion yields for a variety of materials including peptides, lipids, drugs, polymers, inorganic salts, and various small molecules have been measured and molecular ion yields for many of these species exceed unity. Multiplicity measurements show that up to seven molecular ions of leucine-enkephalin (YGGFL) can be detected from the impact of a single projectile. SI yields measured with ~500 keV Au_{400}^{+4} are generally one to two orders of magnitude greater than those obtained with 130 keV Au_3^+ and 50 keV C_{60}^+ projectiles.

The high molecular ion yields observed suggest the internal energies of ions emitted from massive cluster impacts are relatively low. In order to address this

hypothesis, a novel method for measuring secondary ion internal energies was developed using a series of benzylpyridinium salts. Using this method, the internal energies were measured to be ~0.19 eV/atom, which is a factor of five less than that seen in atomic-SIMS.

Sample metallization is shown to be ineffective for further increasing secondary ion yields with Au_{400}, despite observations from previous molecular dynamic simulations. Coincidence mass spectrometry is applied to nanometric chemical segregations found on samples coated with thin layers of gold and silver. It is possible to measure the surface coverages of the metallic and underlying organic layers using mass spectrometry in a non-imaging mode.

To

my mother,

who sacrificed so

that I could succeed,

and my wife, whose love

has carried me through

every struggle I've

encountered

ACKNOWLEDGEMENTS

I would first like to acknowledge the sound guidance that Dr. Schwiekert has provided me over the past four years. I could not have asked for a more patient, wise, or encouraging research advisor. I would also like to acknowledge a fellowship I received from the U.S. Department of Homeland Security. This funding allowed me to be much more productive during my graduate studies. Thanks to my committee members, Dr. Vigh, Dr. Holzenburg, Dr. Russell, and Dr. Goodman, who have supported me throughout the course of this research.

Dr. Verkhoturov, you have taught me more about practical experimentation and culture than I could have learned anywhere else in the world. It was a pleasure to "delve" into real science with you. Dr. James, thank you for signing off on all the stuff I dragged back from surplus even though it added five pages to your inventory list. Dr. Fernandez-Lima, you have taught me many things, like how to windsurf and how to get things done. I look forward to doing more of both with you in Miami. Dr. Della-Negra, it was truly an honor to work with a master experimentalist. Without you to interpret my data, I don't think any of my papers would have had conclusions. Dr. Perez, I am sorry the molecules I brought you had a "transition state with a bi-furcated reaction pathway that leads to another transition state and a local minimum." Only you could have made sense of that difficult system. Thank you for your help with the thermometer calculations. Dr. North, thanks for sharing your RRKM expertise. You gave me a direction to go when I

was lost in the data. Dr. Delcorte, Dr. Restrepo, and Dr. Prabhakaran, thank you for the MetA-SIMS samples and the simulations of the transmission experiment.

Mike Raulerson, your “hey dude” greeting every morning brightened my day more than you’ll ever know. Sherry, there is always one person in an office that makes the world go round. In our office, you are that person. Veronica and Marcus, it was after I met you two during the graduate visitation weekend that I knew I wanted to join the Schweikert group. Thank you for bringing me in and showing me the ropes to grad school. Mike Eller, grad school would not have been nearly as exciting without you. We had some great times: breaking into a safe, playing twenty questions for twenty hours (straight) on a plane/train/bus ride to France, and crashing our rented Segways into trees. Maybe now I’ll stop bugging you to fix the data analysis software so it doesn’t crash after five spectra. Chao-Kai, thank you for your willingness to do any job at any time. Aaron and Fan, I wish you the best of luck riding “Pegasus”. Feel free to call me whenever she bucks you off.

Finally, thanks to my family for their encouragement and eagerness to help, whether I needed help moving or someone to babysit. Hannah, thank you for putting up with the late nights of scroll-wheel clicking and my meaningless discourses on nanoprojectiles and sputtered ions. Riley, one day you may read this and I want you to know that it was your smiles and laughs that made all the hard work worthwhile. Above all, I thank God for blessing me with the opportunities and abilities that have made this dissertation possible.

NOMENCLATURE

BPA	Bisphenol A
BPY	Benzylpyridinium
CFD	Constant Fraction Discriminator
CID	Collision Induced Dissociation
CMOS	Complementary Metal-Oxide-Semiconductor
DESB	Diethylstilbestrol
DESI	Desorption Electrospray Ionization
GFP	Green Fluorescent Protein
IPNO	Institute for Nuclear Physics at Orsay
LMIS	Liquid Metal Ion Source
MCP	Microchannel Plate
MetA-SIMS	Metal Assisted Secondary Ion Mass Spectrometry
PCB	Printed Circuit Board
PI	Primary Ion
PMT	Photomultiplier Tube
PTSA	p-Toluenesulfonic Acid
RFP	Red Fluorescent Protein
SAMPI	Surface Analysis and Mapping of Projectile Impacts
SI	Secondary Ion
SIMS	Secondary Ion Mass Spectrometry

TDC	Time-to-Digital Converter
TME	Total Matrix of Events
ToF	Time of Flight
QCM	Quartz Crystal Microbalance

TABLE OF CONTENTS

CHAPTER Page

LIST OF FIGURES

FIGURE Page

FIGURE Page

FIGURE Page

FIGURE Page

LIST OF TABLES

CHAPTER I

INTRODUCTION AND LITERATURE REVIEW

Secondary Ion Mass Spectrometry

The physical and chemical interactions of surfaces are regulated on a nanometric scale, representing a significant analytical challenge for their observation and quantification. Many techniques have been developed towards addressing this challenge, often providing complementary information which can be used in concert to generate nuanced characterizations of the sample of interest. Secondary ion mass spectrometry (SIMS) in particular has grown to be an indispensable tool in the surface scientist's toolbox. This technique enables one to determine the chemical composition of a surface by monitoring the emission of surface-specific ions generated via impacts of primary projectile ions. The masses of secondary ions (SIs) created can be determined using any of the traditional mass spectrometric approaches, e.g. Time of Flight (ToF), quadrupole, magnetic sector, etc., yielding identifications for the elemental and molecular composition of the ions and thereby provides a chemical characterization of the top few layers (< 10 nm) of the surface being bombarded. This being said, there are many variables which affect the number and type of SIs detected for a given SIMS analysis. This introductory chapter explains the motivation for the SIMS investigations presented in this dissertation. In particular, the choice of hypervelocity nanoprojectiles is justified in terms of historical developments in primary ion source development. A brief overview

of SIMS is given, but for more detailed explanations readers are referred to reviews on the subject.[1-5]

Dynamic vs. Static SIMS

An important distinction within SIMS pertains to the affect an analysis has on the sample, i.e. whether or not the sample is destroyed by the analysis. For analyses which require the detection of trace species or chemicals located deep within the surface, it is possible to erode, or sputter, the surface such that material is removed and a larger volume of the sample is analyzed. By analyzing sufficiently large sample volumes, it becomes possible to achieve elemental detection limits at the parts per billion (ppb) level via what is known as dynamic SIMS.[1] Additionally, by eroding the sample it is possible to map the distribution of chemical species as a function of depth within the surface. This mode of operation, known as depth profiling, is by definition a destructive analysis technique. The cutoff for distinguishing whether or not the sample is consumed during a SIMS analysis is determined by the dose of primary ions required to generate the secondary ion mass spectrum. Below ~10^{13} primary ions/cm^2 the probability of multiple projectiles striking the same sample region is low and hence very little material is removed from the surface.[6] This mode of operation, known as static SIMS, limits the ultimate sensitivity but reduces fragmentation of surface molecules, allowing for the ejection of intact molecular ions as well as the monitoring of submonolayer chemical coverages. In limiting the number of primary ions which can be used for an analysis, it becomes obvious that a projectile more efficient in creating SIs will produce a more informative mass spectrum.

Atomic SIMS

Since the first application of "canal ray" induced secondary ion emission to surface analysis by Herzog and Viehbock,[7] researchers have continually sought primary ion sources capable of producing more secondary ions for a given dose of primary ions. Early SIMS studies utilized atomic primary ion beams nearly exclusively due to the ease with which they can be generated and manipulated.[8] The efficiency of a given primary ion can be described using a figure of merit known as the secondary ion yield, which is defined as the number of SIs emitted per primary ion impact.

Two parameters of particular importance for describing SI yields observed in atomic ion bombardment are the projectile/target atom mass ratio and projectile kinetic energy. The number of atoms emitted from the surface is greatest when the impacting ion has a similar mass to the target atoms.[9] This results in an optimal collision cross-section and improves energy transfer from the projectile to the target atoms. Increasing the impact energy of the SIMS projectile is one of the most reliable routes to improved SI yields.[10, 11] However, at kinetic energies of ~100-150 keV,[12, 13] sputter yields, and presumably SI yields, from atomic projectile impacts plateau at the point of maximal nuclear stopping power. Stopping power refers to the rate at which projectile energy is deposited in the solid during penetration. For eV to keV projectiles, "knock-on" interactions of the primary ion nucleus with nuclei of the solid largely determine the total stopping power. As the primary ion kinetic energy is further increased, these interactions become less frequent resulting in a reduction of the SI yield.

For higher energy species (MeV), electronic interactions come to dominate the stopping power term. In this way, SI yields can be recovered and further increased, but the feasibility of this approach has traditionally been limited by its requirement for large particle accelerators to generate sufficient ion kinetic energies. A proven alternative to electrostatic ion acceleration is the use of high energy fission fragments. MacFarlane and Torgerson showed in the 1970's that fission fragments from a ^{252}Cf source could be used to generate substantial yields of intact quasi-molecular ions using a relatively simple experimental arrangement.[14] This plasma desorption mass spectrometry (PDMS) technique has given way to other ionization methods including matrix assisted laser desorption ionization (MALDI) and electrospray ionization (ESI) which are capable of producing more molecular ions for larger species without the limitations associated with a radioactive source. MeV-SIMS remains an active field of research due to its prospects for molecular analysis of biologics.[15]

Extensive sputter yield measurements for primary ions with various masses, charge states, and impact energies on different target materials have allowed for the development of detailed theoretical descriptions of the atomic ion sputtering process.[9, 13, 16] Sputtering refers to the process by which species are ejected from the surface by an incoming projectile. Generally speaking, keV atomic ion penetration in solids occurs in a ballistic fashion. This process is often described as a series of "billiard ball" collisions initiated by the primary ion "cue ball". Kinetic energy is transferred to an ever increasing number of surface atoms. Through a series of intermediate collisions, a small fraction of the impacted atoms will have kinetic energies directed back towards the surface, as

shown in Figure I-1. Atoms and molecules within the top few layers of the surface with sufficient kinetic energy to overcome the surface binding forces are emitted. For a typical atomic ion bombardment, 0.01 to 100 atoms are emitted per incident primary ion. A small fraction of these sputtered species (up to 0.01)[17] will undergo ionization to generate the desirable secondary ions which can then be mass analyzed. This theory of collision cascade sputtering described here along with models for describing thermal spike (heavy keV ions) and electronic (MeV ions) sputtering have been incorporated into a software package, known as *The Stopping and Range of Ions in Matter* (SRIM), [18] which is widely-used in the fields of SIMS and accelerator physics. This program simulates atomic ion penetration and sputtering processes, providing quantitative range and sputter yield estimates which agree well with experimental measurements.

Absolute secondary ion yields using atomic primary ions vary substantially depending on the projectile and target material considered. They are a convoluted result of the sputtering and ionization efficiencies and range from 10^{-8} to 10^{-2} SIs per primary ion.[1, 17] This means that between 100 and 10^{8} primary ion impacts are required to generate a single analytical species. These values correspond to atomic secondary ions with molecular ion yields being still smaller.

Polyatomic Cluster SIMS

In an effort to overcome the vanishingly small ion yields of atomic primary ions, some researchers began turning to cluster ion projectiles for SIMS analyses. The original catalyst for these investigations was the observation that diatomic and triatomic ion

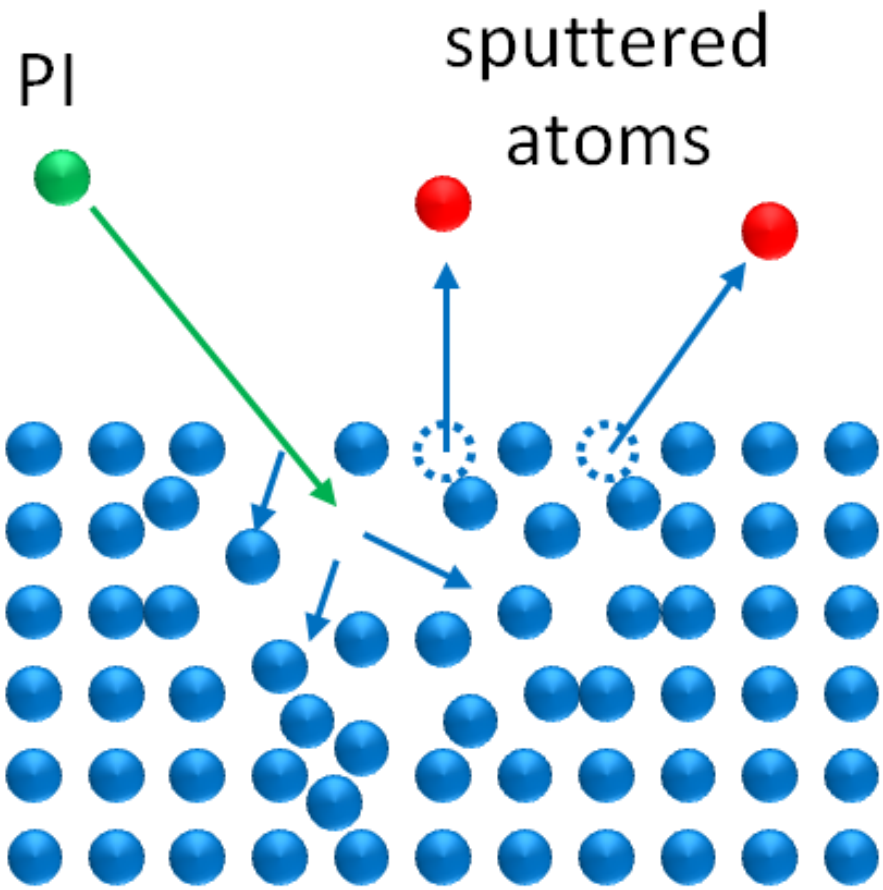

Figure I-1. Collision cascade process resulting in sputtered atoms.

beams generate a higher sputter yield than that of an equal velocity atomic ion multiplied by the number of atoms in the cluster.[19, 20] Blain et al.[21] and Appelhans and Delmore[22] concurrently reported the first observations that enhanced sputter yields could be translated into enhanced SI yields in 1989. This means that the enhancement factor (ε) shown in Equation 1.1 is greater than unity.[23]

$$\varepsilon = \frac{Y_{A_n}(KE)}{nY_{A_1}(KE/n)} \tag{1.1}$$

The effect is even more pronounced for high mass (> 200 amu) organic molecules which are poorly emitted during atomic ion bombardment.[22, 24] A simple conclusion which can be drawn from equation 1 is that the more constituents a projectile contains, the higher the SI yield for a given species. Supralinear enhancement is retained for projectiles of up to 9 atoms but becomes linear with further increases in nuclearity.[12, 25] These findings have resulted in the development of many new cluster projectiles which have steadily grown in size and complexity.

The study by Blain et al. reported SI yield enhancements obtained with a variety of projectiles including coronene ($C_{24}H_{12}$), coronene dimer ($C_{48}H_{24}$), phenylalanine ($C_6H_5CH_2CH(NH_3)\ COOH^+$), decarboxylated phenylalanine fragment ($C_6H_5CH_2CH(NH_3)^+$), and cesium iodide cluster ($(CsI)_nCs^+$) primary ions.[21] The source used to create these PIs was based on PDMS technology, using the ^{252}Cf fission fragment to desorb and ionize these molecules from thin foil targets. These ions were then accelerated towards the sample surface to be used as SIMS primary ions. The flexibility of this source also enabled its use for the production of other cluster projectiles such as C_{60}^+ and heavy metal oxide clusters ($(M_2O_3)_nMO^+$; M = Bi, La; n = 0-

3). [26, 27] For their study, Appelhans and Delmore developed a PI source capable of producing SF_6^- and SF_6^0 projectiles from sulfur hexafluoride gas via electron capture.[22] This primary ion source and equivalent SF_5^+ sources have been used for many static SIMS analyses since this first example.[28-30]

Development of the liquid metal ion source (LMIS)[31] eventually led to its implementation as a SIMS cluster ion source. LMISs mate well to SIMS applications due to their range of cluster sizes produced, high ion [25]current output, and excellent focusing characteristics. Benguerba et al. first applied a gold LMIS to SIMS, using Au_n^{+q} (n = 1-5, q = 1,2) clusters to measure enhancement factors for the range of projectiles.[32] The same study also incorporated a gallium LMIS, though only atomic ions were observed from this source. Gallium, indium, gold, and bismuth liquid metal ion sources have found wide use in the SIMS field, particularly for imaging applications.[33] The development of LMISs for SIMS is of particular interest, as all data reported in this dissertation have been obtained using gold and bismuth LMISs. A detailed description of the production, operation, and characterization of the gold LMIS used can be found in refs. [34] and [35].

The energy dependence of polyatomic ion SI yields is largely an extension of the atomic ion study. Studies with SF_5^+ have shown that the sputter rate measured from cluster ion impacts in the keV energy range initially increase linearly.[36] Expanded energy range measurements with Au_{1-5}^+ projectiles impacting a gold solid revealed that, like atomic projectiles, cluster sputter yields reach a maximum consistent with the nuclear stopping power.[12] Another interesting finding from this study was that the

maximal sputter yields were obtained for clusters with the same total kinetic energy and not the same energy per atom. The sputter yield enhancement over the range of n = 1-5 was determined to be proportional to n^2.[12]

Massive Cluster SIMS

The search for even larger cluster ion sources has led to the development of massive cluster projectiles with significantly greater nuclearity than the polyatomic sources described above. Much of the technology for generating these large clusters has been adapted from the fields of micromachining[37] and materials processing.[38] It has long been known that large clusters exhibit enormous sputtering yields (up to 10^5 atoms/PI)[39] which can be used to clean and smooth surfaces.[40]

The first massive clusters to be used for SIMS analyses were large water[41] and water/glycerol[42] clusters. Beuhler and Friedman formed massive water clusters ($(H_2O)_nH^+$, n = 80-3000) using a free jet expansion of ionized water vapor in a carrier gas.[43] Condensation of the gaseous water molecules results in the formation of singly ionized clusters at atmospheric pressure. The sizes of these clusters could be tuned by altering the carrier gas and temperature. After passing through a differential pumping region the desired cluster mass was selected using a quadrupole mass analyzer. Mahoney et al. showed that by increasing the liquid viscosity with glycerol it is possible to eliminate the need for differential pumping.[44] This was done using an electrohydrodynamic ionization source which operates similar to an electrospray ionization source, only the emitter tip is maintained within the high vacuum region and not at atmosphere. In this way, multiply charged aqueous/glycerol clusters (mass $\approx 10^7$

amu, q > 100) are formed within the vacuum. Two other benefits to this approach are the production of a multiply charged projectiles and the ability to enhance secondary ionization via projectile matrix delivery. Increased charge states allow projectiles to obtain higher kinetic energies and therefore sputter yields with a given accelerating voltage. The authors also introduce to concept of matrix delivery via projectile impact which is done by adding ammonium acetate or other electrolytes to the water/glycerol mixture. On impact these electrolytes are dispersed within the plume, promoting ionization of the sputtered species.

The discovery of buckminsterfullerene (C_{60})[45] rapidly led to its implementation as a SIMS projectile. Della-Negra et al. [46] used a Cs ion gun to generate C_{60}^- ions which were then injected into a tandem accelerator. At 200 keV these ions can be converted to C_{60}^{+q} (q = 1-3) via electron stripping interactions with background nitrogen gas molecules. The projectiles were then accelerated to energies of up to 10 qMeV. Secondary ion yields in the 10's of percent range were measured for various clusters of carbon atoms, CsI molecules, and valine molecules produced from high energy C_{60} impacts.[47] Diehnelt et al. later showed it was possible to generate C_{60}^+ using the same PDMS mediated approach described above where the fission fragment is used to desorb and ionize C_{60} from a thin layer deposited on a mylar foil.[48] A more efficient effusion source was eventually developed and commercialized by the Vickerman group.[49, 50] This source creates gaseous C_{60} via sublimation of buckminsterfullerene powder. Once in the gas phase, $C_{60}^{+1,2}$ can formed using electron impact ionization. Buckminsterfullerene has

become the reference standard for cluster ion projectiles[51] due to its capabilities for molecular ion imaging[33] and molecular ion depth profiling.[52]

Massive argon clusters were the next projectiles to enter the SIMS arena. Gas cluster ion beam technology originally developed for smoothing semiconductor surfaces was adapted for SIMS by Yamada et al.[53] These large clusters of argon atoms (Ar_n^+, n = 1000-4000)[54] are created via supersonic expansion from a nozzle and then ionized via electron impact ionization. These beams have found particular application in molecular depth profiling due to the high depth resolution achievable.[55] Another problem that argon clusters circumvent is the issue of underlayer damage. Previous molecular depth profiling studies with other projectiles have revealed decreases in the molecular ion signal as a function of depth. Massive argon clusters have small penetration depths and most if not all of the projectile atoms are evaporated from the surface for each impact.[56] This means that molecules below the sputtered layer remain intact and samples can be profiled to much greater depths.

The newest massive primary ion source, introduced in 2004, is capable of producing clusters containing hundreds of gold atoms. By altering various instrumental parameters, Bouneau et al. found that much larger gold clusters could be formed from the same LMIS they used to produce polyatomic clusters.[57] Specifically, this was done by increasing the extraction voltage applied to the source and concurrently adjusting the correct values on the Wien filter to pass projectiles with high m/q values. Projectiles produced by this source are multiply charged and range in size from the monatomic Au_1^+ all the way up to Au_{120q}^{+q} (q = 1-9). The most intense massive projectile produced by the

source has an n/z ≈ 100 with a most probable charge state of 4. Peptide yields measured using this Au_{400}^{+4} projectile at 40 keV were 1000 times larger than yields measured with 10 keV Au_1^+.[34] The authors of this study also noted that peptide molecular ion yields actually increase with primary ion doses up to 2 x 10^{13} ions/cm^2. This was contrasted with the Au_5^+ projectile which displayed a 10x reduction in molecular ion signal at a dose of just 8 x 10^{12} ions/cm^2. The authors proposed that the implantation of these large, high mass clusters result in an increased nuclear stopping power, thereby increasing the amount of energy deposited in the near surface region. This matrix effect increases the sputter yield and consequently SI yield of the projectile. Despite the efficiency of this massive projectile, only two research groups, the original researchers at the Institute of Nuclear Physics in Orsay, France and the Schweikert group at Texas A&M University, currently operate gold LMISs capable of producing the massive gold clusters. However, with the introduction of a commercial massive gold cluster ion gun, the Cobra ExB from Orsay Physics, massive gold clusters are poised to become more prominent within the field of SIMS.

Motivation for Hypervelocity Gold Nanoprojectiles

Molecular dynamics simulations of massive gold clusters have proposed mechanisms for describing the massive cluster-solid interaction. These simulations offer estimates for various experimental parameters including projectile ranges[58-61] and sputter yields.[62 63-65] The interaction can roughly be divided into two categories depending on whether the projectile is impact a target with light or heavy atoms. Simulations suggest massive cluster impacts on light atom targets (organics) result in a hydrodynamic

penetration range that is proportional to $E/n^{2/3}$, where E is the kinetic energy and n is the number of atoms in the projectile.[66] These simulations also predict minimal sputtering of the organic material,[67] though this observation is in disagreement with numerous experimental measurements of high SI yields for light atom organic molecules and minerals.[68-77] For heavy atom targets (metals, gold and silver in particular), massive cluster impacts are proposed to cause "the formation of surface heat spikes, resulting in violent microexplosions of the surface layers."[64] Indeed, many studies have proven massive gold clusters are efficient for analyzing metallic surfaces,[78] particularly metallic nanoparticles.[79-81] Due to computational limitations, nearly all molecular dynamics simulations referenced above were limited to projectile kinetic energies of less than 50 keV, possibly explaining the discrepancy between the predicted sputter yields and the observed SI yields.

The sparse data available for Au_{400} at high impact energies (0.2-4 MeV) shows that more than 10 glycine molecular ions can be generated for each projectile impact. [82] Another article by Della-Negra et al. reports a mass spectrum obtained using a single projectile impact. These measurements advocate for increasing the impact energy beyond that currently available in the first generation massive gold cluster SIMS instrument at Texas A&M. However, the limited scope of test molecules analyzed at high energy leaves multiple questions to be answered. Do the SI yields for large organic molecules continue to increase with impact energy similar to the small glycine molecule (75 amu) studied? Can analytically significant ions still be generated at high impact energies or does fragmentation become more dominant?

The new instrument used for studies contained in this dissertation has been designed to accelerate clusters to energies of up to 130 qkeV, four times that of the previous gold cluster SIMS instrument. This increase was driven by the desire to maximize the attainable SI yields while maintaining a reasonable cost of construction and ease of operation. An added benefit of the Au_{400}^{+4} projectile most commonly used is the high median charge state which allows for the generation of 520 keV projectiles using only a 130 kV accelerating potential.

This dissertation reports a series of measurements utilizing massive gold cluster projectiles at these higher kinetic energies. This work has entailed the construction of a one-of-a-kind SIMS instrument, a detailed assessment of the instrument's performance, measurements of physical parameters regarding the massive gold cluster-solid interaction, and application of this tool to describing nanoscale chemical heterogeneity within surfaces. This second generation instrument (described in Chapter II) follows on previous efforts by the Schweikert group to measure SI yields and multiplicity (described in Chapter IV) and implement coincidental ion mass spectrometry techniques (described in Chapter VI) using massive gold projectiles. Attributes of the projectile impact event such as collective effects in the cluster projectile's penetration range (described in Chapter III) and the internal energies of emitted secondary ions (described in Chapter V) will also be addressed. Chapter VI will additionally detail an attempt to further increase SI yields via metallization of organic surfaces. The capability for analyzing positive SIs from massive cluster impacts in addition to negative SIs has also been realized for the first time in our laboratory. The instrument (shown in Figure I-2),

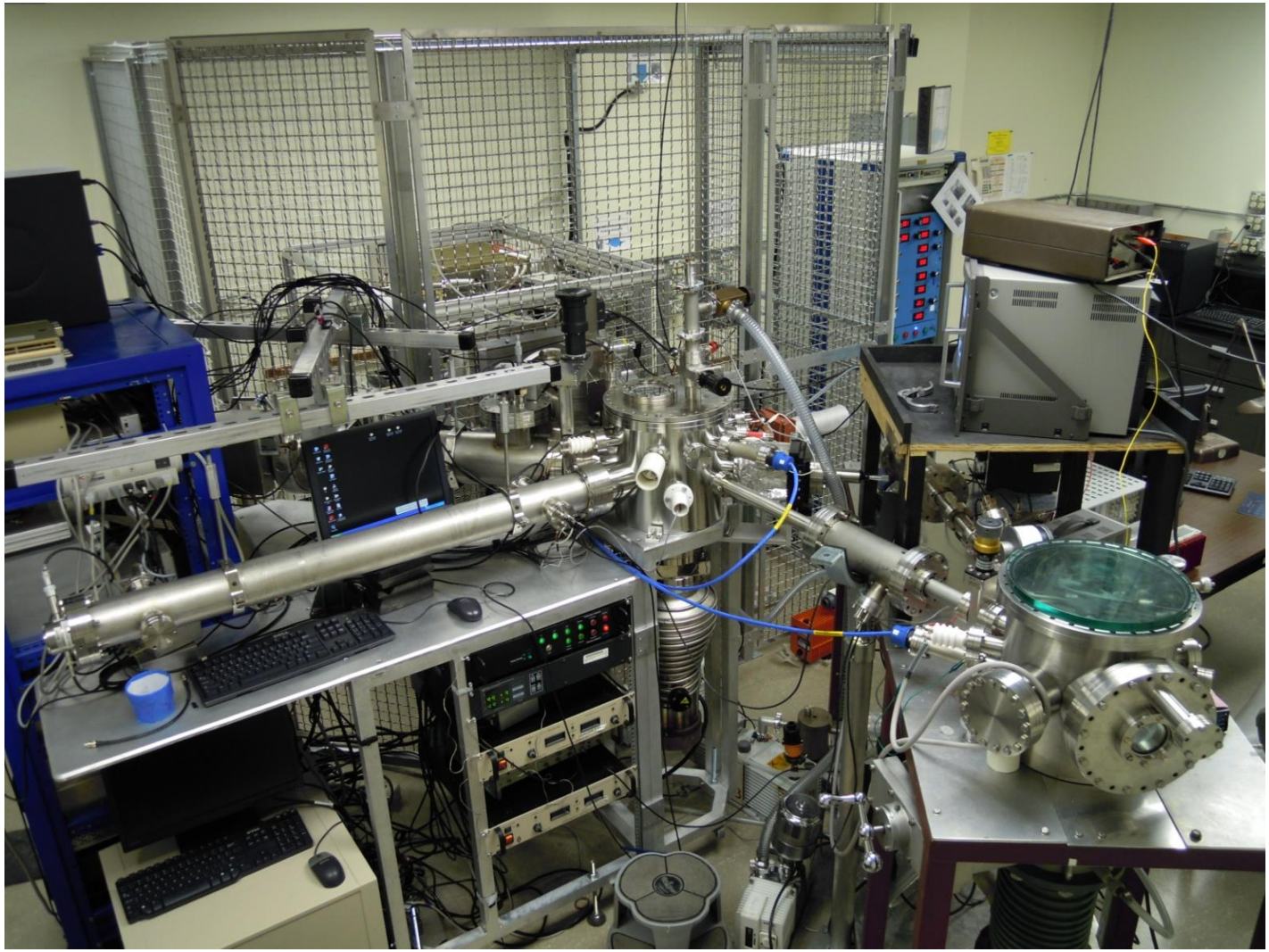

Figure I-2. Custom-built instrument featuring a high voltage LMIS platform coupled to two SIMS analysis chambers

while large, is housed in a single, reasonably-sized room and can easily be operated by a single user. It represents a balance of theoretical projectile optimization and technical feasibility in a truly unique analytical tool that will be demonstrated throughout the following chapters.

CHAPTER II

INSTRUMENTATION AND METHODOLOGY

This chapter describes the instrumentation and methodology developed to enable observation of SI emission from surface impacts of gold clusters with impact energies of up to 130 qkeV. All data reported in the following chapters were obtained using this new gold cluster SIMS instrument which has been constructed at Texas A&M University. The major components of the instrument are shown in Figure II-1. The instrument description below follows the progression of a projectile impact event. These events begin with projectile beam creation, selection, focusing, and pulsation to obtain a single, mass-selected projectile which is directed towards the sample surface in one of two chambers available for analysis. Following projectile impact, electrons and ions are extracted from the sample surface and directed towards custom-built detectors. The construction of these detectors will be discussed as well as the electronics required for processing the signals they generate. A general procedure for operation of the instrument is provided with advice for troubleshooting common issues. As a second generation instrument, much of the methodology and instrumentation is replicated from the first generation which has been described in detail.[35, 83, 84]

Pegasus High Voltage Platform

Liquid Metal Ion Source. The novelty of the current gold cluster SIMS instrument derives from the implementation of a Pegasus high voltage ion source platform designed and built by collaborators at the Institute for Nuclear Physics in

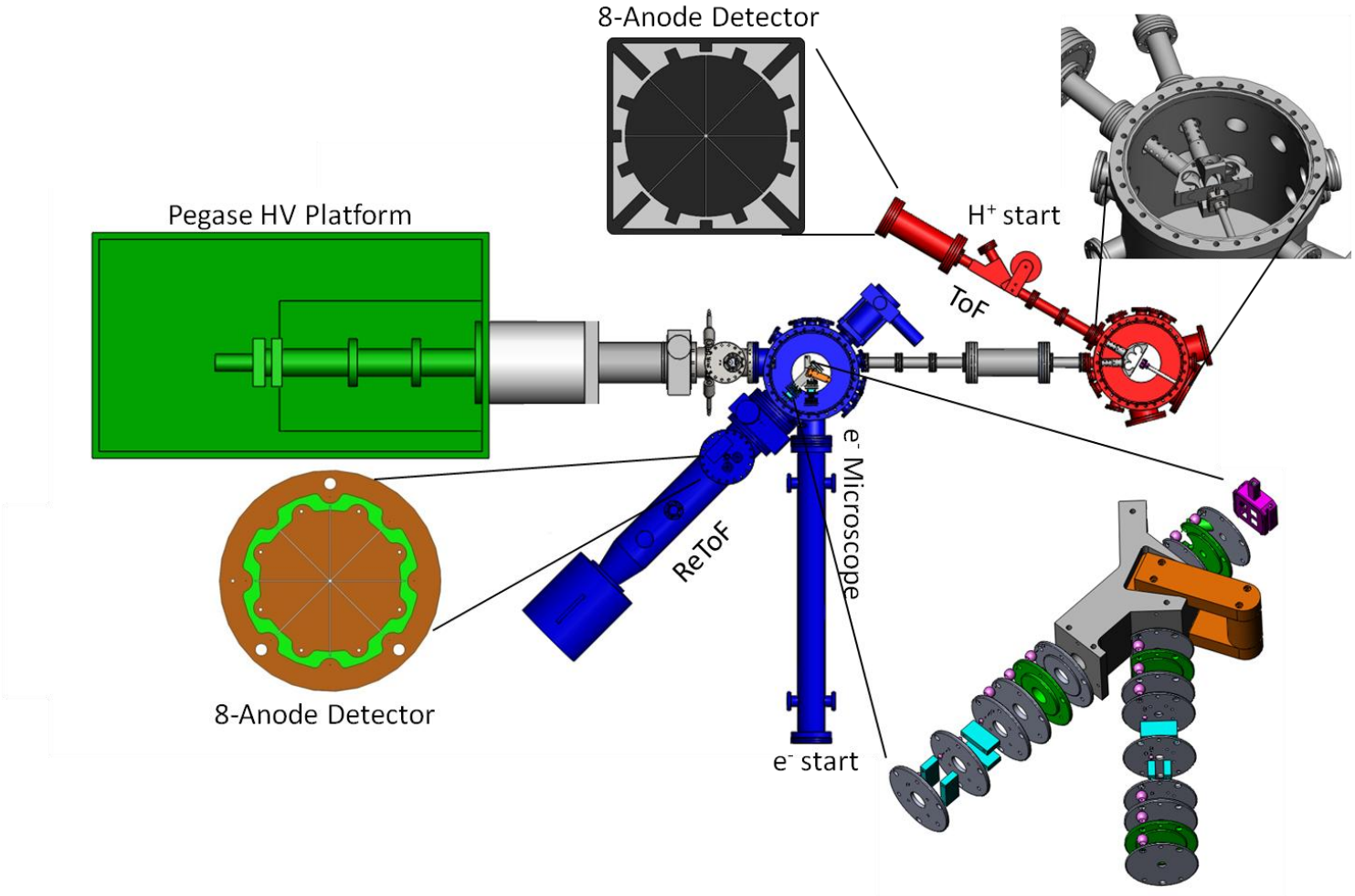

Figure II-1. Labeled overview of the custom gold cluster SIMS instrument at Texas A&M University.

Orsay (IPNO), France.[85] This platform utilizes the same gold LMIS design as the first generation instrument. For details regarding the construction and operation of the gold LMIS readers are referred to the Ph.D. dissertations of Rickman and Pinnick.[35, 84] Briefly, the source is constructed from a tungsten wire (Ø 200 μm) which is wound into a barrel-shaped reservoir that is then filled with a Au-Si eutectic (97 % Au, 3 % Si, Academy Precision Metals, Albuquerque, NM). This eutectic has a melting point of ~363 ^{o}C, much lower than the melting point of pure gold (~1,064 ^{o}C). Once prepared, the source is introduced to the LMIS positioning chamber which is pumped by an Adixen ATP 400 turbomolecular pump (400 l/s) and has a base pressure of ~10^{-7} torr. To initiate the source, a current is passed through the tungsten wire reservoir, heated the eutectic to its melting point. The source is maintained at a high voltage (6-10 kV) relative to a counter electrode, causing the molten eutectic to creep along an electrolytically etched tungsten needle which intersects the barrel. Once the eutectic reaches the tip of the needle, a Taylor cone[86] is formed, creating gas phase droplets from the metallic liquid.

Beam Characterization. A primary ion spectrum obtained from the Pegasus platform is shown in Figure II-2. This spectrum displays the relative intensities of all projectiles which can be observed from the Au/Si LMIS. The list of projectiles includes Au_{1-5}^{+2}, $Au_{1-5}Si^{+2}$, Au_{1-9}^{+}, $Au_{1-9}Si^{+}$, and large distribution of massive clusters (Au_n^{+q}). The major component of the gold beam is Au^{+}. This is also observed using the platform Faraday cup, where the Au^{+} species typically exhibits a beam current of ~200 nA. As a

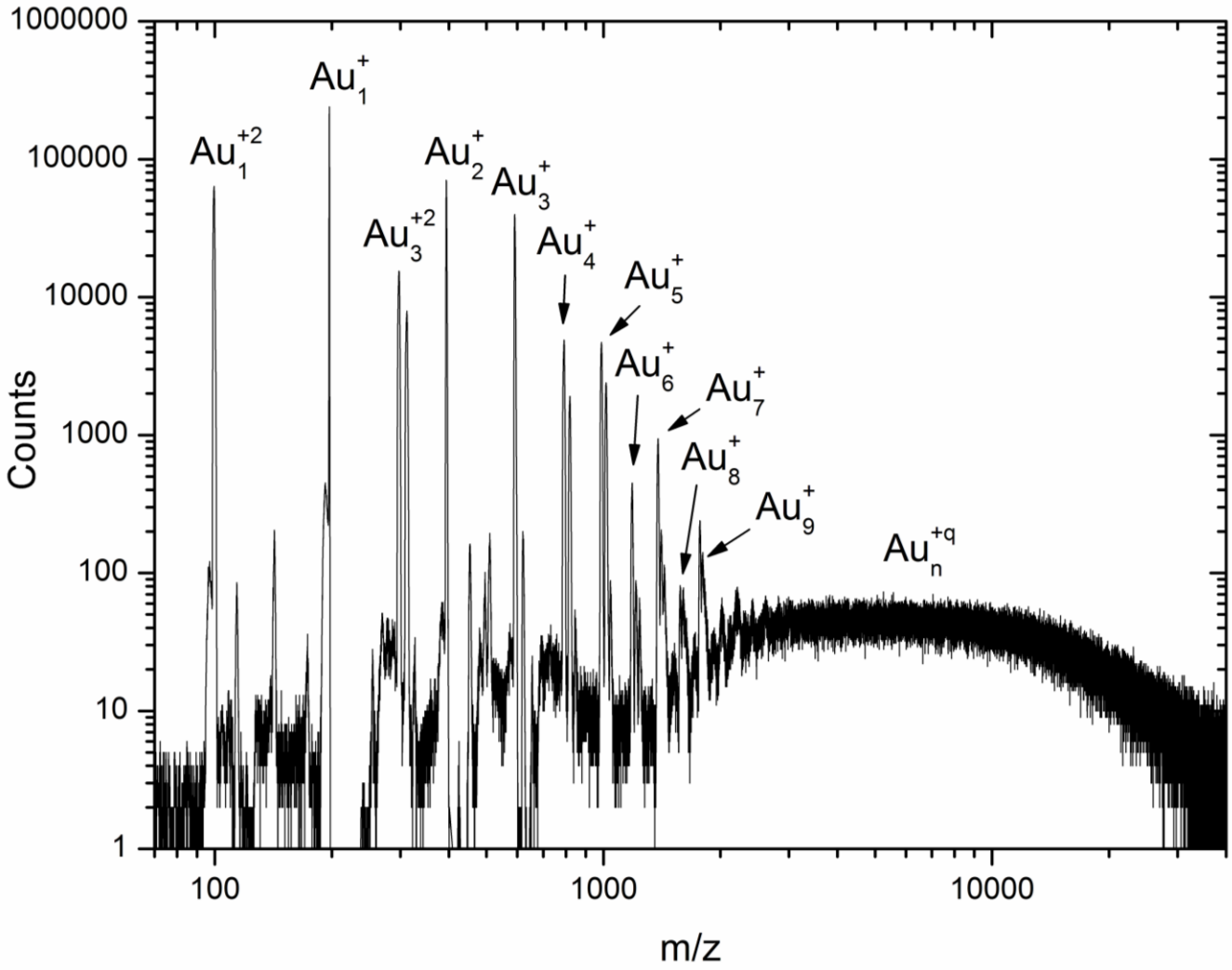

Figure II-2. PI spectrum observed from the Pegasus gold liquid metal ion source.

reference, the beam current obtained for the entire gold beam is normally 250-300 nA. As Au_2^+, Au_3^+, and increasingly larger gold clusters are considered the fluence for each projectile is reduced. Odd-numbered clusters are preferred, as seen by the oscillating intensities of the various cluster sizes. The massive cluster distribution, seen as a hump at high masses in the spectrum, extends from m/q 2,000 up to m/q 30,000. The average massive cluster is determined by the current limitation applied to the extraction power supply. In the spectrum given, a 20 µA source current limitation was used providing a massive cluster distribution centered at m/q 8,000. In order to obtain a distribution centered at m/q 20,000 (corresponding to the Au_{400}^{+4} projectile), the source extraction current is increased to 50 µA. This effectively increases the high voltage applied and results in the emission of larger gold "droplets" from the source. Clusters emitted under these conditions have been found to contain an average of 400 gold atoms and a charge state of +4, giving these projectiles an n/q ratio of ~100.[57]

Lens and Wien Filter. Emitted gold ions are accelerated to ~7.5 keV through the counter electrode aperture (Ø 1.5 mm) which is positioned ~500 µm from the needle tip. The amount of gold extracted from the source is controlled by altering the current limitation for the high voltage power supply biasing the counter electrode. A second acceleration stage is used to give the projectiles a total kinetic energy of 20 keV. The beam of projectiles is then focused using a high voltage Einzel lens (~14.5 kV) and introduced to a Wien filter for mass selection. The source generates a beam of gold projectiles ranging in size from monatomic gold atoms to clusters with over 1,000 constituents. Using crossed magnetic and electrostatic fields (Wien Filter) it is possible

to select a projectile (or distribution of projectiles) with a given mass to charge ratio. Technically the Wien filter is a velocity filter, but because projectiles are accelerated to a common kinetic energy, their velocities (v) are proportional to the square root of their kinetic energy (K), as shown in Equation 2.1, and they can thus be separated by mass (m).

$$v = \sqrt{\frac{2K}{m}} \tag{2.1}$$

The trajectory for each ion is determined by the net effect of the Coulomb and Lorentz forces acting on it as shown in Equation 2.2.

$$F_{net} = F_{Coulomb} + F_{Lorentz} = (qE) + (qv \times B) \tag{2.2}$$

Rearrangement gives Equation 2.3 which shows that for a given electric field strength (E) and magnetic field strength(B), ions with a certain velocity (v_0) will experience zero net force and therefore have a linear trajectory through the velocity filter.

$$v_0 = \frac{E}{B} \tag{2.3}$$

Substituting Equation 2.1 for the velocity we obtain Equation 2.4

$$\sqrt{\frac{2K}{m}} = \frac{E}{B} \tag{2.4}$$

which shows these field strength settings are particular to a certain mass, given a constant kinetic energy. Substituting the definition for electric field strength (Equation 2.5) and solving for the applied voltage (V) gives Equation 2.6

$$E = \frac{V}{d} \tag{2.5}$$

$$V = Bd\sqrt{\frac{2K}{m}} \tag{2.6}$$

where d is the distance between the electrostatic deflectors (12.3 mm for the Wien filter used). Selection of a given projectile is achieved by altering this voltage while maintaining a static magnetic field (~0.172 Tesla for 1.2 amps applied to the electromagnet). Equal potentials of opposite polarity ($V_{\pm}$) are applied to 12 cm long deflector plates separated by 1.2 cm above and below the beam axis, with positive polarity on the top plate and negative polarity on the bottom plate. This means $V = 2V_{\pm}$ and Equation 2.6 becomes Equation 2.7 when the parameters for this particular Wien filter are used.

$$V_{\pm} = Bd\sqrt{\frac{K}{2m}} = (0.172\text{ T})(0.0123\text{ m})\sqrt{\frac{3.20\times10^{-15}\text{ J}}{2m}} \approx \frac{8.46\times10^{-11}}{\sqrt{m}} \qquad (2.7)$$

Here m is given in kilograms. Using conversion factors, Equation 2.8 allows for one to calculate the voltage which should be applied to obtain a projectile of a mass given in amu.

$$V_{\pm} = \frac{2076}{\sqrt{m}} \qquad (2.8)$$

The magnet field strength of 0.172 T given above is an effective field strength which was back-calculated using a known set of voltage/projectile mass settings. The actual field strength is slightly higher. The field is underestimated because the electrostatic deflector rails are actually U-shaped rather than flat as shown in Figure II-3. This shape helps confine the beam in the horizontal direction, but it results in an effective electrode spacing that is smaller than the 0.123 m used in the calculation.

Deflectors and Faraday Cup. Exiting the Wien filter, the mass-selected beam encounters a set of vertical and horizontal electrostatic deflectors which allow for minor

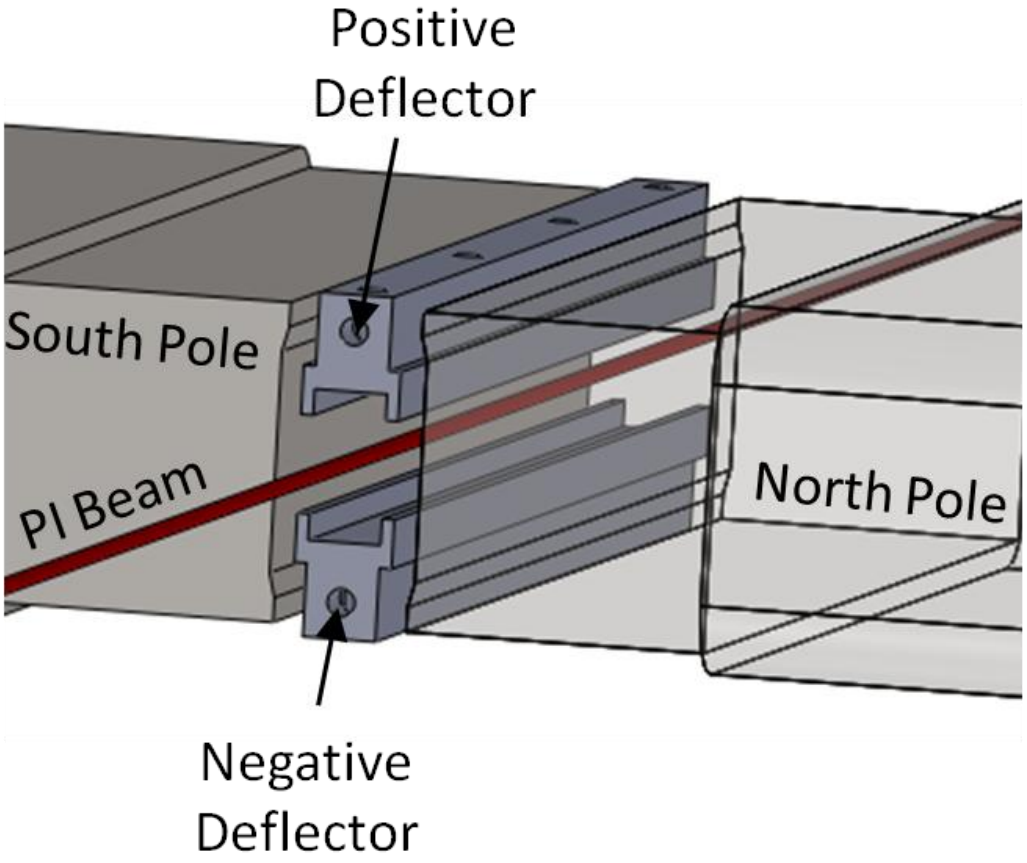

Figure II-3. Three-dimensional drawing showing Wien filter electrode geometries.

adjustments of the beam trajectory. Afterwards the beam is collimated using one of four apertures (Ø 3 mm, 1 mm, 500 μm, and 200 μm) to reduce the fluence and beam diameter to the desired values. Each of the beam conditioning steps described above is monitored using a removable Faraday cup at this point. The beam current delivered to the Faraday cup is measured using a picoammeter (Keithley 6485) located on the platform.

Accelerating Lens. Once beam conditions on the platform are optimized the Faraday cup is removed, allowing the beam to exit the platform and enter the trumpet-shaped lens that accelerates ions to high energy (up to 120 qkeV). This accelerating lens is mounted within an insulating vacuum break which maintains the potential difference between the platform voltage and the grounded analysis chambers. This region is pumped by an Edwards EXT 255H turbomolecular pump (220 l/s) and has a base pressure of 5×10^{-7} torr. The source Einzel lens can be used to modify the focusing characteristics of the accelerating gap. In the current arrangement it is possible to obtain a quasi-parallel beam with a diameter of a few hundred micrometers for the massive cluster beam. It is also possible to change the Einzel lens potential to achieve a spot size of 10 μm. However this focal point occurs at ~20 cm from the accelerating gap which is within the beamline before the first analysis chamber. Design considerations for the platform with discussion of these focusing parameters are given in ref. [85].

A specially designed quad deflector system is mounted at the exit of the accelerating gap to accept the high energy beam and correct the trajectory of ions deflected by the accelerating lens. This deflector system, shown in Figure II-4, enables deflection of the

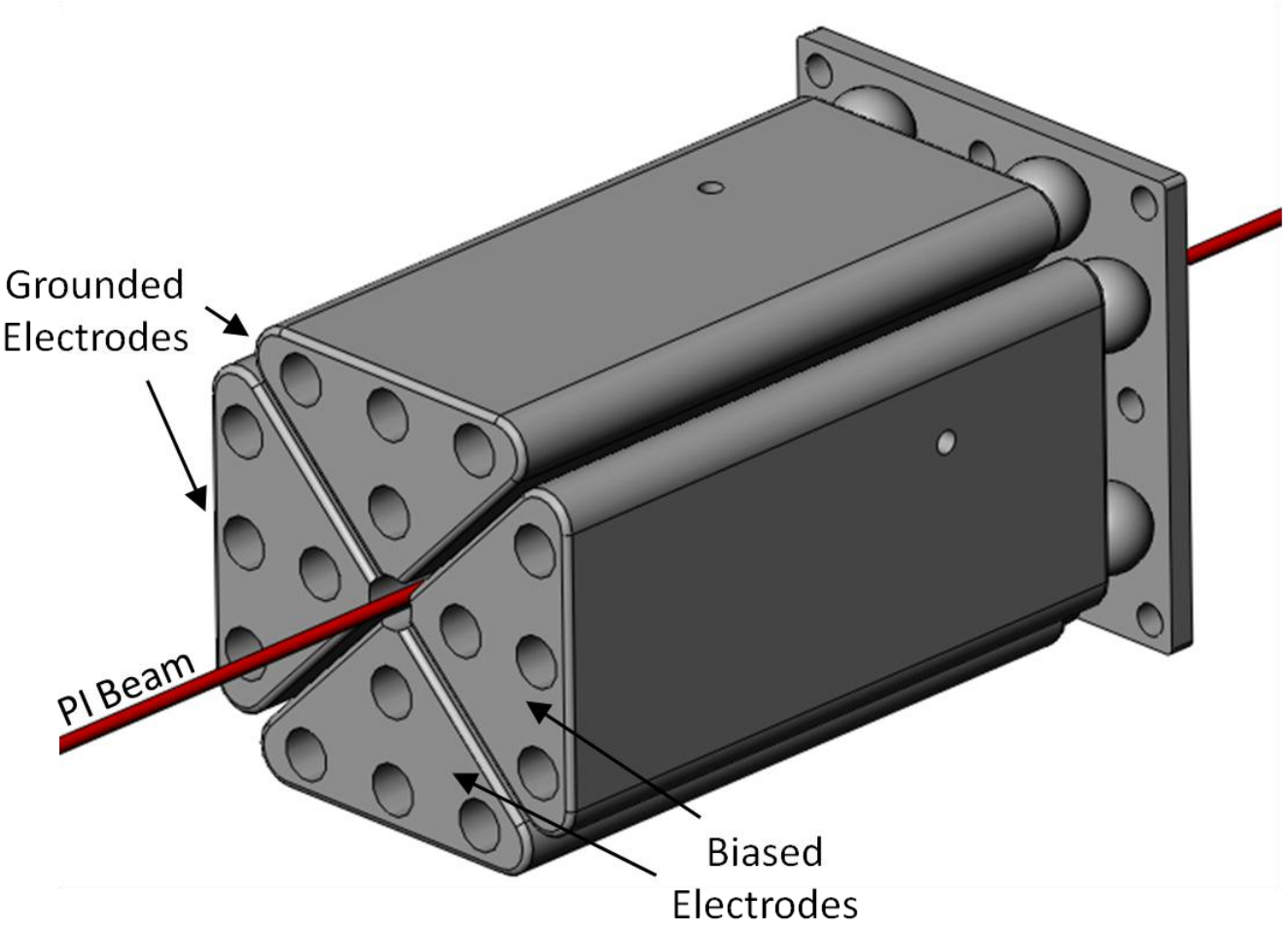

Figure II-4. Three-dimensional drawing quad deflector electrode geometries. Grounded entrance plate not shown.

high energy beam through the use of extend electrode geometries and small inter-electrode distances. Ceramic bearings are used to mount the electrodes with high mechanical precision while also providing electrical insulation from the grounded entrance and exit plates.

Safety Interlock System. Figure II-5 shows the Pegasus platform with major components labeled. From these images it is possible to observe the high voltage insulator legs and vacuum break which isolate the platform from the floor and analysis chambers, respectively. This insulation allows the entire platform, including power supplies, vacuum pumps, and vacuum chamber, to be floated to upwards of 100 kV using a high voltage power supply (Spellman SL300). All pumps and power supplies are powered using an isolating transformer which allows passage of 120 V AC power while maintaining the 100 kV DC bias between the platform and ground. The Pegasus platform is located within a grounded safety cage that features a three part safety interlock system that shuts off the floating voltage case of an unauthorized entry. The safety interlock system includes a pressure switch mounted on the sliding cage of the door which ensures the door remains closed and locked during operation. There is also a switch that ensures the high voltage grounding rod used to ground the platform is properly mounted on the wall outside of the cage during operation. The final safety interlock comprises a key activated switch required to activate the high voltage. The same key is used for this interlock and the grounded safety cage such that the key must be removed from the interlock in order to unlock the cage and gain access.

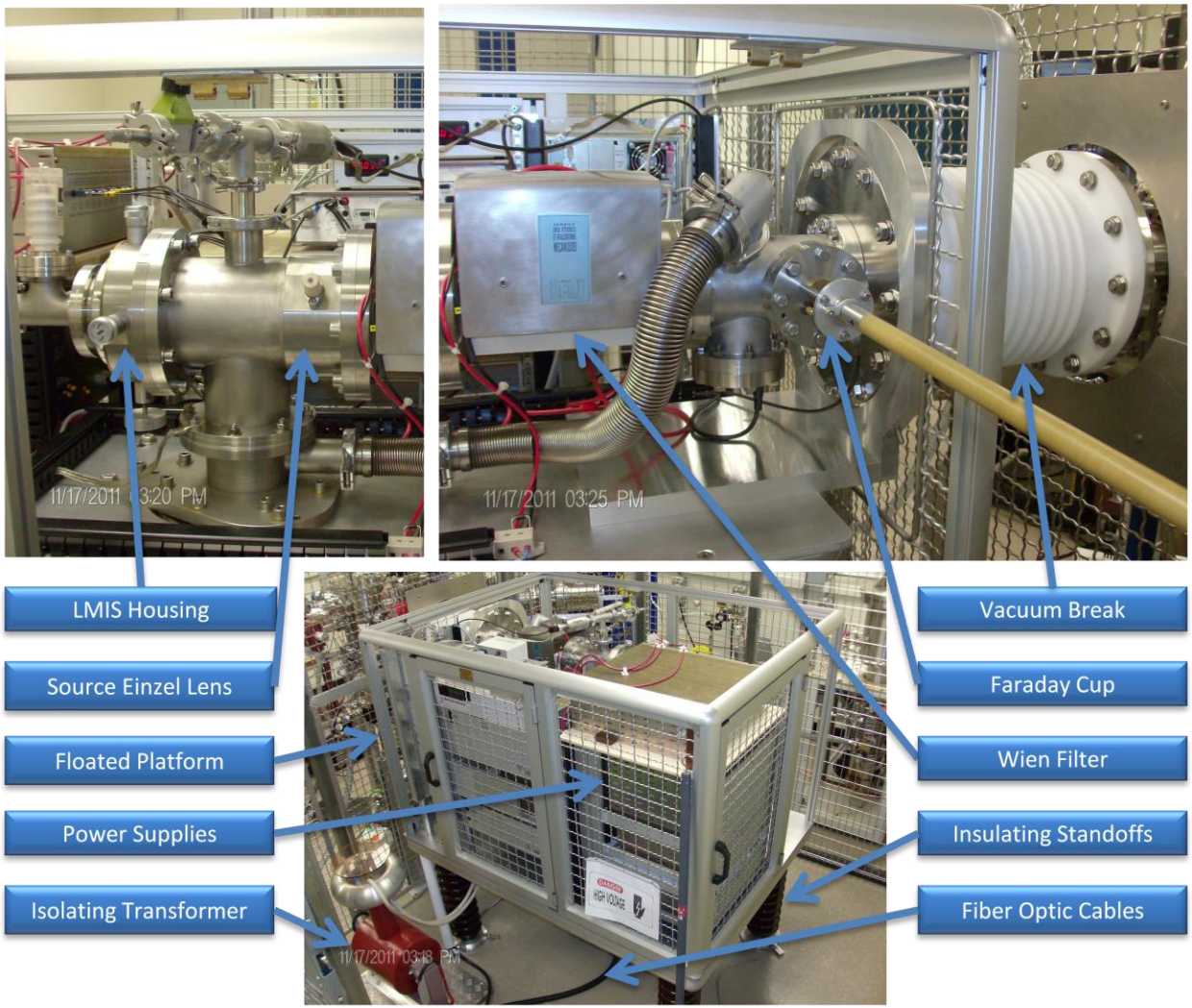

Figure II-5. Pegasus high voltage ion source platform with major components labeled.

Control Panel. All electrical components on the Pegasus platform are monitored and controlled from a central control panel located outside the grounded cage. Fiber optic cables covert reference voltages generated at the control panel into logic signal which are then transferred to the high voltage platform. The insulating properties of fiber optic cables allow the control panel to be maintained at ground while the platform is at high voltage. On the platform, the logic light pulses are converted back into reference voltages which are then input to each of the power supplies. Readback reference voltages from each power supply are transferred back to the control panel in the same manner so that applied voltages can be observed from the control panel. The beam collimator on the platform is operated using two (X and Y) motorized linear positioners (Orsay Physics). These positioners are controlled via fiber optics from a laptop at the control panel. A custom LabVIEW® interface was developed for this purpose. The vacuum region of the Pegasus platform can be isolated from the analysis chambers using a pneumatically operated gate valve which is controlled from the control panel. In this way, either the platform or analysis chambers can be vented to atmosphere while maintaining vacuum on the opposite side of the gate valve.

Pulsation Chamber. Immediately following the beamline gate valve is a pulsation chamber which houses deflectors for correcting the beam trajectory as well as a pulsing electrode. Prior to entering the deflector/pulsing plate assembly, the beam passes through a multi-slit collimator mounted on a linear positioner to eliminate stray projectile trajectories. This collimator has two slits (0.5 mm and 1 mm widths) that intersect the beam at a 45^{o} angle relative to horizontal. The deflector/pulser electrode

arrangement in Figure II-6 shows the 30 mm x 30 mm plates which are positioned 5 mm apart. The horizontal deflector plates feature one plate which is grounded while the opposite plate is biased. Vertical deflection is achieved by biasing the deflector above the beam. Time-varying high voltage logic pulses are applied to the plate below the beam line using a high voltage switch (Behlke HTS 151-03-GSM) which is driven by a pulse generator. This pulsing procedure, known as the differential impulse sweep method,[87] disperses the beam in the vertical dimension above and below the beam axis such that only a small fraction of projectiles are able successfully pass through a collimators farther down the beamline. In the case of the first analysis chamber, three different apertures (Ø 5 mm, 500 µm, and 200 µm) mounted on an X,Y,Z stage (Huntington VF-108 and Huntington TS-275-155) ~30 cm from the pulsing chamber perform the collimation. For the second analysis chamber, a 2 mm aperture positioned ~2 m from the pulsing chamber performs the collimation. The pulsing potential is varied from + 1 kV to -1 kV at a rate of 10 kHz when operating in linear time of flight (ToF) mode and 3 kHz when operating in reflectron ToF mode. A slower pulsing frequency is required in reflectron mode because the extended flight times of ions reduce the acquisition duty cycle. Under these pulsing conditions, the beam current is reduced via collimation in order to achieve a projectile impact rate of ~1,000 Hz. Following pulsation, the individual projectiles pass through a second quad-deflector unit which directs projectile trajectories towards the analytical surface and aligns the bombardment region with ion/electron extraction optics.

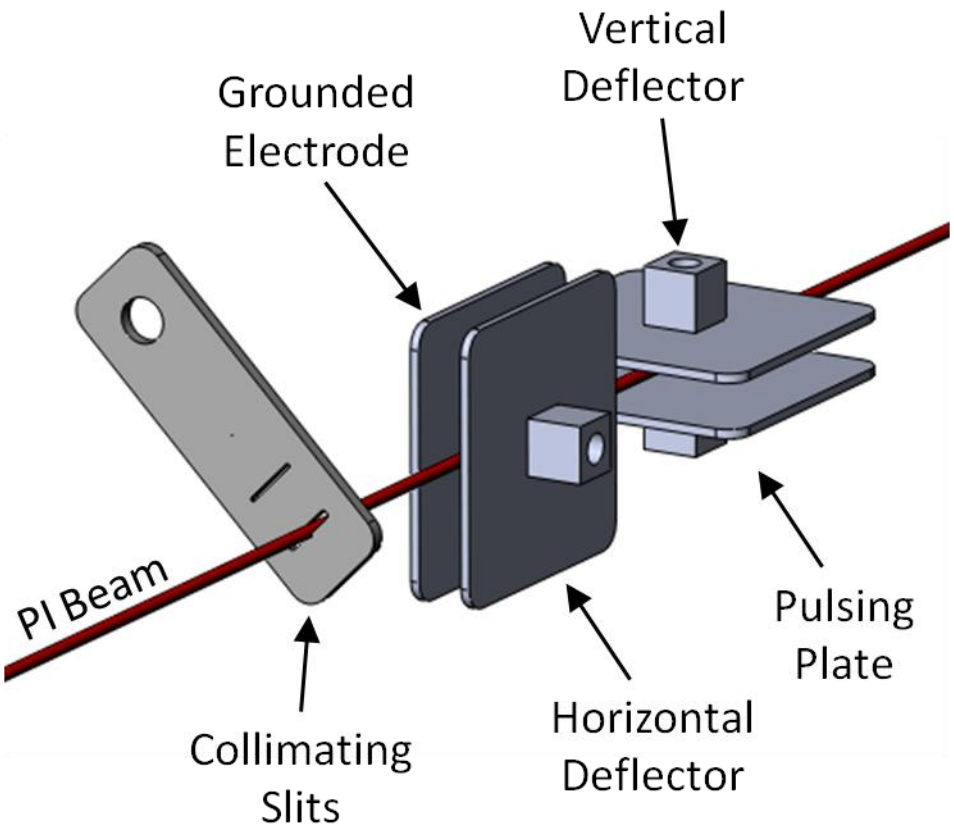

Figure II-6. Three-dimensional drawing showing pulsing chamber electrode geometries.

First Analysis Chamber

Single projectiles isolated in time and space impact the analytical surface in one of two analysis chambers. The first chamber (base pressure of ~10^{-6} torr) features a high resolution reflectron ToF leg and an electron emission microscope. The second chamber (base pressure of ~10^{-7} torr) features a linear ToF leg and a flexible mounting system, enabling fundamental investigations which require instrument geometry modifications.

Sample Holder. In the case of the first analysis chamber, samples are mounted within the custom designed sample holder shown in Figure II-7. Up to four 1 cm^2 samples can be loaded into the holder and then introduced to the vacuum chamber via a load-lock system. This system is operated by attaching the sample holder to a linear push/pull rod (MDC K-CRPP-1) and then clamping the rod's KF 25 flange to a small introduction chamber on top of the analysis chamber. This chamber is evacuated by a rotary vane mechanical pump to a pressure of ~10^{-2} torr. A vacuum gate valve isolating the introduction chamber from the main analysis chamber is opened and the sample holder is transferred into the high vacuum chamber. The holder design features vertical grooves down either side which mate to grooves on the holder dock mounted in the analysis chamber. As the holder is lowered into the dock using the push rod, spring-loaded set screws press the holder towards the front of the dock such that the holder can repeatedly be introduced to the same mounting position with precision. The sample dock is mounted on a Ø 0.500" ceramic rod which provides mechanical support and electrical insulation. Positioning of the entire assembly is controlled using an X, Y, Z stage (Thermionics FLMM-275-50-1 and Thermionics XY-B450C-T450T-2.5-1).

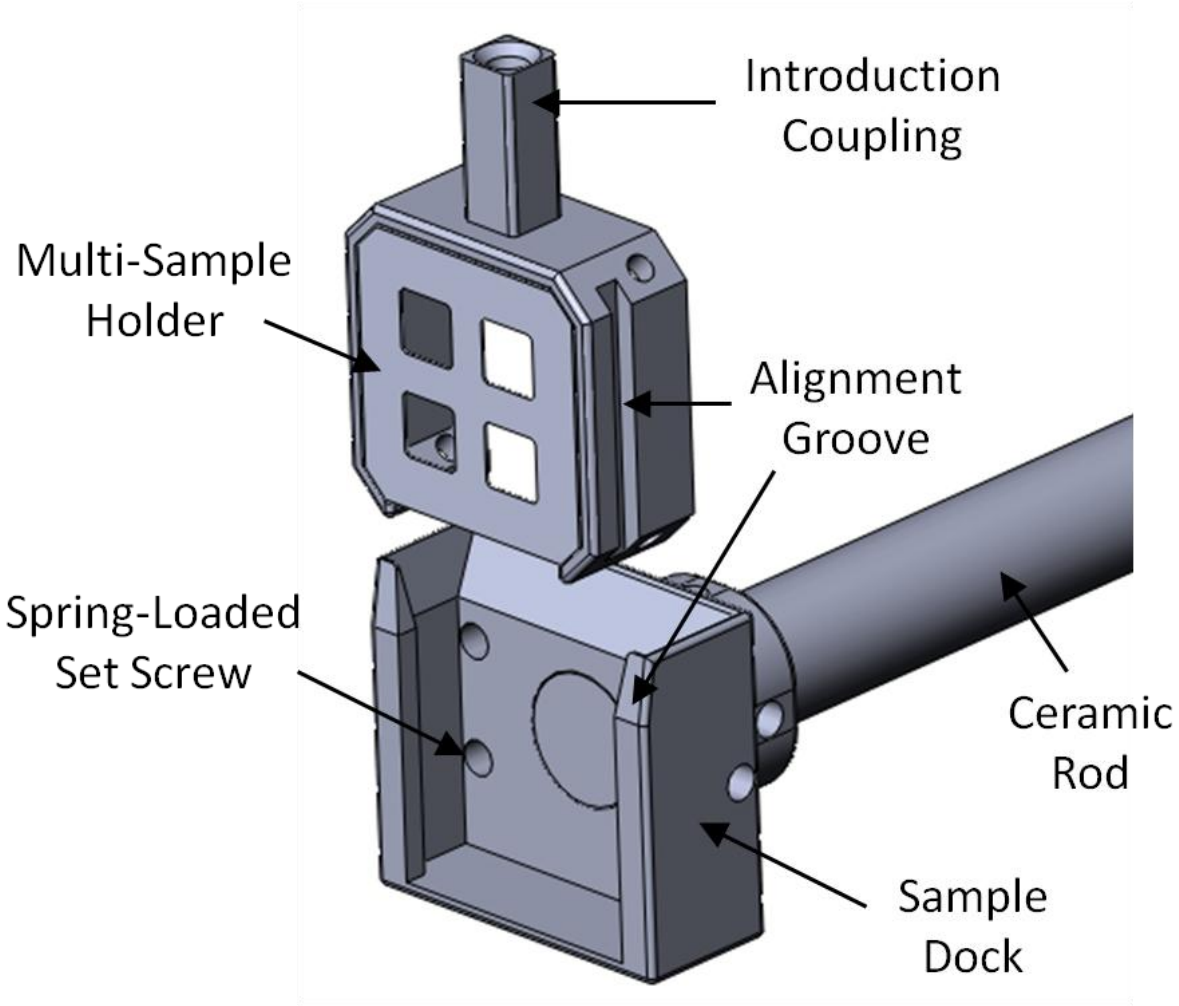

Figure II-7. Three-dimensional drawing of sample holder and docking station.

Electron Optics. For negative ion analysis, the sample holder and dock are biased at -10 kV and the holder surface is positioned ~7 mm away from a grounded extraction electrode with a 3 mm aperture. This aperture acts as an immersion objective lens, accelerating electrons and negative ions away from the surface, through the hole, and into a series of ion optics which separate and analyze the different species. The trajectories of the 10 keV particles are focused to a point within a magnetic prism using a three element Einzel lens. The weak magnetic field (~30 Gauss) deflects the trajectories of the high velocity electrons by 45^{o}, transferring the image of the surface impact location through the achromatic point of the prism. This process leaves the low velocity ion trajectories relatively unperturbed. Electrons continue on to a series oflenses and deflectors which transfer the electrons to a microchannel plate-based detector. The lens system is capable of operating as an electron emission microscope (EEM) when lens values are properly adjusted. This capability was not utilized for data presented in this dissertation. Instead, the lens system was operated in "collection" mode where settings are adjusted to optimize electron transmission without regard for imaging characteristics. For details on the electron mapping capabilities of the EEM, readers are directed to refs. [88-92].

The three-dimensional rendering in Figure II-8 shows the spatial arrangement of the various ion optics contained in the first analysis chamber. The EEM consists of the extraction lens, magnetic prism, two Einzel lenses, and set of deflectors shown in the figure as well as an additional Einzel lens, set of deflectors, and microchannel plate (MCP) detector not shown. The electron detector (Beam Imaging Solutions BOS-18)

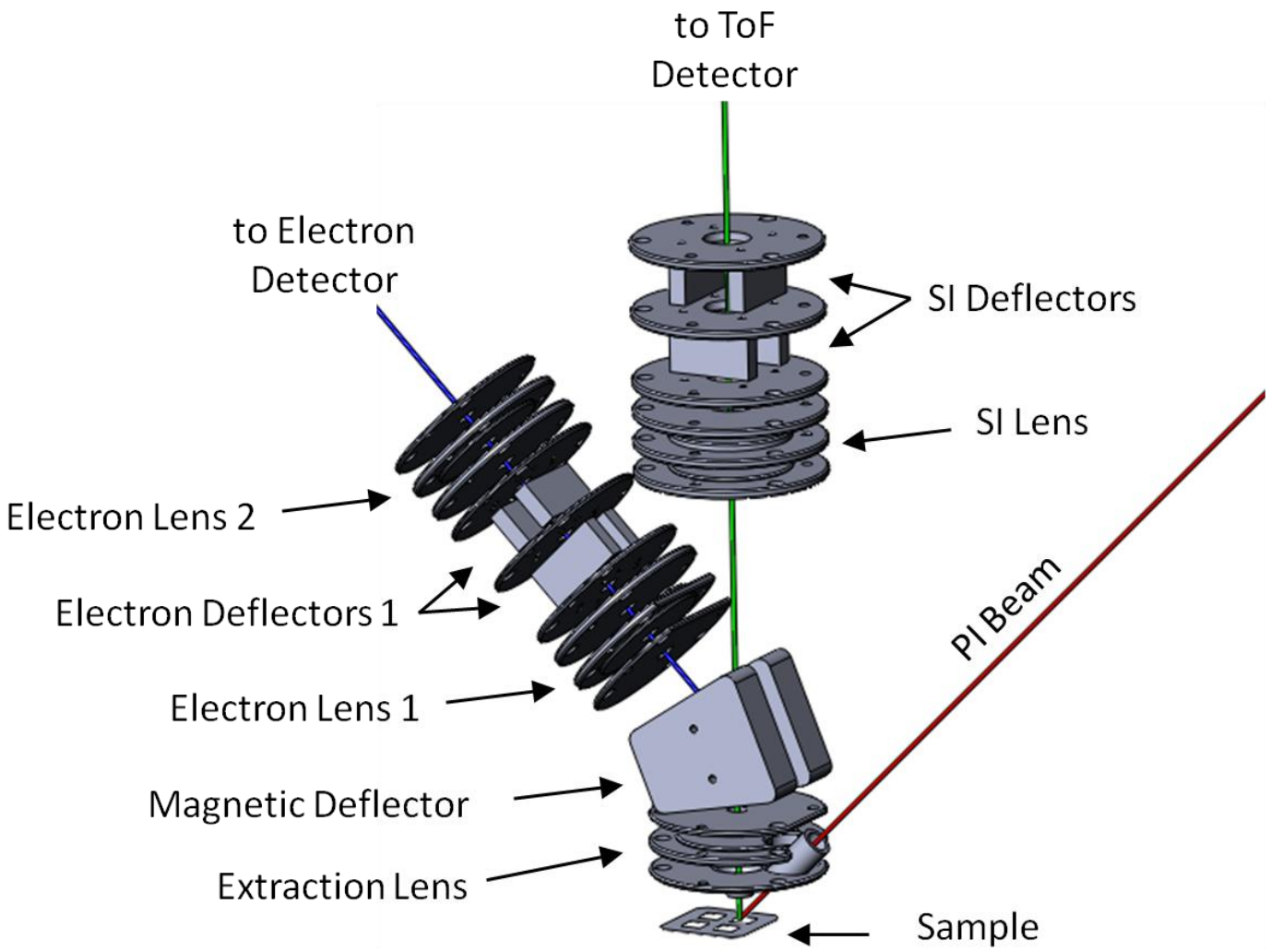

Figure II-8. Three-dimensional drawing showing geometries for all electrodes housed in the first analysis chamber.

features a phosphorus screen which enables visualization of electron impacts on the detector. This capability assists in optimization of the electron lenses and deflectors in collection mode. In imaging mode, the phosphorus screen projects a magnified image of the electron trajectories. A high speed CMOS (complementary metal-oxide-semiconductor) camera can be used to record the illuminated spots generated by electron impacts. Multiple electrons are detected per projectile impact and, using a center of mass calculation, the projectile impact location on the surface can be determined. This impact location coordinate is coupled with the ToF mass spectrum for each projectile impact, so that a chemical map of the surface can be constructed. Again, this capability was not utilized for the current data set. The electron detector was simply used to generate a signal for initiating the ToF measurement.

Reflectron ToF. Returning to secondary ions exiting the magnetic prism, they next enter a second Einzel lens that corrects the trajectories which were focused to satisfy electron transmission. SIs then pass through a set of deflector plates on the way to a dual stage reflectron (IPNO)[93] mounted 1.13 m from the sample surface. The reflectron is tilted at an angle of 1.4^{o} below the beam axis so that ions enter the ion mirror, are reflected, and exit the ion mirror at an angle of $\sim 2.8^{o}$ above their entrance trajectory. The SI detector is mounted in a grounded housing above the flight tube axis, 63 cm from the entrance of the reflectron. The custom built detector assembly shown in Figure II-9 features a chevron MCP stack (Photonis 34251) with eight detection anodes mounted on a multi-angle tilt stage. The stage is designed to allow for tilt about the transverse horizontal axis (pitch, φ) and the vertical axis (swing, θ) using linear and

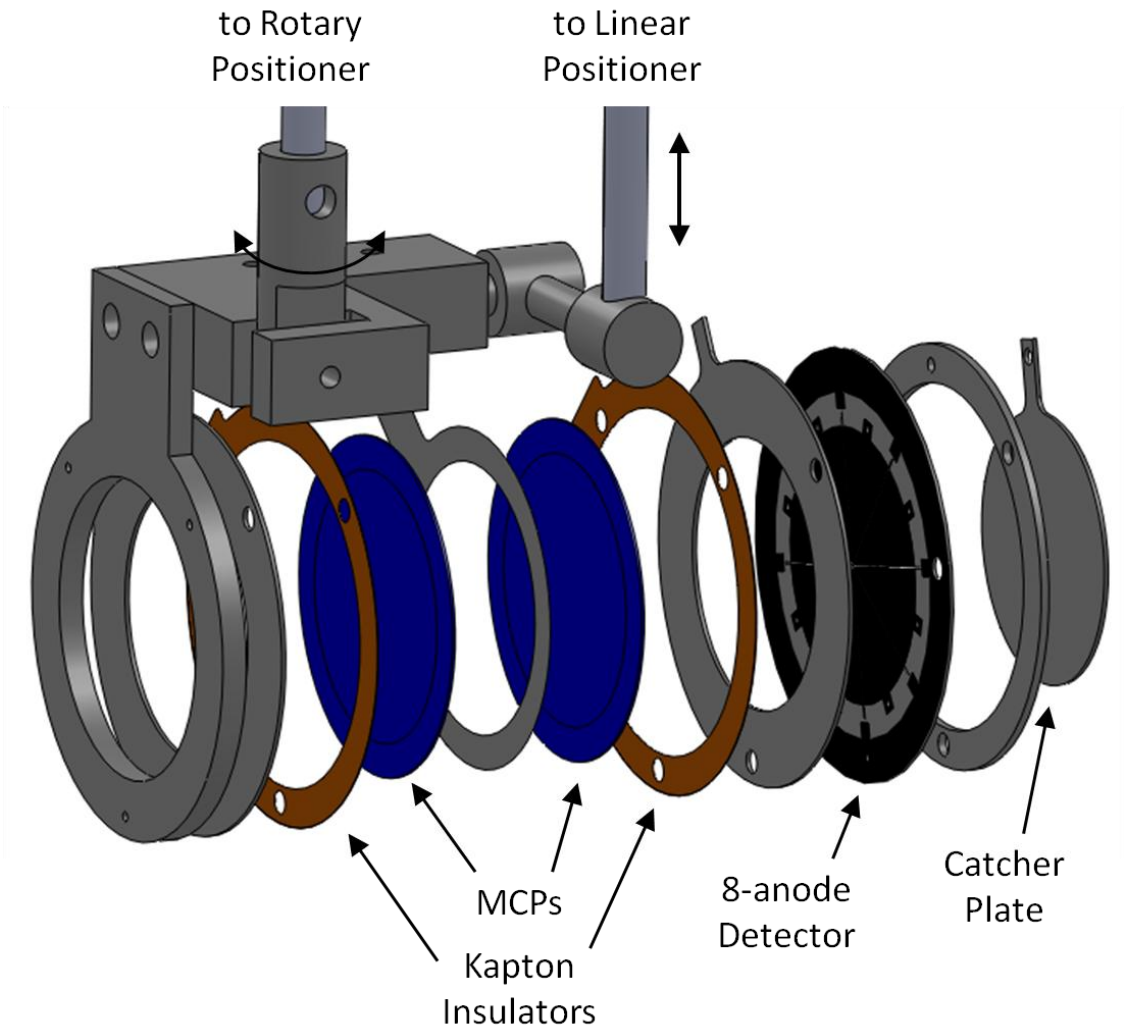

Figure II-9. Three-dimensional drawing of reflectron ToF multi-anode detector.

rotary vacuum positioners. This capability allows the detection surface of the MCPs to be aligned parallel to the sample surface, thereby maximizing the achievable mass resolution in reflectron mode.

Multi-Anode Detector. A new, high active area detector was developed to improve the detection efficiency of SIs. The new mounting scheme employed also has better mechanical stability which reduces the probability of MCP breakage over the previous generation detectors. The anode is based on previous designs which utilize printed circuit board (PCB) technology to form isolated conductive surfaces on top of an insulating substrate. The PCB material between the conductive anodes is removed to reduce charge accumulation from electron fluxes which are deposited on the insulating layer. The anodes independently transmit the transient voltage spikes from the MCP output to signal processing electronics. In this way, the dynamic range of the pulse counting detector is determined by the number of individual anodes on the circuit board.

In the current instrument eight-anode boards are employed both in the reflectron detector and in the linear SI detector of the second analysis chamber. An eight-anode detector was chosen because the constant fraction discriminator (CFD) and time-to-digital converter (TDC) units used both contain from eight individual processing ports. Taking advantage of precise machining procedures to reduce the size of gaps between the individual anodes to just 400 μm, an active area of over 96 % is achieved in the current multi-anode. Table II-1 shows how this detector compares to earlier versions.

The transient voltage signal from each anode is transferred to a separate port within an 8-port CFD (Ortec CF8000) which converts the signal to a TTL logic pulse.

Table II-1. Comparison of Various Eight-Anode Detector Designs

Detector Generation	Distance Between Anodes (mm)	% Active Area	% Dead Space
1	1.83	78.2	21.8
2	0.84	89.8	10.2
3 (current)	0.40	96.1	3.9

This signal is then transferred to the TDC (Orsay Physics CTNM4) which time stamps each signal relative to the start signal received with a time resolution of either 250 ps or 400 ps, depending on the TDC model. The time-stamped SI signals are then saved on a personal computer by the data acquisition software. For more details regarding the electronics and signal processing methodology, please refer to Rickman's dissertation.[84]

Second Analysis Chamber

By moving the sample dock out of the beamline, it is possible to pass projectiles through the first analysis chamber and on to a second analysis chamber. The transfer tube between the chambers houses a high voltage Einzel lens which collects and refocuses the ~5 mm quasi-parallel beam of projectiles back down to a few hundreds of micrometers within the second analysis chamber. A three-dimensional drawing of this Einzel lens, which can be biased to ~35 kV, is shown in Figure II-10. As mentioned above, the second analysis chamber is designed to be easily modified according to the study at hand. For the purpose of this dissertation, the most commonly used experimental arrangement of this chamber will be described.

The assembly shown in Figure II-11 allows for the analysis of samples mounted within the multi-sample holder, as in the first chamber. Samples can be introduced through a load-lock system here as well. The sample holder is again mounted on an X,Y,Z stage, but is instead positioned 10 mm away from a grounded extraction grid (90 % transmission, Precision Eforming MN17). Unlike the first analysis chamber, both positive and negative SI analysis can be performed in chamber 2. The potential applied

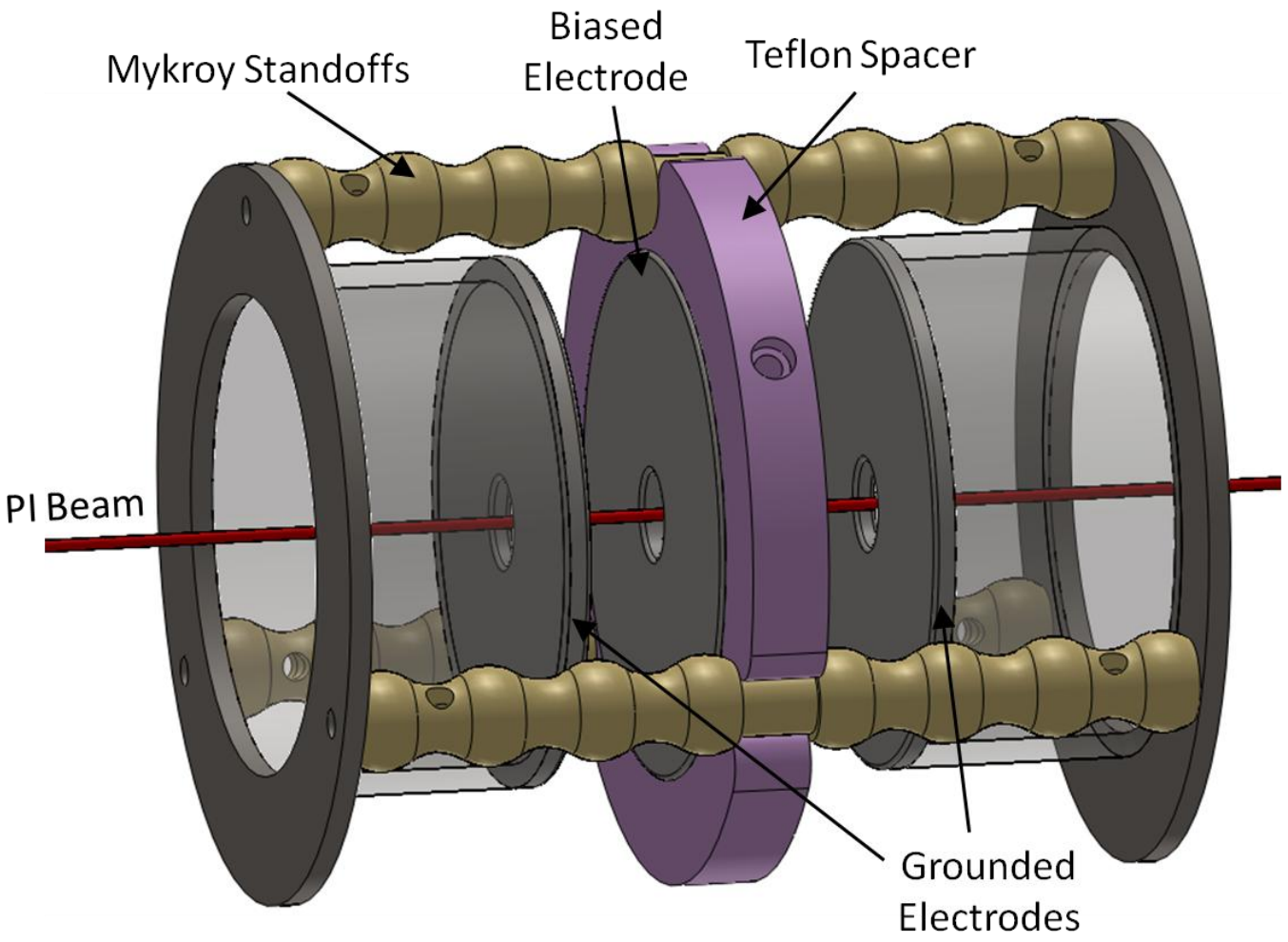

Figure II-10. Three-dimensional drawing of the high voltage Einzel lens mounted between analysis chambers 1 and 2.

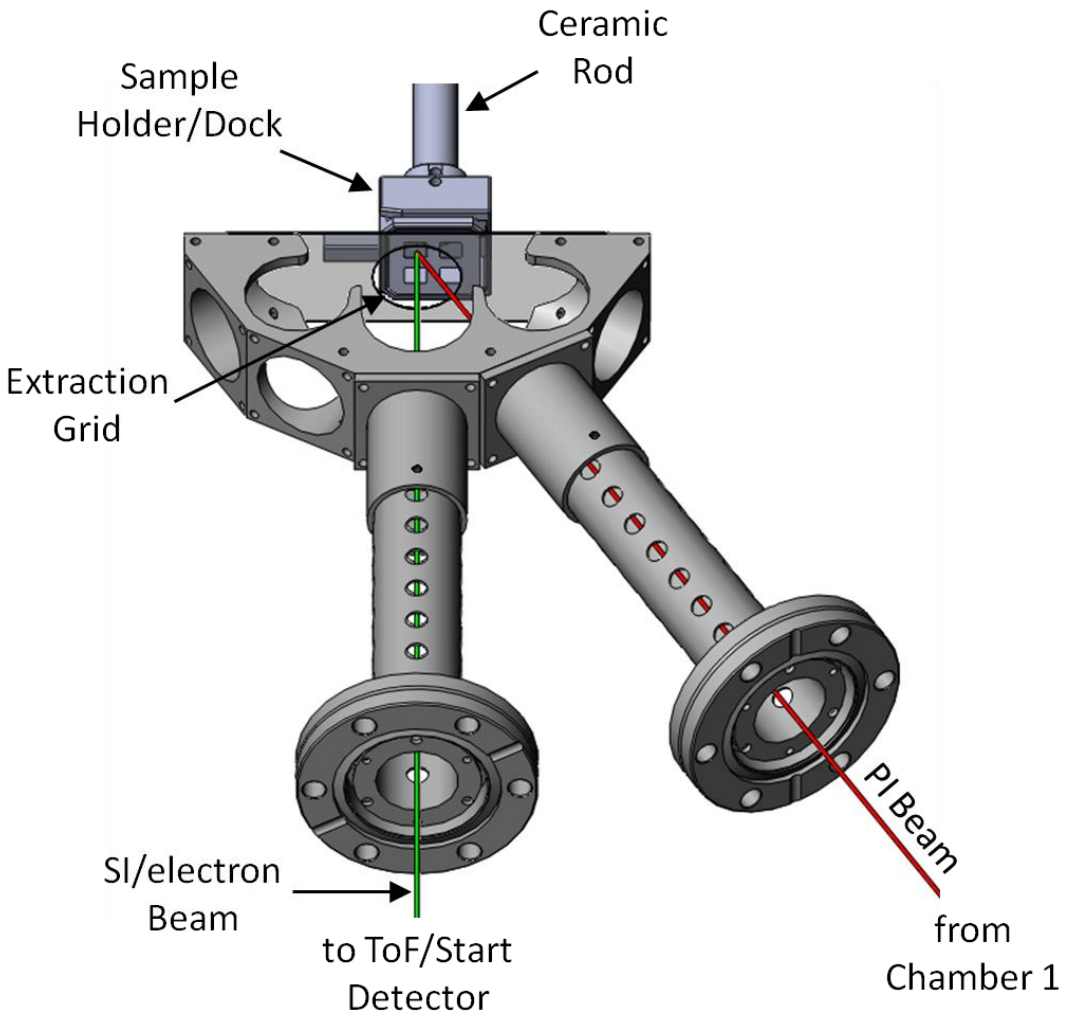

Figure II-11. Three-dimensional drawing of second analysis chamber instrumental geometry.

to the sample holder (± 10 kV) determines whether cations or anions are accelerated from the surface towards the SI detector 1.02 cm away. In the case of positive mode, protons are used to initiate the ToF measurement for heavier ions. This is done by deflecting the protons 30^{o} above the beam axis to a separate chevron MCP (Photonis 30286) detector with a single anode. The 0 .126 Tesla field required for this deflection is generated by a 12,000 turn electromagnet. Deflection of the protons also results in a mass-dependent reduction in ion transmission. Significant losses are observed for ions below approximately 50 amu. Negative ion analysis is achieved by reducing the current through the magnet wire so that electrons and not hydrogen atoms are turned 30^{o}. Ion transmission is recovered under these conditions.

The flexibility of the second analysis chamber is visible in Figure II-11. The central mounting block is machined so that the sample can be accessed from multiple different angles along the horizontal axis as well as above and below the block. The block is mounted via vented tubes which mate Con Flat flanges on the chamber. This mounting system gives excellent stability and alignment of ion optics.

Instrument Operation

A schematic drawing of all internal components of the massive gold cluster SIMS instrument is shown in Figure II-12. This figure reveals the overall complexity of the device which arises from the number of components involved. To assist in the operation of the Pegasus platform, outlines of the startup, shutdown, and emergency shutdown protocols are included as Appendix A. These outlines give step by step procedures for initiating and terminating experiments with the high voltage ion source. A

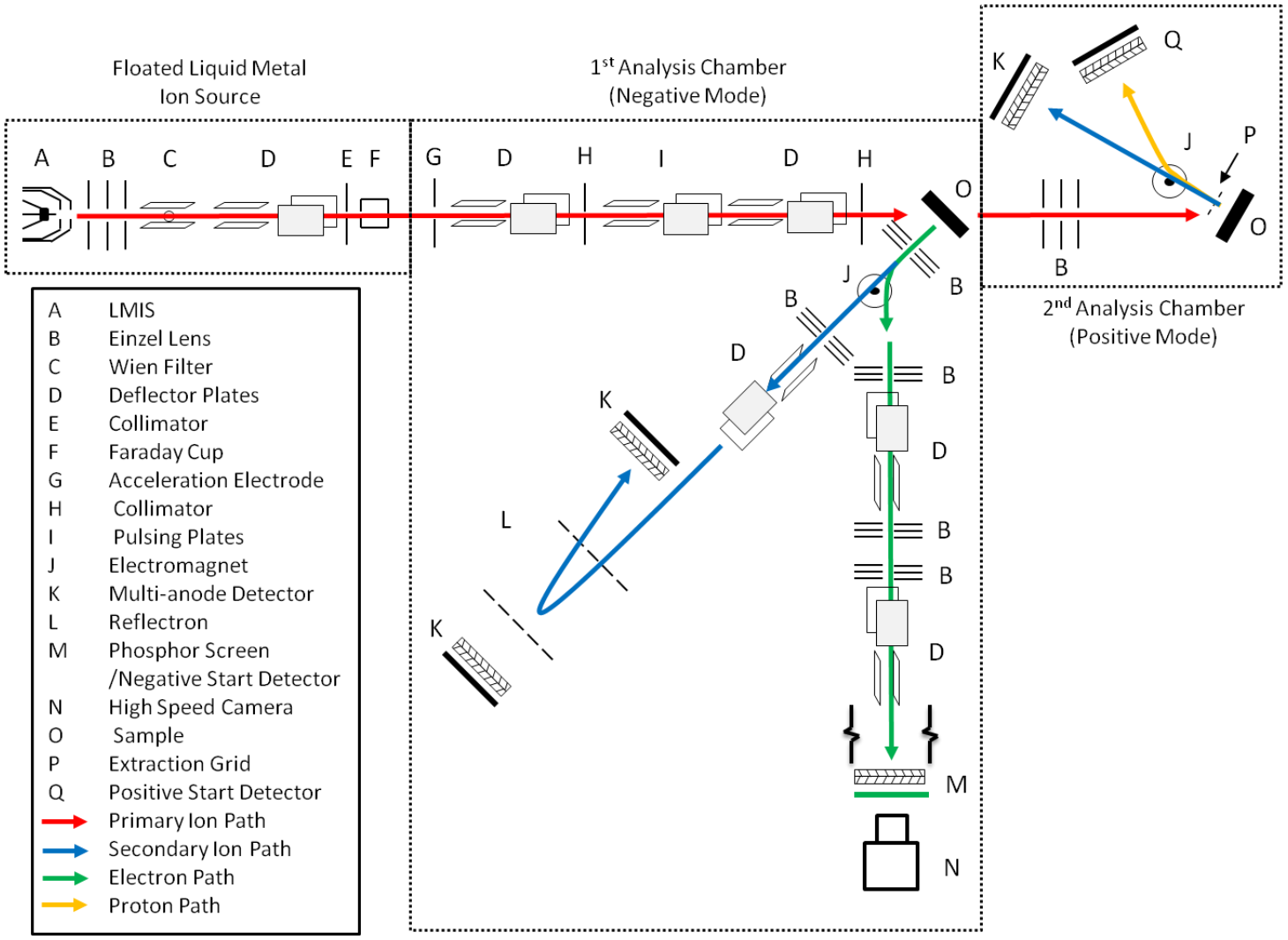

Figure II-12. Schematic overview of all components of the custom gold cluster SIMS instrument at Texas A&M University.

procedure for the acquisition of SIMS data is more difficult to provide, as experiments goals tend to vary depending on the study at hand. However, as a sample case, the general procedure for acquiring a mass spectrum using the Au_{400}^{+4} projectile in the first analysis chamber is provided below.

Using the startup procedure in Appendix A, it is possible to obtain a 1-2 nA Au_{400}^{+4} beam at the sample holder in chamber 1 with the collimator set to the largest aperture (5 mm). This can be confirmed using a picoammeter to measure the current from the beam focused onto the sample dock. Once an adequate beam is obtained at the dock, the pulse generator is initiated to reduce the beam fluence and the sample holder can be introduced via the load-lock system. All lenses, deflectors, and detectors as well as the reflectron and sample voltages can be turned on at this point. Provided that the applied voltages have not changed since that last instrument operation, some signal should be detected on both the electron and SI detectors.

A PI spectrum can be obtained by using the pulser as a start signal and the electron signal as a stop. This procedure measures the time it takes projectiles to travel from the pulser to the sample surface. A peak should be observed in the ToF spectrum corresponding to Au_{400}^{+4}. To optimize this peak, all beamline deflectors (except those on the platform) should be varied to maximize the number of electron counts observed. Once a maximum is reached, the deflectors and magnet current should be varied to obtain the highest number of electron counts. At this point a smaller collimator (typically Ø 500 µm) can be introduced in place of the 5 mm collimator to eliminate stray projectiles, reduce the number of impacts, and purify the ToF spectrum. This is done by

varying the position of the collimator in the Y and Z dimensions until a maximum is found. The electron count rate should be ~1,000 counts /s. If the count rate is low the PI or electron beam trajectories need to be optimized. If the count rate is high, additional collimators should be introduced on the platform or before the pulsing chamber. Once a count rate of 1 kHz is achieved, the SI deflectors are varied to maximize the number of SI counts.

A SI spectrum of ~10,000 events can now be obtained to test the experimental performance. Further optimization of the SI deflectors should be performed so that equivalent numbers of a selected ion are detected across all eight detector anodes. This anode distribution measurement is automated with the data acquisition software. Once the SI mass spectrum is sufficiently optimized, the total mass spectrum of 10^6-10^7 impact events can be collected. At a rate of 1 kHz, a spectrum of 10^6 events can be acquired in ~17 minutes.

As an example of a mass spectrum which can be acquired in this manner, Figure II-13 shows a mass spectrum of glycine which was vapor deposited on a stainless steel support. From this spectrum it is possible to measure the mass resolution of the reflectron ToF analyzer to be ~1433 at mass 149. This value is significantly higher than the 200-300 mass resolution observed for a 1 m linear ToF (as in chamber 2). Also visible from this spectrum is the prolific production of glycine molecular clusters out to $(5M-H)^-$. A more detailed description of the types, yields, and multiplicities observed from glycine and other test samples is provided in Chapter IV.

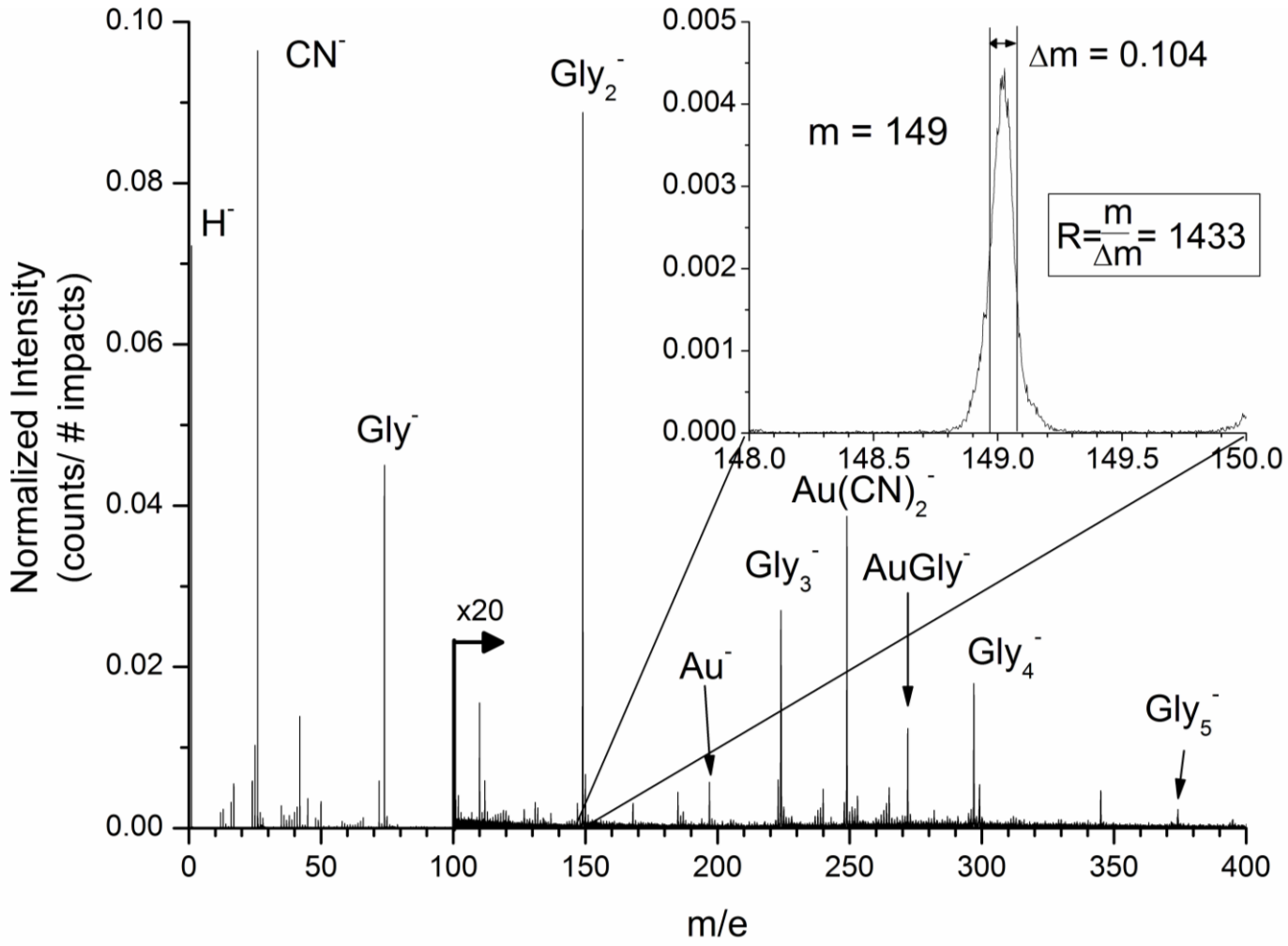

Figure II-13. Mass spectrum of glycine vapor-deposited on a stainless steel substrate analyzed by 340 keV Au_{400}^{+4}.

Event-by-Event Bombardment Detection Methodology

Using individual projectile impacts to generate meaningful mass spectra constitutes a unique SIMS approach. This event-by-event bombardment detection methodology allows for the observation and measurement of fundamental phenomena that are not accessible when a beam or pulse of multiple projectiles is used. Each projectile impact event is characterized by the mass analysis of all SIs generated by a single PI impact before the next PI impacts the surface. Specialized electronics and software are used to acquire the data.

Specifically, ion signals are collected in a digital, pulse counting mode such that detection of individual SIs are recorded into a mass spectrum for each impact event. This process is repeated up to 10^7 times with all events summed to give a total mass spectrum. The data from each individual mass spectrum is retained by the Total Matrix of Events (TME) data acquisition software developed in-house. Using a custom data analysis software program (Surface Analysis and Mapping of Projectile Impacts, SAMPI),[92] this information can be recalled in a variety of ways. One method is to measure the total ion multiplicity. This plot is a histogram which shows the number of ions detected for each impact event. A further option is the selected ion multiplicity function, which shows how many ions of a given type are emitted for each impact. The average values of the total and selected ion multiplicities are the total and selected SI yields, respectively. Examples of these multiplicity measurements are displayed in Chapter IV.

It is also possible to generate coincidence mass spectra, which are composed of only the impact events which generate a selected ion of interest. The coincidence

spectrum is a display of all ions which are co-emitted with the ion of interest. Monitoring ion co-emission allows one to observe chemical distributions on surfaces at the spatial resolution of individual impact events. An example of how ion co-emission can be used to extract information about nanometric surface features is given in Chapter VI. Coincidence analysis has been expanded in the SAMPI program to include investigations of double-coincidence (spectra that produce two ions of interest) and anti-coincidence (all spectra that do not produce the ion of interest).

Time of Flight Mass Spectrometry

All mass spectra reported in the following chapters were acquired using time of flight (ToF) mass analysis. As the name suggests, ToF mass spectrometry measures differences in the times of flight for ions of different masses but identical kinetic energies. For a reflectron ToF arrangement, the total time of flight measured for a given ion is a sum of the time spent in each of the accelerating, first field free, reflectron, second field free, and decelerating regions, as shown in Equation 2.9.

$$t_{tot} = t_{acc} + t_{ff1} + t_{ref} + t_{ff2} + t_{dec} \tag{2.9}$$

The time spent in the accelerating region is determined by the Coulomb force acting on the charged particle in a uniform accelerating field. (Equation 2.10)

$$t_{acc} = \sqrt{\frac{2md_{acc}^2}{qV_{acc}}} \tag{2.10}$$

where m is the particle mass, d_{acc} is the distance across the accelerating region, q is the charge of the particle, and V_{acc} is the accelerating voltage applied. The time spent in the

first and second field free regions can be found by assuming all potential energy of the accelerating field is translated into kinetic energy, as shown in Equation 2.11.

$$K = P = qV_{acc} = \frac{1}{2}mv^2 \tag{2.11}$$

where v is the velocity at the exit of the accelerating region. Rearranging and inserting the velocity definition (Equation 2.12), we obtain Equation 2.13.

$$v = \frac{d}{t} \tag{2.12}$$

$$t_{ff1,ff2} = d_{1,2}\sqrt{\frac{m}{2qV_{acc}}} \tag{2.13}$$

where $d_{1,2}$ is the distance travelled in field free region 1 or 2. Time spent in the reflectron depends on the depth to which the ions penetrate (d_{ref}). This depth is given by Equation 2.14.

$$d_{ref} = \frac{K}{qE} = \frac{qV_{acc}}{qV_{ref}/L} = \frac{V_{acc}L}{V_{ref}} \tag{2.14}$$

where L is the length of the reflectron. The time required to penetrate to this depth is

$$t_{ref/2} = \frac{d_{ref}}{v/2} \tag{2.15}$$

and the total time in the reflectron is

$$t_{ref} = 2t_{ref/2} = \frac{2d_{ref}}{v/2} = \frac{4d_{ref}}{v} \tag{2.16}$$

The time spent in the decelerating region (created by the voltage applied to the font of the detector) is given by

$$t_{dec} = \frac{(d_{dec}^2\sqrt{2m})(\sqrt{V_{acc}+V_{dec}}\pm\sqrt{V_{acc}})}{V_{dec}\sqrt{q}} \tag{2.17}$$

where d_{dec} is the distance travelled in the decelerating region and V_{dec} is the voltage applied to the detector. Incorporating all times we obtain Equation 2.18.

$$t_{tot} = t_{acc} + t_{ff1} + t_{ref} + t_{ff2} + t_{dec}$$

$$= \sqrt{\frac{2md_{acc}^2}{qV_{acc}}} + d_1\sqrt{\frac{m}{2qV_{acc}}} + \frac{4d_{ref}}{v} + d_2\sqrt{\frac{m}{2qV_{acc}}} + \frac{(d_{dec}^2\sqrt{2m})(\sqrt{V_{acc}+V_{dec}}\pm\sqrt{V_{acc}})}{V_{dec}\sqrt{q}} \quad (2.18)$$

This equation shows that the ToF for a given ion is proportional to the square root of its mass. The mass of any peak in a time of flight spectrum can be determined using a mass calibration to convert the ToF spectrum to a mass spectrum. Practically this is done by fitting Equation 2.19 to two or more known ToF/mass data points.

$$t_{tot} = a\sqrt{m} + b \quad (2.19)$$

where a is the slope and b is the intercept of a line. Depending on the spread of times measured for a given ion, the resultant peak in the mass spectrum will have a mass resolution (R) of

$$R = \frac{t_{tot}}{2\Delta t} = \frac{m}{\Delta m} \quad (2.20)$$

where Δt and Δm are the full widths of the time or mass peak at half the maximum intensity, respectively. The mass resolution parameter is a measure of the precision with which an ion mass is measured, with higher mass resolution being desirable.

CHAPTER III

BI-DIRECTIONAL EMISSION FROM THIN CARBON FOILS IMPACTED BY MASSIVE PROJECTILES*

Introduction

It has long been recognized that the impact of hypervelocity massive clusters on solids differs in the resultant dynamics from those occurring for atomic or small cluster ions of comparable velocities[89, 94-96]. Yet little is known about this impact regime, beyond observations of impact craters/holes and reports of abundant secondary ion (SI) emission[47, 91, 97]. Visualization of impacts of individual massive clusters, e.g. 100 – water molecule ions or Au_n^{+q} ($100 \leq n \leq 1000$; $q = 1\text{-}10$) at velocities of 10 to 100 km/s on thin carbon films shows craters of size and depth roughly correlated with the projectile size and energy[98-100]. Remarkably, their range significantly exceeds that of equal velocity atomic ions, a feature attributed to the clearing-the-way effect[58, 59]. This effect is not observed for polyatomic ions with up to seven atoms[101] but is observed in simulations of 13 atoms[102]. The effect also seems to disappear for projectiles with >200 keV/atom[103]. The morphological observations and molecular dynamic simulations indicate an energy deposition process in a hydrodynamic flow[61]. A distinct characteristic of the massive cluster solid impact is the extreme energy density and pressure transient. This provides a

* Part of this chapter is reprinted with permission from "Bidirectional Ion Emission from Massive Gold Cluster Impacts on Nanometric Carbon Foils" by J.D. DeBord, S. Della-Negra, F.A. Fernandez-Lima, S.V. Verkhoturov, and E.A. Schweikert, 2012. *The Journal of Physical Chemistry C*, Copyright [2012] by the American Chemical Society.

medium for chemical reactions under non-classical conditions as they may occur, for example, in impacts of hypervelocity nano-sized dust particles in interstellar space[104].

Data from previous impact experiments and simulations are 'unidirectional', that is, they either record the surface morphology or ejecta from the impact side, or they document projectile transmission with visualization of holes in carbon foils or excisions in virus particles[105]. In this study we recorded the concurrent SI emission in both directions from a thin carbon foil so that we could evaluate the parameters of the massive cluster – solid interaction which affect the SI emission, with particular attention given to the projectile size and target thickness.

Experimental Details

A schematic for the experimental setup is shown in Figure III-1. The instrument consists of a dual time of flight (ToF) mass spectrometer which permit the analysis of SI's emitted from both sides of a thin carbon foil bombarded by massive clusters. A negative accelerating potential is applied to the thin foil sample while 90% transmission grids on either side of the target are maintained at ground. The transmission and detection efficiencies are equivalent for both ToF legs. For the presentation and discussion of the results we have decided to designate SI ejection back in the direction of incoming projectiles as backward emission and SI ejection in the opposite direction where, for some experiments, the projectiles exit the foil as forward emission. The impact of a massive cluster is detected via electron emission in the backward direction after magnetic deflection. The electron signal given by a microchannel plate detector serves as the start for both the forward and backward ToF measurements. This procedure

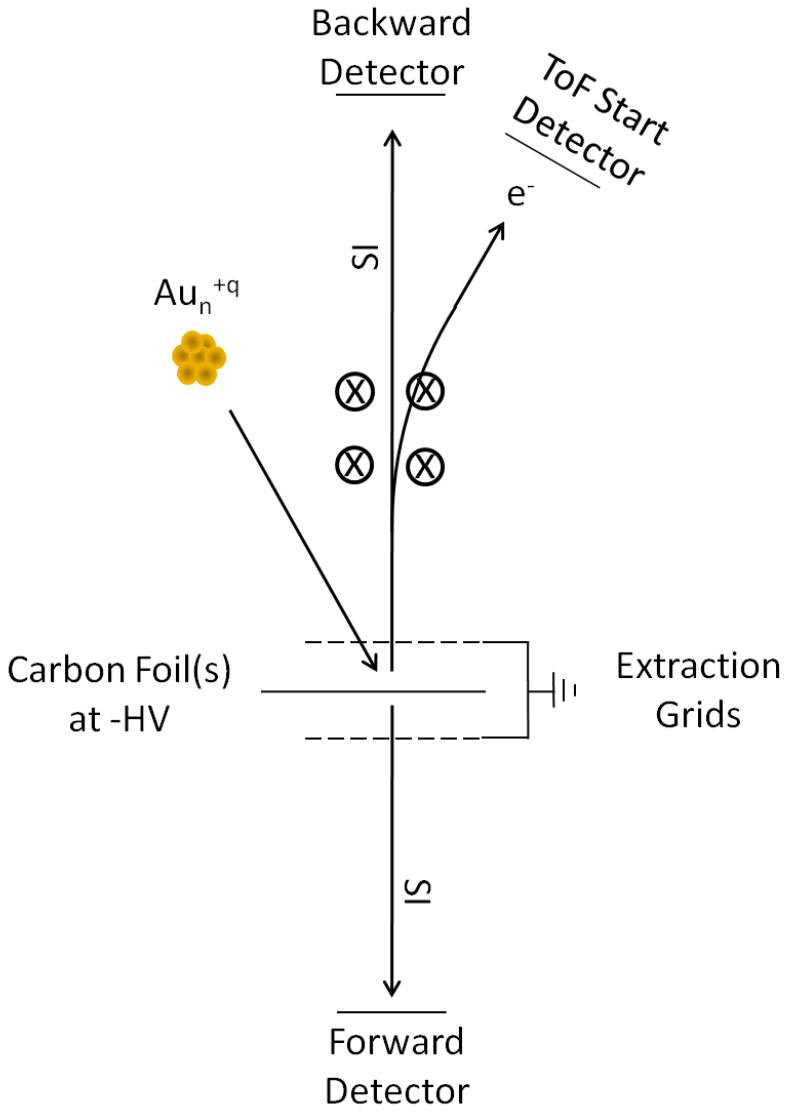

Figure III-1. Experimental setup for bi-directional ToF analysis of SI's from thin carbon foils.

creates the same impact trigger independent of sample thickness and avoids artifacts from holes in the foils. In order to monitor the fate of projectiles that pass through the foil, a second thin foil is utilized. For these experiments, both foils are positioned between the grounded extraction grids with the distance between the two foils estimated at 100 µm.

Amorphous carbon foils with thicknesses of 5, 15, 20, and 40 nm were obtained from the Arizona Carbon Foil Company (Tucson, AZ). The thickness values given by ACF were monitored by Rutherford Backscattering (and the energy loss by Au_1 at 0° incidence) with the range of the thicknesses being ±15% for a large area. Foils for mass spectrometric analysis were supported on an 81% transmission nickel grid. The 30° incidence angle of the projectile increases the path length by 15% (5, 15, 20, and 40 nm become 5.8, 17.3, 23.1, and 46.2 nm, respectively).

Gold cluster beams were provided by the 130 kV Pegase platform described in ref. [85]. The different beams used include Au_3^+ and massive Au_n^{+q} clusters with n/q = 30, 50, 100, and 200. Beam specifications (energy, charge, etc.) are presented in Table III-1 with the median charge states extracted from data given in ref. [57].

The experiments have been performed event by event with a bombardment rate of less than 1000 Hz whereby the term event refers to the impact of a single projectile and subsequent detection of emitted secondary ions prior to the impact of the next projectile. The impact frequency is achieved through the use of collimators and kHz range pulsation. A more detailed description of the event by event methodology can be found in ref. [73]. The n/q selection is monitored by the projectile ToF measurement

Table III-1. Gold Cluster Projectile Characteristics

n/q	<q>	energy/q (keV)	energy/at (keV/at)	total energy (keV)	$n^{2/3}$ area[a]	$E_T/n^{2/3}$ energy per unit area[a]
30	3	110	3.7	330	20	16.43
50	3	110	2.2	330	28	11.69
100	4	110	1.1	440	54	8.10
200	5	110	0.55	550	100	5.50
100	4	125	1.25	500	54	9.21

[a] The cross-sectional area and energy per unit area are obtained assuming a ballistic model (i.e., projectile range is proportional to the energy per unit area).

between the pulsing plates and the detection of electrons emitted backward from the target.

Characterization of the Amorphous Carbon Foil Targets

Separate samples were prepared for transmission electron microscopy (TEM) analysis by mounting the 5, 15, and 20 nm foils on copper TEM support grids. These samples were impacted with 130 qkeV Au_{100q}^{+q} projectiles at an impact angle of 45^{o}. Bright field TEM images were then obtained using an FEI Tecnai G^2 F20 ST FE-TEM for impacted and non-impacted samples of each thickness. All analyses were performed with 200 keV electrons incident normal to the foil surface.

Transmission electron microscopy was used to investigate the projectile bombardment. The foils were found to be largely intact, uniform, and free from pinholes. The TEM images provided in Figures III-2, III-3, III-4, and III-5 show surface features created by 130 qkeV Au_{100q}^{+q} projectiles in 5, 15, 20, and 40 nm carbon foils, respectively. For the 5 nm foil, the amorphous carbon is completely removed from the tracks such that a hole is created, as shown by the lack of grainy features inside the hole. Similar holes were also observed for the 15 and 20 nm thick carbon foils, though some amorphous carbon material remains within the tracks either as a result of surface relaxation or incomplete penetration (Figures III-3 and III-4). The diameters of holes in the 5 nm foil range from 3-12 nm with the majority of holes measuring ~10 nm. Hole diameters in the 15 nm foil are reduced by nearly a factor of two relative to holes in the 5 nm foil. Interestingly, the density of holes observed in the 5 and 15 nm foils are similar

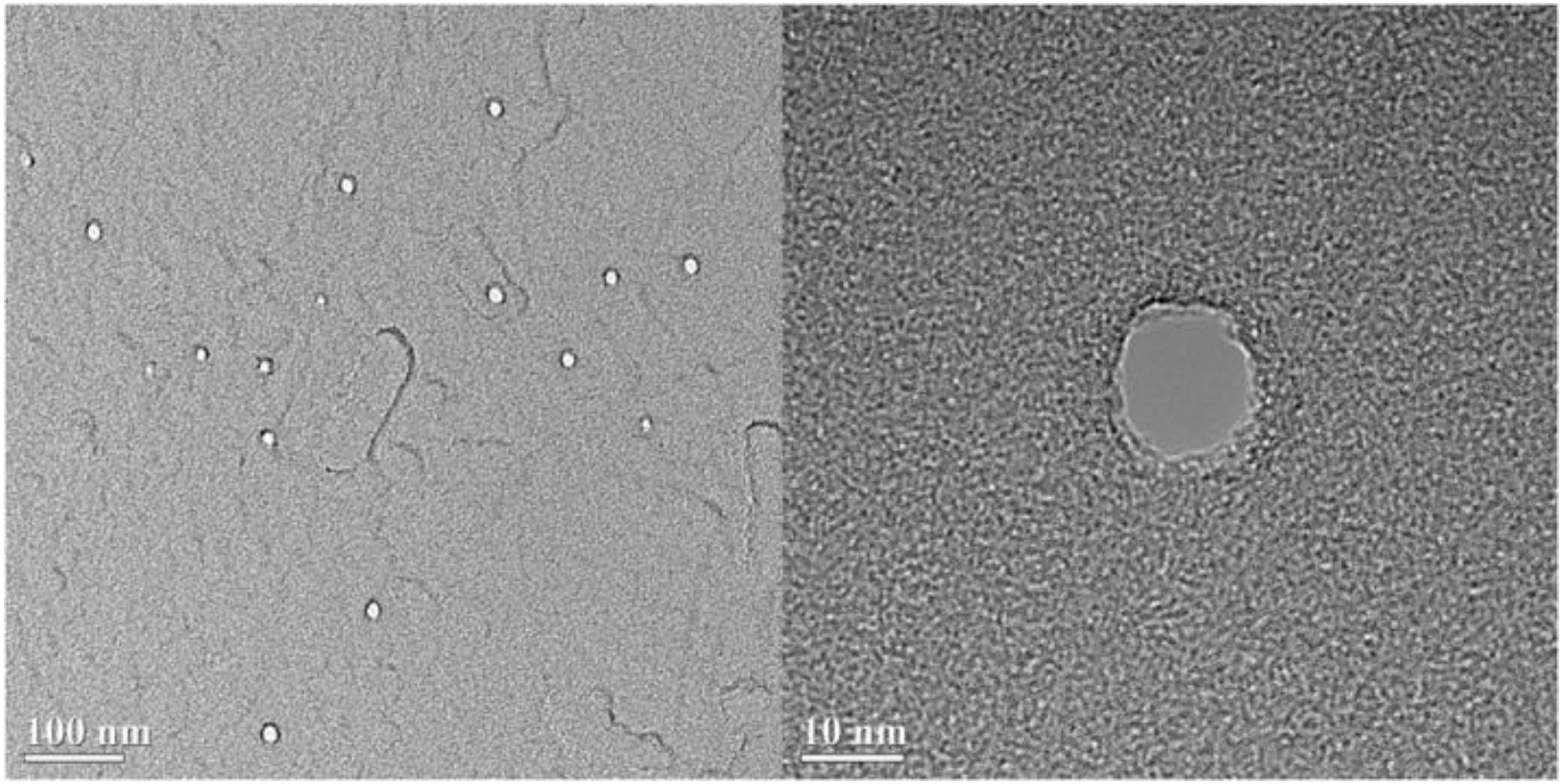

Figure III-2. (left) TEM image obtained from a 5 nm thick carbon foil impacted with 130 qkeV Au_{100q}^{+q} projectiles. Projectile tracks appear as lighter circular regions. (right) High magnification image of a hole in the 5 nm foil shows the width of the hole to be approximately 10 nm.

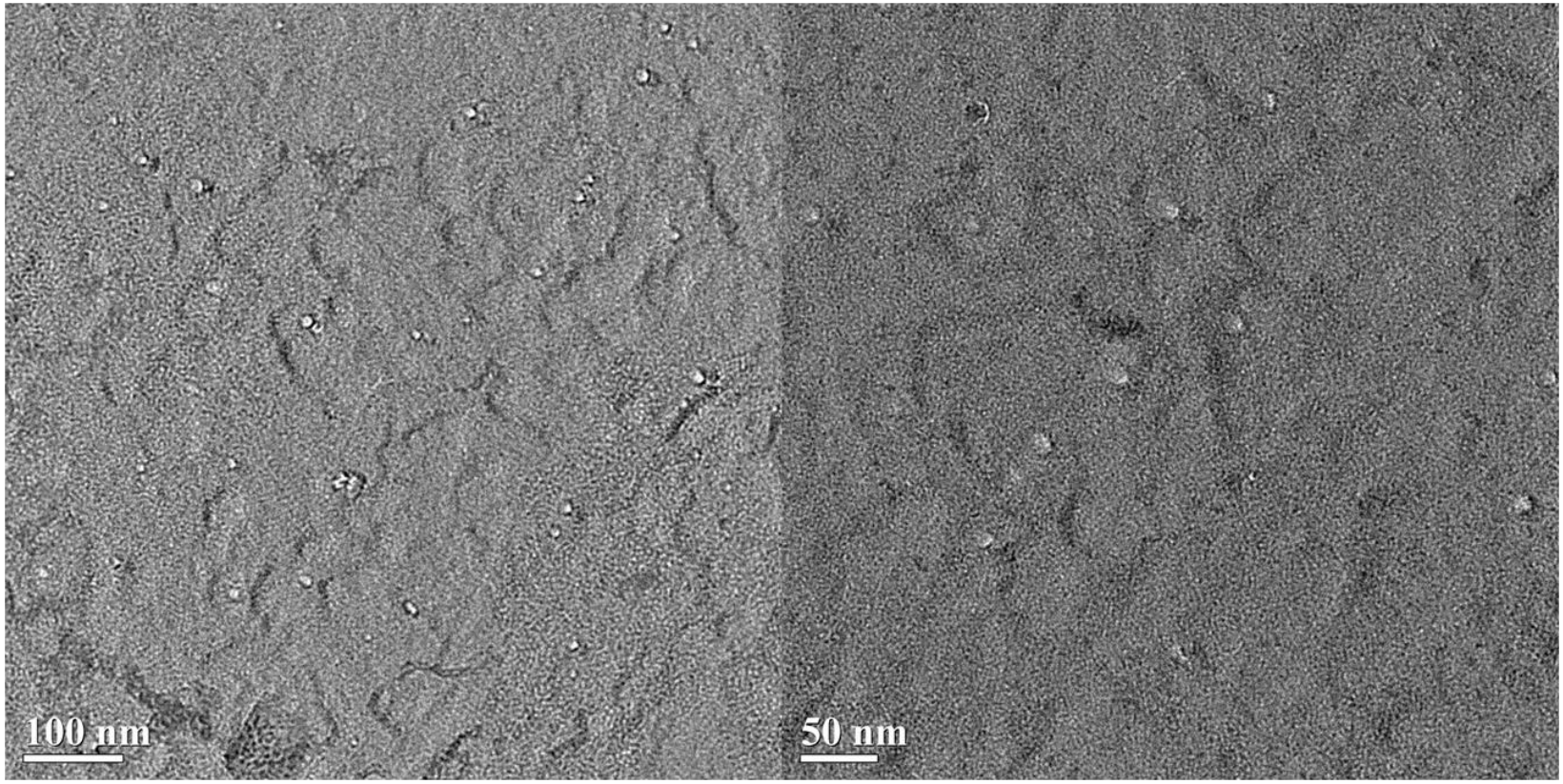

Figure III-3. (left) TEM image obtained from a 15 nm thick carbon foil impacted with 130 qkeV Au_{100q}^{+q} projectiles. Projectile tracks appear as lighter circular regions. (right) High magnification image of partial holes in the 15 nm foil.

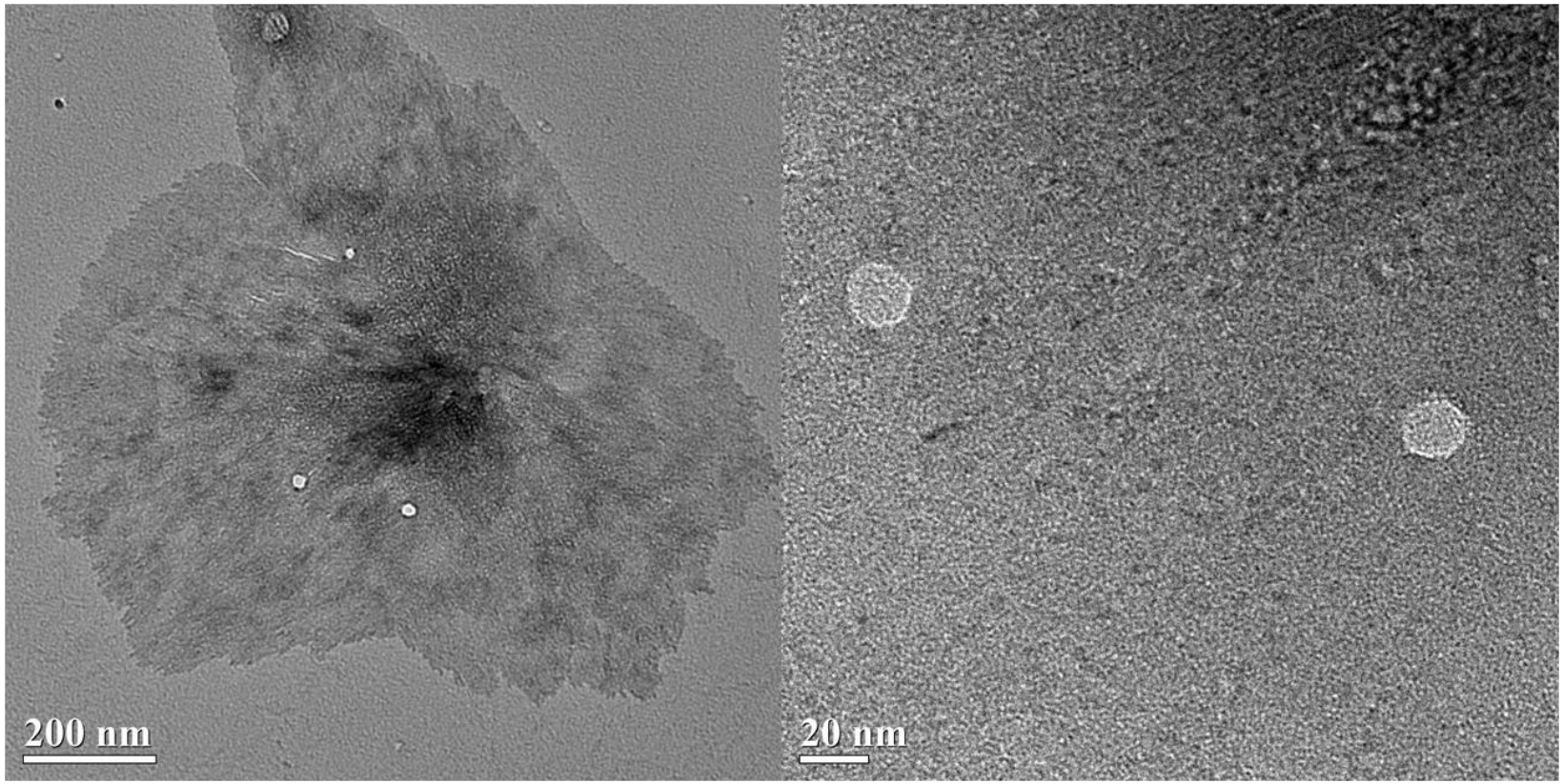

Figure III-4. (left) TEM image obtained from a 20 nm thick carbon foil impacted with 130 qkeV Au_{100q}^{+q} projectiles. Projectile tracks appear as lighter circular regions. (right) High magnification image of partial holes in the 20 nm foil.

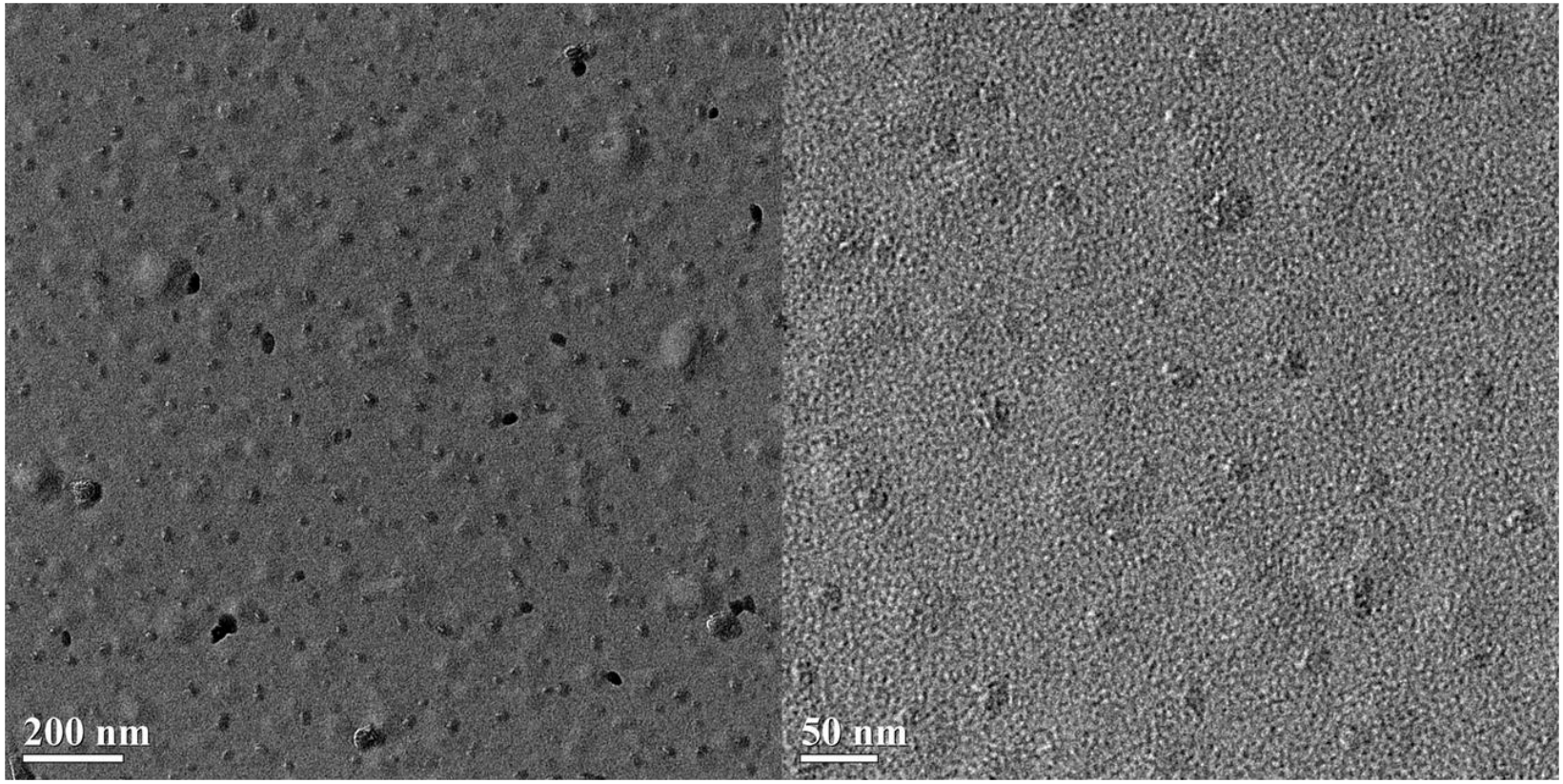

Figure III-5. (left) TEM image obtained from a 40 nm thick carbon foil impacted with 130 qkeV Au_{100q}^{+q} projectiles. (right) High magnification image of projectile tracks in the 40 nm foil.

with ~10^9 holes/cm^2, but the number of holes in the 20 nm foil is drastically reduced. In fact, the tracks shown in Figure III-4 are only visible due to their contrast against a rare graphitic defect in the 20 nm foil. This result suggests that most of the projectiles are unable to pass through the 20 nm foil, and therefore brackets their range between 15 and 20 nm. TEM images of the 40 nm amorphous carbon foil (Figure III-5) reveal graphitic particles formed during the manufacturing process which appear as dark features in the micrograph. These features represent only a small portion of the total surface area and are not expected to largely influence SI emission or projectile ranges. Projectiles tracks are barely visible in the 40 nm foil, especially under high magnification. These images provide direct evidence of projectile penetration through the impacted foils and provide a basis for interpreting the results that follow.

The simultaneously acquired forward and backward mass spectra from 125 qkeV Au_{100q}^{+q} projectiles impacting a 15 nm thick carbon foil are presented in Figure III-6. The carbon clusters emitted backward (Figure III-6a) show an odd-even oscillation similar to that observed with various other energy deposition mechanisms (e.g. collisional and electronic sputtering, laser ablation) on different carbon structures[48, 106-108]. The well-studied backward cluster emission, with maxima of C_n^- occurring for even values of n, is explained by cluster ion fragmentation within the accelerating region[107]. The distribution of co-emitted clusters in the forward direction differs significantly from the backward distribution. Another significant difference between the spectra is the near absence of H^- and C^- in the forward mass spectrum. As shown in Figure III-6, the emission of molecular ions (lauryl sulfate, $C_{12}H_{25}SO_4^-$, mass 265; alkylbenzene

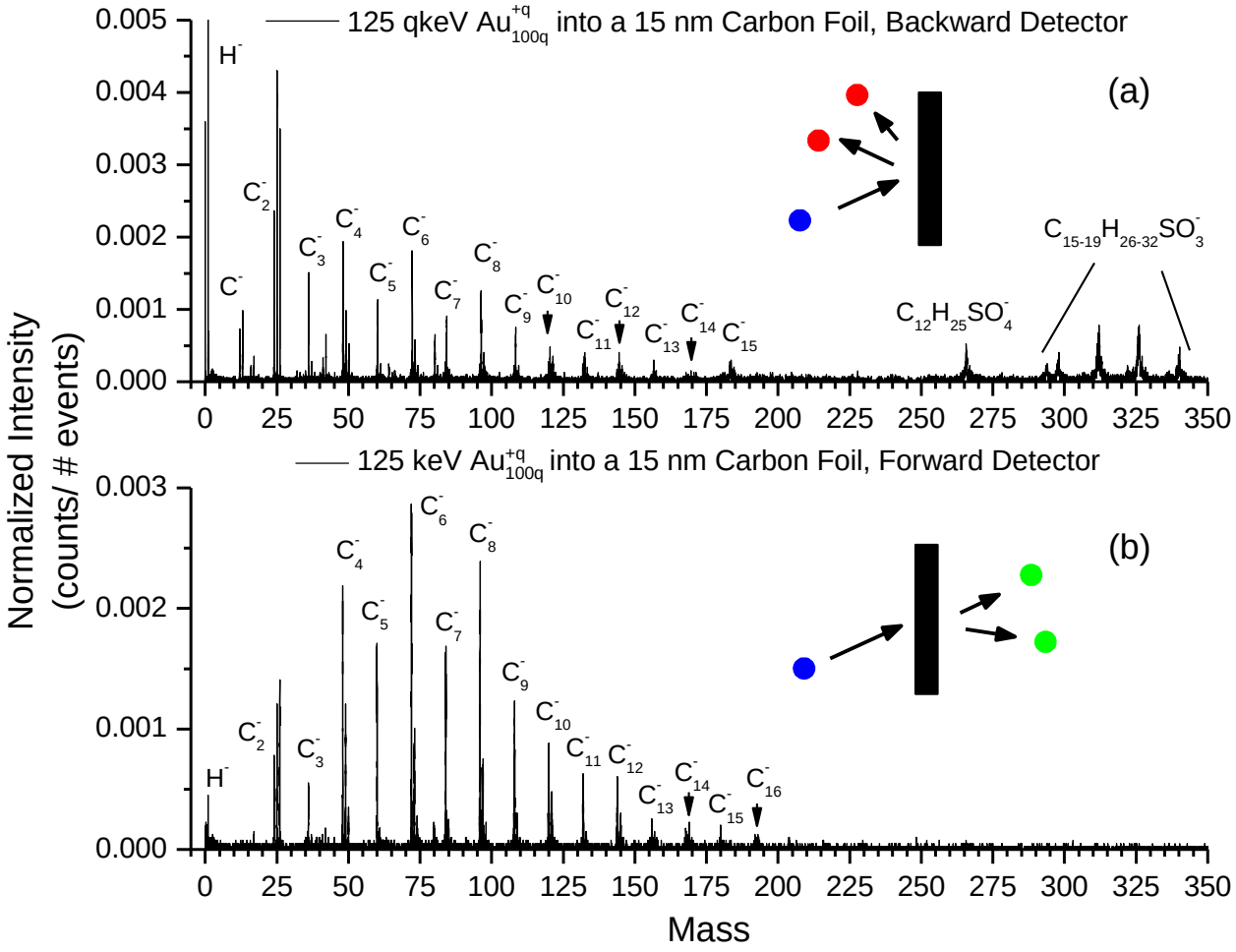

Figure III-6. Negative mode ToF mass spectrum obtained in the (a) backward and (b) forward directions from a 15 nm thick carbon foil impacted by 125 qkeV Au_{100q}^{+q} projectiles.

sulfonate derivatives, $C_{15-19}H_{26-32}SO_3^-$, masses 294, 298, 312, 326, 340) attributed to surfactant chemicals is observed in the backward direction but not in the forward direction. All experiments have been performed with the same conditions of target preparation without surfactant observation in the forward direction. The reproducibility of the results has been measured in the forward direction, with a maximum yield variation of ±12.5 %, but no alteration of the carbon cluster distribution. In the backward direction, the ratio $Y(C_n)/Y(C_nH)$ changes by ~ 20 %, with this variation being related to the contribution of the surfactant.

The experimental setup described allows for the study of effects induced by the variation of different instrumental parameters. These parameters and the corresponding observables are summarized in Table III-2. For a given energy and cluster size the range and linear energy loss in a given solid are fixed. Therefore, variation of the sample thickness permits the observation of the energy density, interaction depth, and energy transfer mechanism in both the forward and backward directions. Similarly, we are able to determine the influence of the energy/velocity for a given projectile and the influence of the projectile size by adjusting these respective variables.

Effect of Foil Thickness of Secondary Ion Emission

Figure III-7 presents the simultaneously acquired ion yields in the forward and backward directions for three different foil thicknesses. In the case of the 5 nm foil (Figure III-7a), the SI yields and the C_n^- cluster distributions are similar for both directions. The momentum transfer process does not play a role in forward emission and the energy deposited by the projectile in the target volume induces almost the same SI

Table III-2. Summary of the Information Provided by Various Experimental Parameters

parameters		measurements	information	
beam (Au_n^{+q})	sample	SI emission	backward emission	forward emission
velocity & n fixed	thickness	yields as f(thickness)	depth of interaction	depth of interaction or attenuation range
velocity & n fixed	thickness	cluster distribution as f(thickness)	depth of interaction, electronic excitation, coherent effect	coherent motion signature
velocity for a fixed n	thickness	yields as f(thickness), cluster distribution as f(thickness)	influence of the impact energy	range as f(V), energy loss as f(V), coherent motion
n for a given velocity	thickness	yields as f(thickness), cluster distribution as f(thickness)	influence of n	range as f(n), coherent motion, energy loss as f(n)

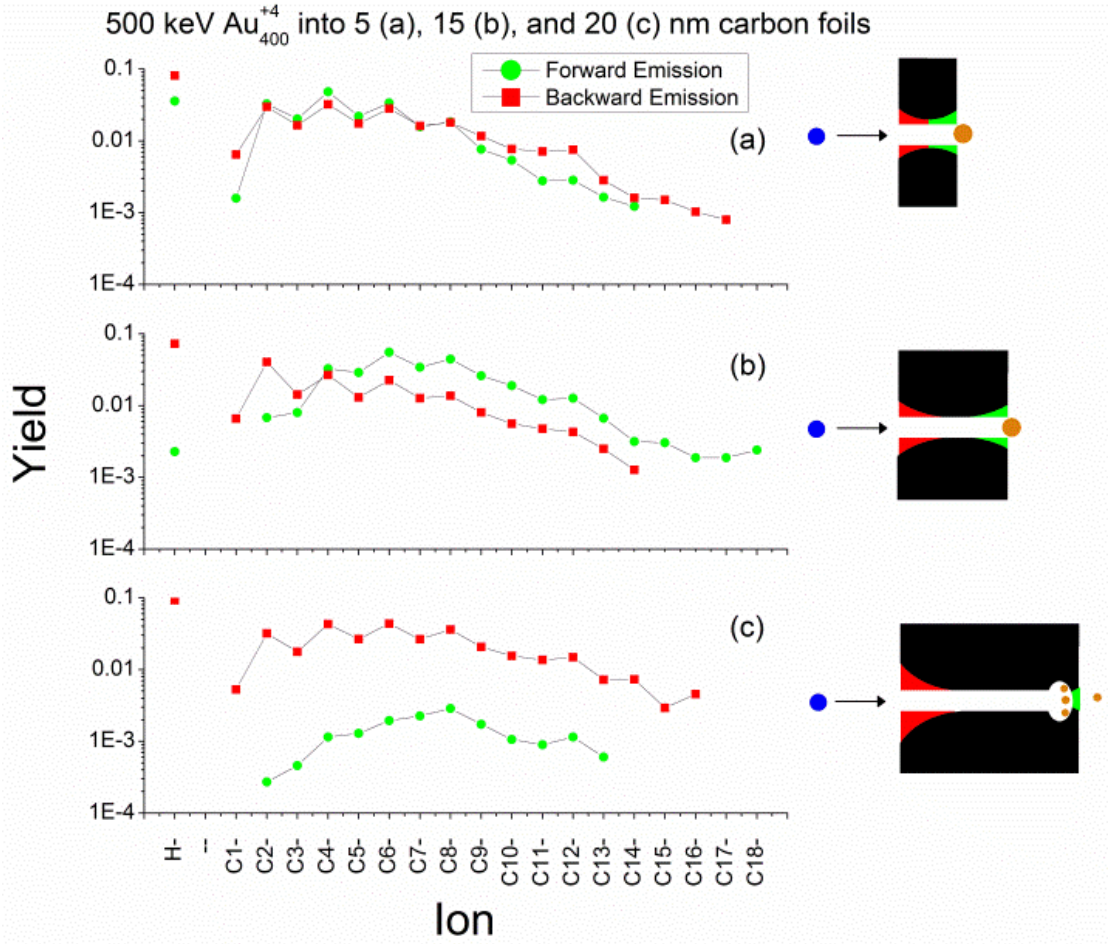

Figure III-7. Yields for H^- and carbon cluster (C_n^-) species obtained in the forward and backward directions from (a) 5, (b) 15, and (c) 20 nm thick carbon foils impacted by 125 qkeV Au_{100q}^{+q} projectiles. Corresponding interaction figures shown at right.

emission. The interaction volume and ion formation process are the same for both sides of the foil. This is supported by the observation of H^-, C^-, and C_2^- and similar C_nH^- distributions. For the 15 nm foil (Figure III-7b), C_n^- and C_nH^- distributions are different between the two directions. The backward emission is similar to that obtained with the 5 nm carbon foil with H^-, C^-, and C_2^- emission and a C_n^- distribution slightly shifted to larger clusters. This comparison indicates that the emission process does not change drastically and that the energy available for emission increases for the thicker foil. Concerning the forward emission, there is a significant shift toward carbon clusters with a high number of constituents as shown in Figure III-7. There is an increase of the total ion emission but a decrease in the yields of light ions such as H^-, C^-, CH^-, and C_2^-. These results indicate that the emission process is different for the two sides and that the energy deposited in the solid is probably higher than in the 5 nm case. These two points are attributed to the increased interaction volume, where more projectile energy can be deposited. In the case of the 20 nm foil (Figure III-7c), the forward and backward carbon cluster distributions are similar to the previous 15 nm foil. The yields do not change for the backward direction, though a small shift toward higher mass is observed in the carbon cluster distribution relative to the 15 nm foil. These results indicate that the forward and backward emission processes do not change for the 15 and 20 nm foils. The backward SI yields are almost equal to the previous values, a sign that the plateau for energy deposition has been reached. In other words, the increased foil thickness does not increase the amount of energy useful for backward SI emission. Therefore, the depth of interaction must be smaller than 17.3 nm (15 nm/sin 30°). On the contrary, the increase

of the thickness from 15 nm to 20 nm induces a decrease of the forward SI emission by a factor of 10 without modification of the carbon cluster distribution. The rate of H^-, C^-, CH^-, and C_2^- emission disappears or is very low. The two consequences of this observation are that the added distance of 5.8 nm introduces an important attenuation for the energy transfer to the surface and that the depth of interaction for forward emission is less than 5.8 nm. The slowing down of the projectile leads to a decrease of the energy deposited at the foil surface facing the forward direction. This result allows the range of the Au_{100q}^{+q} massive projectile in amorphous carbon at these energies to be bracketed between 15 and 20 nm, which is consistent with the TEM results. This range value deviates from the ballistic projection, where the theoretical range is proportional to the energy per cross sectional area as given in Table III-1. Such a deviation can be explained by electronic stripping which generates a high charge state on the projectile and causes additional slowing. The measured range lies between that of equal velocity atomic ions (3-6 nm for this energy range) and the range calculated from a ballistic model (~100 nm).

The carbon cluster yields can be approximated by lognormal distributions as seen in Figure III-8. These curves show the increase of the average mass of the C_n^- distribution as a function of the thickness for forward emission. The odd and even carbon clusters are addressed independently to show the lognormal fits have nearly the same function for each, despite the oscillatory nature of the yields. The curves show a general shift toward larger average cluster size with the increasing foil thickness, despite the yield reduction for the 20 nm foil. Analysis of the backward spectra (data not shown)

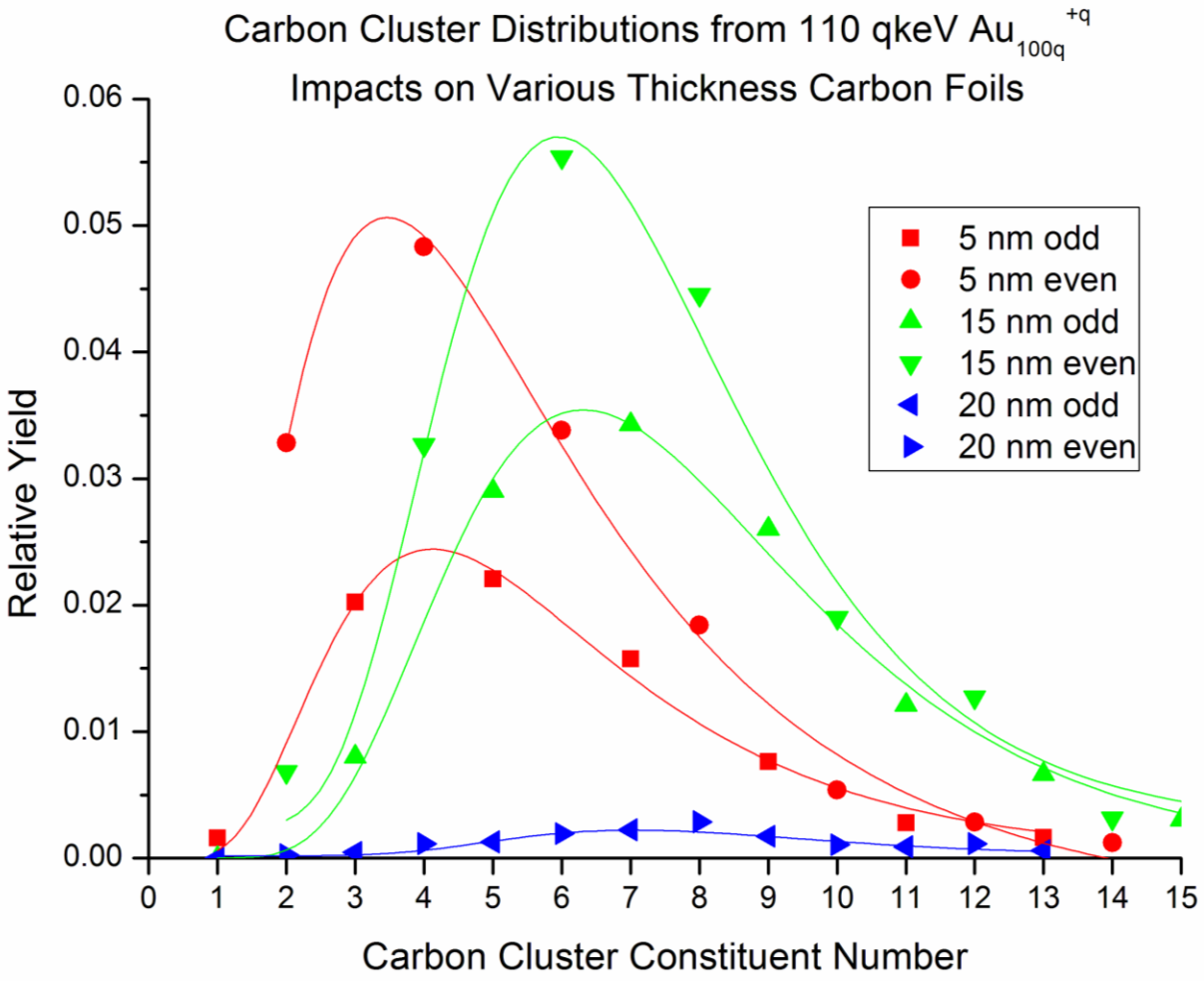

Figure III-8. Lognormal fits of the odd and even carbon cluster distributions of 5, 15, and 20 nm carbon foils observed in the forward direction.

reveals two contributions to the final cluster distribution: one for the light carbon species (C^-, C_2^-, and C_3^-) and a second for the larger clusters. It appears that the mechanism for creation of lighter species is absent in the case of forward emission.

Effect of Projectile Size and Energy on Secondary Ion Emission

Forward and backward SI emission from a 15 nm thick carbon foil impacted by the gold trimer and various massive gold clusters are shown in Figure III-9. The interaction of Au_3^+ with a solid is very well defined, in particular for forward emission where only the independent collision cascades play a role. In this case, only atomic ions and small carbon clusters are emitted. The backward spectrum reveals the emission of larger carbon clusters out to C_{14}^-, but with yields 2-3 orders of magnitude lower than the massive projectiles. Concerning the massive clusters, the backward SI yields and carbon cluster distributions are the same for all massive cluster projectiles. The process of emission does not change with the nano-droplet constituent number from 90 to 1000 gold atoms. The nearly constant value of the SI yields, regardless of the projectile, is surprising because with this set of projectiles the nano-droplet cross section increases by a factor of 5, the total energy by a factor of 2, and the range in the frame of a ballistic approach decreases by a factor of almost 3. The forward SI yields present a two order increase as a function of the projectile constituent number (n). This pronounced behavior does not largely affect the carbon cluster distribution. The process of ionic emission does not change, but the results indicate that the slowing down of the smaller particles is much quicker than that of the heavier particles, in spite of a much higher initial velocity. This observation contradicts the ballistic approach which may not apply in this velocity

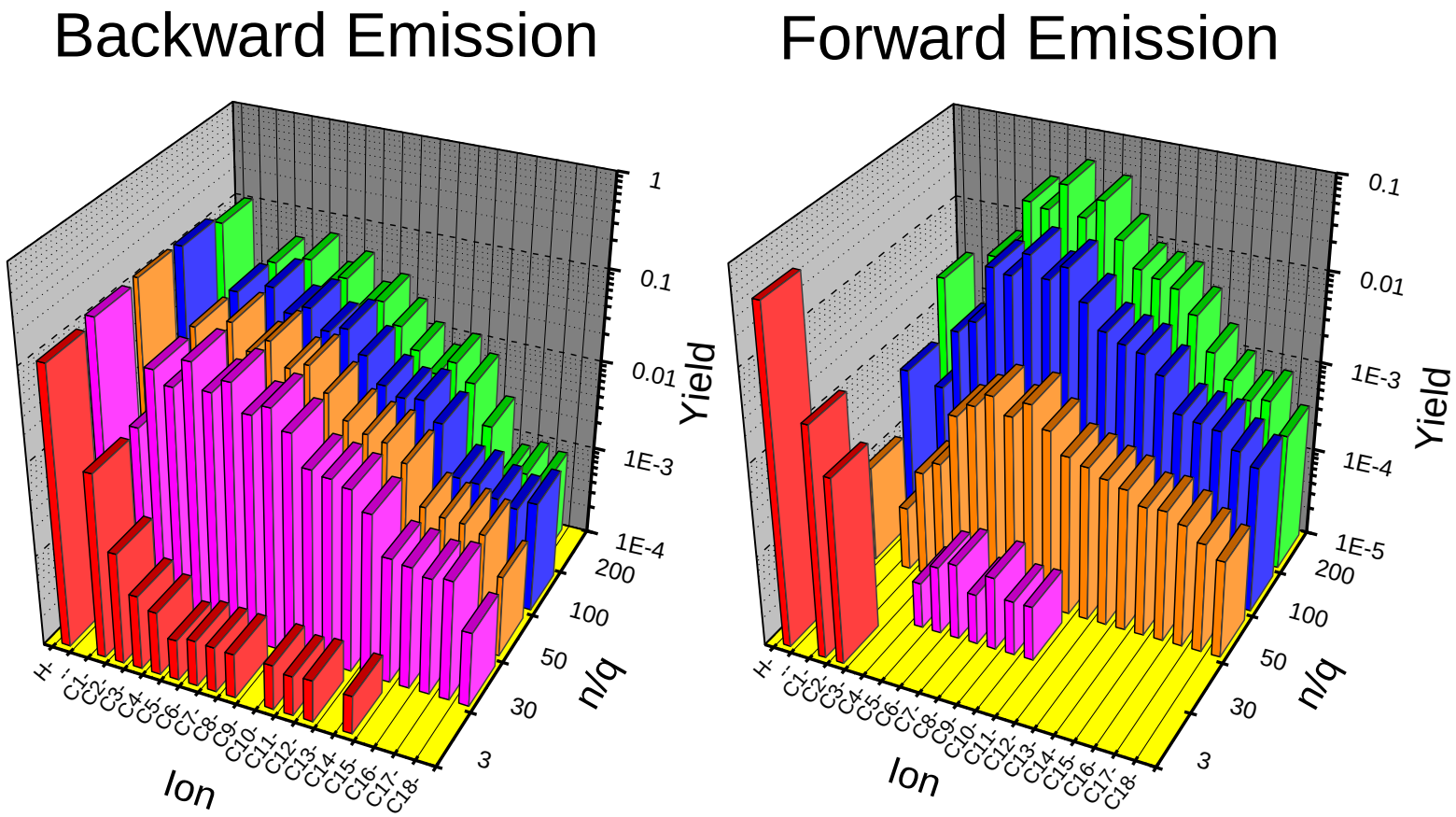

Figure III-9. Negative ion yields for H^- and carbon cluster species obtained in the forward and backward directions from a 15 nm thick carbon foil impacted by various size Au_n^{+q} clusters at 110 qkeV.

range. Also, for these clusters which have a majority of atoms at the surface of the projectile, atoms can be easily stripped or peeled during the penetration such that the shrinking or fragmentation of the projectile ultimately leads to the shorter range. For heavy particles, this process exists, but the inner core constitutes a more significant portion of the projectile and stripping does not significantly reduce the size of the projectile.

The main result from this experiment is that the forward carbon cluster distribution is not affected by the massive projectile size or velocity; only the yields are increased for larger or faster projectiles. The forward emitted H^-, C^-, and C_2^- yields increase more rapidly than the larger carbon clusters. The ionic emission of light elements requires processes which can only occur when the projectile velocity is not too low at the exit surface. Projectile passage across the surface leads to electronic excitation, allowing for an electron attachment mechanism.

In Figure III-10, a comparison of the forward SI yields for massive clusters of different sizes and impact energies reveals the plateau of SI emission for the 15 nm thick carbon foil. There is a clear threshold of projectile size that develops, such that the n/q = 30 and n/q = 50 projectiles are not capable of generating the maximum SI yields due to their supposed range limitations. Also, within the energy range of these experiments (95-125 qkeV) there is only a moderate increase in the forward SI yields. This suggests that the n/q = 100 and n/q = 200 projectiles at these energies are able to fully penetrate the 15 nm foil and deposit similar amounts of energy at the exit surface.

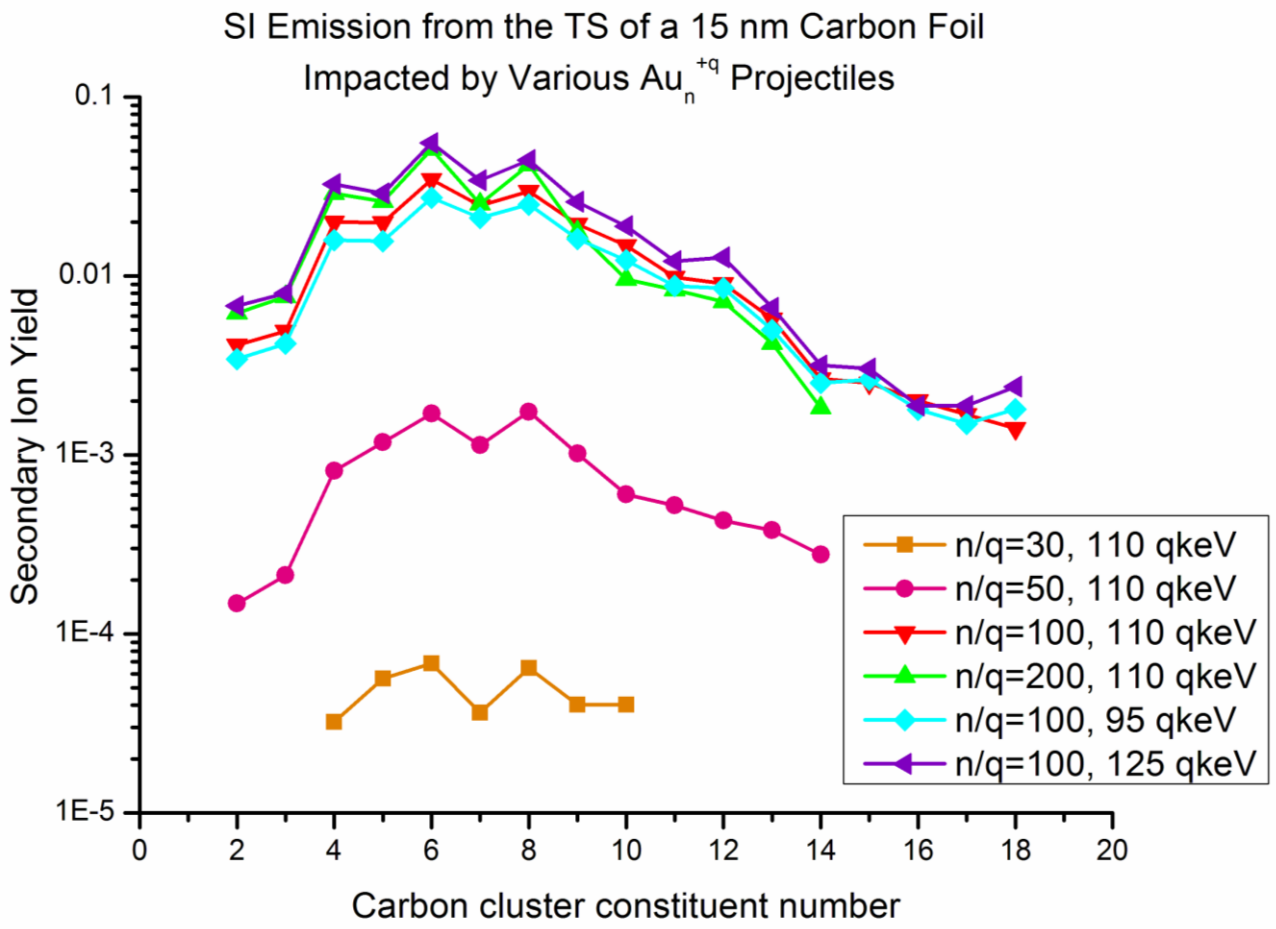

Figure III-10. The carbon cluster ion yields in the forward direction from a 15 nm thick carbon foil as a function of projectile size and energy.

Projectile Fate After Impact

As mentioned above, determining the fate of the projectile is critical for understanding the interaction it has within the solid. It is possible to observe the final state of the projectile after passage through the foil indirectly by monitoring the forward SI emission. Figure III-11 shows the forward SI yields from a single 5 nm foil as compared to two 5 nm foils separated by a 100 μm wide gap between. We observe an order of magnitude reduction in the SI yields between the single and double foil targets while maintaining nearly identical cluster distributions. It may be noted that the total thickness of the stacked foils is less than the 15 nm foil which gave abundant forward emission as shown in Figure III-7b. Using SI emission as an indicator for projectile transmission, we can assume that less than 10% of the projectiles penetrate the second foil sufficiently to cause emission in the forward direction. The most likely cause for this reduction is that the projectile fragments significantly at the exit of the first foil, generating smaller projectiles at low velocities which go on to impact the second foil. If the projectile retained most of its mass, then we would expect total ion yields comparable with the 5 and 15 nm thick carbon foils, signaling complete penetration. Instead, the data suggests that during passage within the solid, the massive gold cluster exhibits a cohesive motion between its constituents which is capable of generating energy deposition conditions suitable for large carbon cluster emission. In other words, the atoms of the cluster travel through the material in close proximity to one another, even up to depths of 20 nm. However, in the case when the cluster reaches the exit of the

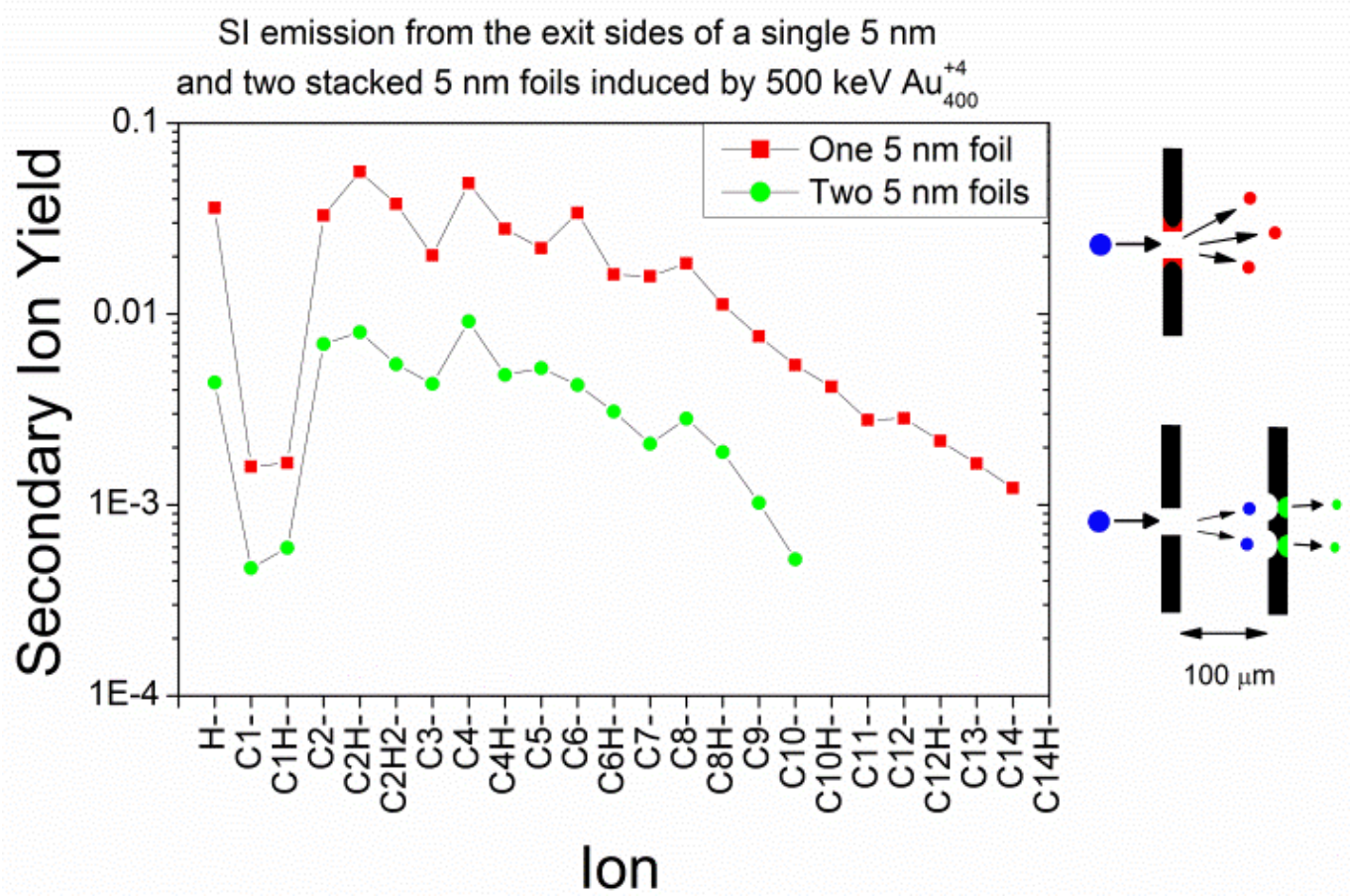

Figure III-11. Forward SI yields from a single 5 nm and two stacked 5 nm carbon foils impacted by 125 qkeV Au_{100q}^{+q}. Proposed interaction schematics are shown for the (top right) single foil and (bottom right) stacked foils.

solid, the high charge state and internal energy of the projectile likely results in fragmentation/Coulomb explosion which reduces the projectile to atomic and small polyatomic components. This assumption of a high charge state has been used previously to explain the high emission yields of H^+, H_2^+, H_3^+, and C^+ observed in the backward direction[82]. There are some clusters within the size distribution of the beam that may retain a central core after penetration through the first foil which can continue on to cause forward emission from the second foil.

Conclusion

We show that the foil thickness determines the observable cluster distribution for forward emitted ions, with thicker foils giving distributions shifted toward larger clusters. This observation reveals a new mechanism for ion emission based on the massive gold clusters' ability to physically push material out of the carbon foil. The process can be considered mesoscopic in nature, akin to hydrodynamic penetration. The momentum of the projectile is more efficiently transferred to the ejecta as translational energy as opposed to internal, vibrational excitation. The reduction in energy density at the exit surface can also be deduced from the virtual absence of light ions in the mass spectrum. We suggest that carbon clusters emitted in the forward direction have a lower average internal energy than the corresponding backward-emitted clusters. This work also gives tangible evidence of projectile size dependent ranges proposed by previous theoretical work as a clearing-the-way effect. The ranges are larger than atomic ions of the same velocity (between 3 and 6 nm in our experiments), but are five to ten times

lower than values predicted by a ballistic model. Using a dual foil experiment, we are able to indirectly observe the disintegration of the massive gold clusters at the exit of a thin foil. During passage through a solid, the gold cluster constituent atoms are minimally scattered, i.e. they travel in a coherent motion. For foil thicknesses which are less than the projectile range, the impact energy cannot be dissipated and the projectile will fragment once it is no longer confined within the solid.

CHAPTER IV

SI YIELD AND MULTIPLICITY MEASUREMENTS*

Introduction

Much current research in the field of SIMS focuses on the issue of maximizing secondary ion (SI) yields to improve detection efficiency, especially for molecular species. Attempts to address this problem have been directed at either enhancing the ionization probability of sputtered species through the addition of a matrix, such as cesium,[109] water clusters,[110] ionic liquids,[111] or glycerol,[112] or improving the general secondary ion yield through the use of novel primary ions, such as C_{60},[26] water clusters,[113] argon clusters,[114] or metal clusters.[115, 116] Massive gold clusters have previously been proven as a path to improved SI yields.[73] This research seeks to further display the efficiency of the Au_{400}^{+4} projectile at high impact energies by describing the types, yields, and multiplicities of secondary ions observed for molecules from a variety of different chemical classes. This chapter reports data for various peptides, lipids, and small molecules which have been analyzed with the new high voltage Au_{400} SIMS platform. SI yields for the polymer poly(methylmethacrylate) are also provided in this dissertation in Chapter VI. Some test molecules are also used to assess the influence of impact energy on secondary ion yields within the energy range accessible by this

* Part of this chapter is reprinted with permission from "Characteristics of Positive and Negative Secondary Ions Emitted from Au_3^+ and Au_{400}^{+4} Impacts" by J.D. DeBord, F.A. Fernandez-Lima, S.V. Verkhoturov, E.A. Schweikert, and S. Della-Negra, 2012. *Surface and Interface Analysis*, Copyright [2012] by John Wiley and Sons.

instrument as well as by comparison to measurements with other instruments. Measurements performed at 280-520 keV represent a relatively unexplored energy regime for the Au_{400}^{+4} projectile, as previous experiments have been restricted to impact energies significantly higher[82] or lower[72] than those currently available. These previous measurements serve as a benchmark for assessing the overall performance of the new instrument.

Peptides

The ability to detect and quantify peptide molecules on surfaces presents an important analytical challenge due to their pervasive biological relevance. The limited masses of many small peptides make them accessible for the SIMS technique, as evidenced by the many reports of SIMS peptide analyses.[117-122] However, many of these studies are limited to the analysis of peptide fragment ions rather than the intact molecular species due to the low molecular ion yields afforded by atomic and small polyatomic projectiles. This significantly complicates unambiguous identification of peptide species, especially within a complex matrix. The use of multivariate statistics to generate fingerprint identifications of peptides from the fragment ions allows researchers to circumvent the need for molecular ions.[123, 124] However, the ability to generate high SI yields of peptide molecular ions via SIMS greatly simplifies their analysis and eliminates the need for intensive spectral processing. To assess the efficiency of Au_{400} in this capacity, the current study presents molecular and fragment ion yields measured from four different peptides: leucine-enkephalin, angiotensin I, angiotensin II, and angiotensin III.

Experimental Details. All peptides were purchased from Sigma Aldrich (St. Louis, MO). One mg/mL solutions of each peptide in 1:1 MeOH/H_2O were electrospray deposited in atmosphere onto either stainless steel supports(negative mode) or gold-coated silicon wafers (positive mode) from Silicon Vally Microelectronics (Santa Clara, CA). Substrates were chosen to eliminate spectral interferences because each displays limited ion emission in their respective polarities. Spectra containing ~10^6 impact events were acquired using the experimental setup described in Chapter II. All data was collected using the event-by-event detection methodology with the negative ion analyses performed in chamber 1(520 keV impact energy) and positive analyses performed in chamber 2 (440 keV impact energy). Up to eight isobaric ions can be detected per impact event using the eight anode detector previously described.

Types of Peptide Ions Observed. Representative negative and positive ion spectra for leu-enkephalin (YGGFL, Figure IV-1) are characterized by the abundant emission of intact molecular ion signals (transmission corrected yield of 1.7 molecular ions per PI in negative mode) as well as abundant small fragment ions (<200 amu), including peaks corresponding to atomized products such as CN^- (transmission corrected yield of 2.1 in negative mode) and individual amino acid residues L, F, and Y. Peaks corresponding to the apparent synthetic impurity YGGGFL, which contains an extra glycine residue, and the leu-enkephalin dimer ($(2M-H)^-$) are also visible as a deprotonated molecular ions in negative mode. Peaks corresponding to backbone fragmentation are curiously absent from the 200-500 mass region of the two spectra with the exception of the b_2 and y_2 fragments observed in positive mode. Additional analysis of leu-enkephalin

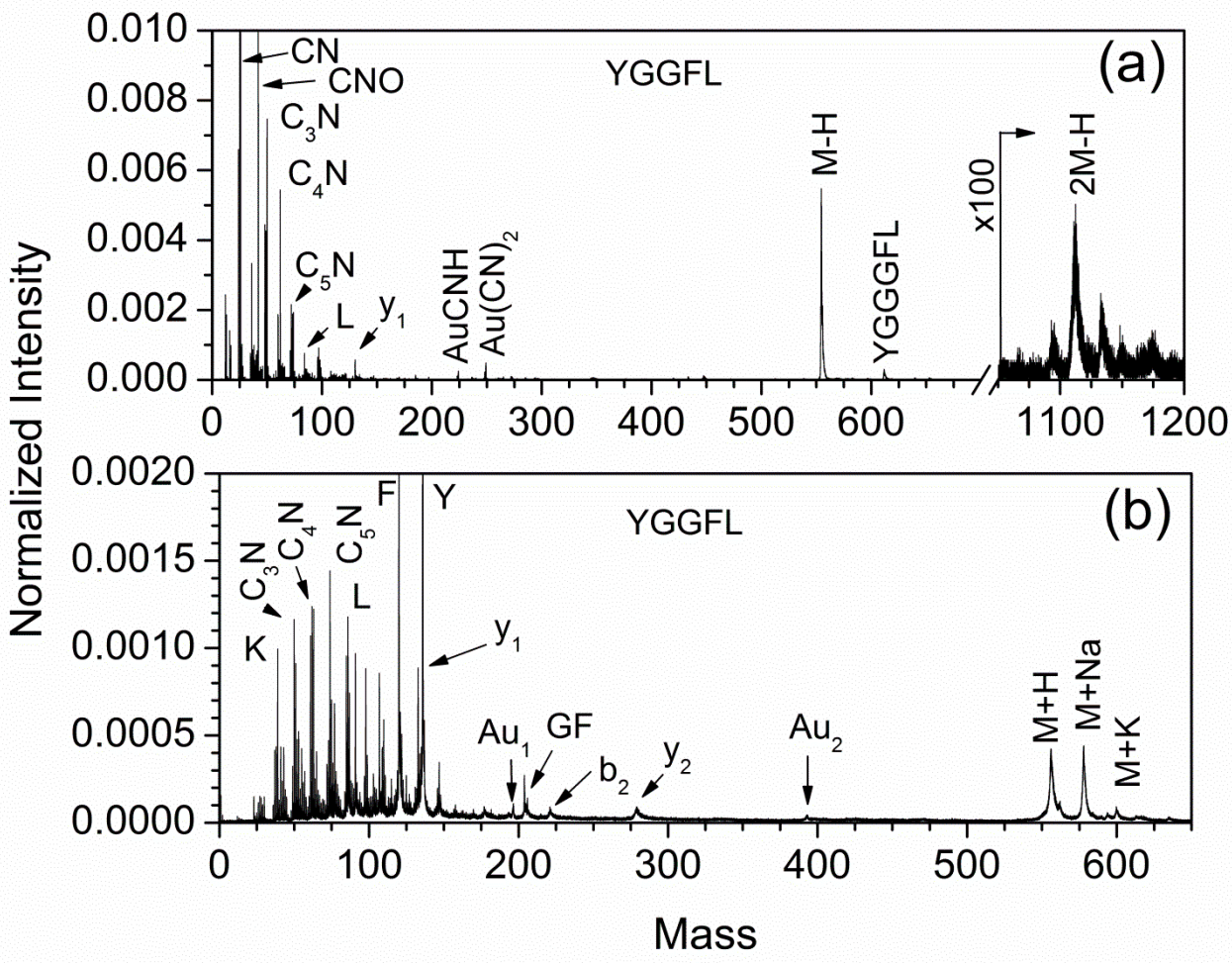

Figure IV-1. (a) Negative and (b) positive mass spectra for a neat electrosprayed surface of leu-enkephalin analyzed by 520 keV and 440 keV Au_{400}^{+4} projectiles, respectively.

fragmentation as it pertains to the amount of internal energy accumulated in the molecule is presented in Chapter V.

Similar observations of high molecular and fragment ion yields with the near absence of backbone fragment peaks are replicated for all other peptides analyzed. The negative ion spectrum of Angiotensin I (DRVYIHPFHL, Figure IV-2a) displays abundant low mass peaks for CN^-, CNO^-, and other small atomization-recombination products. Peaks at masses 224 and 249 correspond to the gold adduct ions $AuCNH^-$ and $Au(CN)_2^-$, respectively. These species are formed when projectile atoms are re-emitted from the surface and combine with the thermodynamically stable CN^- species as described in previous reports.[77, 99] These species are observed for nearly all nitrogen containing organic molecules when analyzed by Au_{400} and are seen for all four peptides in this study. Immonium ions for the arginine or proline (mass interference), aspartate, and histidine are observed in positive mode. A c_1 fragment, named according to the Roepstorff and Fohlman system,[125] is the largest identifiable fragment from angiotensin I. However, quasi-molecular ion species are observed in both positive and negative polarities. The negative spectrum shows a deprotonated molecular ion as well as a peak for the loss of water and a peak for the loss of water and ammonia. The positive molecular species are distributed among peaks for the protonated, sodiated, and potassiated ions. These ions with masses of over 1,300 amu occur with yields similar to small fragment species. With smaller projectiles, molecular ion yields are typically more than an order of magnitude less intense than small fragments.[126]

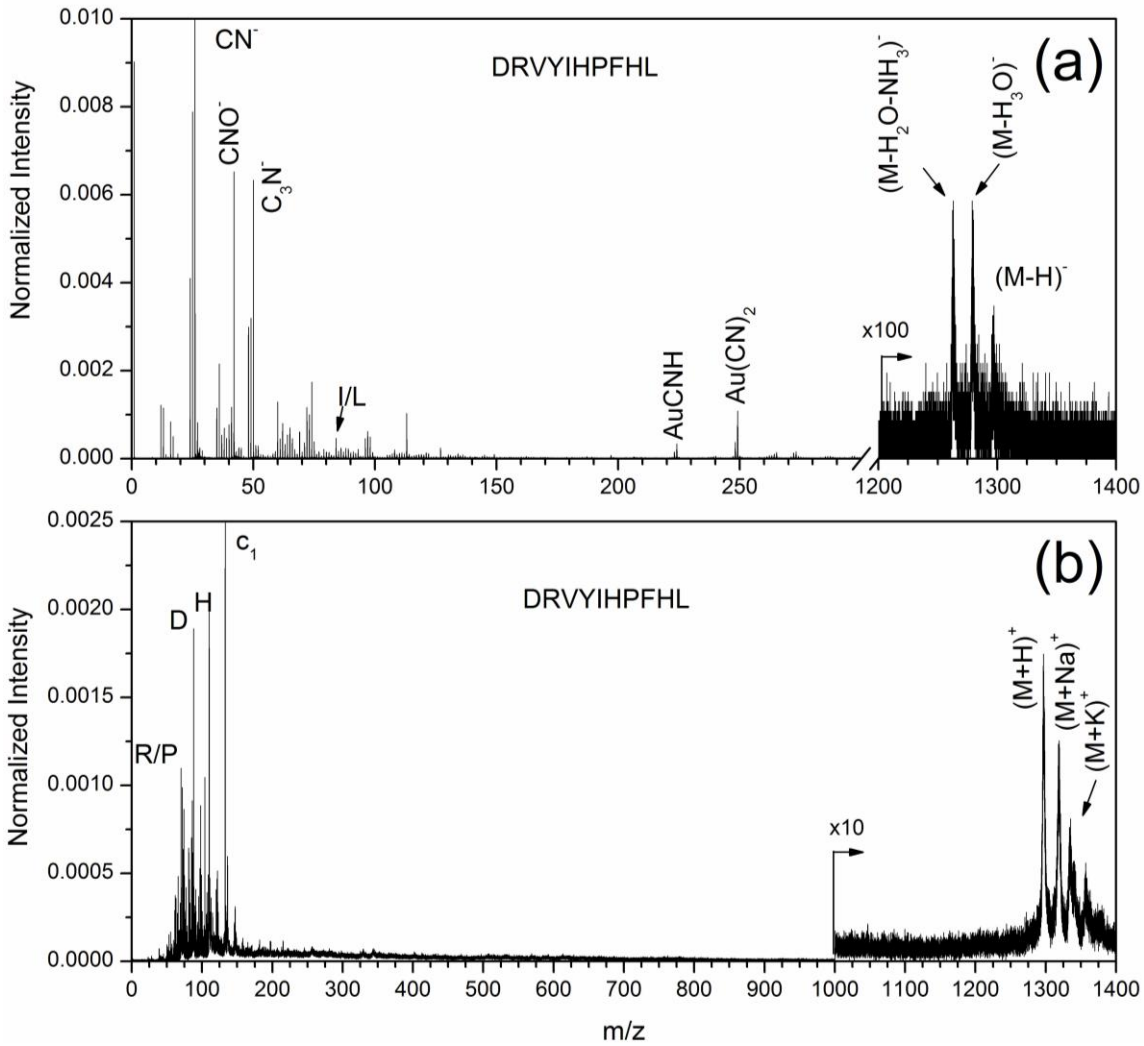

Figure IV-2. (a) Negative and (b) positive mass spectra for a neat electrosprayed surface of angiotensin I analyzed by 520 keV and 440 keV Au_{400}^{+4} projectiles, respectively.

Positive and negative ion spectra for angiotensins II and III are provided in Figures IV-3 and IV-4, respectively. The angiotensin II spectrum exhibits similar characteristics as those previously described. In addition to the immonium fragments and quasi-molecular ion peaks, fragments corresponding to the a_3 fragment as well as an internal RV fragment are observed in positive mode. Reaffirming the assignment of the a_3 fragment is the presence of a peak for a side-chain loss from the a_3 fragment (d_{a3}). These species are the largest sequence specific fragments observed from the peptides analyzed.

Spectra for angiotensin III reveal quasi-molecular ion peaks intense enough to be displayed on the same linear scale the low mass region, a rare observation for SIMS analyses. However, the presence of significant Au_n^+ peaks in the positive spectrum suggests the deposited sample layer does not completely cover the gold substrate within the analyzed beam spot. This means the molecular ion peaks would be even more intense given a full surface coverage.

Peptide SI Multiplicity. By acquiring data using an event-by-event methodology, it is possible to access unique fundamental measurements such as the number of ions emitted for a given impact event, referred to as the multiplicity. With software developed in-house, one can extract not only the total number of ions emitted from an impact (total ion multiplicity), but also the number of a selected type of ion emitted per event (ion selected multiplicity). Figure IV-5 shows the total and selected ion multiplicities extracted from the negative mode leucine-enkephalin spectrum in Figure IV-1. Also

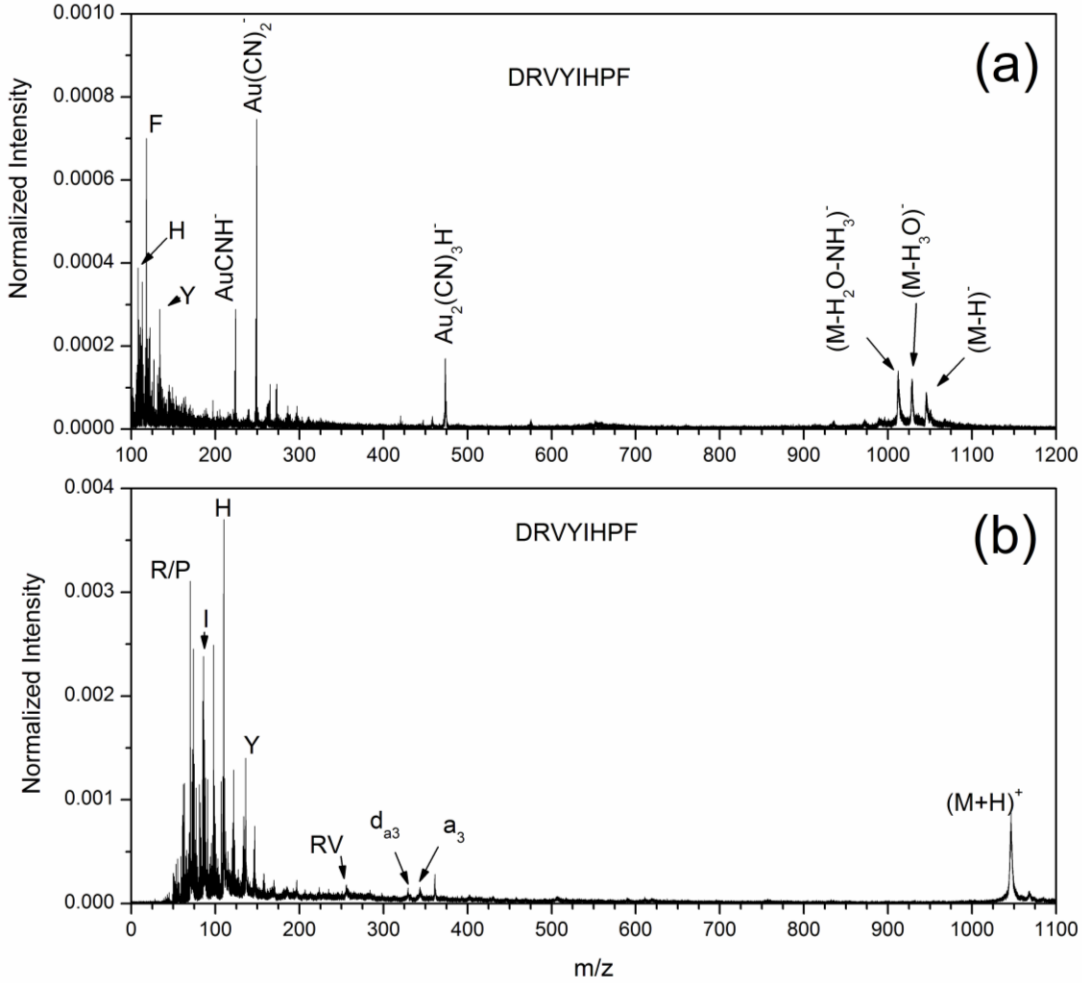

Figure IV-3. (a) Negative and (b) positive mass spectra for a neat electrosprayed surface of angiotensin II analyzed by 520 keV and 440 keV Au_{400}^{+4} projectiles, respectively.

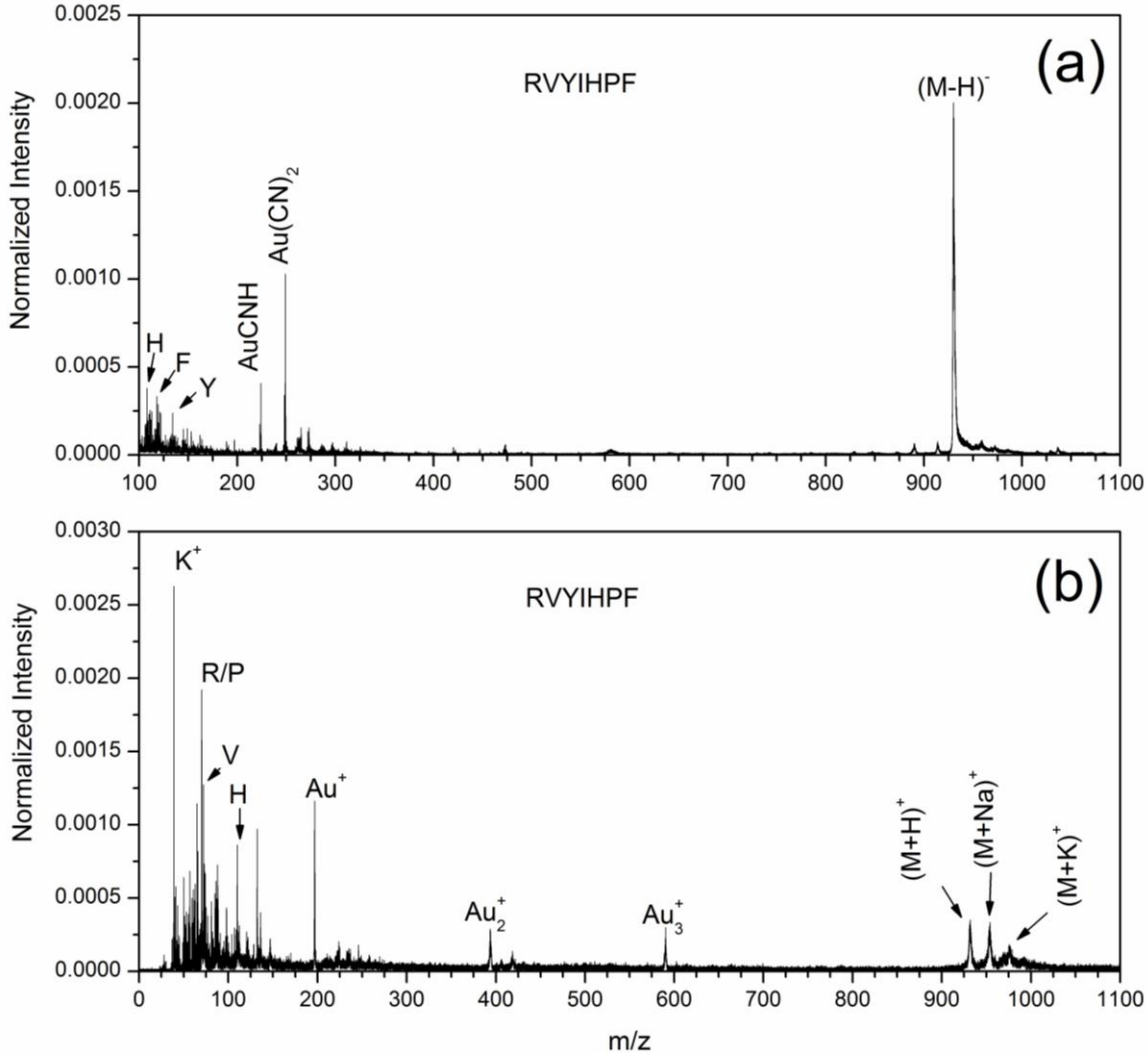

Figure IV-4. (a) Negative and (b) positive mass spectra for a neat electrosprayed surface of angiotensin III analyzed by 520 keV and 440 keV Au_{400}^{+4} projectiles, respectively.

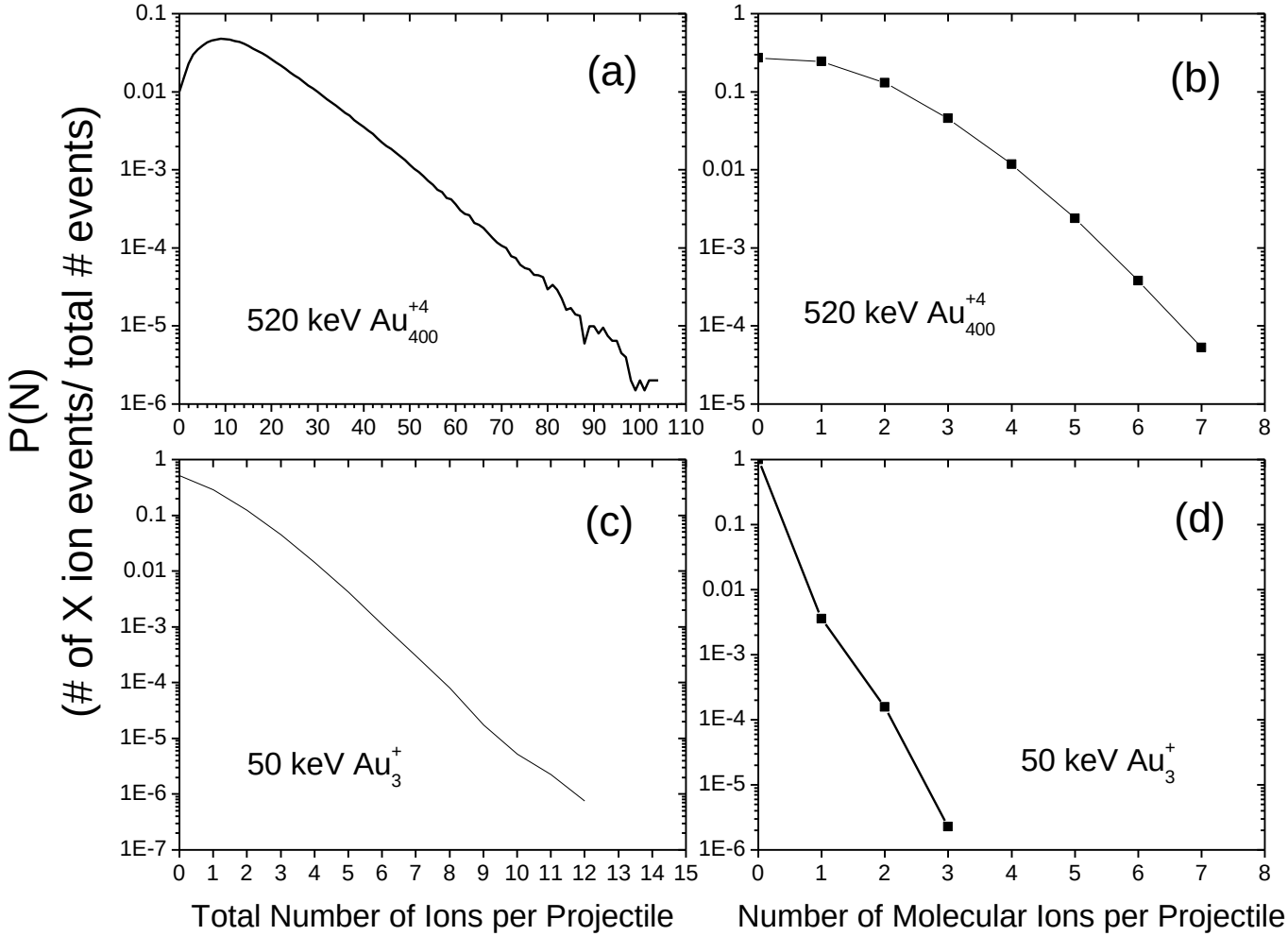

Figure IV-5. Total negative secondary ion multiplicity distributions for (a) 520 keV Au_{400}^{+4} and (b) 50 keV Au_3^+ and molecular ion selected multiplicity distributions for (a) 520 keV Au_{400}^{+4} and (b) 50 keV Au_3^+ measured per projectile impact on a neat electrosprayed surface of leu-enkephalin. Results not corrected for transmission efficiency.

shown are the multiplicities observed from an analysis of the same sample using a 50 keV Au_3^+ projectile. Considering first the case of Au_{400}, the total ion multiplicity plot (Figure IV-5a) shows that the most probable number of ions emitted for a given event is ~10. However the distribution extends out to more than 100 SIs detected per event. This causes the average number of SIs to be ~13.3. The selected ion multiplicity for the deprotonated molecular ion is similarly impressive, with up to 7 molecular ions being detected for some impact events. The detection of such high isobaric multiplicity is by no means efficient, considering all seven ions must strike seven out of eight different anodes, but it does confirm the existence of such events. The average number of molecular ions per impact is 1.7 (as given by the yield), with the distribution showing that more than ~75 % of impacts generating at least one molecular ion. It is also important to note that the figures given are not corrected for transmission efficiency, which is 59 % for this setup.

The distributions measured for Au_3 impacts (Figure IV-5c,d) show that SI multiplicity is much lower for the small polyatomic projectile. For both the total and selected multiplicities, the most probable result of a gold trimer impact is that no SIs are detected. Even the most efficient Au_3 impacts result in the detection of only 12 SIs. The multiplicity for molecular ion producing events is even lower, with more than 99 % of impacts not producing a detectable molecular ion. There are some events which produce up to 3 molecular ions, but the probability of such events is on the order of 10^{-6}. For a typical acquisition of 10^6 impacts this amounts to just one or two highly efficient impact events.

Peptide SI Yields. The yields for CN^- and two quasi-molecular ions observed from the four sample peptides in negative mode are shown in Figure IV-6a. These yields are calculated by dividing the area under the peak of interest by the total number of projectiles used to generate the signal (~10^6). These values are corrected for the transmission efficiency in the first analysis chamber ToF (59 %). The graph reveals a few interesting trends. First, the yield of CN^- is greater than unity in all cases and varies by less than a factor of three for the different peptides. Second, the deprotonated molecular ion yield appears to show a mass dependence, such that the observable SI yield is inversely proportional to the mass of the peptide. Third, the yield of the $(M-H_3O)^-$ species increases with the mass of the peptide. This finding suggests that the deprotonated molecular ions of larger peptides fragment to generate this water elimination product. Figure IV-6b gives the positive ion yields for two amino acid residues common to all four peptides (F and Y) as well as the protonated and sodiated molecular ion species. These values are corrected for a 90 % transmission efficiency of the second chamber ToF. The yields measured for most of these ions are in the range of 1-10 %, with any mass dependent trends being difficult to discern. It is important to note once again that the angiotensin III sample was not completely coated with analyte and all yields are therefore underestimated by 10-20 %. The numerical yields for detected negative ions from angiotensins I, II, III, and leu-enkephalin are given in Table IV-1. Yields for $Au(CN)_2^-$ detected from each of the peptide samples are also provided. While not a characteristic fragment of the peptides, this adduct offers a method for monitoring

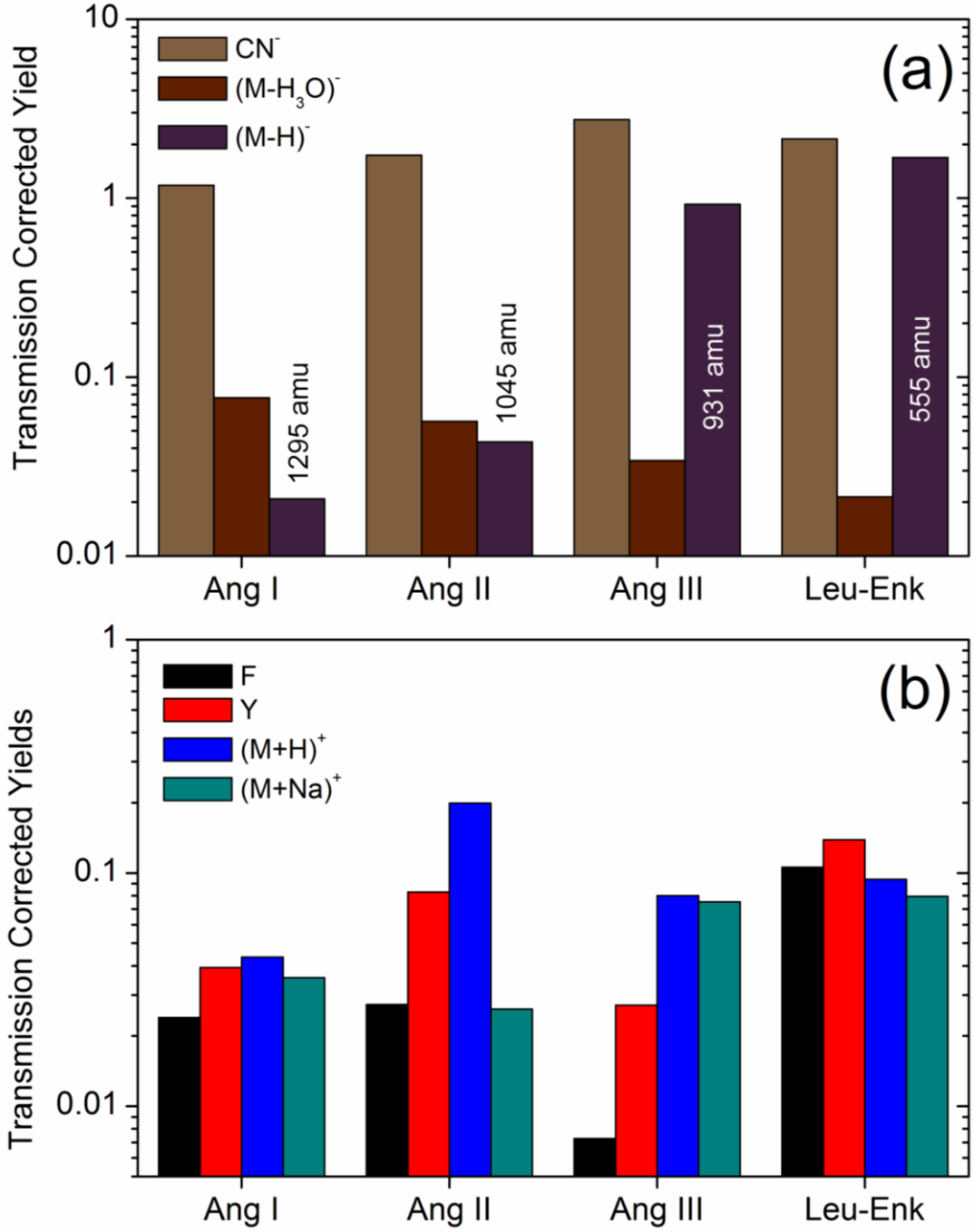

Figure IV-6. (a) Negative quasi-molecular ion yields measured from angiotensins I, II, III, and leu-enkephalin using 520 keV Au_{400}^{+4}. (b) Positive ion yields measured for F and Y immonium ions as well as the protonated and sodiated molecular ions for all peptides analyzed by 440 keV Au_{400}^{+4}. Data corrected for 59 % or 90 % transmission efficiency in negative or positive mode, respectively.

Table IV-1. SI Yields for Negative Ions Obtained from Impacts of 520 keV Au_{400}^{+4} on Neat Peptide Targets

	Angiotensin I		Angiotensin II		Angiotensin III		Leu-Enkephalin	
Ion	Mass	Yield	Mass	Yield	Mass	Yield	Mass	Yield
M-H	1295	0.021	1045	0.044	931	[0.92]	554	[1.69]
2M-H	----	----	----	----	1860	0.002	1109	0.043
CN	26	[1.18]	26	[1.74]	26	[2.74]	26	[2.14]
P/R	68	0.009	68	0.022	68	0.015	----	----
V	70	0.012	70	0.032	70	0.006	----	----
I/L	84	0.026	84	0.062	84	0.039	84	0.067
D	86	0.013	86	0.034	----	----	----	----
R	98	0.025	98	0.061	----	----	----	----
H	108	0.019	108	0.039	108	0.020	----	----
F	----	----	118	0.055	118	0.013	118	0.015
P	----	----	124	0.012	124	0.030	----	----
Y	----	----	134	0.030	134	0.012	134	0.018
y_1	----	----	164	0.010	----	----	130	0.093
a_2-NH_3	----	----	225	0.006	----	----	----	----
y_2	----	----	261	0.009	----	----	----	----
Y_2	265	0.008	----	----	----	----	----	----
b_2	----	----	----	----	----	----	219	0.005
$Au(CN)_2^-$	249	0.062	249	0.062	249	0.079	249	0.041

Data corrected for 59% transmission efficiency. Values in brackets are underestimated due to limited detection efficiency of the 8-anode detector for high multiplicity events.

gold atoms which have been stripped from the projectile and re-emitted from the surface.[77, 99] For the peptides analyzed, this yield varies by only a factor of two, confirming the various surfaces have similar densities, atomic compositions, and work functions.

Lipids

Lipids play critical roles in the structural integrity of cell membranes,[127] energy storage,[128] and many other biological functions.[129] They also constitute the majority of dried biological tissue by mass. Because lipids exist at such high natural concentrations within biological matter, they have proven particularly amenable to mass spectrometric imaging with MALDI and SIMS.[130, 131] However, as in the peptide example, SIMS researchers have traditionally relied on fragment ion signals like PO_3^- and phosphocholine ($C_5H_{15}NO_4P^+$) to map lipid distributions. These small fragments are not necessarily representative of the actual lipid distribution and do not provide information regarding the molecular composition cellular membranes. This study offers the Au_{400} projectile as a means to generate higher SI yields for analytically significant lipid species that enable more informative descriptions of lipid distributions.[132, 133]

Experimental Details. All lipids were obtained from Avanti Polar Lipids (Alabaster, AL). The lipid samples were dissolved in a Chloroform : Methanol : Water (65:35:8) (v:v) solution and sprayed onto stainless steel or gold-coated silicon wafer substrates. Spectra were obtained in the same manner as the peptide analysis.

Types of Lipid Ion Observed. Five different lipids, each representing different lipid classes, were selected to investigate the types of ions which can be observed from

Au_{400} impacts on lipidic surfaces. Figure IV-7 displays positive and negative ion mass spectra obtained from 1,2-dipalmitoyl-sn-glycero-3-phosphocholine (16:0 PC). Characteristic ions from these spectra can be divided into three types: quasi-molecular ions, head group fragments, and tail group fragments. The positive spectrum of 16:0 PC gives abundant signals corresponding to many different head group fragments (masses 86, 104, 125, 147, 166, 184, and 206) as well as the sodiated quasi-molecular ion at 756.6 amu. This list includes the phosphocholine (mass 184) ion unique to lipids from the phosphocholine class. Proposed structures for all labeled peaks are provided in Figure IV-7. The tail group specific ion at mass 255 is observed only in negative mode due to the presence of the carboxylate moiety. Negative mode is also advantageous for the observation of PO_3^-, which is the most intense signal in the spectrum. The production of 16:0 PC quasi-molecular ions in negative mode necessitates elimination of the positively charged aminium group. This type of fragmentation is observed at masses 718.5, 674.5, and 646.5. An apparent quasi-molecular ion peak positioned at mass 723 is observed, though the structure of this species is not obvious.

Figure IV-8 shows spectra for 1,2-dimyristoyl-sn-glycero-3-phosphoethanolamine (14:0 PE). Intense Au_n^+ peaks in the positive spectrum suggest the 14:0 PE coverage within the analysis spot is less than 100 % allowing for emission from the Au substrate. This molecule exhibits similar emission to 16:0 PC because both have similar head group structures, as shown by the identified analyte specific peaks. Abundant quasi-molecular ions are observed in both polarities via the addition or loss of a proton. Sodiated and di-sodiated molecular ions are also observed in positive mode.

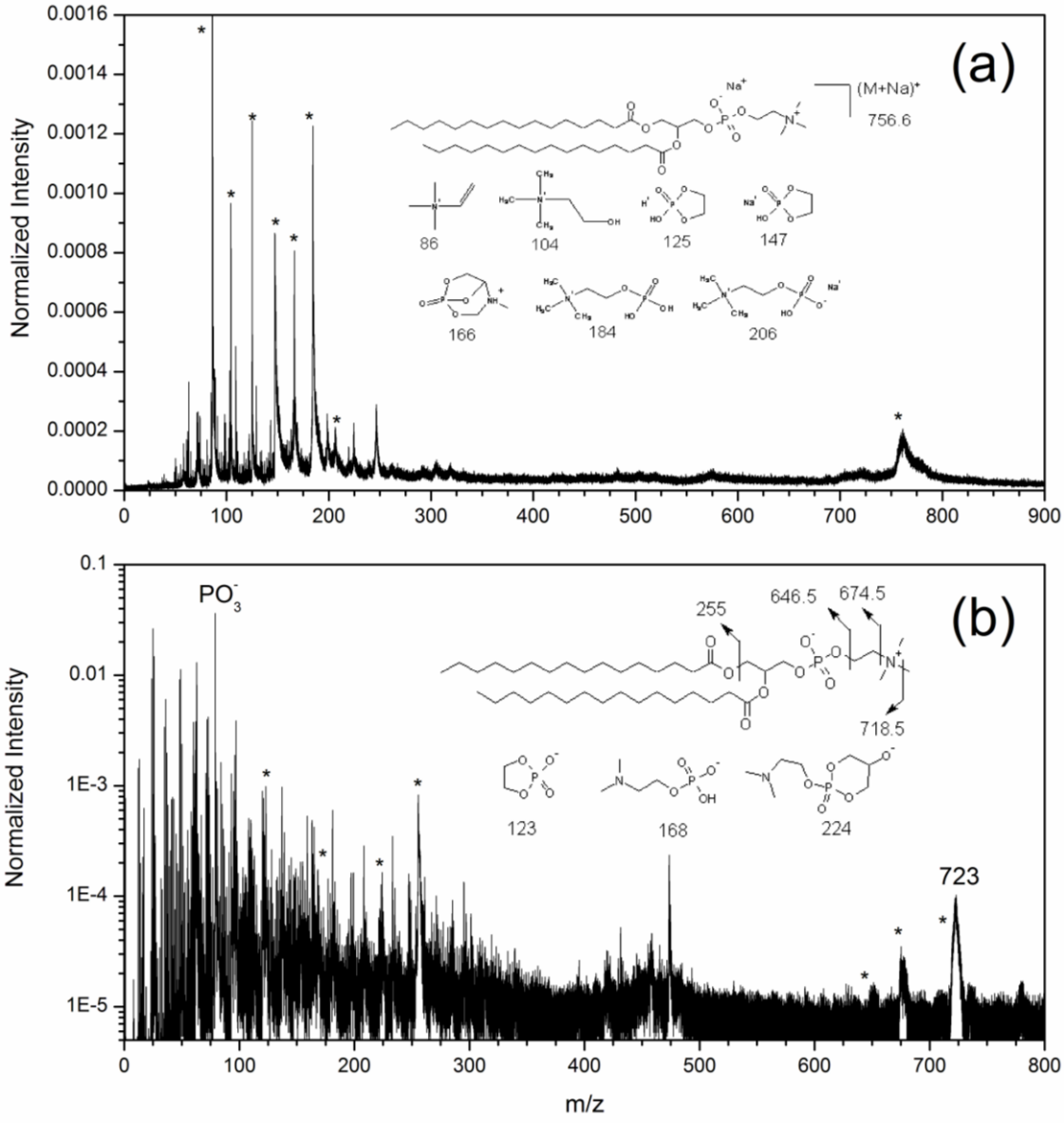

Figure IV-7. (a) Positive and (b) negative mass spectra for a neat electrosprayed surface of 1,2-dipalmitoyl-sn-glycero-3-phosphocholine analyzed by 520 keV and 440 keV Au_{400}^{+4} projectiles, respectively.

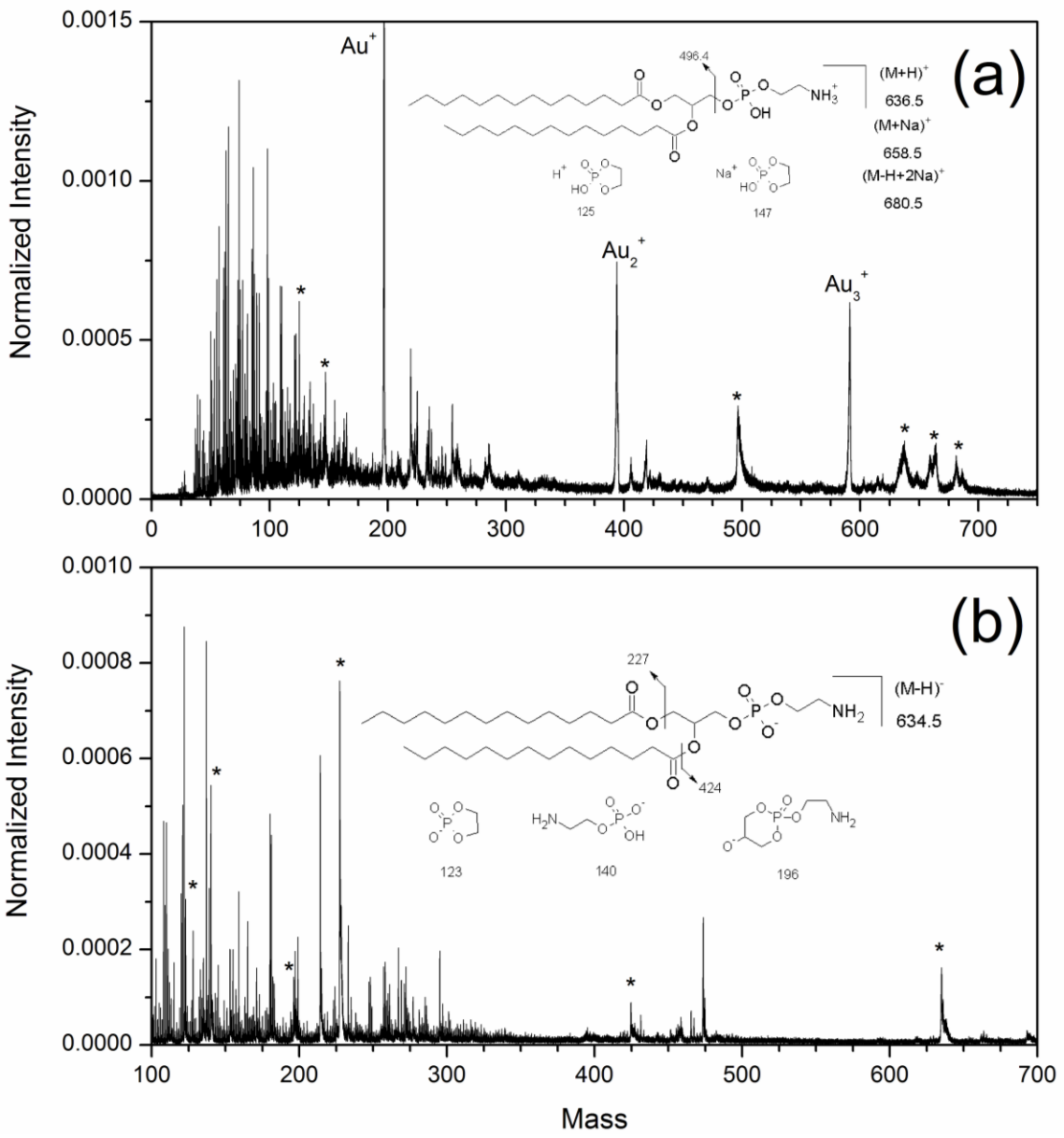

Figure IV-8. (a) Positive and (b) negative mass spectra for a neat electrosprayed surface of 1,2-dimyristoyl-sn-glycero-3-phosphoethanolamine analyzed by 520 keV and 440 keV Au_{400}^{+4} projectiles, respectively.

Head group specific peaks are present in both spectra (positive: masses 125 and 147; negative: masses 123, 140, and 196) with most species involving rearrangement of the phosphoethanolamine group. For tail group specific peaks in the positive mode, a peak at mass 496.4 corresponding to the loss of phosphoethanolamine is observed. In negative mode, the alkane carboxylate tail group is seen like for 16:0 PC. A peak at mass 424 from the loss of one fatty acid tail (not observed for 16:0 PC) is also labeled.

The sphingomyelin lipid analyzed (d18:1/16:0 SM) belongs to the sphingolipid class and consists of a phosphocholine head group mated to a ceramide tail structure. The ceramide structure contains a sphingosine tail and fatty acid tail as shown in Figure IV-9. Also shown in this figure are the mass spectral features in positive and negative polarities which can be attributed to d18:1/16:0 SM. The head group peaks previously identified for the phosphocholine head group (positive: masses 86, 104, 125, 147, 166, 184, and 206; negative: masses 123, 168, and 224) are also present in these spectra. Quasi-molecular ion species are shown for both spectra, corresponding either to the addition of sodium in positive mode or the loss of the methyl or amminium group in negative mode. Curiously, no tail group specific peaks could be identified in either polarity.

To illustrate the Au_{400} projectile's capability for identifying molecular species within a mixture, Figure IV-10 shows the negative spectrum obtained from a surface coated with a mixture of porcine cerebral sulfatides (major component 18:1/24:0 ST). Sulfatides are composed of a sulfated galactosyl head group coupled to a ceramide tail moiety. The acquired spectrum exhibits multiple fragments peaks from this sulfated

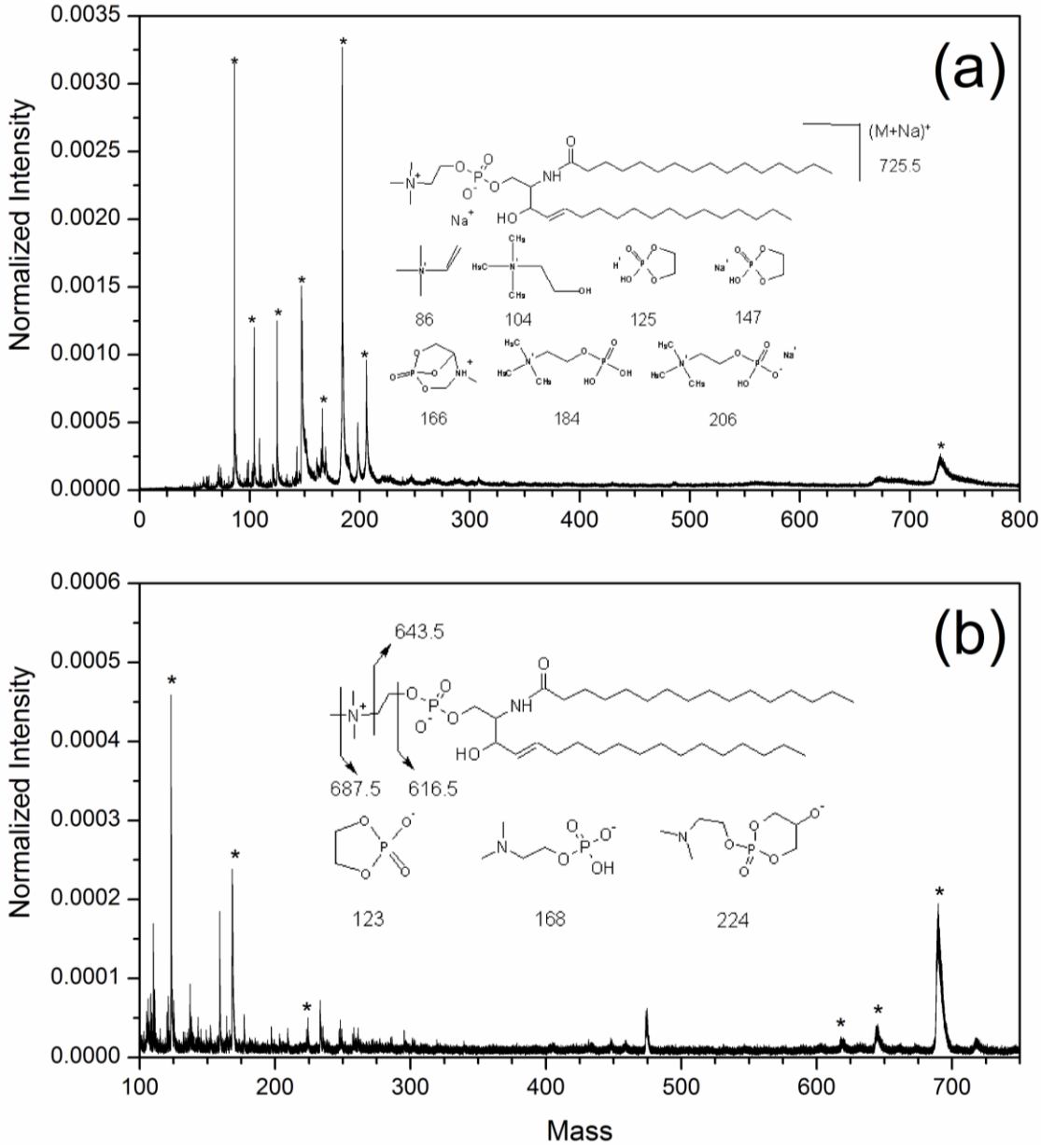

Figure IV-9. (a) Positive and (b) negative mass spectra for a neat electrosprayed surface of d18:1/16:0 sphingomyelin analyzed by 520 keV and 440 keV Au_{400}^{+4} projectiles, respectively.

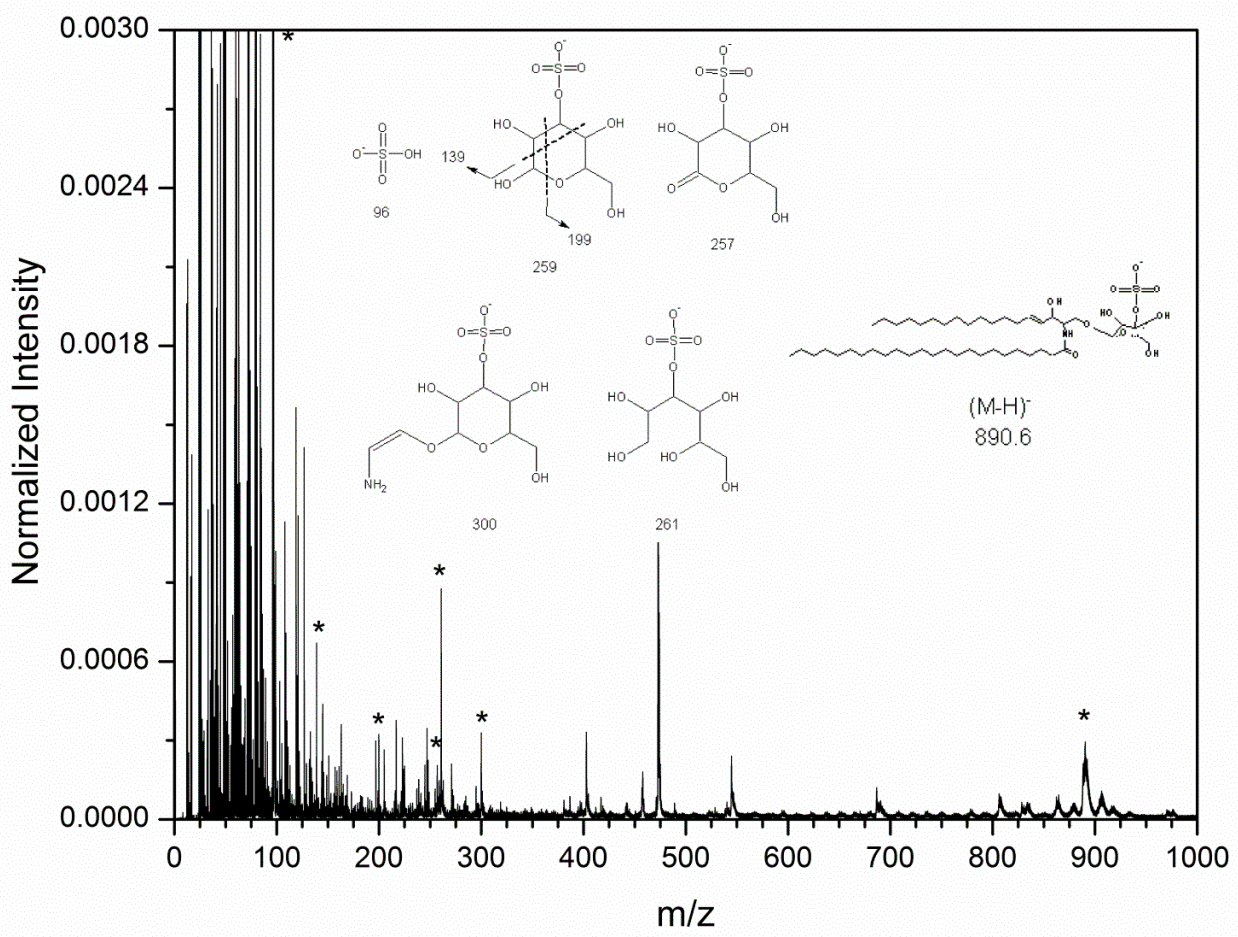

Figure IV-10. Negative ion mass spectrum for a neat electrosprayed surface of a mixture of porcine cerebral sulfatides analyzed by 520 keV Au_{400}^{+4} projectiles.

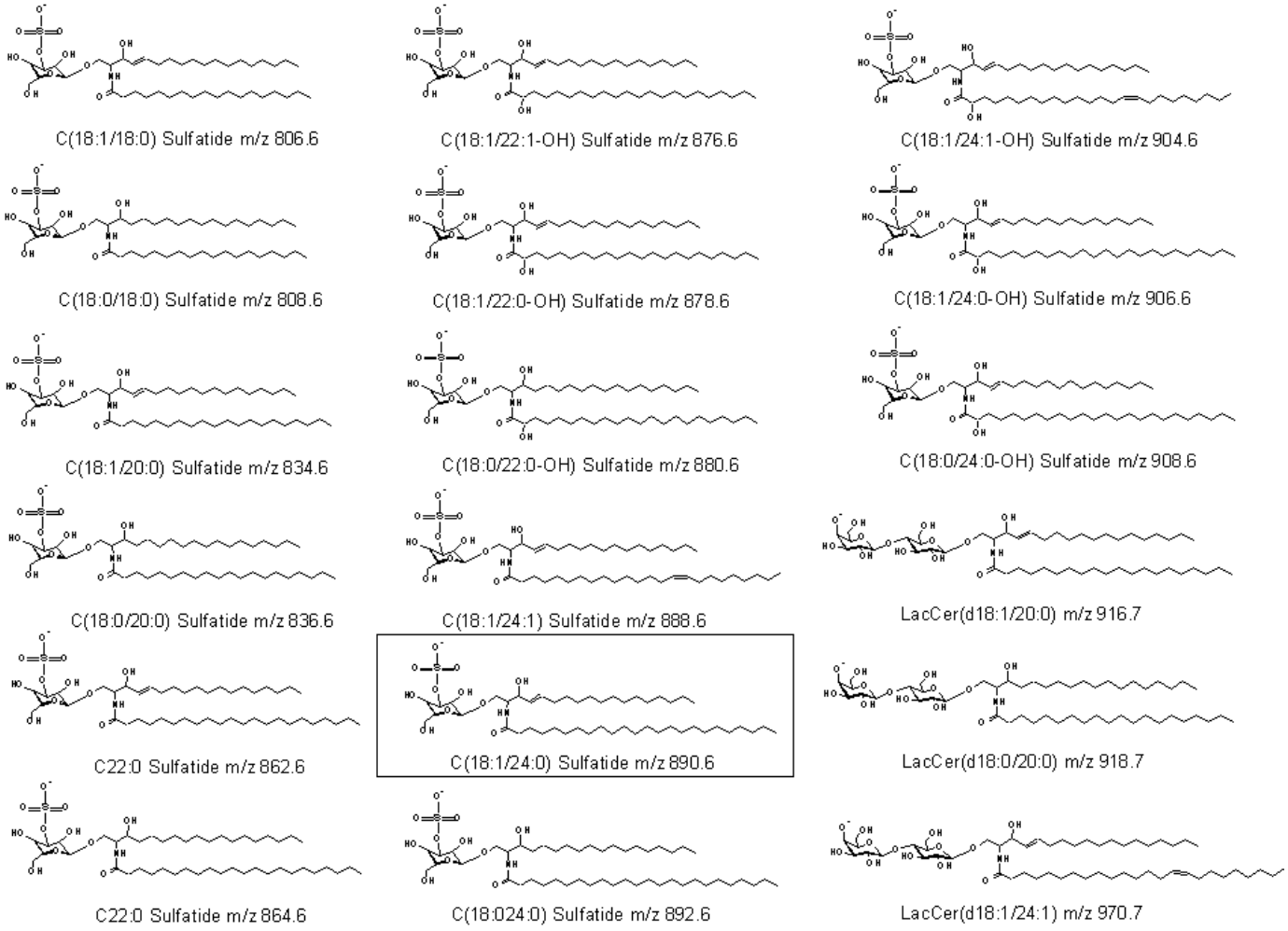

Figure IV-11. Major Molecular species observed from a mixture of porcine cerebral sulfatides.

galactosyl head group including the abundant HSO_4^- ion and peaks at masses 139, 199, 257, 259, 261, and 300. Like in the case of sphingomyelin, no ceramide specific peaks are observed from the tail group. The peaks listed thus far classify the sample lipids as sulfatides, but offer no information regarding the molecular identities of the lipid species. In order to identify the actual structures, intact molecular ions are required. Figure IV-10 reveals many abundant molecular peaks for sulfatides in the range of 600 amu to over 1300 amu. The structures for the most abundant species identified using the web-based Lipid Maps Structure Database[134] are shown in Figure IV-11. These lipids, found in the 800-1,000 amu range, differ in three ways: (1) the lengths of the hydrocarbon tails (2) the presence or absence of a hydroxyl group on the fatty acid tail (3) the addition extra galactosyl moieties to the head group. Nearly all peaks in the 600-1,300 amu range can be attributed to sulfatide-based lipids, with some species containing up to six linked saccharides in the head group. The ability to generate quasi-molecular ions from this range of sulfatide species is clearly essential for their proper identification.

The last lipid considered is 1-stearoyl-2-oleoyl-sn-glycero-3-phospho-(1'-rac-glycerol) (18:0/18:1 PG). This lipid features a glycerophosphate head group which is linked to two fatty acid chains. The negative ion spectrum in Figure IV-12 reveals peaks corresponding to head (masses 153, 171, 211, 227) and tail (masses 281, 283, 509, and 511) group fragments as well as the deprotonated molecular ion (mass 775.5). This list of peaks accounts for most of the abundant species with masses greater than 100 amu.

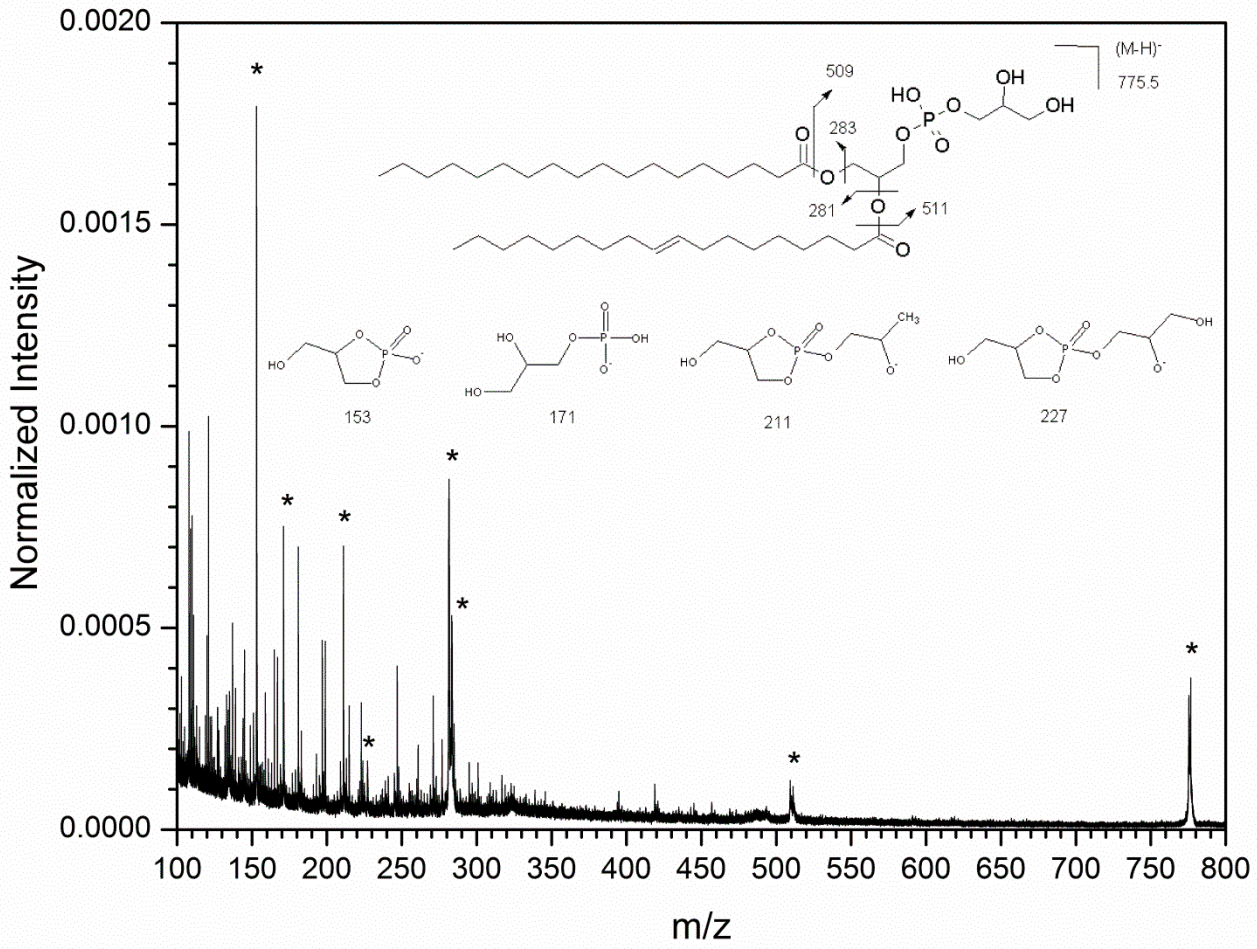

Figure IV-12. Negative ion mass spectrum for a neat electrosprayed surface of 1-stearoyl-2-oleoyl-sn-glycero-3-phospho-(1'-rac-glycerol) analyzed by 520 keV Au_{400}^{+4} projectiles.

Au_3 and Au_{400} Comparison. At higher masses, it is possible to observe dimer and trimer species of the 18:0/18:1 PG molecular ion. This is shown in Figure IV-13 ,which compares spectra obtained from the same 18:0/18:1 PG sample using 130 keV Au_3^+ and 480 keV Au_{400}^{+4} projectiles. This comparative measurement is made using the same instrumentation, detection scheme, and sample for both projectiles. In the case of 130 keV Au_3^+, previous studies have shown that secondary ion emission reaches its maximum around 30-40 keV/atom [135]; that is, the spectrum shown in Figure IV-13a corresponds to a near optimal impact energy for the polyatomic projectile (130 keV/3 ≈ 43 keV/atom). A comparison between Figure IV-13a and 13b shows that the molecular ion signal for Au_{400}^{+4} impacts increases by just over two orders of magnitude relative to Au_3^+ impacts. Also, the production of dimer and trimer species is unique to the massive cluster projectile.

Energy Dependence of Lipid SI Yields. Figure IV-14 shows the variation of secondary ion emission as a function of projectile kinetic energy for the case of Au_{400}^{+4} impacts on a 18:0/18:1 PG model target. The secondary ion yield increases with projectile energy for all abundant analyte-specific and molecular ion signals. The negative ion yields displayed in Figure IV-14a increase by approximately 1.5-fold over the 340-520 keV energy range. Despite this rather limited energy range, it is possible to establish the trend of increasing ion yields. Also, the molecular ion yield appears to increase proportionally with the fragment species, such that greater fragmentation at high impact energies is not observed.

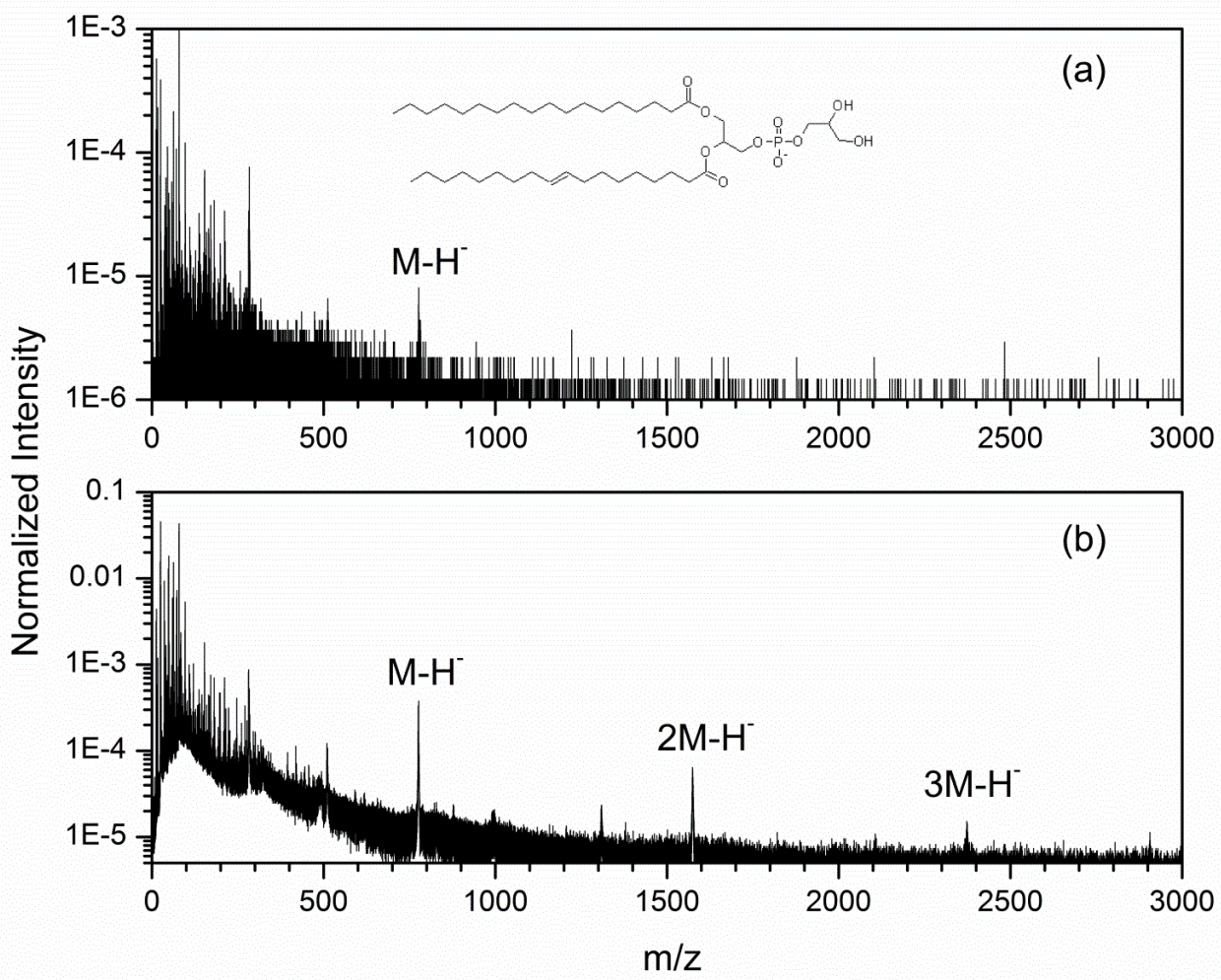

Figure IV-13. Negative ion mass spectra for a neat electrosprayed surface of 1-stearoyl-2-oleoyl-sn-glycero-3-phospho-(1'-rac-glycerol) analyzed by (a) 50 keV Au_3^+ and (b) 520 keV Au_{400}^{+4} projectiles, respectively.

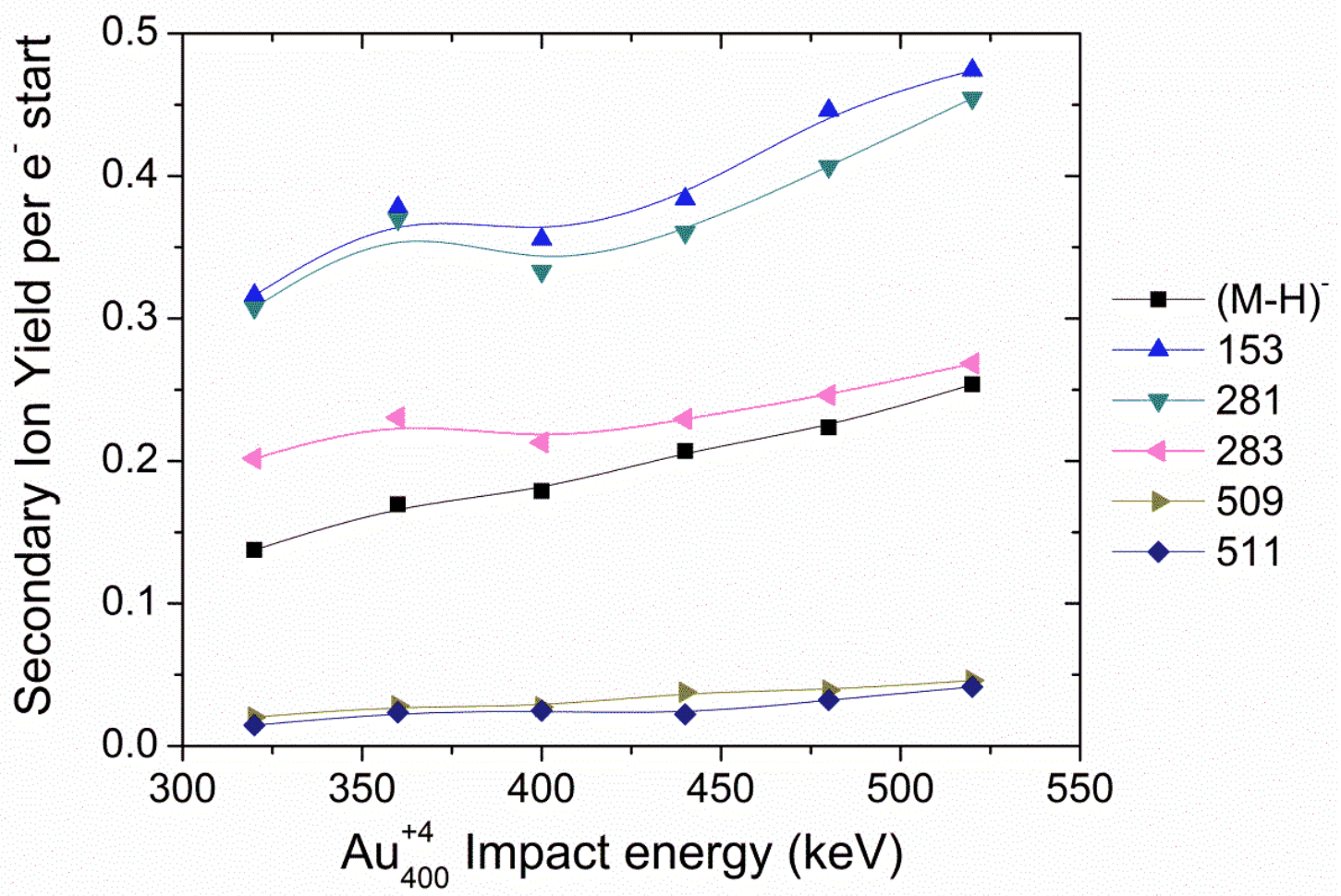

Figure IV-14. Negative ion yields measured from 1-stearoyl-2-oleoyl-sn-glycero-3-phospho-(1'-rac-glycerol) using Au_{400} over a range of impact energies. Data corrected for 59 % transmission efficiency.

Lipid Ion Yields. Transmission corrected ion yields for all lipids discussed above are compiled in Table IV-2. The selected yields include the most abundant head group, tail group, and molecular ion observed for each species where available. Additional abundant quasi-molecular ions are included as well. PO_3^- represents the most abundant species observed from the four phospholipid classes analyzed (18:0/18:1 PG, 16:0 PC, 14:0 PE, and d18:1/16:0 SM). The transmission corrected yield for this species was greater than unity for three of the four molecules. The ion yields for all other fragment and molecular ions range from one percent up to a few ten's of percent (0.01-0 .29 SIs/projectile).

Organic Molecules Below 300 amu

In addition to "large" molecule analysis, massive cluster remain viable for the investigation of smaller molecules as well. This section reports SI yields for these species with limited molecular masses. The test subjects selected for this study include a common synthetic precursor material (p-toluenesulfonic acid), a hormonal drug (diethylstilbestrol), a plastics additive (bisphenol A), an amino acid (glycine), and a series of benzylpyridinium salts used measure the internal energies of emitted species in Chapter V.

Experimental Details. P-toluenesulfonic acid, diethylstilbestrol, bisphenol A, 1-(4-nitrobenzyl)pyridinium bromide), and glycine were purchased from Sigma Aldrich (St. Louis, MO). 1-(4-methoxyphenyl)methylpyridinium tetrafluoroborate, 1-(4-methylphenyl)methylpyridinium bromide, and 1-(4-chlorophenyl)methylpyridinium chloride were purchased from the Florida Center for Heterocyclic Compounds

Table IV-2. Positive and Negative Secondary Ion Yields for Various Lipids Analyzed by 520 keV (Negative Mode) and 440 keV (Positive Mode) Au_{400}^{+4}

Ion Polarity	Species	18:0-1 PG	16:0 PC	14:0 PE	16:0-1 SM	24:0-16:1 ST
Negative	PO_3^- (79)	[2.50]	[1.83]	[1.68]	[0.80]	-----
	Head Group	0.29 (153)	-----	0.070 (140)	0.099 (166)	-----
	Tail Group	0.27 (281)	0.18 (255)	0.25 (277)	-----	-----
	$(M-H)^-$	0.15 (775.5)	-----	0.074 (635.5)	0.19 (689)*	0.28 (891)
	$(2M-2H+Na)^-$	0.038 (1574)	-----	0.022 (1294)	-----	-----
	$(3M-3H+2Na)^-$	0.010 (2373)	-----	-----	-----	-----
Positive	Head Group	-----	0.20 (184)	0.035 (125)	0.40 (184)	-----
	$(M+H)^+$	-----	-----	0.082 (636.4)	-----	-----
	$(M+Na)^+$	-----	0.16 (756.5)	0.033 (658.4)	0.17 (726.6)	-----

Ion masses given in parentheses. Data corrected for 59 % and 90 % transmission efficiencies in negative and positive modes, respectively. *Yield for $(M-CH_3-H)^-$ given. Values in brackets are underestimated due to limited detection efficiency of the 8-anode detector for high multiplicity events.

(Gainesville, FL). 1-(4-cyanobenzyl)pyridinium chloride was purchased from Otava (Toronto, Ontario, Canada). One mg/mL solutions of each molecule in 1:1 MeOH/H_2O were electrospray deposited in atmosphere onto either stainless steel supports(negative mode) or gold-coated silicon wafers (positive mode) from Silicon Vally Microelectronics (Santa Clara, CA). Substrates were chosen to eliminate spectral interferences because each displays limited ion emission in their respective polarities. Spectra were acquired as described previously.

Types of Small Molecule Ions Observed. A series of small organic molecules are presented as test subjects for establishing the ion yields expected for molecular species in the low mass range. Negative ion spectra for three of these example molecules are included in Figure IV-15. All three molecules display intense deprotonated quasi-molecular ion and dimeric molecular ion peaks. The p-toluenesulfonic acid (PTSA, Figure IV-15a) and diethylstilbestrol (DESB, Figure IV-15b) samples additionally give sodiated dimer species. The low mass regions (< 100 amu) of the diethylstilbestrol and bisphenol A (BPA) spectra contain carbon clusters of oscillating intensity, with even-numbered clusters being more intense. This behavior is commonly observed for anionic carbon clusters.[107]

The positive ion spectra measured for a series of five benzylpyridinium (BPY) salts are shown in Figure IV-16. These molecules are used to evaluate ion internal energies in Chapter V, but are presented here as models for positive SI yield measurements. The spectra are generally characterized by the production of only two analyte specific peaks corresponding to the intact molecular ion (M^+) and the fragment

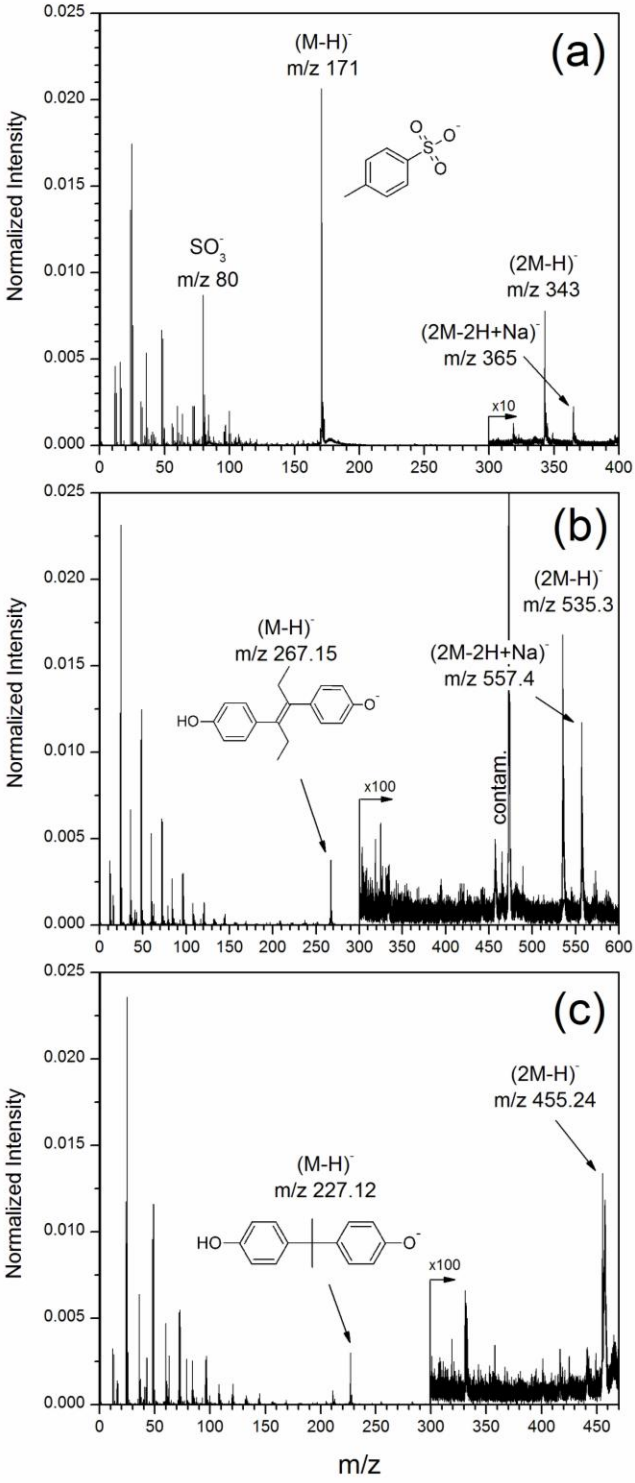

Figure IV-15. Negative ion mass spectra for neat electrosprayed surfaces of (a) p-toluenesulfonic acid, (b) diethylstilbestrol, and (c) bisphenol A analyzed using 520 keV Au_{400}^{+4} projectiles.

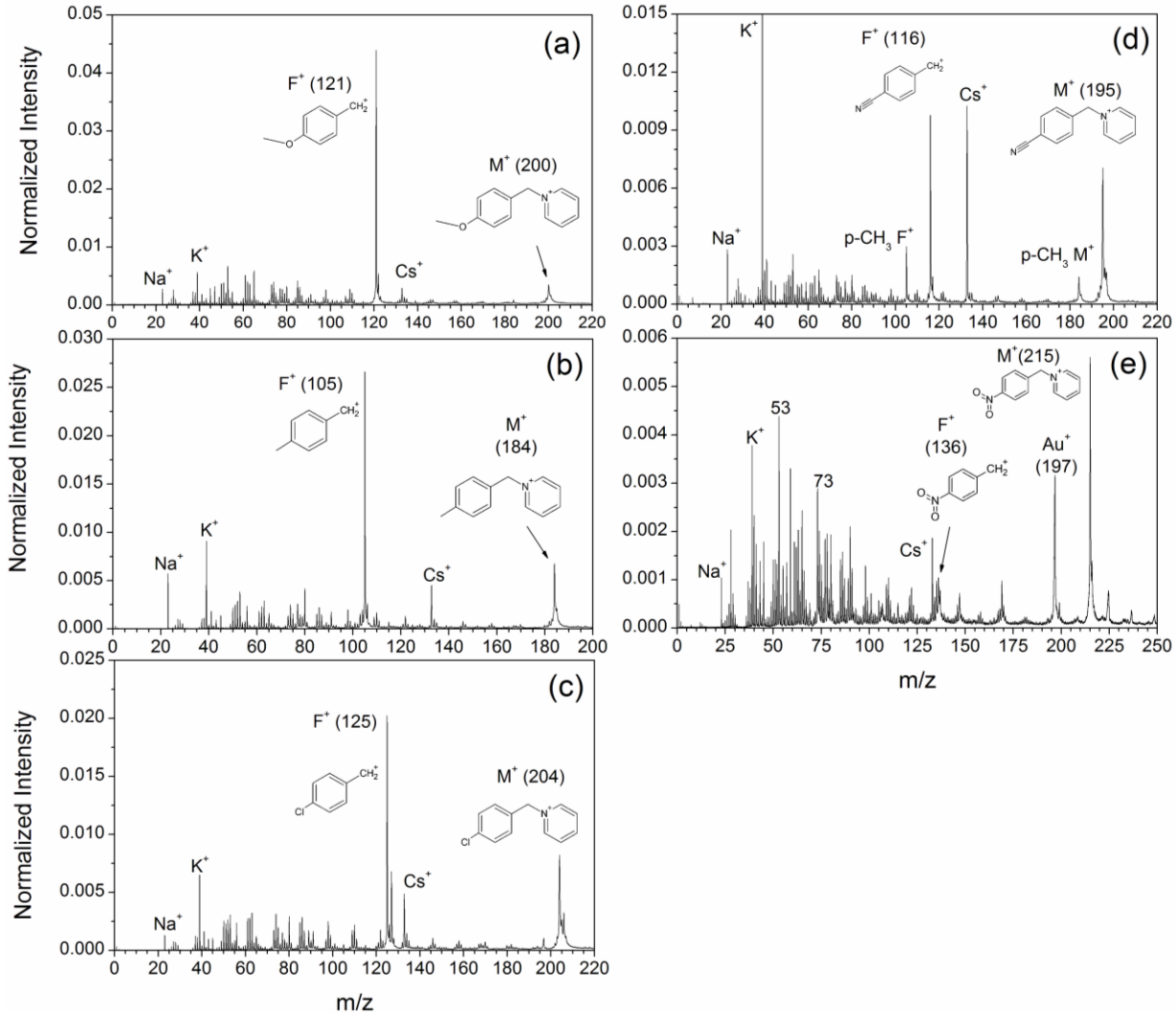

Figure IV-16. Positive ion mass spectra for neat electrosprayed surfaces of (a) p-OCH_3, (b) p-CH_3, (c) p-Cl, (d) p-CN, and (e) p-NO_2 BPY salts analyzed using 520 keV Au_{400}^{+4} projectiles.

formed through loss of a neutral pyridine ring ($(M-C_5H_5N)^+$). The positive spectra shown also exhibit alkali metal contaminants Na^+, K^+, and Cs^+. Surface mass spectrometry is particularly sensitive to alkali metal contamination due to the high ionization efficiencies of these ions.[136] The cesium contamination observed derives from the CsI standard used to calibrate the ToF mass spectrometer. CsI is sputtered during analysis, coating nearby electrodes and allowing for transfer to subsequent samples which are analyzed. Inclusion of both analyte specific peaks, the alkali ion peaks, and an Au^+ peak from the substrate in the p-NO_2 BPY spectrum accounts for all major peaks observed in the spectra.

Small Molecule Ion Yields. SI yields measured for p-toluenesulfonic acid, diethylstilbestrol, bisphenol A, and the amino acid glycine are provided in Table IV-3. The molecular ion yields for BPA and DESB are quite similar at 22 % and 31 %, respectively. A much higher molecular ion yield is measured for PTSA (206 %), likely due to the excellent ionization efficiency of the strong acid. Yields for the dimers of each species are again similar for BPA and DESB (~ 1.0 % each) with PTSA giving a yield nearly an order of magnitude higher (9.0 %). The PTSA spectrum also shows a peak for the trimer with a yield of nearly 1 %.

Glycine is included in this ion yield investigation due to its previous use as a yield calibration standard at various Au_{400} impact energies.[82] The glycine yields provided have been corrected for absolute detection efficiency, meaning these values account for a 59 % transmission efficiency and a ~35 % detection efficiency using an MCP detector for 10 keV ions in this mass range. This analysis shows that over six deprotonated glycine molecules are emitted on average for each Au_{400} impact event. The

Table IV-3. Negative Ion Yields for Various Small Organic Molecules Analyzed by 520 keV Au_{400}^{+4}

Molecule	Ion	Mass	Yield
Bisphenol A	$(M-H)^-$	227	0.22
	$(2M-H)^-$	455	0.013
	Au^-	197	0.017
Diethylstilbestrol	$(M-H)^-$	267	0.31
	$(2M-H)^-$	535	0.017
	Au^-	197	0.014
p-Toluenesulfonic acid	$(M-H)^-$	171	[2.10]
	$(2M-H)^-$	343	0.090
	$(3M-H)^-$	515	0.008
	SO_3^-	80	[0.62]
	Au^-	197	0.018
Glycine	$(M-H)^-$	75	[6.50]
	$(2M-H)^-$	149	[0.91]
	CN^-	26	[10.2]
	$Au(CN)_2^-$	249	0.38
	Au^-	197	0.041

Data corrected for 59 % transmission efficiency. Glycine data was acquired at 400 keV and is corrected for a 35.4% transmission and detection efficiency. Values in brackets are underestimated due to limited detection efficiency high multiplicity events using the 8-anode detector.

yield for the CN^- fragment is even higher at over 10 SIs per impact. Moving to the glycine dimer (91 %) and $Au(CN)_2^-$ adduct (38 %) it is obvious that Au_{400}^{+4} at 400 keV is capable of producing very high ion yields for some small molecule species.

Energy Dependence. As suggested, glycine SI yield measurements have been performed over a range of energies and these previous measurements offer an excellent standard for assessing performance of the current instrumentation. Figure IV-17 shows data collected for glycine using the first generation gold cluster SIMS instrument at TAMU, the M.P. Tandem accelerator at the Nuclear Institute of Physics in Orsay (France), and the second generation gold cluster SIMS instrument at TAMU. The trend lines added show excellent agreement for the CN^-, $(M-H)^-$, and $(2M-H)^-$ ion yields across the range of energies tested. The $Au(CN)_2^-$ yield measured is less than that predicted by the trendline by about a factor of 2.5. An explanation for this may be that the current measurement was performed in a reflectron ToF while previous measurement were done using a linear arrangement. If the gold adduct exists as a metastable ion, this species may dissociate in flight and be lost before detection. Despite this difference, the other ion yields presented establish both that SI yields in the 100 qkeV range fall on the previous trendlines and that the current instrumentation is operating properly.

A second example of the energy dependence of SI yields for small molecules can be provided using the BPY salts. The yields for the molecular ions of all five BPY species are plotted against the projectile kinetic energy used over the range of 160-440 keV in Figure IV-18. The positive molecular ion yields measured in the second analysis chamber increase by nearly two orders of magnitude over this energy range. This

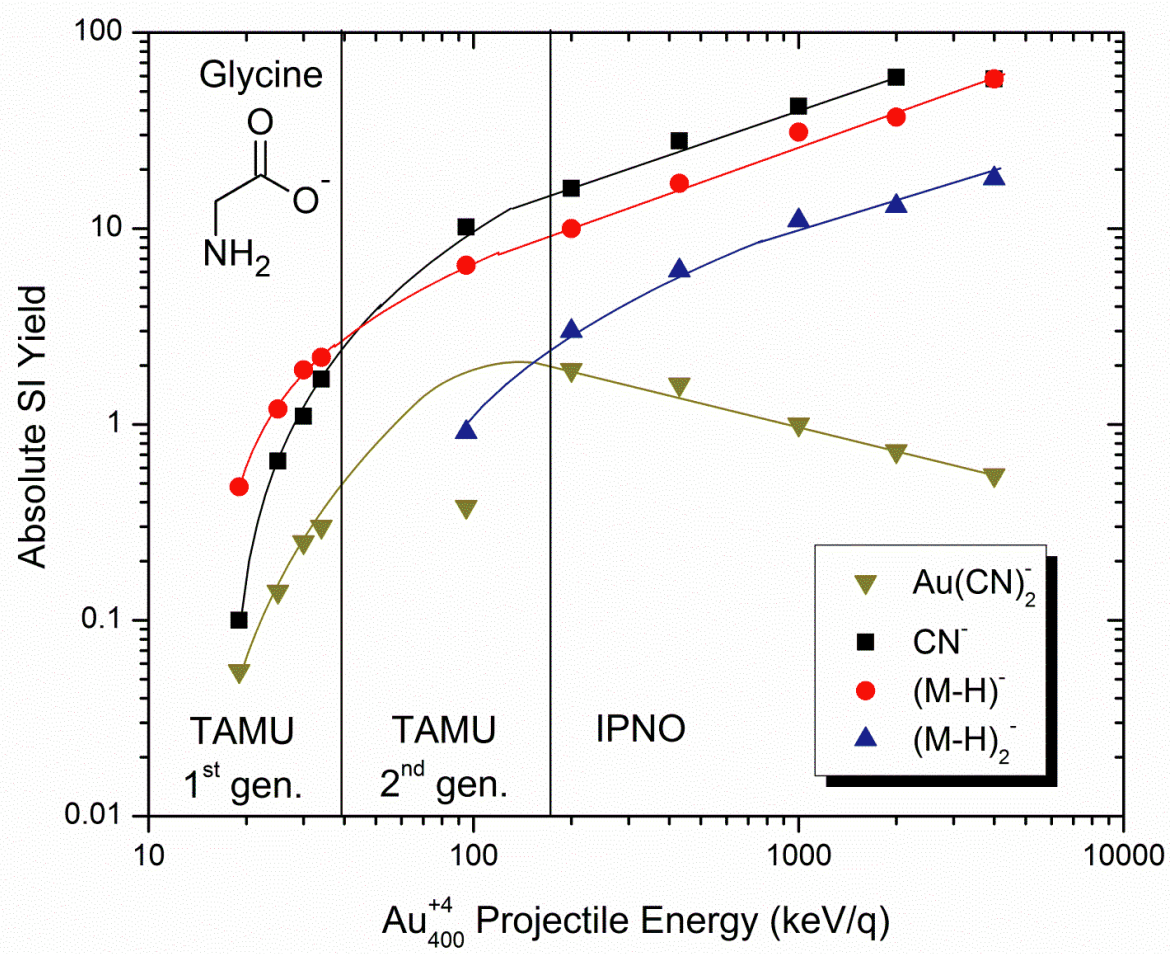

Figure IV-17. Negative ion yields measured from a neat glycine surface using Au_{400} over a range of impact energies. Absolute yields are reported, accounting for transmission and detection efficiencies. Part of the data reported in this figure is reprinted with permission from "Massive Clusters: Secondary Emission from qkeV to qMeV. New Emission Processes? New SIMS Probe?" by S. Della-Negra, J. Depauw, C. Guillermier, and E.A. Schweikert, 2011. *Surface and Interface Analysis*, 43, 62-65, Copyright [2011] by John Wiley and Sons.

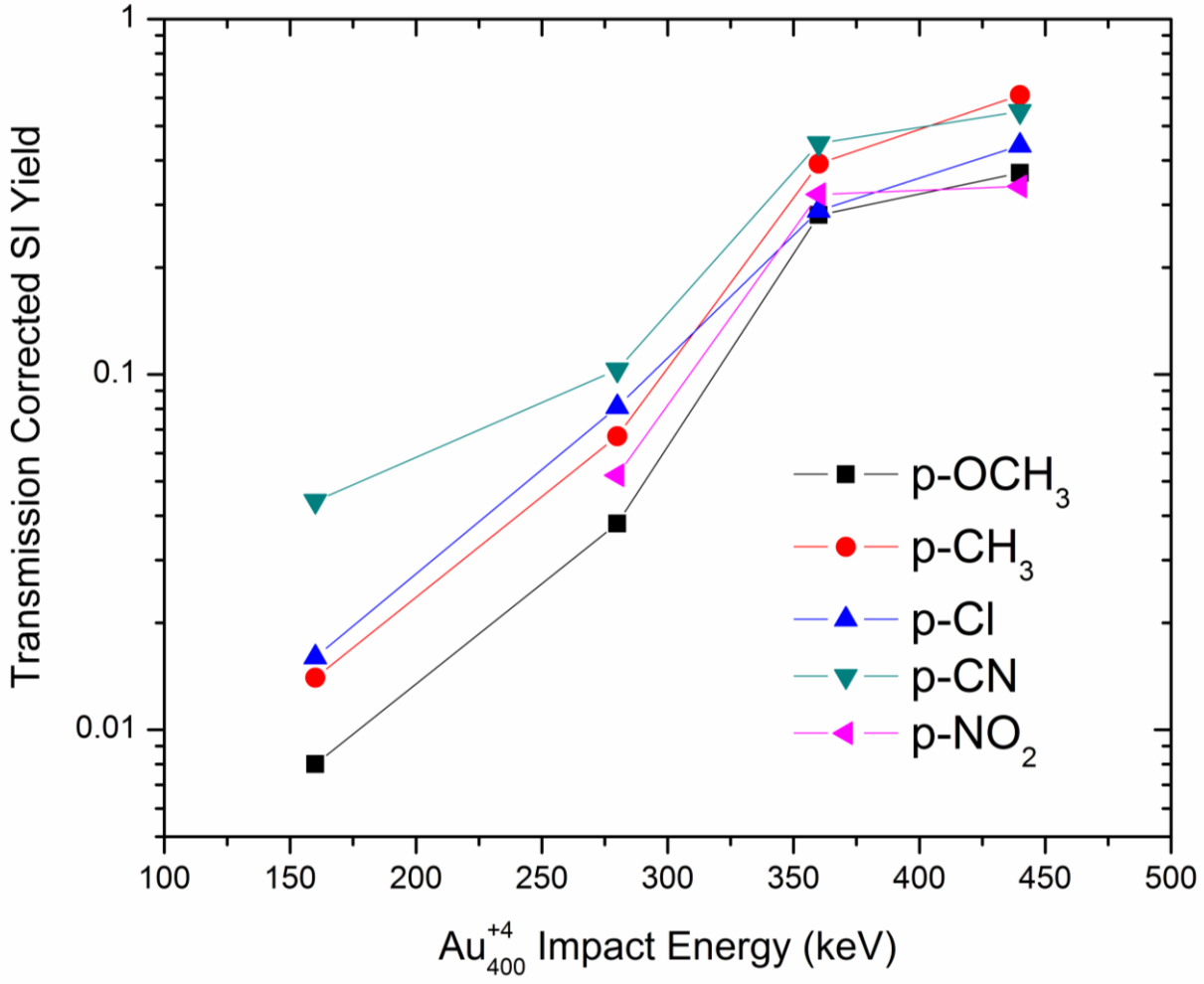

Figure IV-18. Positive ion yields measured from neat BPY salt surfaces using Au_{400} over a range of impact energies. All yields are measured in coincidence with an H^+ start signal and are corrected for 90 % transmission efficiency.

variation is significantly greater than the factor of 1.5 increase observed for the 18:0/18:1 PG example in negative mode. The reason for the drastic change in measured ion yields derives from the method of obtaining the ToF measurement. The event-by-event methodology used necessitates a trigger particle to initiate the ToF measurement. In negative mode electrons serve as the start signal while in positive mode protons are used. The electron yields measured for a variety of surfaces using C_{60} and Au_{400} impacts have shown that many electrons are produced for each projectile impact.[89, 90]

Despite previous reports of high H^+ yields at slightly higher Au_{400} impact energies,[82] this and other unpublished experiments suggest the proton yields decrease drastically with impact energies at the low end of the range being measured. This observation may be convoluted by decreased ion transmission through the magnetic deflector employed (see Chapter II). The result of a proton yield below unity is that instead of measuring the actual number of SIs per impact, the number of SIs emitted coincidentally with H^+ is measured. This ability to measure coincidental ion emission can be used advantageously to monitor ion co-location (see Chapter VI), but in this case, the SI yield must be reported as relative to the detection of H^+ start signals. Numerical values for the BPY ion yields are provided in Table IV-4. SI Yields for the 440 keV impact energy are the most reliable as the proton yield is expected to be close to if not greater than unity. The molecular ion yields at this impact energy range from 34 % to 61 % for the various ions and the fragment ion yields range from 7.8 % to 119 %. The fragment ion yields vary significantly more due to differing fragmentation activation

Table IV-4. Positive SI Yields Measured for Various BPY Molecular and Fragment Ions Analyzed by Au_{400}^{+4} at Different Impact Energies

		Impact Energy (keV)			
Molecule	Ion	160	280	360	440
p-OCH_3	M^+	0.008	0.038	0.28	0.37
	$(M\text{-}C_5H_5N)^+$	0.070	0.31	1.24	[1.19]
p-CH_3	M^+	0.014	0.067	0.39	[0.61]
	$(M\text{-}C_5H_5N)^+$	0.033	0.14	0.79	[0.94]
p-Cl	M^+	0.016	0.081	0.29	0.44
	$(M\text{-}C_5H_5N)^+$	0.027	0.14	0.43	[0.55]
p-CN	M^+	0.044	0.10	0.45	[0.55]
	$(M\text{-}C_5H_5N)^+$	0.047	0.10	0.37	0.37
p-NO_2	M^+	------	0.052	0.32	0.34
	$(M\text{-}C_5H_5N)^+$	------	0.019	0.097	0.078

Data corrected for 90 % transmission efficiency. Values in brackets are underestimated due to limited detection efficiency of the 8-anode detector for high multiplicity events. Yields measured using H^+ as the ToF trigger particle.

barriers for the molecules as discussed in Chapter V. SI yields on the order of 10^{-9} SIs/PI have previously been reported for the p-OCH_3, p-Cl, and p-CN BPY molecules.[137] This gives 440 keV Au_{400}^{+4} roughly 8 orders of magnitude greater SI yields for these BPY salts.

Inorganics

Sample Preparation. CsI was purchased from Sigma Aldrich (St. Louis, MO). A One mg/mL solution of the salt in 1:1 MeOH/H_2O was electrospray deposited in atmosphere onto a stainless steel supports. Mass spectra were obtained as described previously.

Types of CsI Ions Observed. Cesium iodide has been used extensively as a mass spectrometric calibration standard and the types of observable ions have been well-documented.[138] The spectra and ion yields for CsI are reported as a means of gauging projected ion yields for similar inorganic salt materials. The positive and negative spectra of CsI shown in Figure IV-19 are characterized by the production of salt clusters coupled with a single anion or cation ($(CsI)_nCs^+$ or $(CsI)_nI^-$). The negative ion spectrum shows CsI clusters out to $(CsI)_9I^-$ at mass 2467 with each sequentially larger cluster reducing in intensity. The positive spectrum shows an even more extended distribution reaching out to $(CsI)_{14}Cs^+$ at mass 3773. It is important to note that this spectrum was acquired in the first analysis chamber using an H^+ start generated without a strong deflecting magnet. Instead, all 8 of the CFD ports were summed to give the start signal while retaining the multiplicity afforded by the multi-anode detector. The transmission corrected SI yields for CsI clusters in both polarities are reported in Table IV-5. Yields

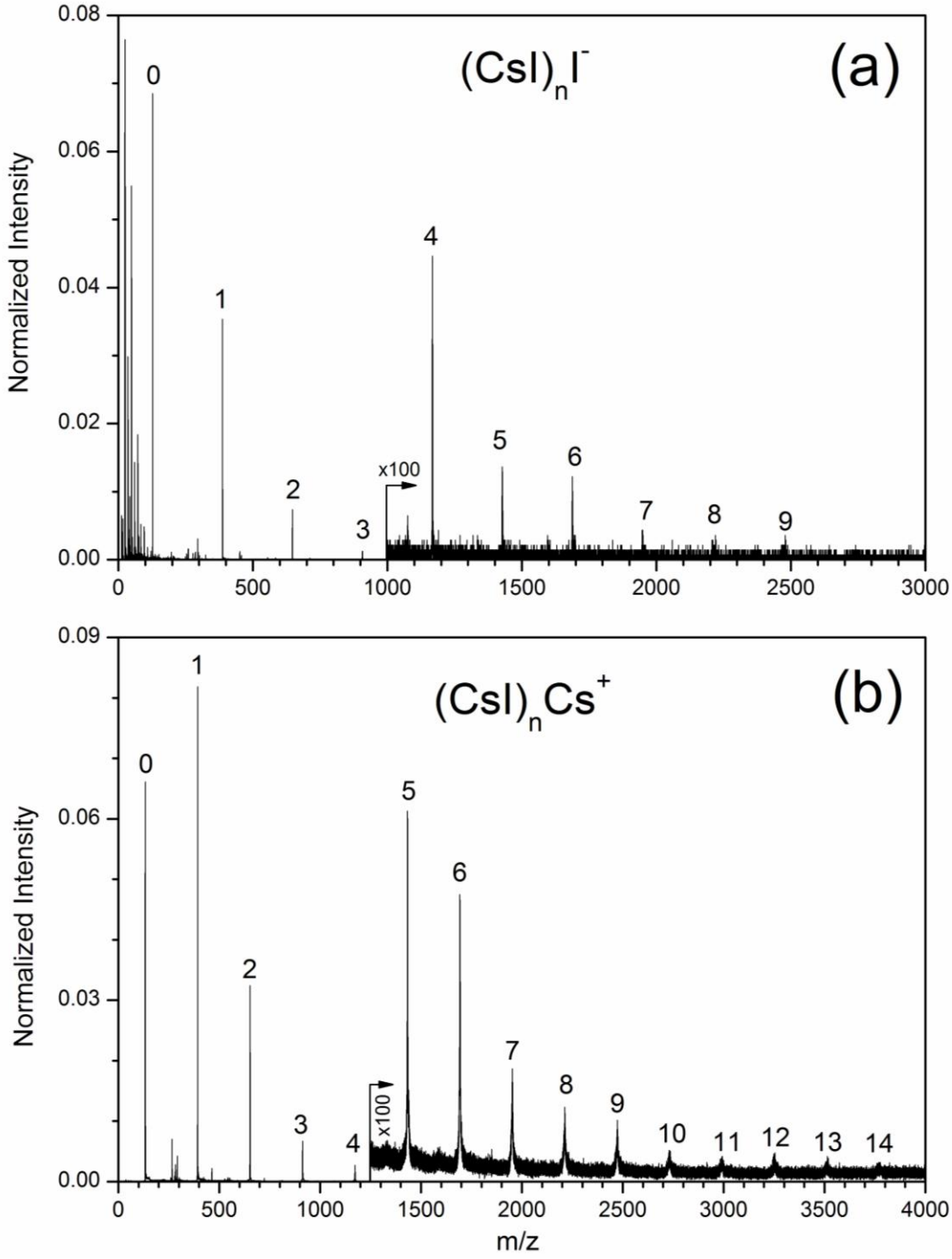

Figure IV-19. (a) Negative and (b) positive mass spectra for a neat electrosprayed surface of CsI analyzed by 520 keV and 340 keV Au_{400}^{+4} projectiles, respectively.

Table IV-5. Ion Yields Measured for CsI Clusters Analyzed with 520 keV (Negative Mode, $(CsI)_nI^-$) and 340 keV (Positive Mode, $(CsI)_nCs^+$) Au_{400}^{+4}

CsI Cluster Number	Negative Ion Yield	Positive Ion Yield
0	[8.761]	[7.161]
1	[7.532]	[7.138]
2	[2.593]	[3.272]
3	[0.774]	[0.907]
4	0.273	[0.633]
5	0.092	0.213
6	0.082	0.193
7	0.041	0.100
8	------	0.062
9	------	0.054
10	------	0.038
11	------	0.034
12	------	0.029
13	------	0.026
14	------	0.022

Data corrected for 59 % transmission efficiency. Values in brackets are underestimated due to limited detection efficiency of the 8-anode detector for high multiplicity events.

reported for clusters 0-3 are underestimated due to the high yields of these species and the inherent limitations of the 8-anode detector (see Chapter II). The yields measured for the range of CsI cluster sizes stretch from ~ 8 SIs per impact for the Cs^+ and I^- species down to a few percent for the largest clusters.

Conclusion

The spectra and yields reported in this chapter offer a metric for assessing the efficiency of the Au_{400} projectile over a range of different chemical classes. The spectra are characterized with the production of many analytically significant peaks, including the molecular ion for all test cases. SI yields greater than unity are observed for easily ionizable small fragments (CN^-, PO_3^-) low mass molecular ions (YGGFL, PTSA, CsI) with higher mass molecules giving yields in the range of 10^{-2} to 1 SIs/PI. These values are as much as 8 orders of magnitude greater than yields reported for atomic bombardment.[137]

Total and selected SI multiplicities are reported for the peptide leu-enkephalin using the Au_3 and Au_{400} projectiles. This comparison offers an insight into the efficiency of the Au_{400} projectile, given some events that produce upwards of 100 total SIs per event and 7 molecular ions per event.

The utility of higher impact energies is shown by comparing SI yields for a range of impact energies. These measurements, performed with a glycerphospholipid, amino acid, and BPY salts, confirm that SI yields increase with projectile kinetic energy. This finding validates the effort invested in constructing this second generation instrument.

CHAPTER V

MEASUREMENT OF THE SECONDARY ION INTERNAL ENERGY DISTRIBUTION*

Introduction

Mass spectrometrists have long recognized the importance of ion internal energy for understanding the relative abundances of mass spectral peaks.[139] The challenge is to quantify the amount of energy imparted to gas phase ions as a function of the ionization technique or other experimental parameters. Two approaches for observing secondary ion internal energies are presented. The first approach uses the pentapeptide leu-enkephalin, a well-known calibration standard in mass spectrometry. Detailed descriptions of this molecule's fragmentation enables its use as a measure of the internal energy accumulated during ionization[140]. Measurements using this fragmentation model are qualitative, allowing for rough comparisons to other excitation techniques.

To extract more quantitative information regarding the energies of SIs emitted from massive metal cluster impacts, a second approach using tailored benzylpyridinium (BPY) probe ions is used. This suite of molecules is attractive for understanding the parameters involved in the generation and manipulation of gas phase ions because: (1) fragmentation largely proceeds via a single pathway; (2) substitution on the benzyl ring

* Part of this chapter is reprinted with permission from "Characteristics of Positive and Negative Secondary Ions Emitted from Au_3^+ and Au_{400}^{+4} Impacts" by J.D. DeBord, F.A. Fernandez-Lima, S.V. Verkhoturov, E.A. Schweikert, and S. Della-Negra, 2012. *Surface and Interface Analysis*, Copyright [2012] by John Wiley and Sons.

enable control of the fragmentation activation barrier; (3) the series of molecules are all similar in mass and structure, giving them similar detection efficiencies in mass spectrometric applications; (4) the use of an organic molecular system should allow for extrapolation to predict internal energies of larger organic species. The benzylpyridinium ion system has been used to characterize a variety of ionization techniques including electrospray ionization,[141] desorption electrospray ionization,[142] matrix-assisted laser desorption ionization,[143] electrospray droplet impact,[144] atomic projectile secondary ion mass spectrometry (SIMS),[137, 145, 146] and cluster projectile SIMS.[147]

Two methods for applying these "thermometer ions" are described. The first utilizes the survival yield method first proposed by De Pauw et al.[141] Internal energy distributions for species emitted from Au_{400}^{+4} and Au_3^+ impacts are measured and compared to distributions previously measured for other ionization techniques. Again, like the leu-enkephalin model, this approach is largely qualitative and while useful for relative comparisons, does not provide the desired absolute quantitation. To achieve more accurate quantitation, a novel procedure for measuring internal energies using the BPY ions is presented for the case of Au_{400}^{+4} impacts.

Leucine-Enkephalin Model

The leu-enkephalin sample was prepared and analyzed as stated in Chapter IV, with the negative (Figure V-1a) and positive (Figure V-1b) ion spectra for leu-enkephalin characterized by abundant emission of intact molecular ions and immonium fragment ions. Only two backbone fragmentation peaks, the b_2 and y_2 fragments are

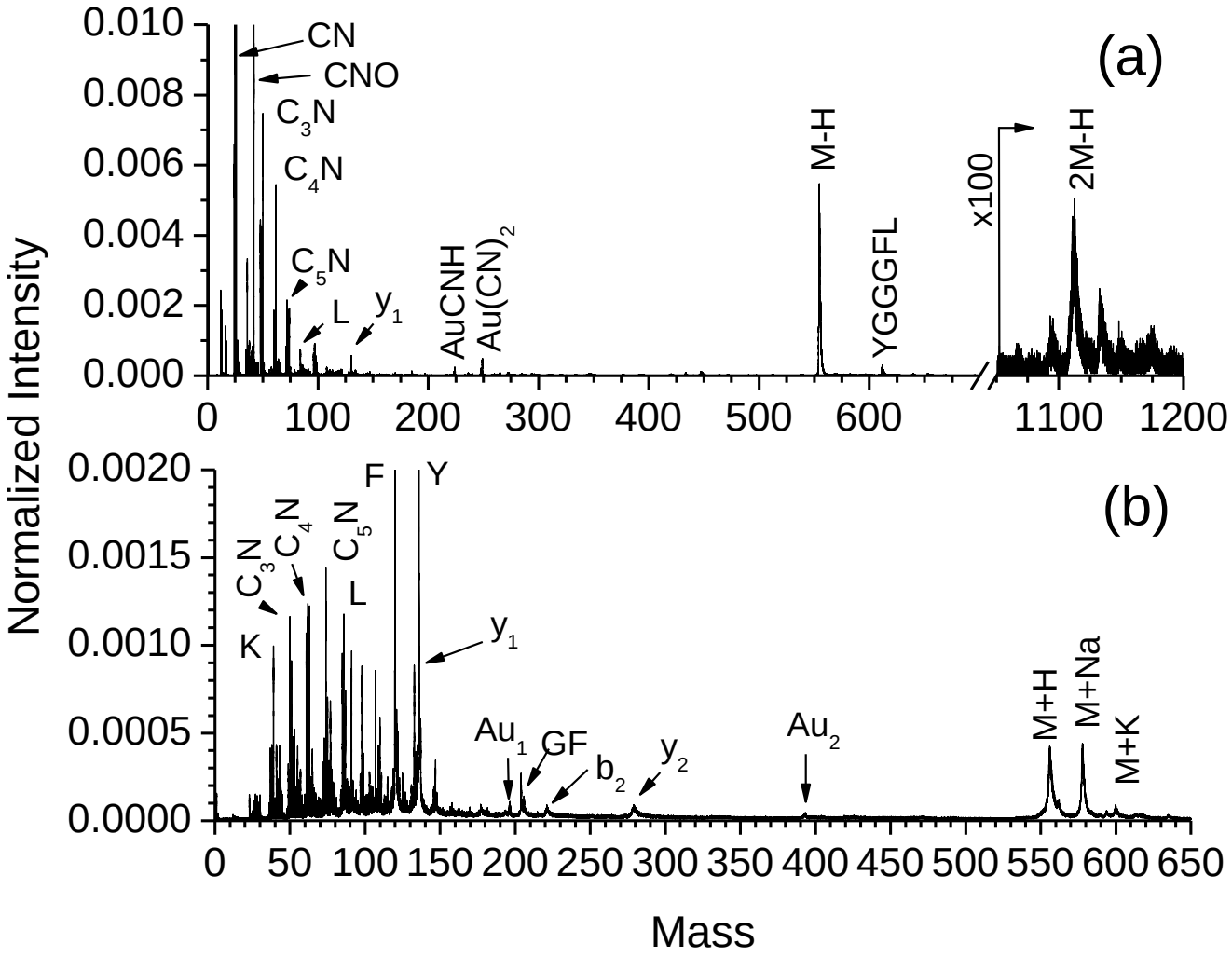

Figure V-1. (a) Negative and (b) positive mass spectra for a neat electrosprayed surface of leu-enkephalin analyzed by 520 keV and 440 keV Au_{400}^{+4} projectiles, respectively.

observed in positive mode, yet these have low intensities relative to the smaller fragments and molecular ion. Typically amino acid residues, such as the F, Y, and L immonium ions observed, result from multi-step fragmentation processes.[140] These fragmentation mechanisms which are often observed in collision or surface induced dissociation (CID or SID) spectra necessitate the survival of many species along the fragmentation tree[140]. The observation of immonium ions without the corresponding parent ions suggests that these ions do not originate from traditional gas phase fragmentation processes but are instead formed under the high temperature/high pressure conditions within the projectile track.

Molecular dynamics simulations have shown that the energy densities which develop within the track and at the crater rim are quite different[148]. This suggests there two general types of emission which can occur from Au_{400} impacts. Emission can occur from within the highly energized crater volume resulting in highly fragmented species, or from the crater rim resulting in molecular emission. Simulations and experimental results have indeed shown that molecular emission occurs from the rim of the impact crater, resulting in ions with internal energies sufficiently low that they survive for analysis [94, 149]. Comparing to reported CID spectra of leu-enkephalin,[140] we can approximate the internal energies imparted to molecular species. The ratio of intact molecular ions to backbone fragments is greater than that obtained with 9eV CID, suggesting the species emitted from the rim of Au_{400} impact craters have relatively lower internal energies. However, the ratio of backbone fragments to immonium ions is smaller than that observed in a 20 eV CID spectrum, meaning the other component of

the emission (close to "ground zero") exhibits much greater initial internal energies than the collisionally activated ions.

BPY Ion Survival Yield Method

Figure V-2 shows the favored fragmentation pathway for a generic BPY ion which yields a substituted benzyl fragment ion (F^+) and a neutral pyridine (Py^0) molecule. By changing the benzyl side group, the activation barrier for this reaction can be modified such that different BPY ions can be used to probe various points along the internal energy distribution. Both theories of calculation described below utilize the framework of this tunable fragmentation pathway

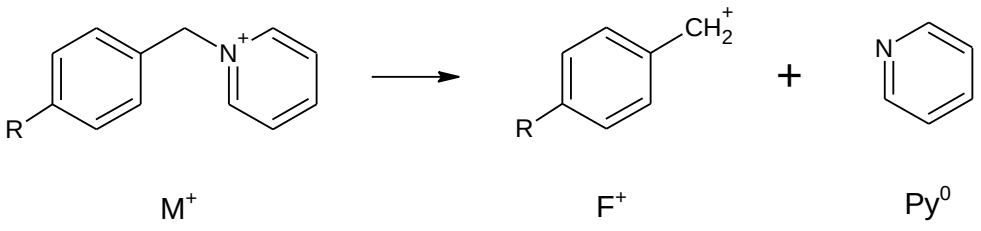

Figure V-2. Preferred Fragmentation Pathway for Benzylpyridinium Ions

All samples were prepared and analyzed as described in Chapter IV. Five BPY molecules (p-OCH_3, p-CH_3, p-Cl, p-CN, and p-NO_2) with a broad range of C-N bond strengths were chosen for experimental investigation. A representative spectrum for p-CH_3 BPY is provided in Figure V-3. The parent (mass 184) and daughter (mass 105) ion peaks represent the only identifiable signals from the BPY salt. Other abundant spectral

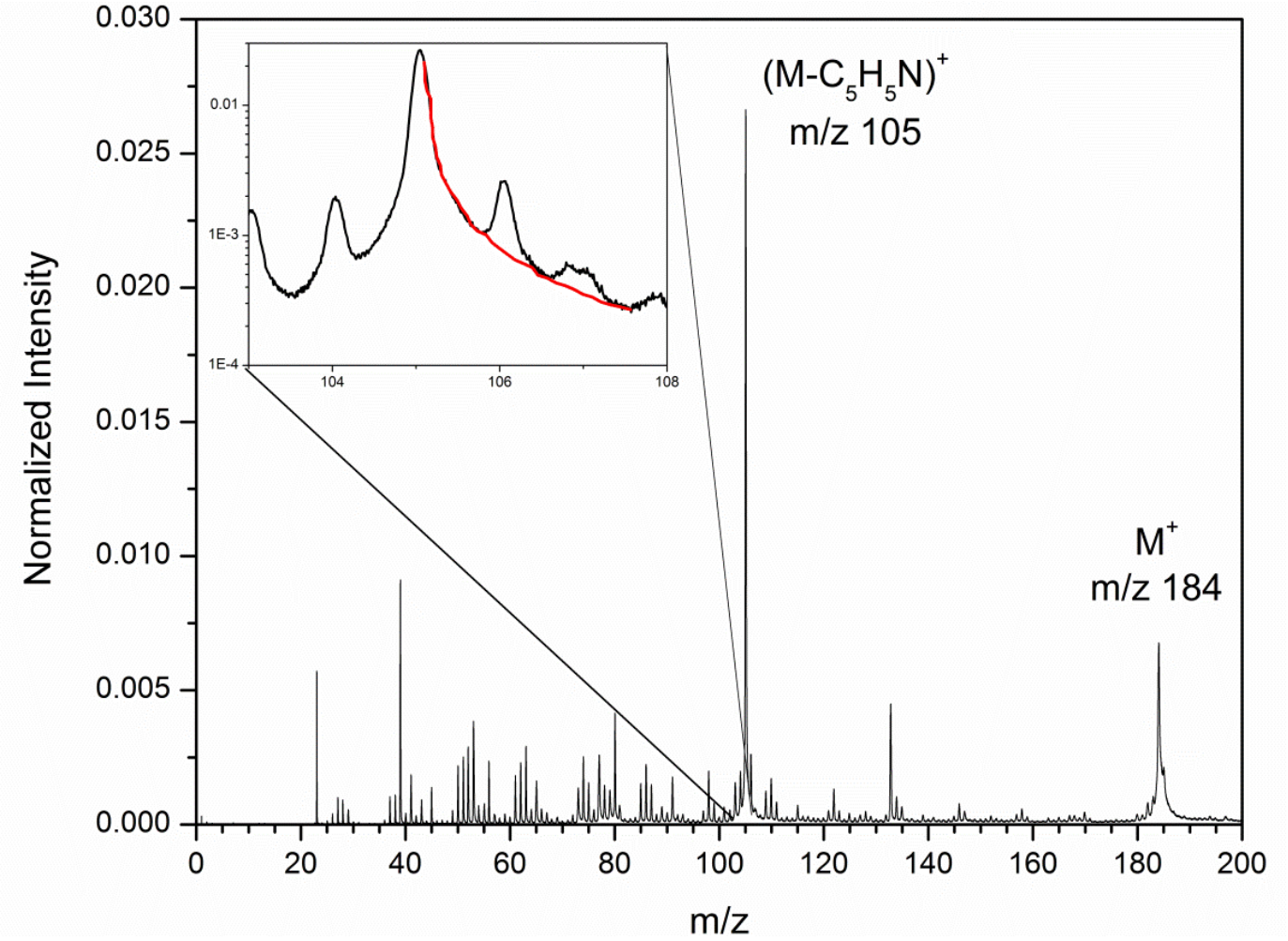

Figure V-3. Mass spectrum of p-CH_3 BPY ion generated by 440 keV Au_{400}^{+4} impacts. Fragmentation tail is highlighted in red.

signatures correspond to common surface contaminants (pump oil, residual gas, etc.). Preliminary measurements using the BPY ions were performed according to the original survival yield method.[146, 150] This method entails plotting a quantity known as the survival yield versus the calculated activation barrier for each BPY ion. The survival yield is defined as the ratio of intact ions detected to the sum of intact and fragment ions detected as shown in Equation 5.1.

$$SY = \frac{M^+}{M^+ + \sum F^+} \tag{5.1}$$

This figure of merit quantifies the fraction of molecular species which survive for detection. Plotting these values against the corresponding C-N bond strengths, which were previously calculated via quantum mechanical calculations at the AM1 level,[151] generates a breakdown curve as shown as shown in Figure V-4a. Boundary conditions are assumed such that the survival yield for theoretical molecules having critical bond energies of 0 eV and 3.5 eV would have survival yields of 0 and 1, respectively.[141] These data points can be fitted with a sigmoidal curve, which upon differentiation gives the distribution of internal energy accumulated on the C-N bond for all molecules. Figure V-4a shows the survival yield plots along with their sigmoidal fits for 440 keV Au_{400}^{+4} and 110 keV Au_3^+. Also plotted are previous data from the literature acquired using electrospray ionization (ESI)[142] and fast atom bombardment (FAB)[146, 150]. The resultant internal energy distributions for the various ionization methods are shown in Figure V-4b. The ESI and FAB experiments serve as references for well-recognized methods of "soft" ionization. The interesting feature common to all data except the FAB data from

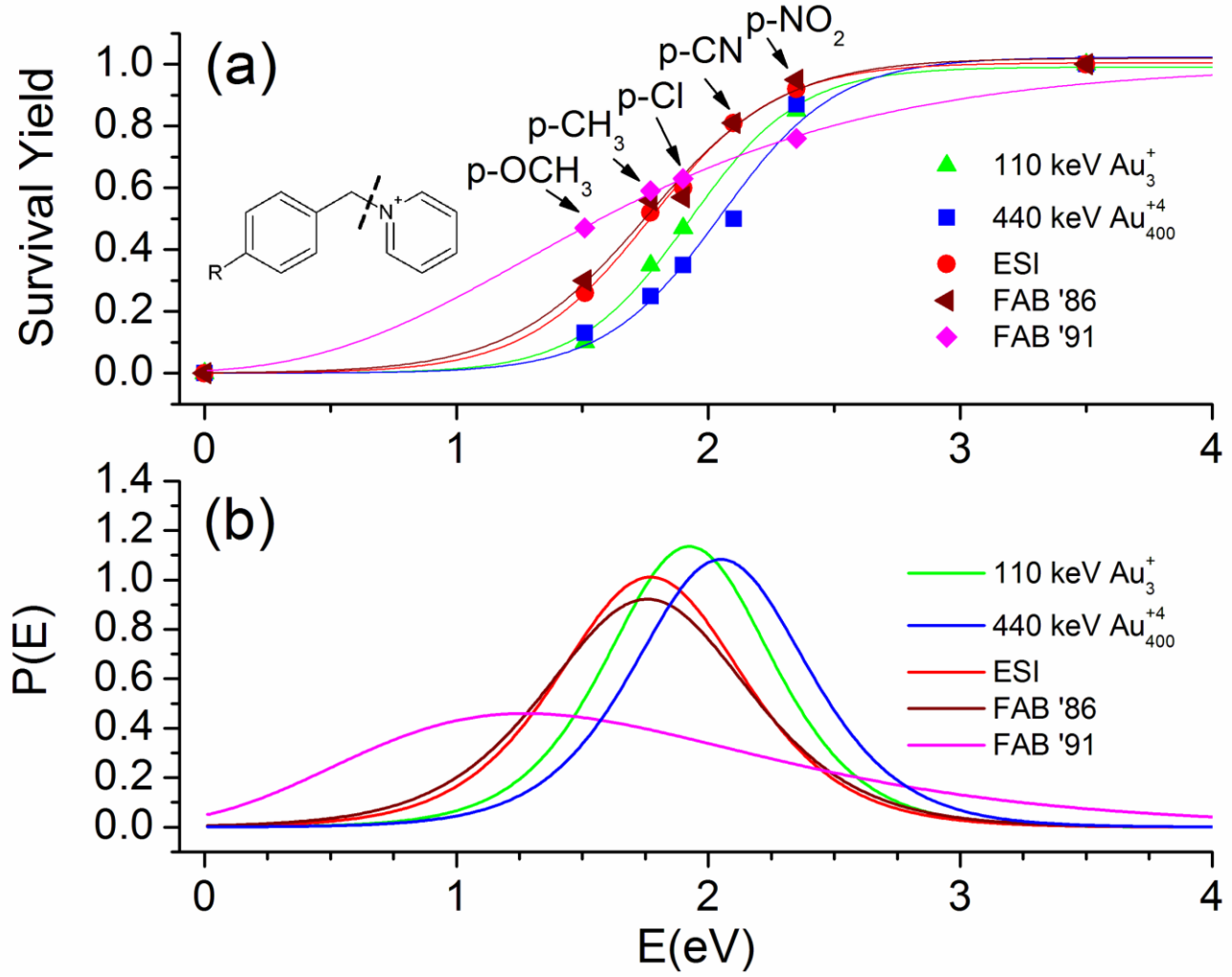

Figure V-4. (a) Breakdown curves and (b) internal energy distributions for various ionization techniques. ESI data is from ref. [142]. The 1991 FAB data is from ref. [150] and the 1986 FAB data is taken from ref. [146].

ref. [150] is that they each have narrow internal energy distributions spanning from approximately 1-3 eV. The FAB data from ref. [150] displays a much broader internal energy distribution which tails off to much higher energies than the other plots shown. The differences between the two sets of FAB data are not addressed in the literature, but can likely be attributed to differences in experimental conditions. The positions of each distribution along the energy axis should be considered qualititative such that ions formed from Au_3^+ and Au_{400}^{+4} impacts have relatively higher internal energies as compared to ESI and FAB. The kinetic shift calculations proposed in refs. [141, 152] to render this data quantitative are beyond the scope of this study. The current calculation is assumed to underestimate the actual internal energy distributions for Au_3^+ and Au_{400}^{+4} impacts, though the relative comparisons to ESI and FAB are maintained with such a systematic error. The similarity between these distributions is rather surprising considering the high energy densities created by the impacting projectiles. The narrow internal energy distribution for SI's produced from Au_{400}^{+4} impacts confirms the observation from peptide spectra that molecular ion emission results from a "soft" desorption/ionization mechanism. The fact that the Au_{400}^{+4} distribution is shifted relative to FAB is also significant because these previous articles suggested that the extraction of analyte species from liquid matrices rather than solid surfaces reduces the internal energies of secondary ions. The present results support this prediction.

However, as stated above, these distributions are not proper measures of the actual internal energy of the ion population but are instead defined as the sum of energy accumulated on the fragmenting bond. With this somewhat awkward definition, the

survival yield method is still useful as a comparative measure of internal energy by modifying parameters on a given instrument,[153] but do not provide absolute values which can be directly compared across instrumentation and ionization techniques. This shortcoming is due to the fact that this procedure ignores the time domain.The time dependence of the fragmentation process necessitates an additional theoretical description of how the fragmentation rate for a given molecule depends on the internal energy imparted.

BPY Ion Variable Fragmentation Ratio Method

Subsequent studies have improved theoretical treatment of the BPY system to account for the time domain.[137, 154, 155] For all three studies, RRKM unimolecular fragmentation theory was used in this capacity. Two of these recent studies recalculated the original AM1 critical bond energies at the B3LYP level to improve calculation accuracy and offered alternate descriptions of BPY ion transition states. Naban-Maillet et al.[155] used a simple pre-exponential factor to characterize the transition states of all BPY ions. In a more rigorous approach, Morsa et al.[154] performed DFT calculations to obtain ground state oscillator frequencies. However, the authors arbitrarily defined the transition state frequencies by eliminating the cleaving oscillator and reducing five random frequencies by 25%.

In this section, the theoretical framework for extracting internal energy information from the analysis of BPY "thermometer" ions is revisited in two distinct thrusts. Firstly, the critical bond energies for all BPY ions are systematically re-evaluated at semi-empirical, density functional, and *ab initio* levels of theory.

Additionally, the ground and transition state oscillator frequencies are calculated at each point along a relaxed potential energy scan to generate a fully developed quantum mechanical description of each molecule. Secondly, a novel approach to extracting ion rate constant and lifetime distributions for these ions from time of flight analyses is introduced. These developments allow for direct conversion of the experimentally measured rate constant distribution into an internal energy distribution via the RRKM formalism.[156, 157]

Computational Details. All calculations were performed using the Gaussian 09 suite of software.[158] Density Functional Theory[159] (DFT) calculations were performed using the B3LYP (Becke-3 exchange[160] and Lee-Yang-Parr correlation[161] functional) level of theory and a Pople triple-ζ quality basis set with diffuse and polarization functions (BSI=6-311++G(2d,p))[162, 163]. Full geometry optimizations were performed and stationary points were characterized via analytical frequency calculations for the parent, daughter ion, and pyridine molecules unless otherwise specified. MP2/BSII (second-order Møller-Plesset perturbation theory[164], BSII=6-311++G(d,p)[162, 163]) geometry optimizations and frequency calculations were performed on the p-Cl parent, daughter ion, and pyridine. Dissociation energies were calculated from CCSD(T)/BSII (Coupled-Cluster Singles and Doubles with perturbative triples) Single Point Energies (SPE) calculations at the B3LYP/BSI optimized geometries (CCSD(T)/BSII//B3LYP/BSI). Dissociation energies were also calculated at the AM1,[165] HF/BSI,[166] B3LYP/BSI, MP2/BSII//B3LYP/BSI, MP3/BSII//B3LYP/BSI, MP4(SDQ)/BSII//B3LYP/BSI, and CCSD/BSII//B3LYP/BSI levels of theory. Lastly,

the dissociation energy of the p-Cl model was also calculated at the CCSD(T)/BSII//MP2/BSII level.

Sample Preparation. 1-(4-nitrobenzyl)pyridinium bromide was purchased from Sigma Aldrich (St. Louis, MO). 1-(4-methoxyphenyl)methylpyridinium tetrafluoroborate, 1-(4-methylphenyl)methylpyridinium bromide, and 1-(4-chlorophenyl)methylpyridinium chloride were purchased from the Florida Center for Heterocyclic Compounds (Gainesville, FL). 1-(4-cyanobenzyl)pyridinium chloride was purchased from Otava (Toronto, Ontario, Canada). One mg/mL solutions of each BPY salt in 1:1 MeOH/H_2O were electrosprayed onto separate gold-coated silicon wafers (Silicon Valley Microelectronics, Santa Clara, CA).

Mass Spectrometry. All analyses were performed using the custom-built SIMS instrument described previously (Chapter II). Two time of flight spectra were generated for each BPY salt sample using 5 and 10 kV secondary ion accelerating potentials applied to the target. This procedure allows for the observation of ion fragmentation across two distinct time windows. The floating potential applied to the LMIS was adjusted to offset the potential applied to the sample which decelerates the projectile. In this way, a final impact energy of 110 x q keV (440 keV for Au_{400}^{+4}) is obtained regardless of the target potential. Upon impact, any secondary ions formed are accelerated (5 or 10 kV) across an 11 mm gap toward a 90% transmission grid maintained at ground. An electromagnet is used to deflect H^+ (protons) toward a chevron microchannel plate (MCP) assembly. The prompt H^+ signal generated is used to register the projectile impact and serves as a start for the ToF measurement. Secondary ions mass

40 and above traverse the magnet with minimal deflection along 1.019 m field free flight path. Ions pass through a second 90% transmission grid where they are post-accelerated across a 33 mm gap towards a second MCP detector which signals each ion arrival time. A diagram of the instrument setup is provided in Figure V-5. All secondary ions signals are acquired for each projectile impact event prior to subsequent impacts, with ~10^6 summed impact events constituting each mass spectrum.

p-NO_2 BPY Ion Exclusion. An original assumption in the survival yield method is that fragmentation proceeds exclusively along the pathway shown in Figure V-1. This means that the survival yield can be determined by considering only the M^+ parent and F^+ fragment. However, a detailed investigation of the p-NO_2 spectrum (Figure V-6) reveals peaks at masses 90, 122, 169, and 199 which can be assigned to additional fragment species. This finding means the survival yield calculation should account for these products. When this correction is applied to the 440 keV Au_{400} breakdown curve in Figure V-4a, the breakdown curve in Figure V-7 is generated. This figure shows that the sigmoidal curve fit is greatly improved when accounting for the multiple pathways of fragmentation. The presence of these competitive fragmentation pathways for the p-NO_2 species is presumably due to the high C-N bond strength which becomes comparable with other bonds throughout the molecule. This analysis suggests the p-NO_2 BPY ion does not follow a single fragmentation pathway as previously reported. As a result, this species is deemed unsuitable for the current investigation and is excluded from subsequent experimental considerations.

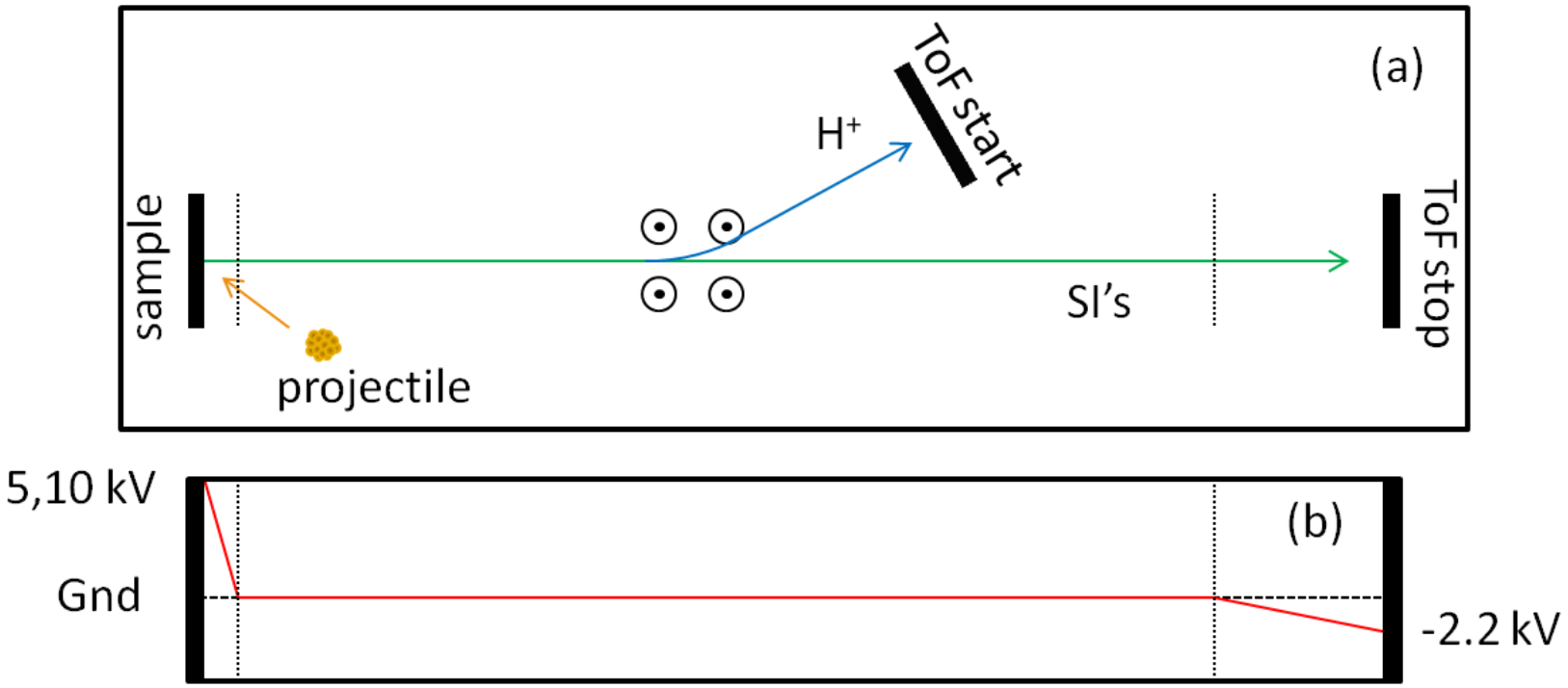

Figure V-5. (a) Schematic view of various electrode positions and ion trajectories.
(b) Electrostatic potentials along the secondary ion flight path. Diagrams not drawn to scale.

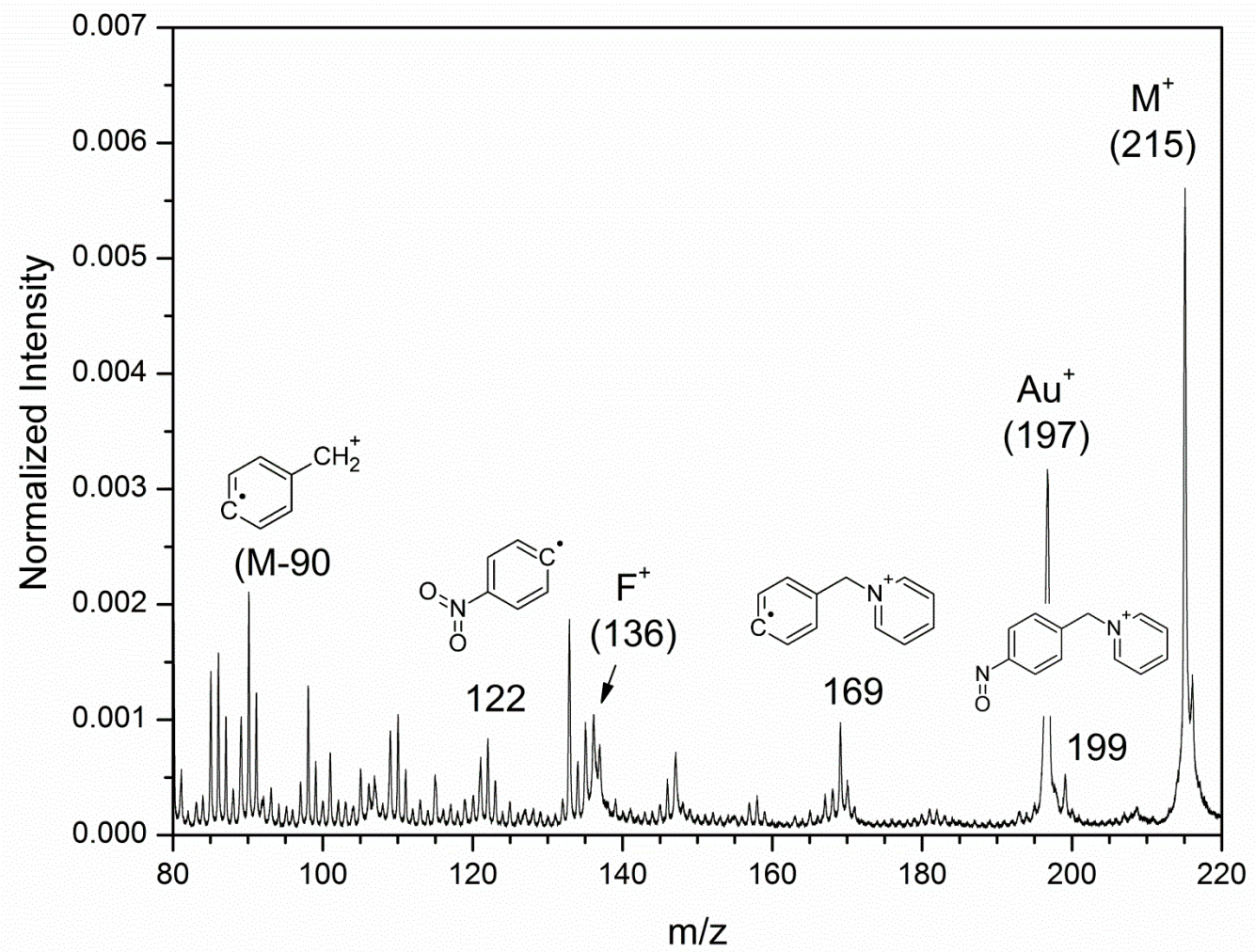

Figure V-6. Mass spectrum of p-NO_2 BPY ion generated by 440 keV Au_{400}^{+4} impacts showing multiple fragmentation products.

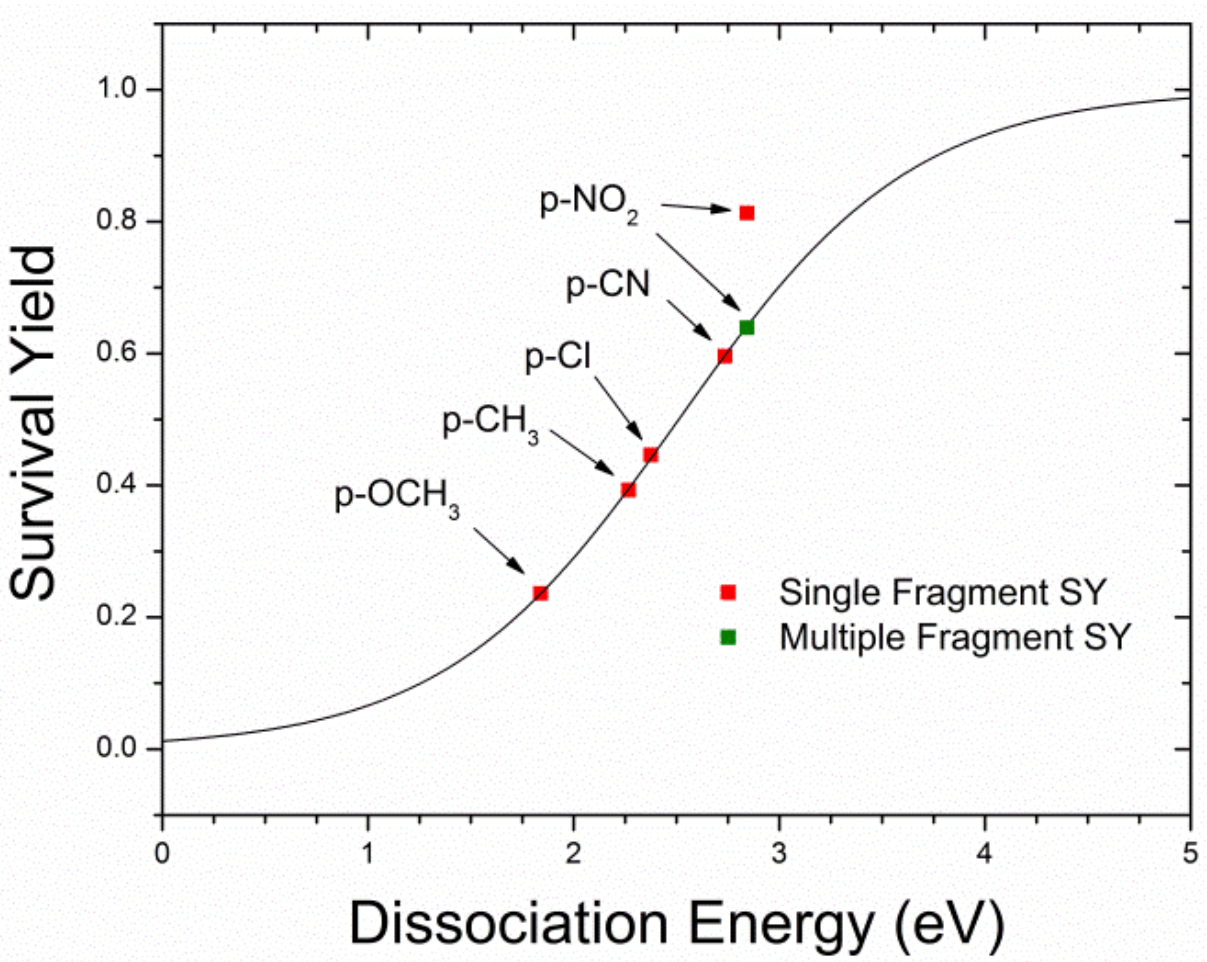

Figure V-7. Survival yield values for five BPY ions generated by 440 keV Au_{400}^{+4} impacts.

Bond Dissociation Energy Calculations

The bond dissociation energies previously reported for the BPY ions were calculated nearly a decade ago at a computationally inexpensive, semi-empirical level (AM1).[167] These values are critically important for an accurate measurement of the internal energy and so we initiated a study to reevaluate them at a variety of computational levels. This was done by calculating the zero-point energies of the intact ion, the daughter ion, and neutral pyridine for each of the BPY ions. The activation barrier for the reaction in Figure V-1 can be approximated by subtracting the zero-point energy of the parent from the sum of the daughter ion and neutral pyridine energies as shown in Equation 5.2.

$$E_d^o = E_{daughter}^o + E_{pyridine}^o - E_{parent}^o \quad (5.2)$$

The results of these calculations are shown in Figure V-8 with their numerical values provided in Table V-1.

This figure shows that the dissociation energies for each molecule vary by as much as an electronvolt across the levels of theory investigated. At the low end, AM1 and B3LYP/BSI energies show modest agreement with the HF/BSI values. However, increasing the level of *ab initio* theory from HF/BSI to MP2/BSII//B3LYP/BSI (which accounts for dynamic electron correlation) results in a significant increase in the calculated bond strengths. As evermore computationally expensive models are considered, moving from MP2/BSII//B3LYP/BSI to MP3/BSII//B3LYP/BSI, MP4(SDQ/BSII//B3LYP/BSI, CCSD/BSII//B3LYP/BSI, and finally CCSD(T)/BSII//B3LYP/BSI, calculated values begin to converge about the

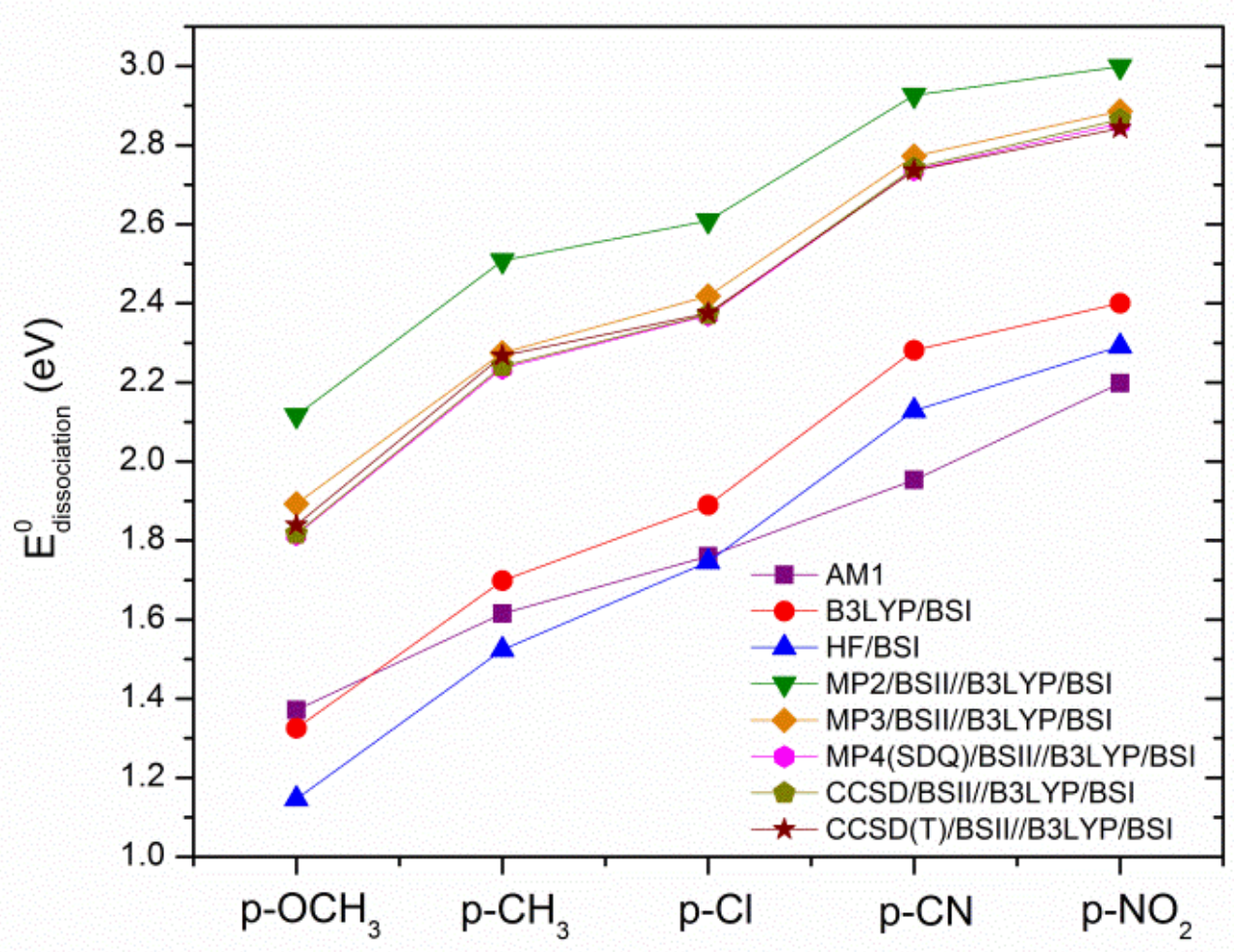

Figure V-8. Dissociation energies calculated for five different benzylpyridinium ions at various levels of theory.

Table V-1. Dissociation Energies for Selected BPY Thermometer Ions

Level of Theory	$E^{o}_{dissociation}$ (eV)				
	$-OCH_3$	$-CH_3$	-Cl	-CN	$-NO_2$
AM1	1.372	1.615	1.760	1.953	2.198
B3LYP	1.325	1.699	1.890	2.282	2.400
HF	1.146	1.523	1.746	2.129	2.291
MP2	2.117	2.508	2.609	2.926	2.999
MP3	1.893	2.275	2.419	2.772	2.886
MP4	1.815	2.236	2.370	2.737	2.855
CCSD	1.817	2.241	2.372	2.742	2.865
CCSD(T)	1.840	2.267	2.375	2.736	2.843

CCSD(T)/BSII//B3LYP/BSI numbers. The agreement between the four highest level *ab initio* models serves as a confirmation that the molecular systems are adequately described. For the purpose of this study, dissociation energies calculated at the gold standard CCSD(T) level will be used. Dissociation energies for the full series of BPY ions from the literature have been recalculated at the CCSD(T)/BSII//B3LYP/BSI level and are presented in Table V-2.

Measurement of the Rate Constant Distributions

Time of flight mass spectrometry is well suited to determining ion fragmentation rates because the time domain is monitored directly. Fragmentation of ions in an accelerating field results in the production of daughter ions which exhibit a velocity deficit measurable by time of flight. Such a spread in velocities appears in the mass spectrum as tail on the fragment peak that extends upward in mass towards the parent ion as shown in the Figure V-3 inset. However, the observed peak is also a superposition of the kinetic energy distribution and instrumental apparatus function, which typically complicates extraction of the pure fragmentation component. The unimolecular fragmentation rate $\left(\frac{dN}{dt}\right)$ of an ion is governed by the amount of internal energy available and can be described using a superposition of exponential decays as shown in Equation 5.3:

$$\frac{dN}{dt} = \int_0^{k_{max}} k\varphi(k)e^{(-kt)}dk = \int_0^{\tau_{max}} \frac{\Phi(\tau)e^{-t/\tau}d\tau}{\tau} \qquad (5.3)$$

where k_{max} and τ_{max} are the maximum rate constant and lifetime, respectively, for a given ion and τ is equal to $1/k$. $\varphi(k)$ and $\Phi(\tau)$ are the distributions of rate constants

Table V-2. CCSD(T)/BSII//B3LYP/BSI Dissociation Energies for the Full Series of BPY Thermometer Ions

Benzyl Substituent	$E^{o}_{dissociation}$(eV)
*p-OCH_3	1.840
*p-CH_3	2.267
*p-Cl	2.375
p-Br	2.371
p-F	2.392
o-CH_3	2.393
m-CH_3	2.417
m-OCH_3	2.491
-H	2.500
m-F	2.668
*p-CN	2.736
m-CN	2.794
*p-NO_2	2.843
3,5-NO_2	3.133

*Molecule used in this study.

and lifetimes generated by the distribution of internal energies. A model previously reported in [168] uses the two-parameter power law function shown in Equation 5.4 to reproduce the conditional distribution of k values present in the fragmentation tail.

$$\frac{dN}{dt} = (a-1)c^{a-1}(t+c)^{-a} \tag{5.4}$$

This function approximates the superposed exponential decays, retaining information about the initial internal energy distribution. Rather than directly fitting the function to the tail, we use its integral (Equation 5.5) to describe the area under the fragment peak.

$$\begin{aligned} N_f &= \int_0^{t_x}(a-1)c^{a-1}(t+c)^{-a} \\ &= 1 - c^{a-1}(c+t_x)^{1-a} \end{aligned} \tag{5.5}$$

This serves to normalize the effect of the initial ion kinetic energies and apparatus function. Here t_x corresponds to the time after projectile impact. When measuring the fragment peak area, the upper time boundary of the integration window determines the time frame over which fragmentation is monitored. The parent peak area can similarly be equated to the fraction of the initial population which does not fragment within the accelerating region as shown in Equation 5.6:

$$\begin{aligned} \mathrm{N_p} &= 1 - \int_0^{\mathrm{t_{acc}}}(\mathrm{a}-1)\mathrm{c}^{\mathrm{a}-1}(\mathrm{t}+\mathrm{c})^{-\mathrm{a}} \\ &= \mathrm{c}^{\mathrm{a}-1}(\mathrm{c}+\mathrm{t_{acc}})^{1-\mathrm{a}} \end{aligned} \tag{5.6}$$

where $\mathrm{t_{acc}}$ is the total time an intact parent ion spends in the accelerating region. In order to evaluate the a and c parameters, it is necessary to first generate a fragmentation ratio quantity which is analogous to the survival yield quantity described above. This ratio,

defined in Equation 5.7, must be measured under two different experimental conditions which probe different time windows of observation.

$$\frac{N_f}{N_p} = \frac{1 - c^{a-1}(c+t_x)^{1-a}}{c^{a-1}(c+t_{acc})^{1-a}} \tag{5.7}$$

This was done by measuring $\frac{N_f}{N_p}$ at two different ion accelerating voltages (5 and 10 kV) for each sample. In this way, the parent ion spends different amounts of time within the accelerating region and undergoes more or less fragmentation accordingly. This generates two versions of Equation 5.7, each with its own unique $\frac{N_f}{N_p}$, t_x, and t_{acc} values. This system of two equations can then be solved to determine the common a and c parameters. Through the derivation provided in [168], it is possible to express the rate constant and lifetime distributions of the parent ion as a function of the calculated a and c parameters as shown in Equations 5.8 and 5.9.

$$\varphi(k) = \frac{c^{a-1}e^{-ck}k^{a-2}}{\Gamma(a-1)} \tag{5.8}$$

$$\Phi(\tau) = \frac{c^{a-1}e^{-c/\tau}}{\tau^a \Gamma(a-1)} \tag{5.9}$$

Rate constant and lifetime distributions calculated for the p-OCH_3, p-CH_3, p-Cl, and p-CN BPY ions are provided in Figure V-9. Significant changes in the fragmentation ratios $\left(\frac{N_f}{N_p}\right)$ were observed for the p-OCH_3, p-CH_3, and p-Cl BPY ions. However, the p-CN BPY ion fragmentation ratio changes by less than 15%, making the determination of a and c for this species less reliable, as evidenced by the shifted rate constant and lifetime distributions relative to the other three BPY ions. Despite this shift, the distribution ordering is retained.

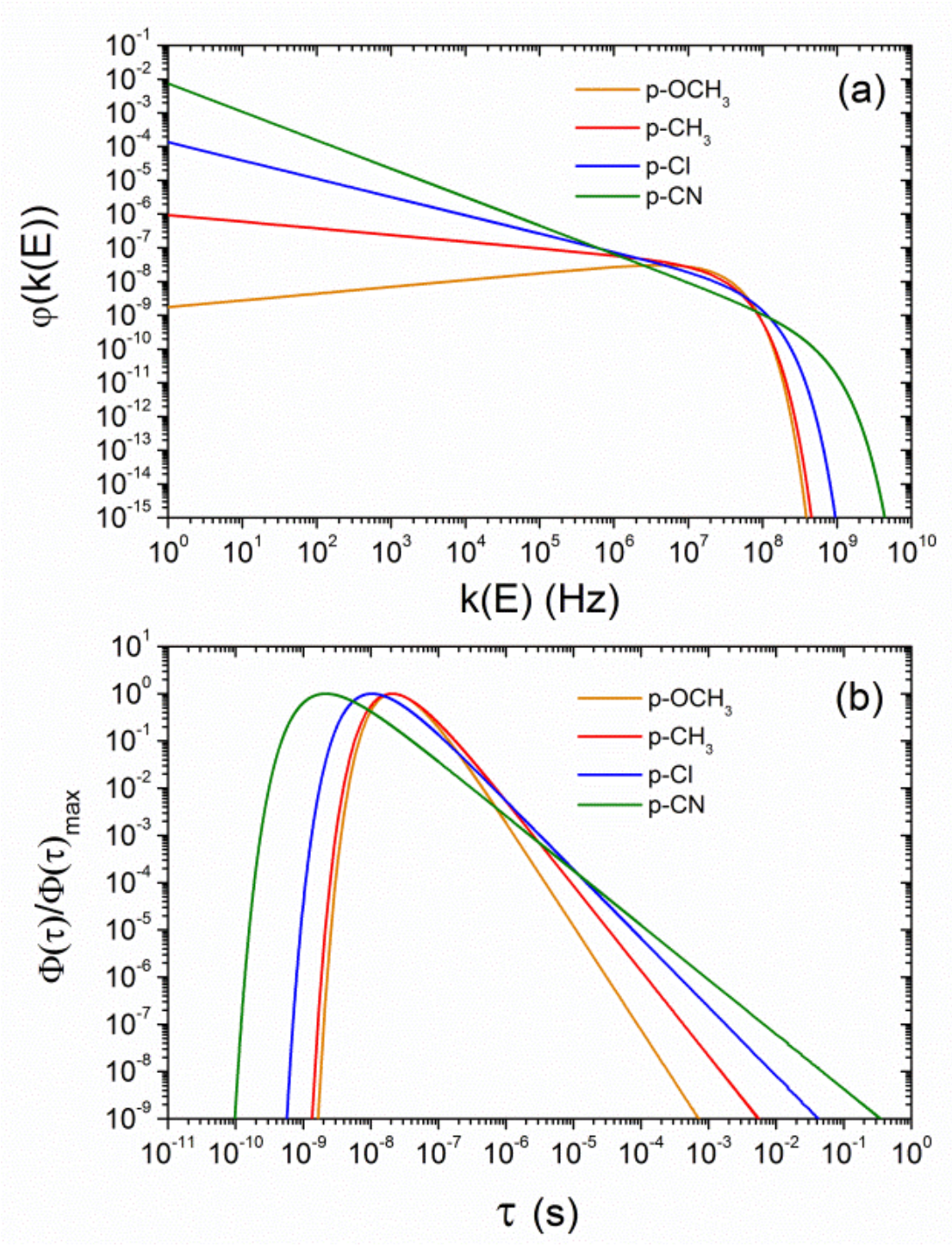

Figure V-9. (a) Rate constant and (b) lifetime distributions measured for four BPY ions generated by 440 keV Au_{400}^{+4} impacts.

The plots in Figure V-9 reveal the extreme ranges of frequencies and lifetimes the rate constant and lifetime distributions respectively cover. Each type of distribution correctly orders the four remaining BPY ions according to their critical bond energies. For the rate constant distribution (Figure V-9a), this means the slope of the left side of the distribution is decreasing for the strongly bound p-CN ion but increasing for the weakly bound p-OCH_3 species. Each of the distributions rapidly decreases as the rate constant approaches the frequency of atomic oscillations. For the lifetime distributions (Figure V-9b), the right side of the p-CN distribution is extended toward longer lifetimes while the p-OCH3 distribution decreases more rapidly. The other two BPY ions are correctly ordered as well. The observed lifetimes are again limited to the time scale of atomic oscillations.

RRKM Unimolecular Fragmentation Theory

MassKinetics, a free RRKM-based mass spectrometry simulation program,[169] was used to calculate the energy dependent reaction rates for each BPY ion. The previously determined bond dissociation energies, ground state oscillator frequencies, and transition state oscillator frequencies are required for this calculation. The ground state frequencies for each parent ion were calculated at the B3LYP/BSI optimized geometry. To find the transition state along the bond dissociation reaction, a relaxed potential energy scan (B3LYP/BSI) along the C-N bond was performed with a step size of 0.1 Å for 30 steps. A frequency calculation was performed at each point and the highest point on the reaction path with 1 imaginary mode corresponding to the breaking of the C-N bond was used to estimate the transition state and its corresponding

frequencies. At longer C-N bond distances, an imaginary frequency emerges for each ion whose mode corresponds to a twisting motion of the parent ion and the pyridine (Figure V-10). For all ions this imaginary mode appears between 1.9-2.1 Å beyond their equilibrium C-N bond distances. Ground and transition state frequencies for the four BPY ions are provided in Table V-3. The MassKinetics software uses these frequencies to determine the number of quantized energy states at the transition state $(\sum^{*}(E - E_d^o))$ and the density of quantum states at the ground state geometry $\big(\rho(E)\big)$ for each molecule according to the traditional RRKM equation:

$$k(E) = \frac{\sum^{*}(E - E_d^o)}{h\rho(E)} \tag{5.10}$$

where h is Planck's constant. A plot of $log\big(k(E)\big)$ versus E at a number of discrete energy values is generated by the MassKinetics program. These relationships are shown in Figure V-11 as the rate constant $\big(k(E)\big)$ versus energy.

The traces for each ion originate at the critical energy because the reaction can not occur for internal energies less than this threshold. Above this threshold the rate constant rapidly increases as the internal energy increases but then levels off as the rate approaches the frequency of a single bond oscillation. The RRKM relationships show that for a given internal energy, the fragmentation rate for more weakly bound BPY ions is much higher than those with a greater critical energy. In order to generate an analytic function to describe the curves in Figure V-11, each dataset was fitted to Equation 5.11 using the web-based curve fitting program available at zunzun.com.

$$log\big(k(E)\big) = xln(E + y) + z \tag{5.11}$$

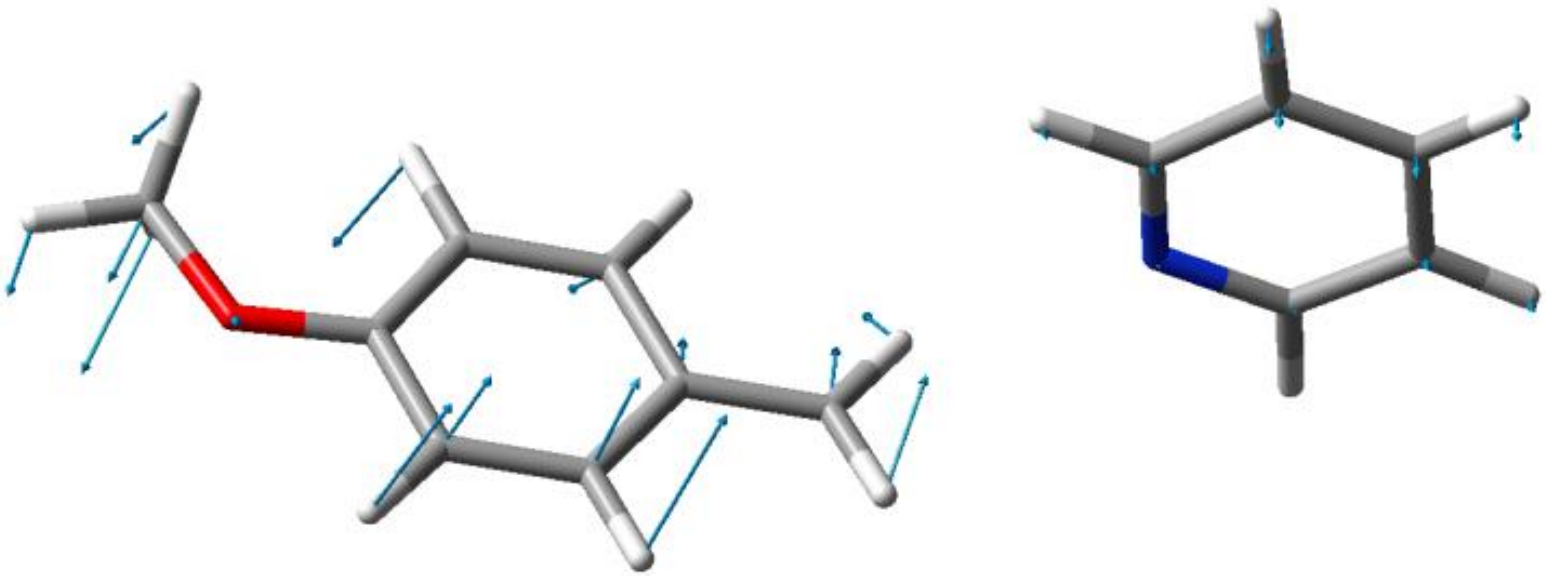

Figure V-10. Imaginary oscillator mode for the p-OCH_3 BPY ion calculated at the B3LYP/BSI optimized geometry 2.1 Å beyond the equilibrium C-N bond distance.

Table V-3. B3LYP/6-311++G(2d,p) Oscillator Frequencies (cm^{-1}) for Selected Benzylpyridinium Ions.

p-OCH3		p-CH3		p-Cl		p-CN	
Gnd	Trans	Gnd	Trans	Gnd	Trans	Gnd	Trans
14	24	17	9	15	9	17	5
43	37	42	24	46	18	40	12
54	53	54	41	50	40	47	15
106	99	56	49	142	78	117	54
164	138	159	88	178	92	144	57
179	151	179	100	247	148	194	98
220	191	273	166	275	273	260	153
229	225	286	308	317	302	284	221
279	242	328	311	365	376	339	352
331	347	380	377	407	388	405	361
345	372	407	392	420	392	411	388
407	398	418	399	435	395	422	389
430	418	449	423	452	423	448	417
446	435	491	465	505	516	483	419
462	446	519	509	601	622	560	556
526	531	614	624	649	633	562	557
545	555	657	641	660	665	612	601
614	627	661	665	689	669	659	615
651	641	696	686	697	671	662	646
661	662	723	712	744	713	694	666
697	708	771	716	774	751	718	711
728	753	777	758	794	761	758	716
774	763	786	762	842	838	777	753
777	771	840	839	846	840	807	759
792	818	854	846	871	864	847	842
828	854	868	851	880	886	856	844
852	866	881	887	952	959	876	873
869	871	948	959	982	993	877	877
882	887	975	983	987	999	955	955
950	966	986	999	988	1005	982	991
962	982	989	999	1010	1005	988	997
980	994	1010	1008	1036	1013	993	1005
988	1001	1018	1013	1043	1019	1006	1010
1012	1003	1040	1021	1044	1027	1039	1012
1025	1013	1042	1026	1079	1034	1043	1017
1040	1020	1044	1027	1109	1048	1045	1022
1042	1028	1065	1034	1122	1088	1079	1043

Table V-3. Continued

p-OCH3		p-CH3		p-Cl		p-CN	
Gnd	Trans	Gnd	Trans	Gnd	Trans	Gnd	Trans
1043	1032	1080	1048	1134	1093	1122	1070
1079	1045	1121	1051	1141	1109	1145	1085
1118	1079	1127	1089	1196	1157	1150	1093
1121	1098	1149	1093	1209	1181	1197	1160
1146	1119	1195	1165	1230	1213	1205	1179
1168	1157	1212	1181	1237	1235	1222	1202
1195	1166	1226	1208	1251	1287	1229	1233
1201	1185	1234	1234	1295	1330	1235	1238
1204	1198	1243	1242	1322	1362	1243	1281
1232	1204	1257	1289	1353	1368	1304	1335
1242	1229	1291	1347	1378	1388	1327	1371
1256	1304	1335	1362	1404	1469	1359	1373
1289	1320	1361	1372	1444	1478	1378	1389
1304	1332	1379	1388	1489	1505	1405	1463
1340	1343	1402	1406	1515	1518	1447	1475
1366	1371	1420	1460	1529	1545	1489	1512
1378	1386	1448	1480	1535	1567	1518	1517
1401	1478	1488	1480	1605	1615	1535	1532
1463	1484	1489	1488	1617	1621	1546	1579
1477	1488	1494	1514	1632	1634	1599	1613
1487	1498	1513	1518	1665	3153	1617	1616
1498	1500	1533	1556	3073	3166	1649	1650
1501	1509	1551	1573	3123	3173	1665	2316
1512	1521	1609	1616	3165	3186	2334	3155
1533	1559	1618	1622	3166	3190	3076	3158
1552	1573	1647	1644	3199	3190	3126	3159
1605	1620	1666	3017	3206	3200	3167	3183
1618	1630	3033	3086	3207	3205	3170	3194
1646	1642	3071	3128	3211	3212	3199	3195
1666	3040	3087	3153	3214	3213	3203	3196
3025	3114	3116	3167	3221	3273	3204	3202
3070	3160	3121	3172	3228		3212	3211
3092	3167	3157	3181			3214	3212
3120	3169	3158	3181			3223	3258
3155	3176	3177	3186			3227	
3160	3178	3181	3193				
3160	3179	3198	3195				
3198	3192	3209	3200				

Table V-3. Continued

p-OCH3		p-CH3		p-Cl		p-CN	
Gnd	Trans	Gnd	Trans	Gnd	Trans	Gnd	Trans
3200	3204	3214	3206				
3209	3206	3220	3272				
3214	3210	3229					
3214	3219						
3220	3254						
3227							

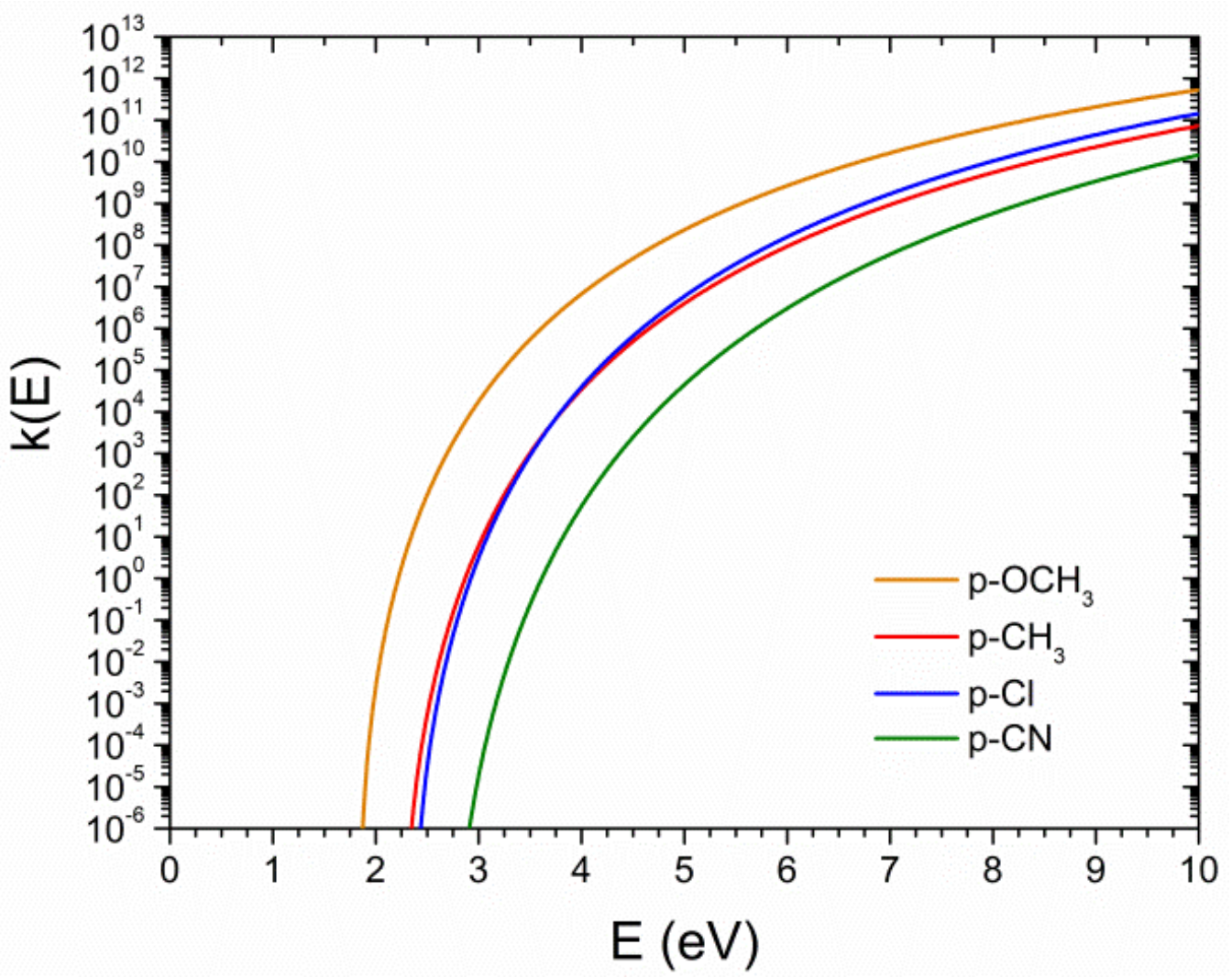

Figure V-11. RRKM relations calculated for four BPY ions.

where x, y, and z are variable parameters. Differentiation of k(E) with respect to E gives Equation 5.12:

$$\frac{dk(E)}{dE} = \frac{xln(10)10^{xln(E_{int}+y)+z}}{E_{int}+y} \tag{5.12}$$

Calculation of the Internal Energy Distributions

The distribution over internal energies for each BPY ion can now be generated according to Equation 5.13:

$$P(E) = \frac{dN}{dE} = \frac{dN}{dk(E)}\frac{dk(E)}{dE}$$

$$= \frac{c^{a-1}e^{-c10^{xln(E+y)+z}}\left(10^{xln(E+y)+z}\right)^{a-2}}{\Gamma(a-1)}\frac{xln(10)10^{xln(E+y)+z}}{E+y} \tag{5.13}$$

which is a product of the rate constant distribution (Figure V-9a) and RRKM fitting curve derivative. The resulting internal energy distributions are shown in Figure V-12. The p-CN BPY ion is shown separately in Figure V-13 because it gives a distribution that is wider and shaped differently than the other three molecules. This variation can be traced to the minimal change obtained for the fragmentation ratio $\left(\frac{N_f}{N_p}\right)$ measured between the 5 and 10 kV accelerating potentials. Similarity in these values results in a broad range of a and c values (Equation 5.7) which can satisfy the system of equations. This makes their determination less precise and results in a poor description of the distribution shape. Conversely, significant differences in fragmentation ratios measured for the other three BPY ions make the sizes and shapes of their distributions more reliable. The a and c values for all molecules as well as other experimentally measured parameters are summarized in Table V-4. The p-OCH_3, p-CH_3, and p-Cl species give

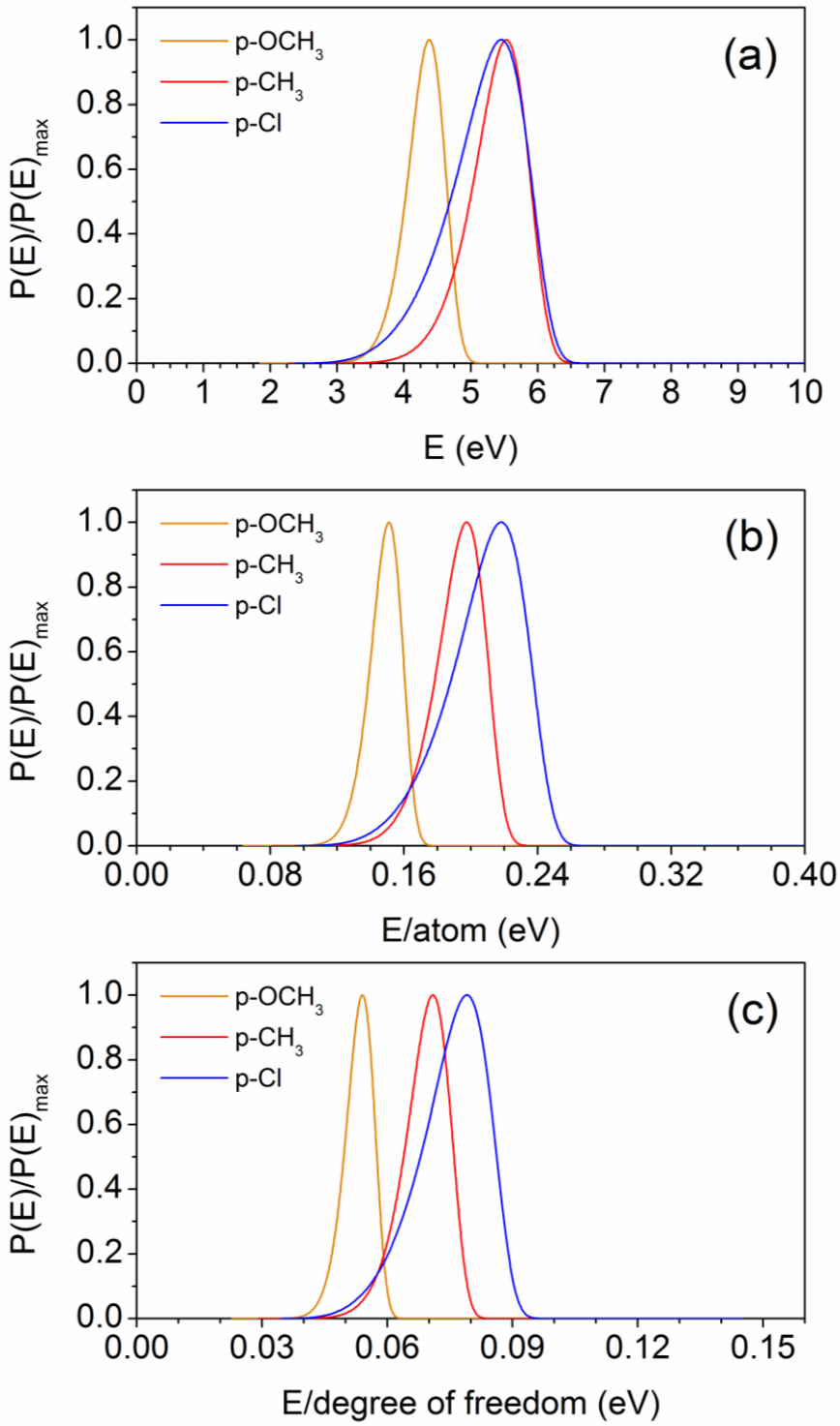

Figure V-12. (a) Total internal energy distributions measured for the p-OCH_3, p-CH_3, and p-Cl BPY ions. Distributions are also normalized (b) to the number of atoms and (c) to the number of degrees of freedom.

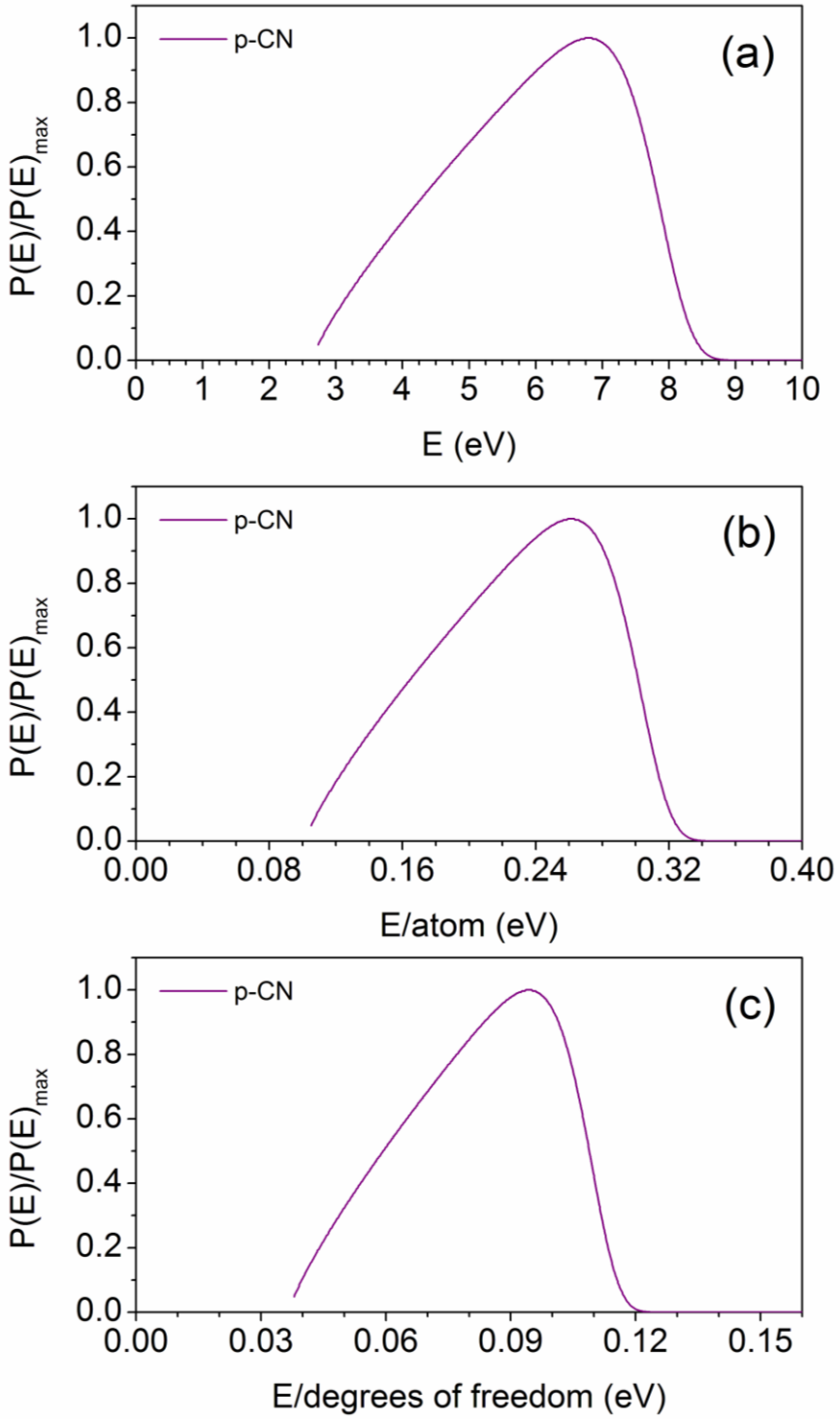

Figure V-13. (a) Total internal energy distribution measured for the p-CN BPY ion. Distribution is also normalized to (b) the number of atoms and (c) the number of degrees of freedom.

Table V-4. Summary of Experimentally Measured Parameters for Selected BPY Thermometer Ions

Parameter		p-OCH_3	p-CH_3	p-Cl	p-CN
5 kV	t_x (ns)	30.1	30.0	30.1	30.1
	t_{acc} (ns)	317	304	317	313
	N_f/N_p	5.184	2.258	1.623	0.713
10 kV	t_x (ns)	21.5	21.3	21.5	21.3
	t_{acc} (ns)	224	215	226	221
	N_f/N_p	2.949	1.431	1.184	0.607
	a	2.201	1.802	1.458	1.157
	c	$4.732\text{x}10^{-8}$	$3.685\text{x}10^{-8}$	$1.513\text{x}10^{-8}$	$2.490\text{x}10^{-9}$
	x	3.982	4.419	4.459	5.026
	y	-1.790	-2.200	-2.295	-2.639
	z	3.579	1.964	2.245	2.938
$\langle E \rangle$ (eV)		4.291	5.371	5.186	5.925
$\langle E \rangle/atom$ (eV)		0.148	0.192	0.207	0.228
$\langle E \rangle/dof$ (eV)		0.053	0.069	0.075	0.082

narrow distributions with a full width of ~1 eV measured at half height. All four BPY ions give total internal energy distributions within the approximate range of 4-8 eV. Normalizing these distributions according to the number of atoms (Figure V-12b) or number of degrees of freedom (Figure V-12c) in the parent molecule reveals an interesting trend. The most probable internal energy value for each of the BPY ions occurs at a different energy. The relative spread in measured internal energy distributions is proportional to differences in the calculated critical bond energies (given in Table V-1). This suggests the bond dissociation energies have a second order effect which results in lower average internal energies measured with the more weakly bound BPY ions and vice versa. The first explanation of this effect centers on the quantum mechanical description of the BPY ion transition states used in the RRKM calculation. Loose transition state fragmentation reactions typically necessitate a variational RRKM description.[170] This approach entails using a variable transition state for each molecule that changes as a function of the internal energy. Such calculations have traditionally been limited to small molecular systems, where the conversion of vibrational modes to translational or rotational modes can more easily be discerned. The variational RRKM method was therefore deemed beyond the scope of this study.

It also remains that the actual energy distributions for the four BPY ions may in fact differ according to their inherent chemical stability. This is the first attempt to quantify the internal energy of secondary ions formed from massive cluster impacts. As such, the ions investigated so not originate as preformed ions in solution but as units within a crystal lattice. The effects of forming ions from the solid phase have largely

been ignored in our treatment and the differing energy distributions may signify that these effects are in fact important.

Despite measuring different internal energy distributions with different BPY molecules, the goal of quantifying the energy of sputtered species has been met. All species have an average energy per atom of ~0.19 eV and an average energy per degree of freedom of ~0.070 eV. These results are reasonable when compared to previous internal energy measurements for various SIMS projectiles. Experiments for 9 keV Xe^+ projectiles measured the internal energies of sputtered metal clusters to be ~1-2 eV/atom[171] while internal energies of 0.17 eV/atom were reported for thymine molecules emitted from 25 keV Bi_3^+ impacts.[172] Molecular dynamics simulations of 20 keV C_{60} impacts on an octane surface suggest most intact emissions have energies less than 0.35 eV/atom.[173] The current result shows that emissions from the even more massive Au_{400} projectile are similar if not lower in energy to those observed for smaller projectiles.

An average internal energy of ~0.19 eV/atom has been reported for electrospray ionization using the same BPY ions as this study.[155] The surprising result that ions formed under such energetic conditions as projectile impacts have internal energies comparable with those formed using a "soft" ionization techniques such as electrospray ionization suggests that cluster SIMS is a viable approach for the analysis of labile molecules.

Conclusion

Two different molecular systems are presented as models for measuring the internal energies of species emitted from cluster impacts on surfaces. The first, using the

leu-enkephalin peptide, offers a rough comparison to CID spectra and suggests two types of emission exist: “ground zero” emission and crater rim emission. A series of BPY ions is used to probe rim emission mechanism which is more important for understanding molecular ion emission. Using the survival yield method, it is possible to show relative similarities between the internal energy imparted via cluster impacts and other ionization mechanisms. The best method presented for extracting quantitative internal energy information involves the careful consideration of various quantum mechanical characteristics of the BPY ions as well as a new framework for measuring molecular lifetimes.

A complete list of oscillator frequencies for the ground and transition states of multiple BPY are reported here, allowing for the elimination of empirical correction factors such as the pre-exponential factor and arbitrary frequency reduction in favor of a complete quantum mechanical description of the BPY system. Bond dissociation energy calculations show that AM1 and DFT calculations, with even larger basis sets than those previously used,[154, 155] are still insufficient for a proper theoretical description. Agreement between the four highest level *ab initio* theories offers a confirmation that the CCSD(T) values presented offer a more accurate approximation of the BPY dissociation energies. Use of the traditional AM1 or B3LYP bond energies in the present study would have significantly underestimated all internal energy distributions, suggesting previous studies utilizing these values may have also underestimated the actual internal energies.

The current method for determining ion internal energies via ToF mass spectrometry can be used as a metric for comparing various parameters across

instrumentation. This first implementation for hypervelocity nanoprojectile impacts allows for relative comparisons with previous measurements that show cluster SIMS is capable of producing ions with internal energies similar to traditionally “soft” ionization techniques. This study shows that it is possible to extract quantitative internal energy distributions via ToF measurements of benzylpyridinium salts.

CHAPTER VI

METAL-ASSISTED SIMS WITH MASSIVE PROJECTILES

Introduction

The scope of secondary ion mass spectrometry for investigating organic surfaces is constrained by the secondary ion yield which is typically a small fraction of the sputtered material.[17] Multiple approaches have been devised for enhancing the SI yield.[26, 73, 109-112, 174, 175] Among these the application of massive projectiles, e.g. C_{60} and Au_{400},[26, 73] or the use of matrix enhancement effects[109-112, 174, 175] have been most effective in increasing the generation of analyte specific ejecta. The current study investigates SI emission observed when combining massive Au_{400} projectile bombardment with matrix enhancement, specifically noble metal (Ag, Au) deposition on organic surfaces. Molecular Dynamics simulations have suggested this combination may further increase the sputter yield.[67] The enhancement is attributed to the greater stopping power of the noble metal which causes more of the projectile's energy to be deposited in the near surface region, rather than in the depth of the solid where it cannot effect emission. This approach, termed metal-assisted secondary ion mass spectrometry (MetA-SIMS), achieves higher ion yields by increasing the overall sputter yield for a given primary ion.

MetA-SIMS has previously been studied with various cluster primary ions including SF_5[176], C_{60}[177], and massive gold clusters[78] with mixed success. The SF_5 projectile showed enhancement for a pharmaceutical drug and polyaromatic dye only in positive mode, massive gold clusters gave a 2-fold enhancement for a fragment ion but

significant reduction for the glycine molecular ion, and C_{60} showed little to no enhancement for a variety of test molecules. For SF_5 and C_{60} primary ions, the limited enhancement could be attributed to the inefficient energy transfer from the light projectile atoms to much heavier gold atoms.[177] Optimal energy transfer should occur when the projectile and target atoms are mass-matched, implying that massive gold clusters are well-suited for application in Au/MetA-SIMS. This work expands the study of MetA-SIMS with massive gold projectiles for analytes other than the experimental test case of glycine.

A critical consideration for the performance of MetA-SIMS is that metal deposition on organic surfaces occurs by nucleation from surface defect sites followed by growth and aggregation. This results in nanoscale islet formation for low coverages and intertwined peninsular structures at higher coverages.[178, 179] The size and shape of the metallic deposits can affect the nature and abundance of the SI emission.[175, 180] We test here the metallic surface coverage with a coincidence mass spectrometry method previously described.[76, 181, 182] The samples examined below included a range of particle sizes, enabling the assessment of size limits for surface features that may be quantified with coincidence mass spectrometry. The use of ion co-emission to extract quantitative surface coverage information has previously been applied to micron-scale photolithography patterns[182] and antibody-labeled nanoparticles (30 nm diameter) on cells[181] However, these systems exhibit chemical segregations of uniform sizes which are larger than those used in the present study. The goal of this study was to address two distinct questions: (1) Does the addition of metal nanoparticles to an organic surface

result in improved secondary ion yields? and (2) Can coincidence mass spectrometry be used to quantify surface coverages of nanometric interfacial features which are smaller than the area sputtered by a single projectile?

Experimental Details

Sample Preparation. Samples chosen for the investigation were poly(methyl methacrylate) (PMMA; $(C_5H_8O_2)_n$; M_w = ~2,000 Da; monomer mass *m* = 100.05 Da, from Sigma Aldrich, St. Louis, MO) and Irganox1010 ($C_{73}H_{108}O_{12}$; M_W = 1176 Da, from CIBA specialty chemicals, NV). The samples were dissolved in toluene with a concentration of 20 mg/ml each. Silicon wafers were cut into 1 cm^2 and cleaned with isopropanol and then dried by flushing nitrogen gas. The sample solutions were then spin coated for 80 s on cleaned silicon substrates with a speed of 4000 rpm and acceleration of 15000 rpm/s. The thickness of these samples has been measured using spectroscopic ellipsometry and found to be 45 nm for PMMA and 47 nm for Irganox.

The samples were then metalized by physical vapor deposition (PVD) using an MBRAUN system, which is equipped with an MB EVAP evaporator, an MB evaporator chamber (SQ) – M- 1 and a thin film monitor (SIGMA SQC – 310). Silver and gold metallization were done for thicknesses ranging from 0.5 to 15 nm. The thickness measurement was obtained via a quartz crystal microbalance (QCM), assuming a sticking coefficient of 1 and the formation of uniform layers. However, as noted earlier, the gold does not form a uniform layer on the organic samples, but rather forms islands whose sizes increase with the quantity of evaporated gold.

Mass Spectrometry. All samples were analyzed in negative ion mode using 520 keV Au_{400}^{+4} projectiles from the custom SIMS instrument described previously (Chapter II). Approximately one million impact events are summed to give each mass spectrum. All ion yields for massive gold cluster analyses are calculated by dividing the peak area by the specific number of impact events used to generate the spectrum. The custom acquisition and processing software retains all ion co-emission information and allows one to extract only the events in which a given ion of interest is emitted. This generates a coincidental mass spectrum which allows for the calculation of surface coverages as detailed below.

Duplicate samples were analyzed by collaborators at the Catholic University of Louvain (Belgium) using a TOF SIMS^5 (ION-TOF) mass spectrometer. The 30 keV Bi^+ beam was obtained from an ION-TOF liquid metal ion source (≈ 0.85 pA AC current; 5 kHz frequency; pulse width bunched down to 0.7 ns). To maximize detection efficiency, secondary ions were post accelerated by a high voltage (10 kV) in front of the detector. ToF spectra were obtained by collecting the secondary ion signals in the mass range of $0 < m/q < 3{,}000$ for 60 s bombardment of a 500 x 500 μm^2 sample area. The number of primary ions used for each spectrum is ≈ 3.18×10^8 ions, resulting in a dose of 1.27×10^{11} ions/cm^2. All ion yields from Bi^+ analyses are calculated by dividing the peak area by the ion dose (3.18×10^8).

Electron Microscopy. In order to understand the morphology of evaporated metal on the thin films, scanning transmission electron microscopy (STEM) imaging was done at 30 kV using a JSM-7600F scanning electron microscope from JEOL. The samples

(PMMA and Irganox) were dip coated on TEM grids (copper grids) and the metal (gold & silver) was deposited for different thicknesses varying from 0.5 nm to 15 nm on those dip coated grids.

STEM images were investigated using the Vision Assistant 8.2.1 image analysis software package from National Instruments. This analysis software was used to measure the size of gold or silver particles formed on the surface. The gold or silver deposits appear as dark objects on a light background. To measure these objects a manual brightness threshold to assign each pixel as metal or organic. The selected pixels were then investigated for the size of deposited silver or gold islands using a circle detection function, which recognizes circular objects within the image. This function outputs the radius, position, and area of each circle larger than two pixels in radius and this data was used further characterization of the samples.

STEM Imaging

Microscopy images obtained for the various thicknesses of Ag deposited on an Irganox 1010 film are shown in Figure VI-1. The other three sets of metal/substrate combinations similarly show highly uniform surface features which differ according to the amount of gold or silver present on the surface. Nanometric islets are initially formed, but these give way to an intricate network of irregularly-shaped structures as the metal surface coverage increases. Metal nanoparticle size distributions calculated from the STEM images for the Irganox 1010 samples with various amounts of silver are shown in Figure VI-2.

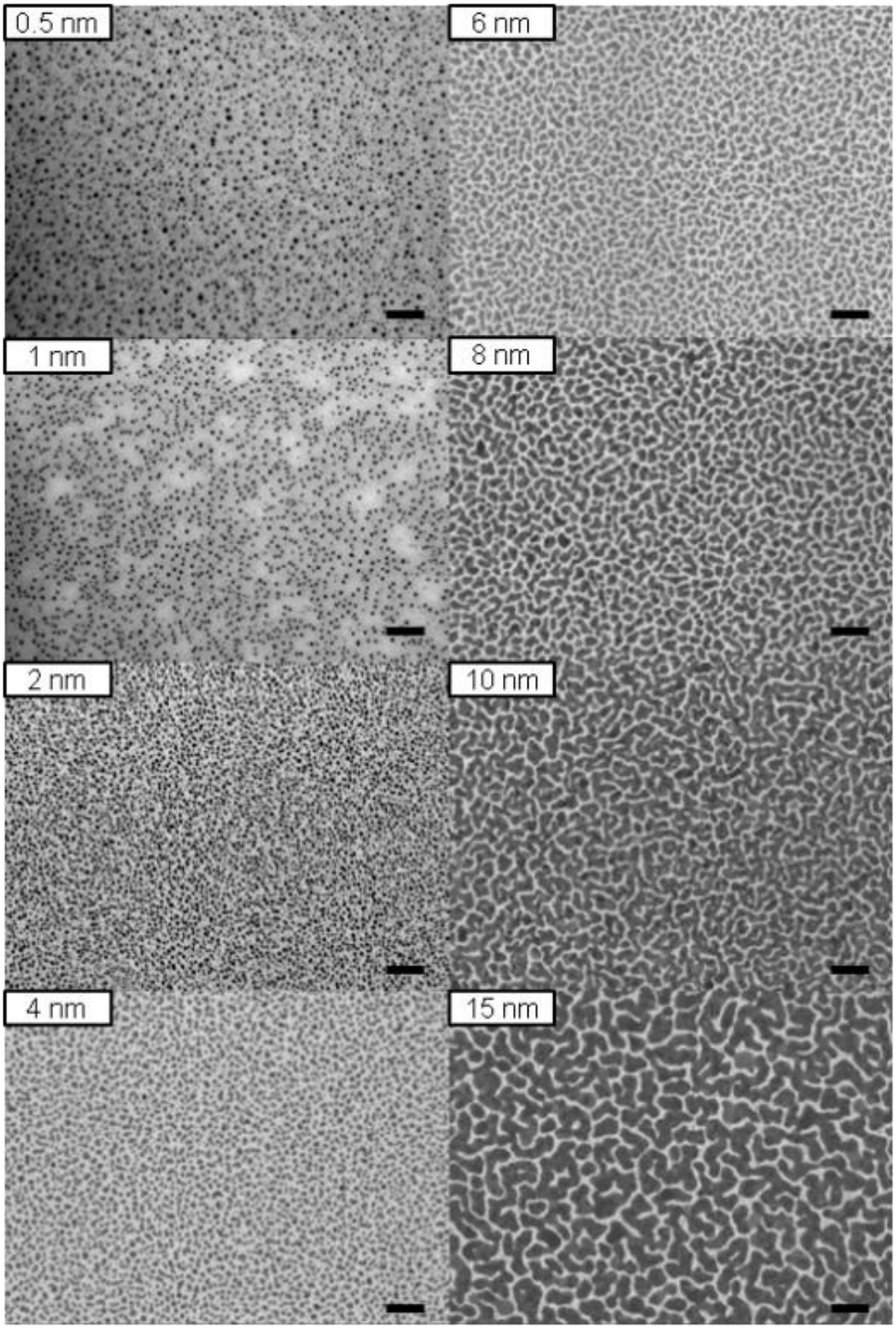

Figure VI-1. STEM images obtained for various amounts of silver deposited on an Irganox 1010 film. Scale bars represent 100 nm.

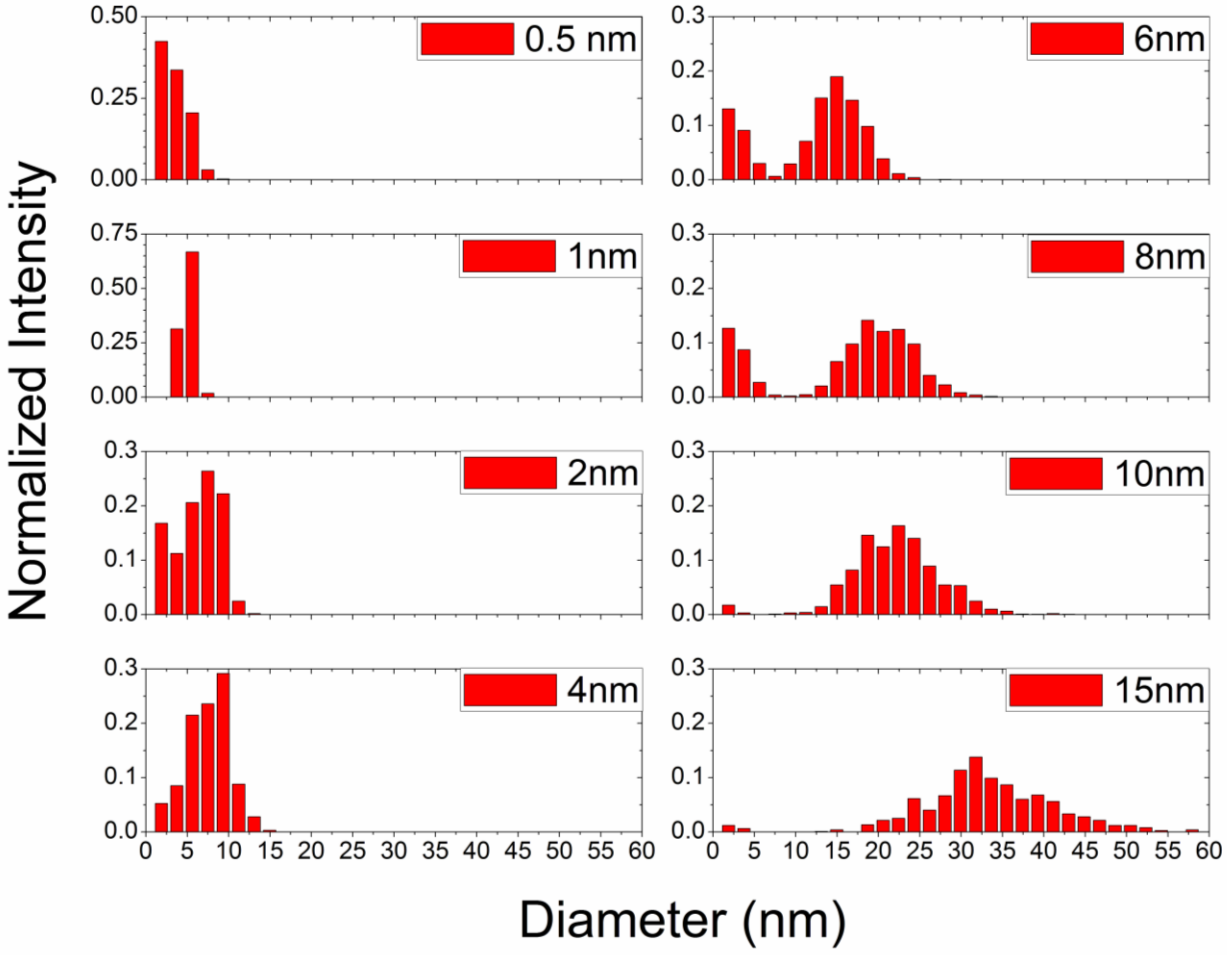

Figure VI-2. Metal particle size distributions measured from STEM images in Figure VI-1.

These plots reveal the gradual shift in average particle diameter from around 2 nm to over 30 nm for the 0.5 nm and 30 nm thick deposits, respectively. Also visible is the width of the size distribution, which also increases with the amount of metal deposited. The size distributions become bimodal for the 6, 8, 10, and 15 nm thick deposits, with a majority of particles being larger agglomerates and smaller features corresponding to interspersed islets. Information about the sizes of metal particles on the surface is critical for understanding and optimizing conditions for enhanced ion emission. Maximal kinetic energy should be transferred from the primary ion to the immediate surface region and so the metal particle should be sufficiently large to accumulate this energy. However, high surface coverages are required to obtain large particle sizes. This results in a depression in the signal which can be attributed to the partial metal overlayer. Metal particles surrounding the impact site will inhibit the emission of underlying organic material, somewhat negating the advantage of increased energy density.

Poly(methyl methacrylate)

For the purpose of this study, PMMA was chosen as a representative polymer due to the abundant negative ions typically observed[183]. Bare PMMA samples as well as samples deposited with increasing amounts of gold and silver were analyzed with both the Bi^+ and massive gold cluster projectiles.

For both projectiles, the low mass region of the bare PMMA spectrum is characterized by the emission of small fragment species, including CH_3O^- (mass 31), $C_3H_3O^-$ (mass 55), $C_4H_5O_2^-$ (mass 85), $C_9H_{15}O_4^-$ (mass 187), and $C_{10}H_{17}O_4^-$ (mass 201).

SI yields for these species as a function of metal deposited are provided in Figure VI-3. A comparison of SI yields obtained by each projectile reveals that the 520 keV Au_{400} projectile exhibits 2-3 orders greater SI yields than 30 keV Bi^+ for most samples. None of the characteristic PMMA ions exhibit an enhancement from the metal overlayer. Instead, the yields decrease with the addition of metal, especially in the case of the gold-coated samples analyzed by 520 keV Au_{400}.

In addition to the low mass PMMA fragment ions, larger polymer chains are detected. Figure VI-4 shows a negative mode mass spectrum obtained from a bare PMMA film analyzed by 30 keV Bi^+. Seven different ion series can be identified, with each peak in these families being separated by 100.05 Da, corresponding to the methyl methacrylate monomer. Proposed ion structures in Figure VI-5 show that each of the series differ only in the terminating species at the site of the chain scission. Six of these ion families exhibit a strong mass dependence, with peak intensities decreasing for each incremental gain in chain length. This is especially evident for ion type A which is rather abundant for $n = 1\text{-}3$, but is not observed for $n > 5$.

Fragment types C-G reveal chain lengths of up to 20-25 units. Ion type B exhibits a very different behavior, with a distribution that is shifted towards longer chain lengths. Species having 11-15 polymeric units are most abundant with shorter and longer chain lengths being reduced in intensity, though peaks are observed out to 30 units. This B type distribution likely represents the actual PMMA size distribution in some form.

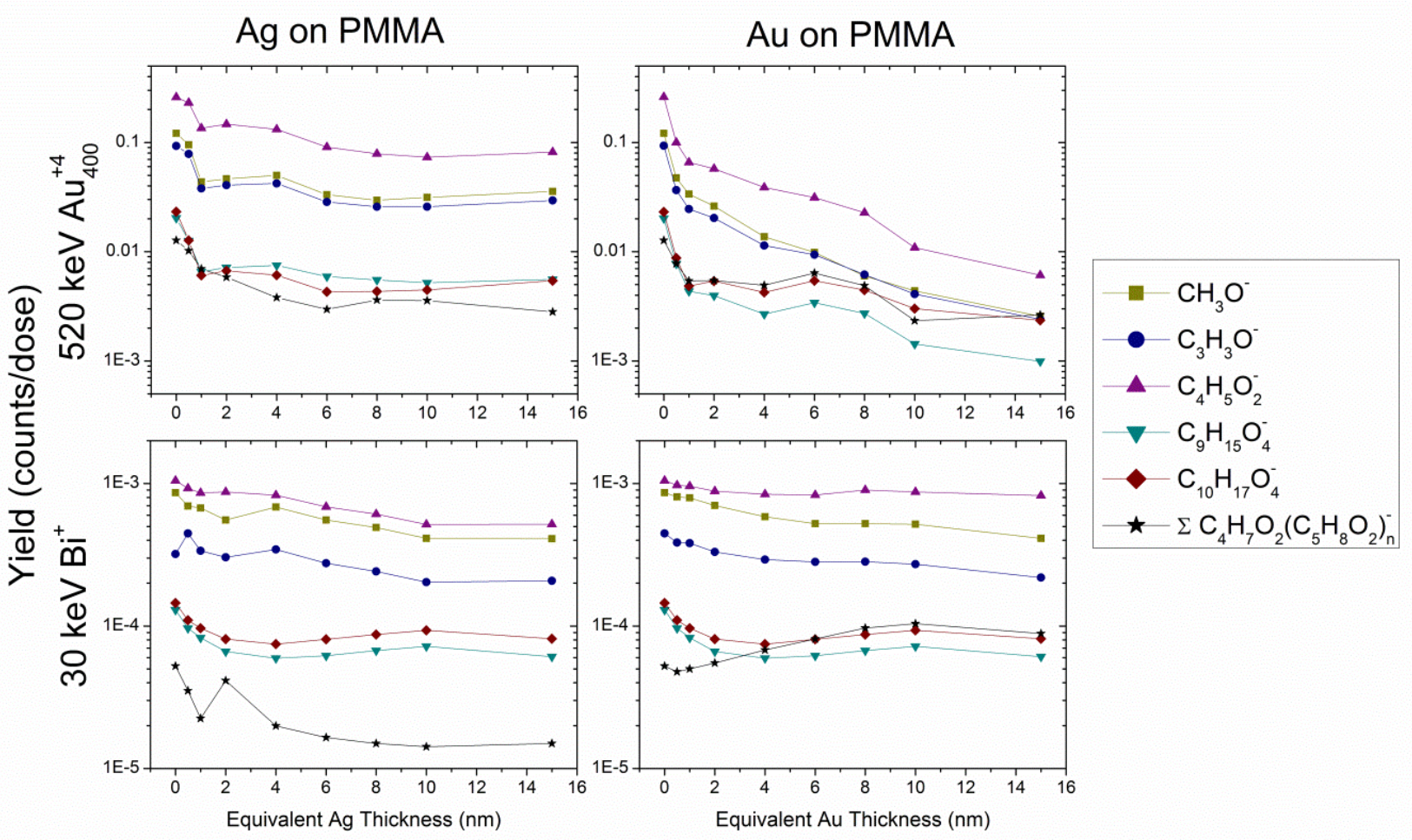

Figure VI-3. SI yields for samples containing various amounts of silver and gold on top of a PMMA film analyzed by massive gold clusters and Bi^+.

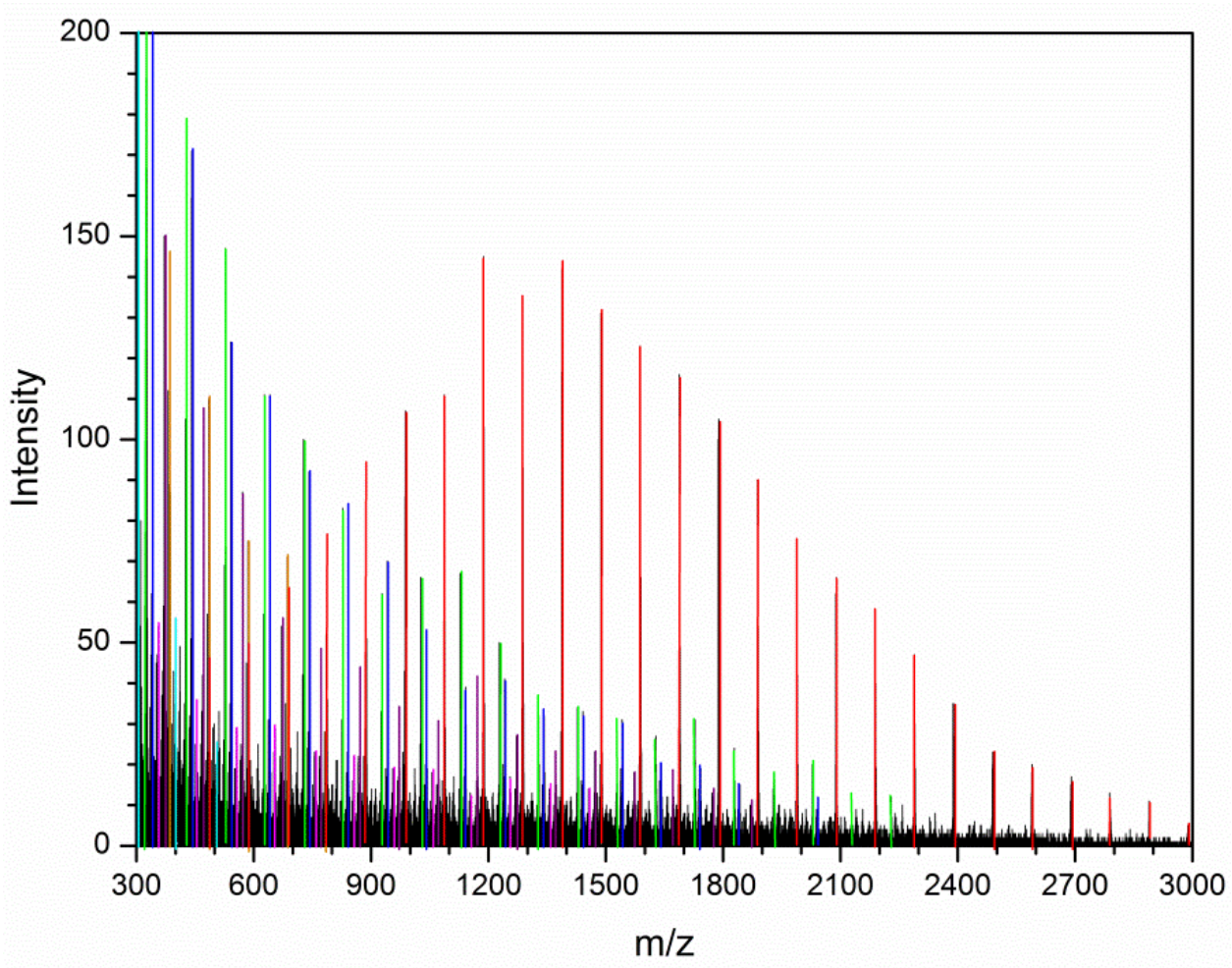

Figure VI-4. Negative mode mass spectrum from atomic-SIMS analysis of a PMMA surface. Peak colors correspond with ion structures in Scheme 1.

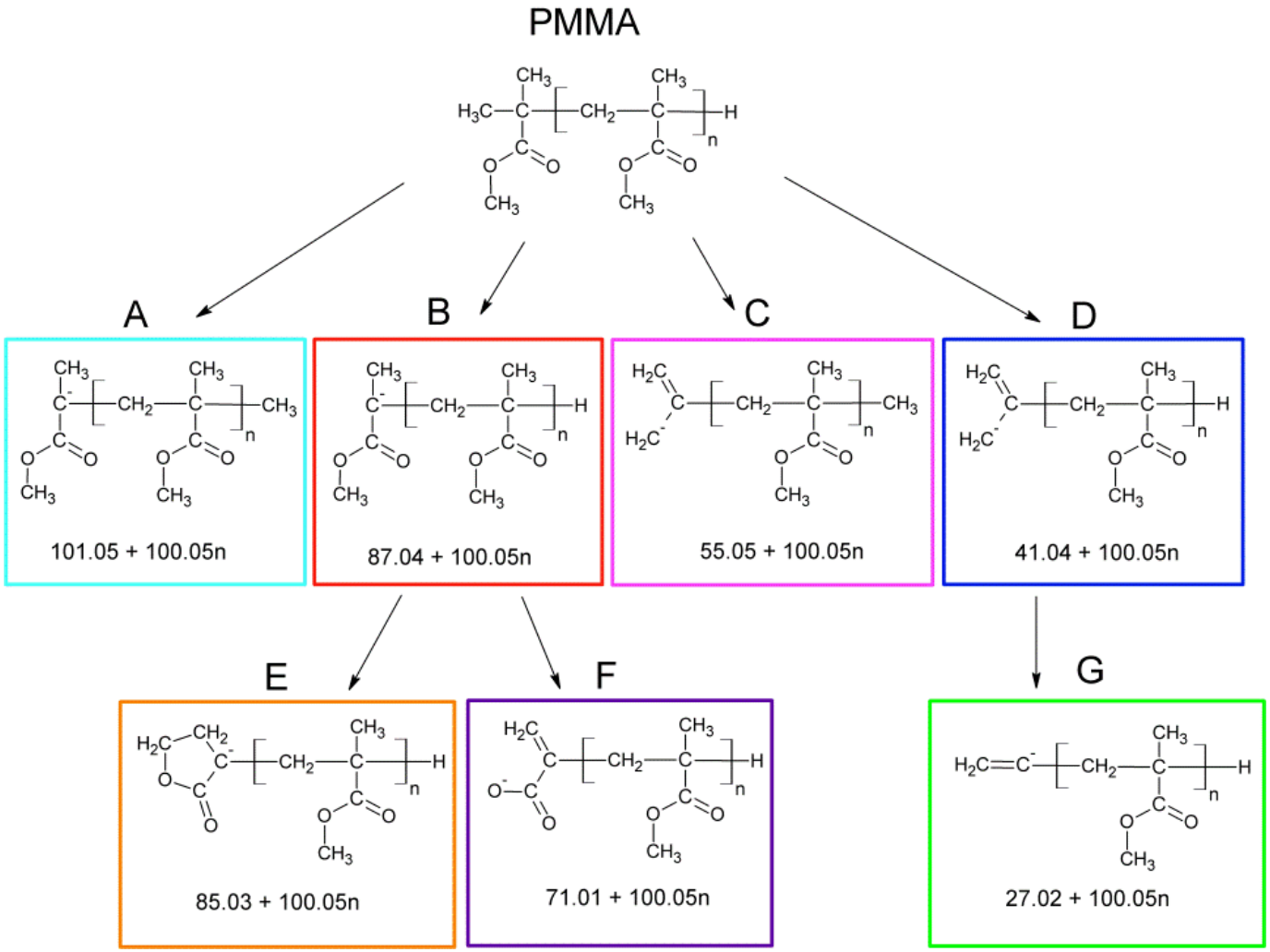

Figure VI-5. Proposed structures for fragment ions observed from Bi^+ bombardment of PMMA.

However, previous studies have shown that fragmentation induced by atomic ion bombardment may shift the observed distribution towards lower masses. In particular Aimoto et al. showed that 19 keV Au^+ analysis of a 1,000 Da polyethylene glycol (PEG) surface suggested the average molecular weight was only 80% of this value while bombardment by 19 keV Au_3^+ gave a molecular weight distribution centered at ~1,000 Da. In our case, the intensity distribution suggests the average molecular weight of the polymer is ~1300 Da rather than the prescribed 2,000 Da; however, this discrepancy can likely be attributed to fragmentation induced by the Bi^+ projectile. Comparison with a PMMA spectrum from massive gold cluster analysis (Figure VI-6) does indeed show a B-type intensity distribution shifted towards higher masses, though a lack of sufficient mass resolution and post-acceleration result in reduced signal-to-noise for this mass range. Another qualitative difference is that only ion types C-G are not observed with the massive gold clusters and ion type A is only observed out to n = 3. These results reinforce the idea that atomic ions impart more internal energy to molecular species and in this case, allow for more energetically expensive fragmentation and rearrangement pathways.

The ion yields for all B-type ions which do not suffer from Ag or Au cluster spectral interferences are summed and plotted as a function of the equivalent metal thickness in Figure VI-3. These ions do not demonstrate the strictly decreasing trend observed for low mass fragments. The aggregate SI yield does not significantly change for Au_{400} bombardment of silver metallized samples. Gold metallized samples show an

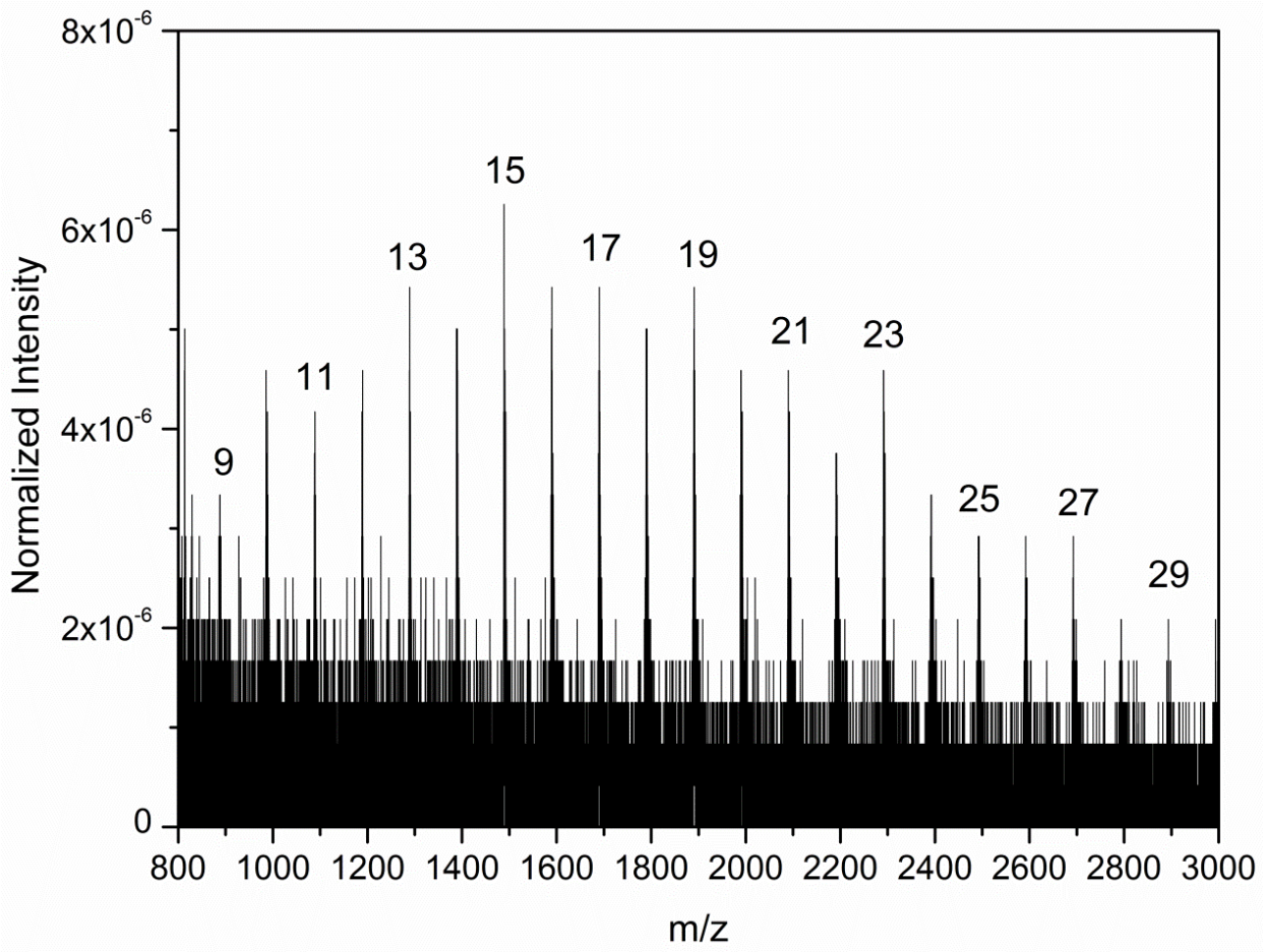

Figure VI-6. Negative mode mass spectrum from massive gold cluster SIMS analysis of a PMMA surface. Observed polymer chain lengths are numbered.

initial dip in the B-type ion yield that is recovered as more gold is added. This suggests there may in fact be a modest signal enhancement which counteracts the effect of a molecular emission inhibiting metal layer. However, this enhancement is not strong enough to result in an overall SI yield increase. The gold metallized samples analyzed with Bi projectiles show a gradual ion yield increase with added gold resulting in a 200% enhancement, but the silver metallized samples give a very different result. The aggregate yield ultimately decreases to ~30% of the native sample with added silver. In all cases, B-type ion yields measured for samples analyzed by Au_{400} are 2-3 orders of magnitude higher than the corresponding Bi analyses.

Irganox 1010

Irganox 1010, a common polymer antioxidant additive, has served as a model analyte for many SIMS depth profiling studies of buried molecular layers.[55] Irganox was also included in a previous MetA-SIMS investigation using Ga and C_{60} projectiles[177], though these analyses were performed in positive ion mode. This study found that Irganox molecular, adduct, and fragment ion yields could be increased by an order of magnitude using gold metallization and a Ga analysis beam, but another order of magnitude was gained by simply using the C_{60} projectile on a bare Irganox surface. C_{60} analysis of the metallized samples gave a slightly reduced molecular ion signal.

Mass spectra from pristine, Ag metallized, and Au metallized Irganox 1010 samples obtained using the massive gold cluster and Bi projectiles are shown in Figure VI-7. Mass spectra of the pristine surface obtained with the ToF SIMS[5] instrument reveal a prominent deprotonated molecular ion peak (mass 1175.7) as well as multiple

satellite peaks. The higher mass peaks are due to ^{13}C isotopic contribution while the lower mass peaks correspond to various combinations of hydrogen losses.[184, 185] Phenolic hydrogen loss to form a carbonyl group as well as the subsequent formation of a quinine methide structure as shown in Figure VI-8 are well-known oxidation mechanisms for hindered phenolic antioxidants.[186].

In the case of Irganox 1010, each of the four (3,5-di-tert-butyl-4-hydroxyphenyl)propanoate groups are available to undergo similar hydrogen losses, creating the envelope of peaks observed in the spectrum. This effect is especially evident upon addition of metal, causing the envelope of peaks to shift downward by approximately four mass units (loss of 4 hydrogen atoms) and broaden to over ten mass units. The prominence of these species after metal deposition suggests the dehydrogenation may be catalyzed by the metallic nanoparticles. This catalytic dehydrogenation is also observed in the case of massive gold projectile impact, though the lesser resolution gives a single peak which shifts in mass and is broadened. In addition to the molecular species, the common Irganox 1010 fragment ions are observed.[187] These include peaks at masses 205.2 ($C_{12}H_{21}O^-$), 231.2 ($C_{16}H_{23}O^-$), and 277.2 ($C_{17}H_{25}O_3^-$) corresponding to fragmentation at different point along the propanoate linker.

The yields for these fragment ions as well as an aggregate sum of quasi-molecular ion peaks, including isotope peaks, for all analyses are presented in Figure VI-9. The sum of molecular ion peaks (excluding oxygen addition peaks) is used to directly compare yields from the two instruments independent of mass resolution.

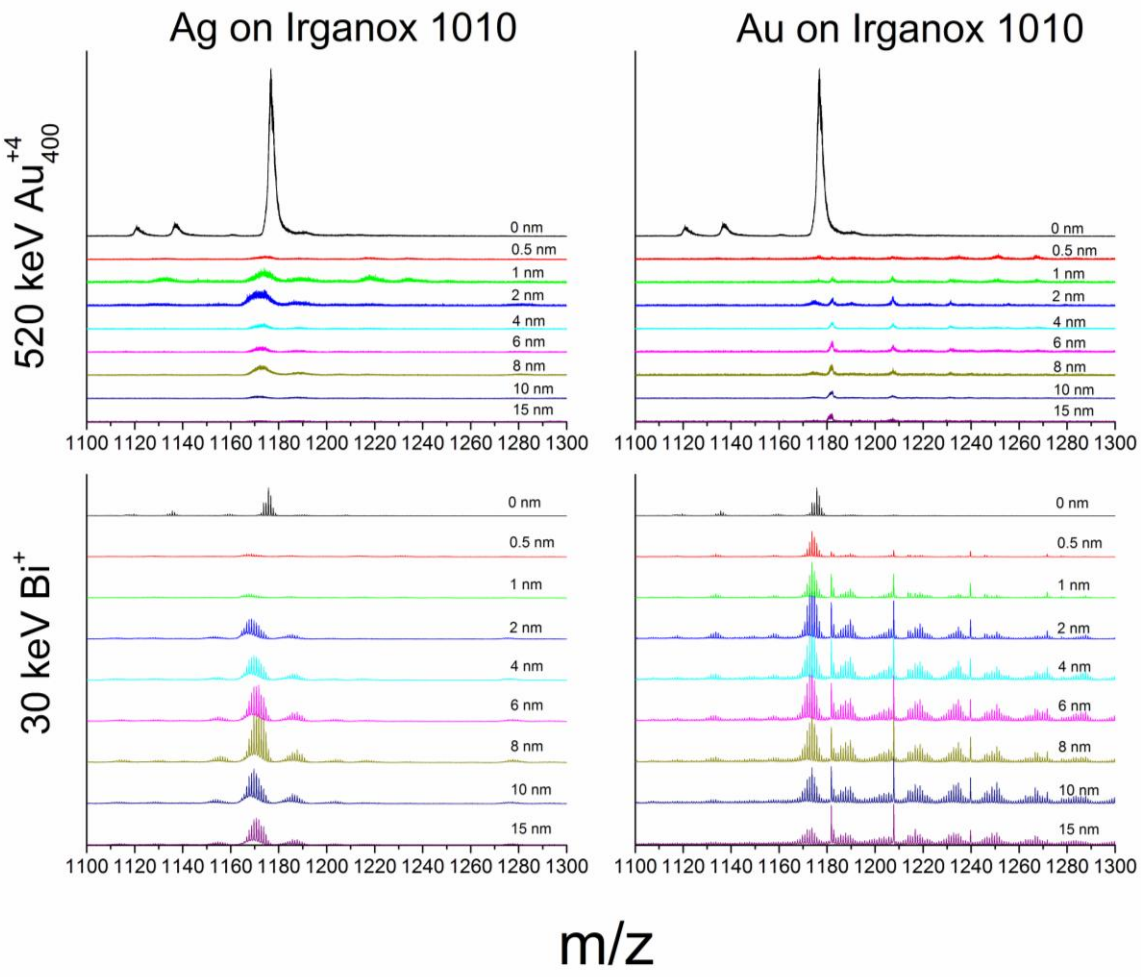

Figure VI-7. Negative mode mass spectrum from samples containing various amounts of silver and gold on top of an Irganox 1010 film analyzed by massive gold clusters and Bi^+ projectiles.

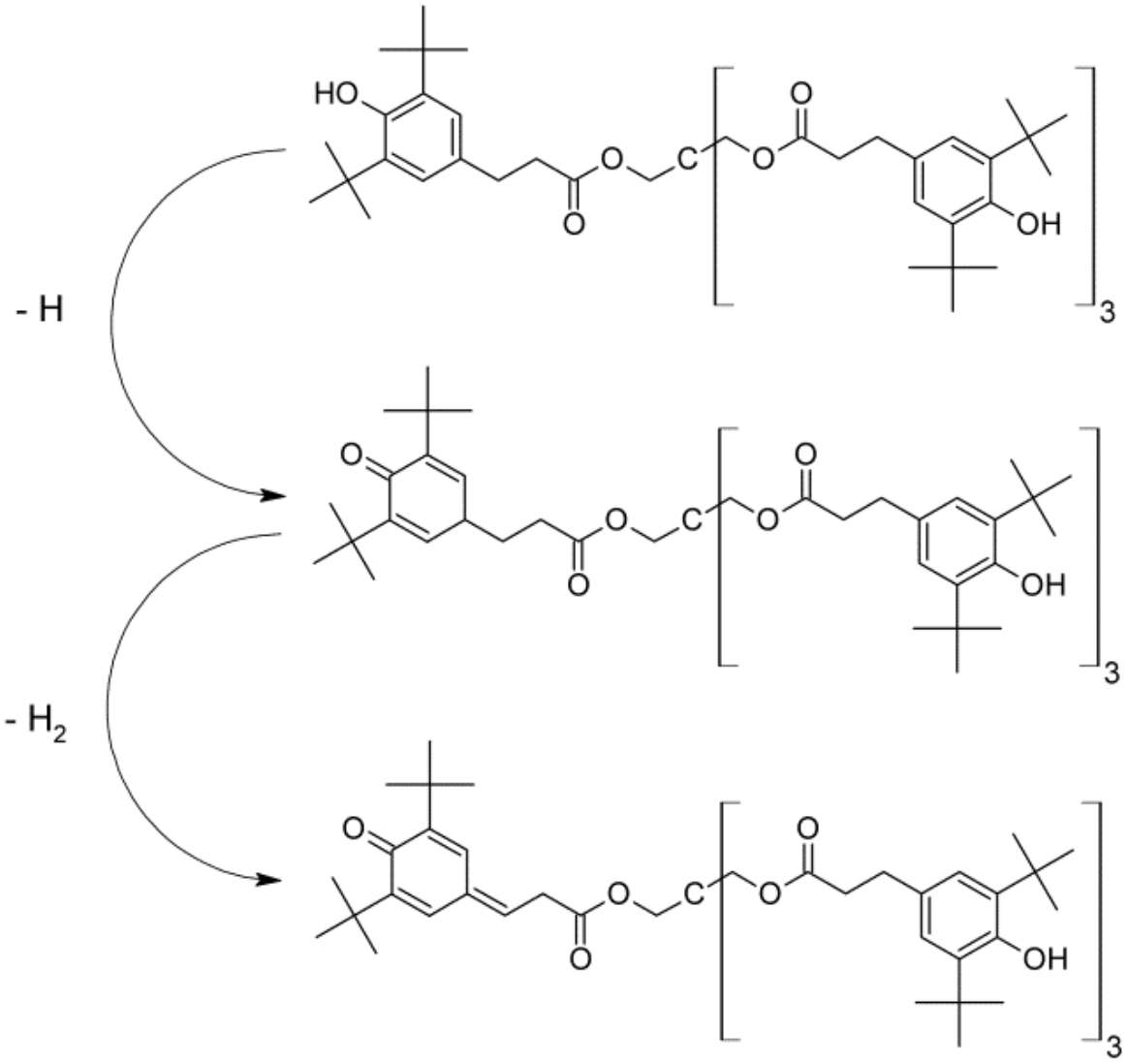

Figure VI-8. Structures for dehydrogenated Irganox 1010 species.

Considering first the quasi-molecular emission from gold metallized samples measured with Bi^+, a general increase in both fragment and molecular ions is observed upon addition of gold to the surface. This enhancement ranges from 1.5-fold for the mass 231fragment peak to 4-fold for the molecular ion envelope. All three fragment ions tracked exhibit a yield plateau after the addition of roughly 2 nm of gold to the surface. This sample also provides the highest yield of molecular ion peaks. The SI yield decreases slightly as more gold is added. Silver metallization reveals a different behavior in which the yields of all characteristic peaks initially decrease upon addition of 0.5 or 1 nm of silver but recover for thicker metal depositions. A 5-fold molecular signal enhancement is obtained for the 8nm thick deposition. The mass 205 fragment shows a 2-fold enhancement relative to the pristine sample while the other two fragments exhibit no enhancement for metallized samples relative to the non-metallized surface. A previous study comparing Ag and Au metallization also noted greater ion yield enhancements with Au relative to Ag. This was attributed the greater mass of the gold atoms which would result in greater energy deposition in the near surface region.[188]

The SI signal depression caused by metallization for Au_{400} analysis is readily visible in Figure VI-9. All monitored signals show a strictly decreasing pattern upon metal addition. This signal reduction is most prominent for the molecular ion aggregate yield, which decreases by 2 orders of magnitude over the span of silver and gold thicknesses studied. This effect is also clearly observed in Figure VI-7 where the pristine sample gives a prominent quasi-molecular ion peak but just a 0.5nm metal deposition

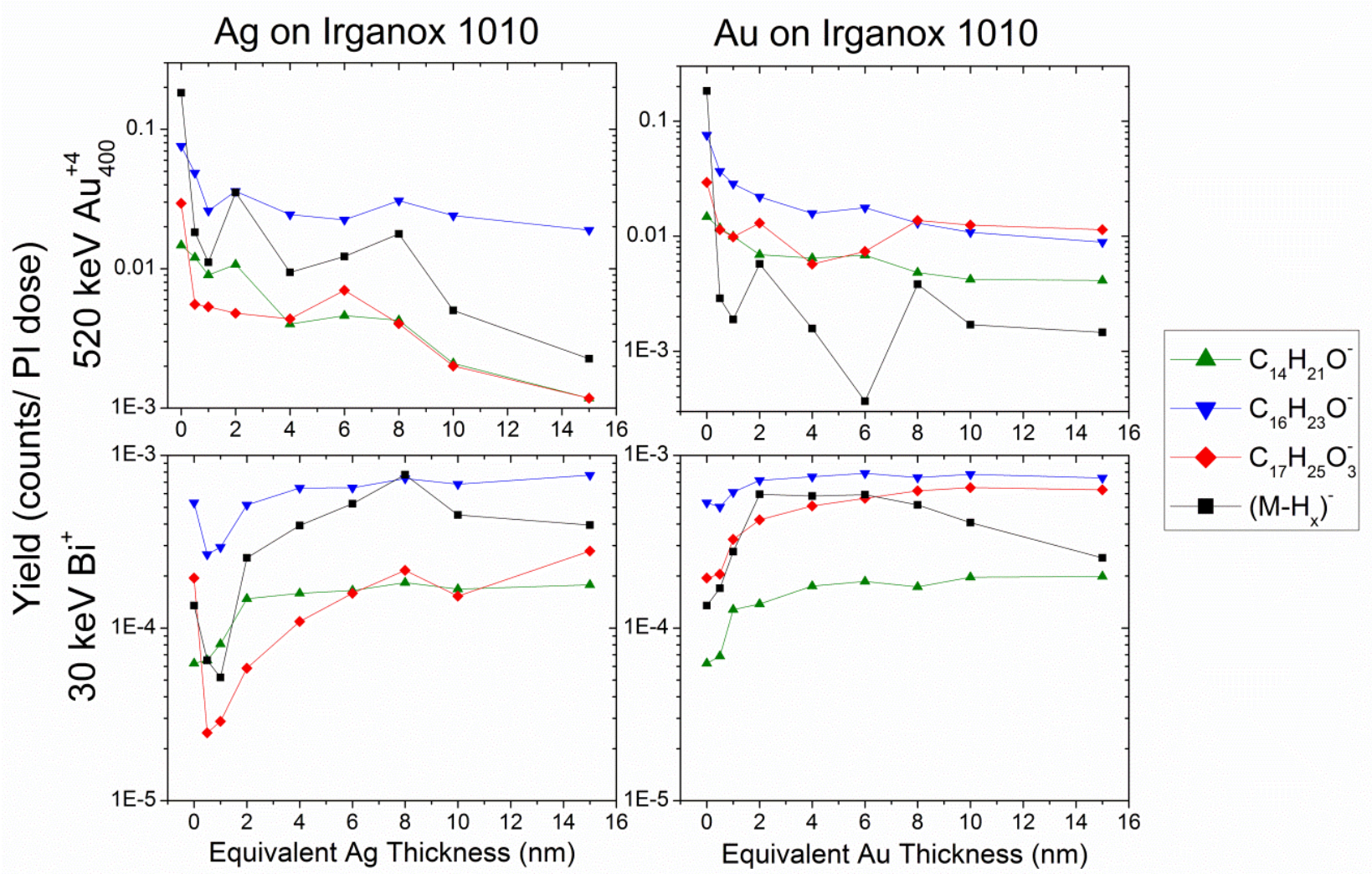

Figure VI-9. Negative ion yields for samples containing various amounts of silver and gold on top of an Irganox 1010 film analyzed by massive gold clusters and Bi^+.

nearly eliminates this signal. The atomic and small metallic clusters present in these samples appear to poison the surface, such that molecular emission is significantly hindered. Molecular desorption from cluster impacts is proposed to occur by a fluid flow mechanism[82, 94] from the rim of the crater generated by the impact. This mechanism may make cluster impacts especially sensitive to the presence of a metal overlayer. As shown in Figures VI-7 and VI-9, a weak signal enhancement of the molecular ion peak is observed for the 2 nm depositions of both silver and gold, but these SI yields remain much lower than those observed from the pristine sample. Overall, the metal layer results in a depression of SI yields observed from Au_{400} impacts, regardless of deposition thickness.

Another interesting feature of the spectra in Figure VI-7 is the presence of multiple groups of peaks at higher masses than the molecular ion. These peaks groups are separated by 16 Daltons on average and correspond to sequential oxygen addition to molecules with varying degrees of dehydrogenation. The addition of up to ten oxygen atoms can be observed for the gold metallized samples. These features are observed only in the presence of metal nanoparticles analyzed with Bi^+. The same features are not seen for the samples analyzed with Au_{400}. Also, both Bi^+ and massive projectile analysis result in the formation of adducts of the type $Au_nC_{2x}H_{2x}O_{2y}$. This type of adduct is not seen for samples deposited with silver.

Ion Yield Comparisons

Figure VI-10 provides a summary of the optimal metallization conditions determined for each projectile. For 520 keV Au_{400} analysis, none of the metallized

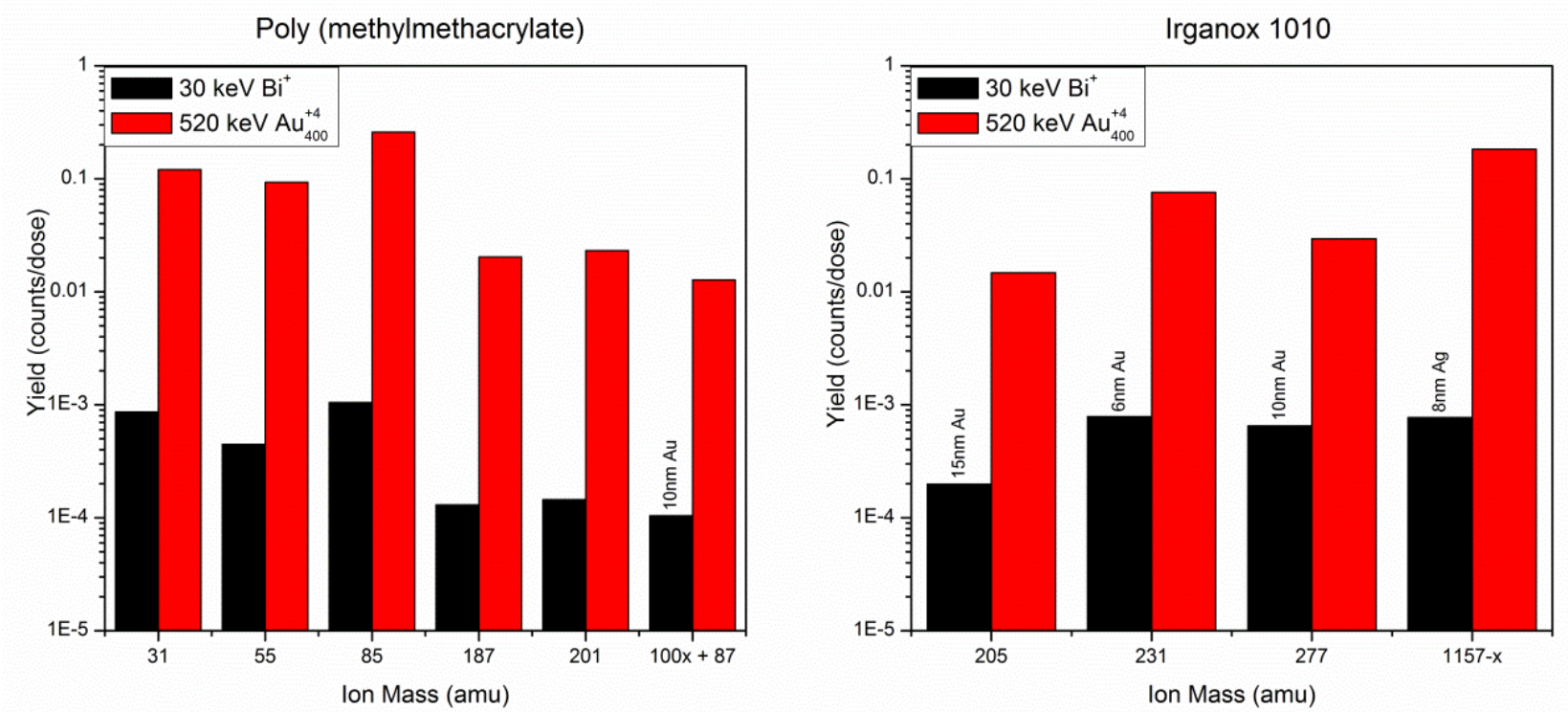

Figure VI-10. Highest yields obtained for each of the characteristic PMMA and Irganox 1010 negative ions obtained from Bi and Au_{400} analyses. Sample metallization conditions are shown above each bar. Yields with no label were obtained from pristine surfaces of the analyte.

samples provided ion yields greater than the pristine sample. The 30 keV Bi projectile did show a significant enhancement upon metallization for many characteristic peaks, though the highest yields for all small PMMA fragments were obtained from the pristine sample. Gold metallization gives the best result for the B-type PMMA high mass ions and all characteristic Irganox 1010 fragments. Metallization with 8nm of Ag gave a slightly higher yield for the Irganox quasi-molecular ion than gold metallization, but generally 6-10 nm of gold on the surface appears to provide the best conditions for 30 keV Bi^+ analysis of the given analytes. Despite the enhancement observed with Bi, Au_{400} provides 2-3 orders greater ion yields for all characteristic species.

Surface Coverage Calculations

The abundant SI emission reported for massive gold cluster bombardment enables its application in the event-by-event methodology described above. This unique SIMS approach allows one to extract information regarding ion co-location with a spatial resolution of ~10 nm.[79, 181, 182] This approach has been well documented for quantifying the surface coverages of chemical segregations with sizes of at least 30 nm.[181] The goal of the current study is to determine whether or not it is possible to extend this methodology to the analysis of nanometric features (metal NP's) which are smaller than the volume sputtered by a single massive gold cluster impact. This non-imaging approach to measuring the coverage for a given chemical component of a surface relies on the ability to properly classify ensembles of impact events according to the type of ions formed. For the given binary system there are three possible types of impact expected. These include impacts on the bare organic substrate, direct impacts on

a metal NP, or impacts on the metal-organic interface. Each of these surface regions has a given probability for emitting ions specific to the substrate or overlayer. However, for NP's smaller than the sputter volume, direct impacts will cause excavation of the underlying substrate and will no longer result in the exclusive emission of metallic species. This reduces the possible number of impact ensembles to those causing substrate emission and those causing both organic substrate and metal layer specific emission. Assuming that ions are emitted from the surface independent of one another, the probability of emitting both ions from a given impact event is the product of their individual yields gives Equation 6.1.

$$Y_{AB} = Y_A \times Y_B \tag{6.1}$$

Substituting the yield definition ($Y_A = \frac{I_A}{N_{eff}}$), where I_A is the observed intensity for ion A and N_{eff} is the number of impacts within the ensemble of interest, gives Equation 6.2.

$$\frac{I_{AB}}{N_{eff}} = \frac{I_A}{N_{eff}} \times \frac{I_B}{N_{eff}} \tag{6.2}$$

Solving for N_{eff}, we obtain Equation 6.3 which allows for a calculation of N_{eff} through the measurement of the two individual ion intensities and their coincidental emission intensity.

$$N_{eff} = \frac{I_A \times I_B}{I_{AB}} \tag{6.3}$$

The ratio of the number of impacts which occur on the surface region of interest, N_{eff}, to the total number of impact events used to generate the spectrum, N_{tot}, gives the surface coverage for the species of interest.

Only the silver metallized sample sets are presented because re-emission of gold from the Au_{400} projectile precludes the quantification of Au from the surface. Two abundant characteristic ions were chosen for each of the chemical species. Masses 85 ($C_4H_5O_2^-$) and 87 ($C_4H_7O_2^-$) were used for PMMA, masses 231 ($C_{16}H_{23}O$-) and 277 ($C_{17}H_{25}O_3^-$) were used for Irganox 1010, and 107 ($^{107}Ag_1^-$) and 216 ($^{107}Ag^{109}Ag^-$) were used for the silver NP's. The results from these analyses are provided in Figure VI-11. The Ag and PMMA coverages measured by SIMS for the range of Ag deposition amounts are plotted along with the surface coverages measured from the STEM images. The Ag coverages measured by SIMS show an increasing trend which parallels the increase observed by STEM, though for both sample sets the 0.5 nm deposition exhibits a greater surface coverage than the 1 nm deposition. It appears that the 0.5 nm samples actually contain more silver than the 1 nm samples. Despite this discrepancy in the amount of silver deposited, the SIMS approach properly detects the relative differences in Ag coverage between the 0.5 nm and 1 nm samples. This can also be seen indirectly via the coverage measurement of the organic layer. Here the 0.5 nm sample gives a smaller organic coverage than the 1 nm sample, again matching with the STEM.

For samples with effective Ag thicknesses of less than 8 nm, the Ag coverage measured by SIMS is overestimated when compared to the STEM data. One factor that may contribute to the disagreement is the influence of impacts which occur adjacent to these small NP's. According to STEM images, metal thicknesses of 8 nm and below

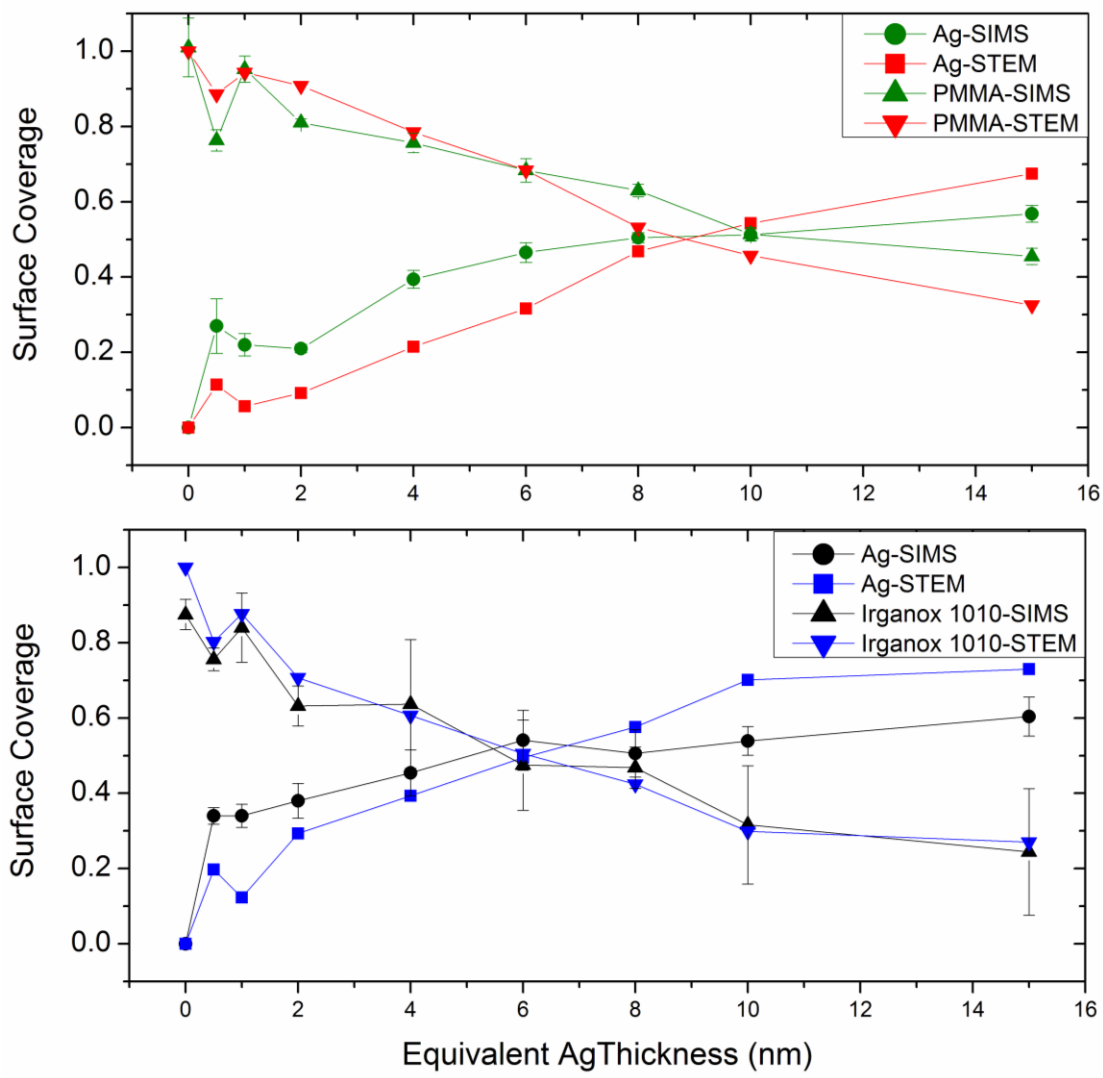

Figure VI-11. Comparison of surface coverages measured by STEM and SIMS for PMMA and Irganox 1010 surfaces coated by various amounts of silver.

correspond to average particle diameters of ≤ 20 nm, approaching the predicted diameter of the impact crater (~10 nm). Therefore, adjacent impacts can be expected to cause emission similar to that observed from direct impacts on the NP's. This means the effective area causing NP-like emission is greater than the actual cross-sectional area of the NP, resulting in an exaggerated coverage measurement. The magnitude of this error is 10-15% though it may also be noted that STEM imaging was performed for replicate samples on a different substrate and not the same samples analyzed by SIMS. Another source of error in this quantification comes from the low silver surface coverage (< 10 %) for some samples. This results in a low probability of Ag_1^- and Ag_2^- co-emission. As revealed by Equation 6.3, accurate measurement of the coincidental intensity (I_{AB}) is critical for obtaining a reliable surface coverage measurement. The PMMA coverage measured for each sample conversely reveals an underestimation relative to STEM.

Figure VI-11 also shows that both the Irganox and Ag coverages obtained for the silver-coated Irganox 1010 samples offer better agreement between the SIMS and STEM measurements. The 1 nm sample does show a pronounced deviation which is also reflected by the reduced Irganox 1010 coverage. Also visible is a systematic underestimation of Ag coverages for the 10 and 15 nm equivalent thicknesses on both the Irganox 1010 and PMMA surfaces. According to the STEM images, the Ag surface for these samples consists of interconnected peninsular morphology rather than the isolated NP's observed for lower coverages. Previous studies have shown that the size of surface features results in the preferential emission of certain cluster ion sizes.[70]

This effect is further illustrated in Figure VI-12 which shows surface coverages measured from the Ag on PMMA sample set using the ion coincidence approach with sequentially larger Ag cluster ion pairs. Each increase in cluster size results in a somewhat reduced surface coverage. The apparent differences in coverages suggest coincidental ion emission can be used to reveal fine structure even within the nanometric Ag features. In order to observe events in which Ag_5^- and Ag_6^- are co-emitted from a single impact, the desorption volume of that impact must contain an abundance of Ag atoms. For impacts on small particles or a large particle-substrate interface, the yield of large Ag clusters is extremely low because sufficient material is not available for their formation. Therefore, the number of impacts capable of forming at least two of these large clusters (in coincidence) is restricted to those occurring on a thick, interior surface of the nanometric object. This selectivity is tunable, as shown by the range of measured surface coverages, such that each ion pair used exhibits a different level of specificity. In this way, a fine structure related to the size and shape of the nanometric objects can be observed.

The depth of emission for the massive gold projectiles in silver can also be ascertained from this set of samples by monitoring the coincidental emission of Au-Ag adducts. These species result from the recombination of Au projectile atoms with Ag atoms from the surface. Similar Au_xAg_y cluster ions have been observed previously,[189] but this is the first report of bimetallic cluster formation by a projectile-surface adduct mechanism.[77] There is a threshold for this emission mechanism because projectile atoms must first be stopped within the target before they can be re-emitted. A previous study

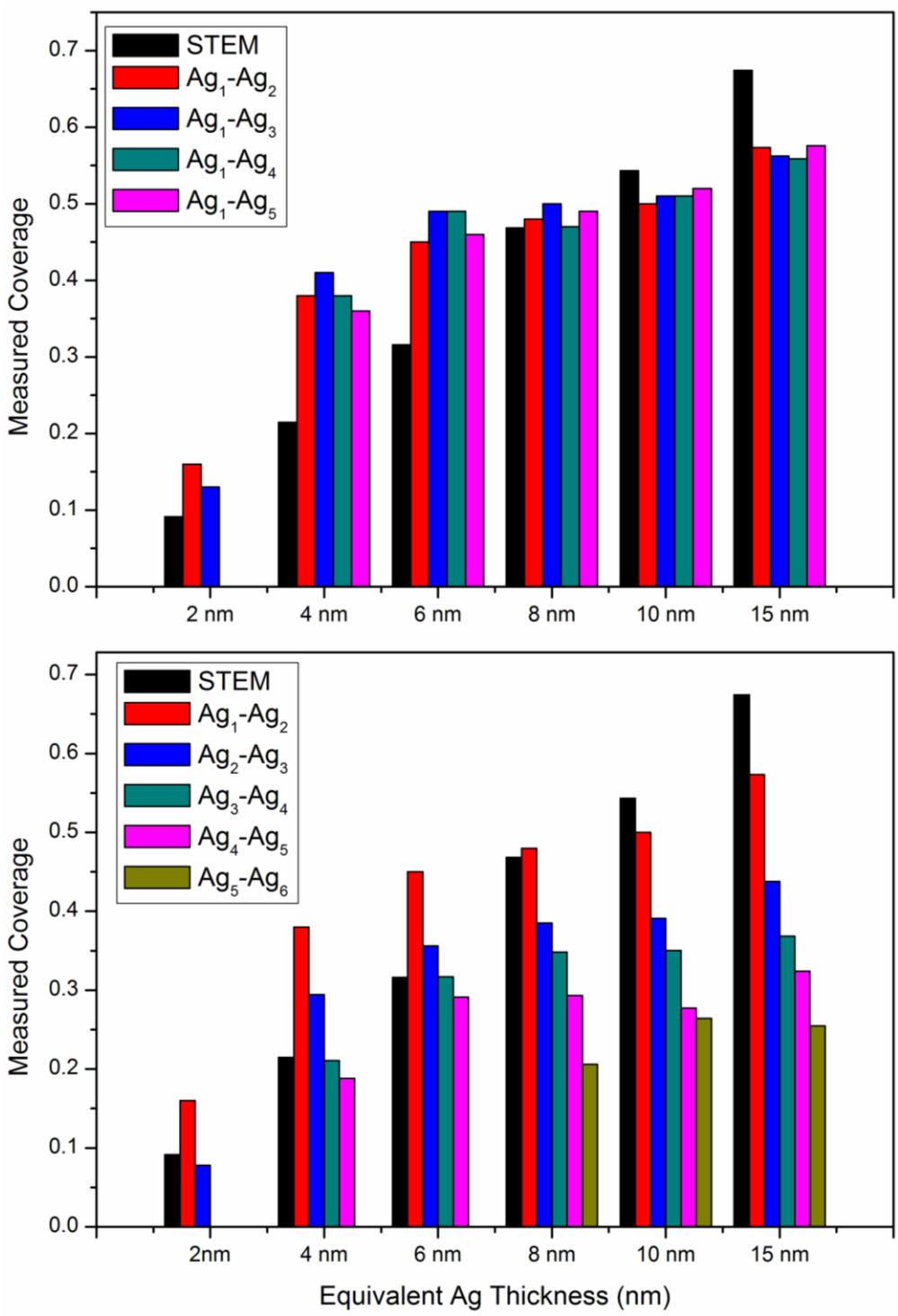

Figure VI-12. Comparison of silver surface coverages measured from the Ag on PMMA sample set using various pairs of silver cluster ions. The surface coverage measured by STEM is shown as a black line.

has shown that the stopping range of the Au_{400} projectile is 15-20 nm in amorphous carbon.[190] Using the two isotopic peaks for $AuAg^-$ (masses 304 and 306), the coincidental methodology described above allows one to calculate the percentage of impacts which result in Au-Ag adduct formation, independent of ionization efficiency considerations. By monitoring ion co-emission rather than a simple yield progression we are able to observe a threshold for adduct formation and hence the depth of emission for Au_{400} impacts. Figure VI-13a shows that the yields for $AuAg^-$ (mass 304) and Ag^- (mass 107) steadily increase as more silver is added to the surface. Au^- (mass 197) also shows a gradual yield increase which can again be attributed to enhanced stopping of the projectile by the thicker silver layer. These observations are contrasted with Figure VI-13b which shows a clear threshold for $AuAg^-$ forming impacts which occurs for silver overlayers with thicknesses of at least 4 nm. Despite uncertainty in the QCM measurement, this depth of 4-8 nm agrees well with the ~10 nm depth of emission previously reported for Au_{400} at a lower impact energy.[68]

The percentage of impacts causing gold re-emission was also calculated using Au_1^- and Au_2^- signals and the results are included in Figure VI-13b. This plot shows an interesting decrease in the gold re-emission which coincides with the appearance of $AuAg^-$ forming impacts. Because Au atoms must be generated from the projectile, gold is the limiting reagent for gold-silver adduct formation. This means that gold atoms are scavenged by the more abundant Ag species ejected, resulting in a decreased probability for pure gold emission. The only manifestation of this effect in the yield

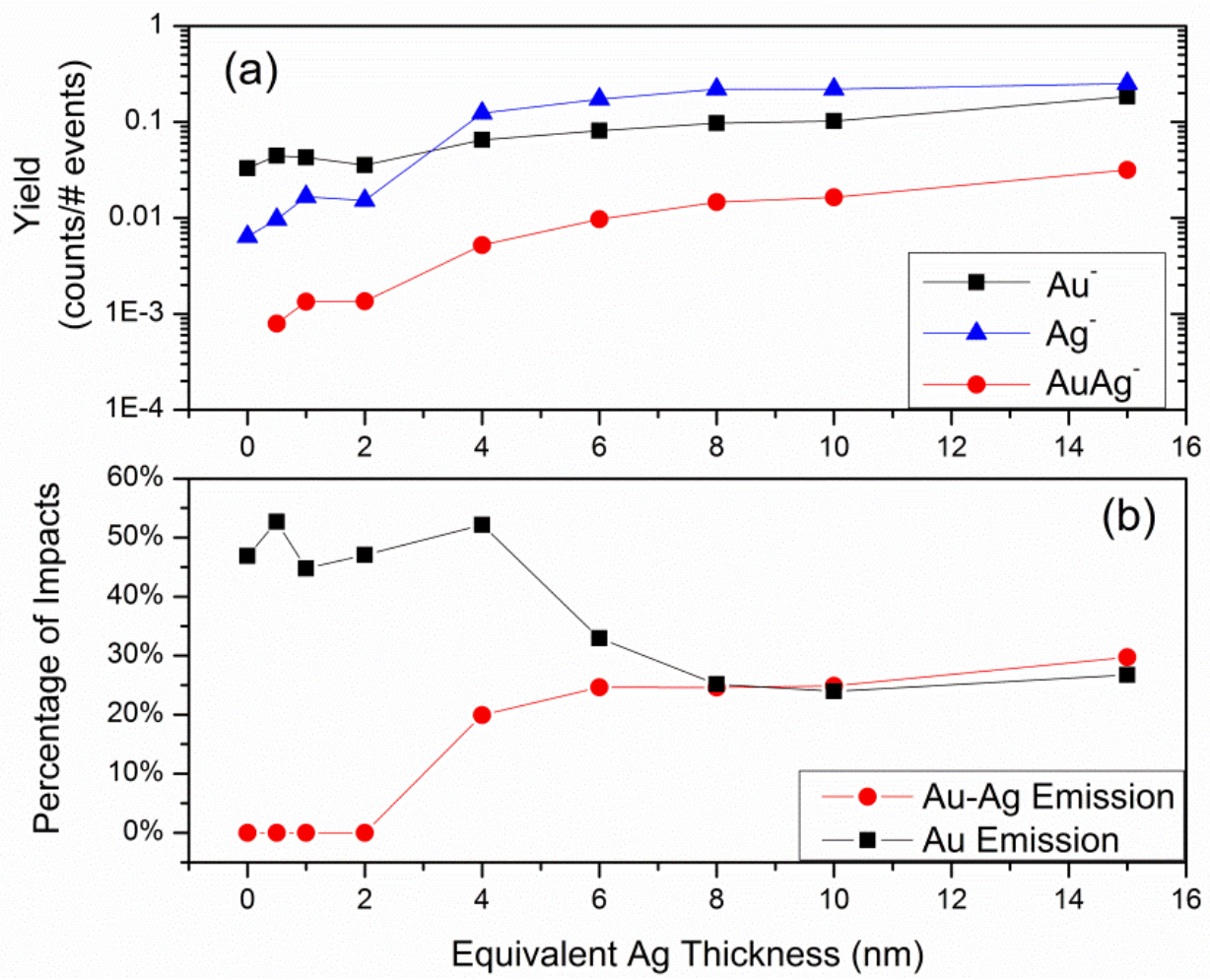

Figure 13. (a) Au^-, Ag^-, and $AuAg^-$ (masses 197, 107, 304, respectively) ion yields for PMMA surfaces coated with various amounts of silver. (b) The percentage of impacts which cause re-emission of either Au projectile species or Au-Ag adducts for various amounts of Ag on a PMMA surface.

progressions is the significant increase in Ag^- and $AuAg^-$ yields between the 2 nm and 4 nm samples which is not replicated for the Au^- yields.

Conclusion

According to the three test samples examined to date, the MetA-SIMS approach is not a viable method for improving secondary ion yields from massive gold projectile impacts. It seems that the previous enhancement observed for CN^- from glycine may be a unique case only applicable for thermodynamically stable species which can be formed through an atomization and recombination mechanism[99]. Despite the lack of a SI yield enhancement, the 520 keV Au_{400}^{+4} projectile displayed 2-3 orders greater SI yields than all 30 keV Bi^+ analyses, while also avoiding the added spectral complexity caused by sample metallization. This study also shows that this approach can be used to quantify surface coverages of nanometric features. However, we report increased error in this measurement for particles with diameters less than ~20 nm. The coincidence methodology also allows one to observe physical phenomena such as projectile-target adduct re-emission at the level of individual projectile impacts.

CHAPTER VII

CONCLUSIONS*

This study has dealt with fundamental aspects of massive gold cluster impacts on surfaces relevant for molecular analysis. The parameters investigated include the projectile range, projectile fate after impact, depth of emission, SI yield, SI multiplicity, and SI internal energy. A test case for employing the event-by-event methodology to probe nanoscale chemical heterogeneity is displayed as well. A brief description of our findings follows.

Physical Parameters of the Cluster-Solid Interaction

Carbon cluster emission from thin carbon foils (5-40 nm) impacted by individual Au_n^{+q} cluster projectiles (95-125 qkeV, n/q = 3-200) reveals features regarding the energy deposition, projectile range, and projectile fate in matter as a function of the projectile characteristics. For the first time, the secondary ion emission from thin foils has been monitored simultaneously in both forward and backward emission directions. The projectile range and depth of emission were examined as a function of projectile size, energy, and target thickness. A key finding is that the massive cluster impact develops very differently from that of a small polyatomic projectile. The range of the

* Part of this chapter is reprinted with permission from "Characteristics of Positive and Negative Secondary Ions Emitted from Au_3^+ and Au_{400}^{+4} Impacts" by J.D. DeBord, F.A. Fernandez-Lima, S.V. Verkhoturov, E.A. Schweikert, and S. Della-Negra, 2012. *Surface and Interface Analysis*, Copyright [2012] by John Wiley and Sons. Part of this chapter is also reprinted with permission from "Bidirectional Ion Emission from Massive Gold Cluster Impacts on Nanometric Carbon Foils" by J.D. DeBord, S. Della-Negra, F.A. Fernandez-Lima, S.V. Verkhoturov, and E.A. Schweikert, 2012. *The Journal of Physical Chemistry C*, Copyright [2012] by the American Chemical Society.

125 qkeV Au_{100q}^{+q} ($q \approx 4$) projectile is estimated to be 20 nm in amorphous carbon (well beyond the range of an equal velocity Au^{+}). Also, using a double foil experiment, projectile disintegration can be observed at the exit of even a 5 nm thick foil.

Secondary Ion Emission Characteristics

Massive gold clusters are a route to significant gains in secondary ion yields relative to other commonly used projectiles. At an impact energy of 520 keV, Au_{400}^{+4} is capable of generating an average of >10 secondary ions per projectile with some impact events generating >100 secondary ions. The capability of this projectile for signal enhancement is further displayed through the observation of up to 7 deprotonated molecular ions from a single impact on a neat target of the model pentapeptide leu-enkephalin. Positive and negative spectra of peptide spectra reveal two distinct emission regimes responsible for the emission of either intact molecular ions or small fragment species.

To investigate whether the high energy density deposited by the massive cluster projectile imparts significant internal energy to SIs, a series of benzylpyridinium salts were used to measure the internal energy distribution of SIs. The theoretical and experimental implementation of this system has been refined to yield a much more accurate and robust method for performing internal energy measurements. The secondary ion internal energy distributions measured from 440 keV Au_{400}^{+4} impacts are surprisingly narrow and low in energy (~0.19 eV/atom) when compared to keV atomic bombardment of surfaces (1-2 eV/atom). The results show that Au_{400}^{+4} impacts are capable of generating molecular species with low internal energies. Molecular dynamics

simulations show that molecular emission occurs from the rim of an impact crater created by the projectile.[191] This mechanism of ion emission is specific to massive clusters and results in species with lower internal energies.[173]

Signal Enhancement by Metallization

The feasibility of metal-assisted secondary ion mass spectrometry (MetA-SIMS) for increasing secondary ion yields from massive gold projectile impacts was investigated using polymeric and plastic additive test molecules. Poly(methyl methacrylate) (PMMA) and Irganox 1010 surfaces were deposited with various amounts of gold and silver and then analyzed using both Bi^+ and Au_{400}^{+4}. The Bi^+ primary ion displayed a five-fold ion yield increase for some species while the massive gold cluster exhibited significant suppression due to the metal overlayer, with more than a ten-fold decrease in ion yields for most species. Despite the enhancement with Bi^+, yields observed from the neat surfaces with Au_{400}^{+4} are two orders of magnitude greater for nearly all species.

Chemical Analysis of Nanometric Surface Features

The metal nanoparticles created by thermal deposition on organic substrates additionally provide a model system for testing the spatial resolution when quantifying nanoscale chemical segregations using coincidence mass spectrometry. Surface coverages for both the metal and organic components measured in a non-imaging follow the same trend as STEM imaging measurements. Also, the co-emission of metallic cluster ions serves as a sensitive tool for detecting differences in the sizes of nanoparticulate metal deposits. The variation in surface coverages measured with

different pairs of cluster ions shows that larger metallic clusters can only be produced from large metallic aggregations on the surface.

Directions for Future Research

The construction of a one-of-a-kind research instrument has significantly expanded the scope of molecular surface analysis. Further research directions are detailed below.

Perhaps the most obvious application for massive cluster SIMS is the investigation of biological surfaces. This instrument's potential for molecular analysis of biological tissues and cells with nanometric spatial resolution is unparalleled among analytical techniques. An initial study observing lipid distributions in brain tissue has been performed.[132] The event-by-event methodology is particularly well-suited drug delivery and biomarker tracing. Using ion co-emission, it may be possible to identify species which are co-located with a drug molecule, such as the active binding sites of target proteins. This tracing study could be done in a label-free manner. However, the analysis of complex surfaces without *a priori* knowledge of their molecular composition raises the issue of whether or not accurate molecular identifications can be assigned with a mass resolution of only ~1,500. A recent paper[192] has reviewed the relationship between instrumental mass accuracy, which depends on mass resolution, and the number of possible chemical identifications. It showed that between 10^3 and 10^5 chemicals from the PubChem database[193] can be found for peaks 200-800 amu (which includes nearly all molecules in this dissertation) if the accuracy of the mass determination is even as low as 100 ppm. One method for improving the accuracy of molecular identification is the use

of coincidental mass spectrometry. This technique enables one to "filter" the spectrum and effectively reduce the number of components within the mixture.[71, 75] This simplified spectrum enhances the certainty of identified species that are co-emitted with a species of interest. Despite this capability, molecular identification accuracy is limited by the current ToF analyzer. An instrumental geometry modification to incorporate an orthogonal reflectron ToF analyzer could improve spectral performance to the point where biomarker discovery studies are possible. Commercial instruments utilizing such analyzers are capable of achieving mass resolutions over 30,000 and mass accuracies below 1 ppm.

Another direction for research which warrants attention is the study of photon emission from cluster impacts. Studies from the Schweikert group have established that photon emission does occur from cluster impacts[194, 195] and that it can be specific to the analyte under observation, as shown by fluorescent emission from green fluorescent protein (GFP) and its analog red fluorescent protein (RFP).[196] A potential application for this type of photon emission includes its use as a trigger signal for the ToF measurement. However, the solid angle of detection for the preliminary studies above were quite low (~0.6 π sr). It is possible to improve this detection efficiency by adding multiple photomultiplier tubes (PMTs) or an array of ball lenses to capture a greater fraction of the emitted photons. A proposed arrangement of the ball lens system is shown in Figure VII-1.

The method for measuring ion internal energies presented in Chapter V is a tool that allows for quantitative comparisons under various experimental conditions. It is

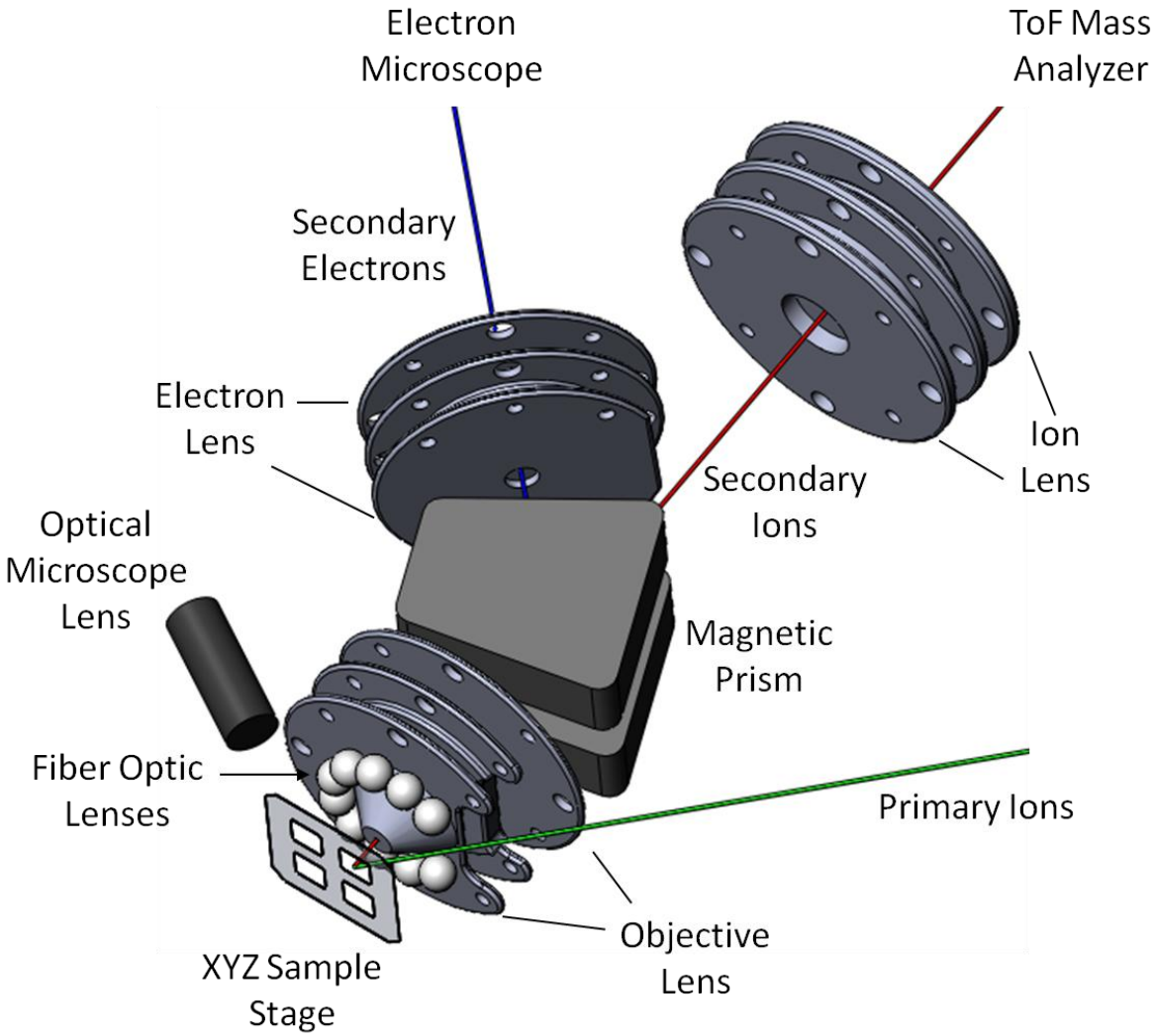

Figure VII-1. Three-dimensional drawing showing the proposed placement of an array of fiber optic ball lenses to improve the detection efficiency of photon emission.

interesting to consider how parameters such as the molecular environment and massive cluster size affect the internal energies of SIs. A study of MetA-SIMS with atomic projectiles showed that SI energies are reduced when a metallic overlayer is used.[137] Similar effects may be present for cluster bombardment. Perhaps the presence of a matrix which would mediate the energy transfer from projectile to SIs could reduce the energy accumulated in their vibrational modes. Another consideration is what effect the presence of ionization enhancing species, such as protonated water clusters ($(H_2O)H^+$)[119] or Cs^+,[109] have on the energies of ions formed.

There are also improvements that could be made to the BPY molecular system utilized in Chapter V. Shortcomings could be overcome by the development of novel "thermometer" ions. One limitation is that fragmentation of BPY ions can only be monitored in positive ion mode. P-toluenesulfonic acid is one chemical that may enable SI internal energy measurements in negative mode. The spectrum of PTSA, shown in Chapter IV, suggests a single fragmentation pathway predominates (a prerequisite for the IE measurement method developed) according to the presence of two large peaks for the molecular ion and SO_3^- fragments. In order for this molecule to be viable, dissociation energies and oscillator frequencies would need to be calculated and the fragmentation pathway would need to be verified. A second improvement upon the BPY system would be the development of a replacement system which incorporates a tight transition state along the fragmentation reaction coordinate. The loose transition state of BPY ion fragmentation complicates the calculation of RRKM fragmentation rate versus internal energy relations. A tight transition state can be identified and described more

easily in the RRKM formalism. This would improve the accuracy in transforming experimentally measured rate constant distributions into the desired internal energy distributions.

Nearly all data reported in this dissertation has been obtained using the Au_{400}^{+4} projectile. Many measurements have displayed the prolific SI emission from impacts of this projectile. However, the development of novel cluster ion sources should not stop here. Trends suggest that larger, more energetic projectiles can provide even higher SI yields and thereby improve the analytical capabilities afforded by a SIMS approach. One route to the generation of larger, more energetic projectiles is electrospray ionization of functionalized nanoparticles. Using this method it is possible to create highly charged nanoparticles that would enable acceleration to higher impact energies using a given accelerating voltage. As an example, 25 nm gold nanoparticles can be generated with upwards of 120 charges per particle.[197] Using this primary ion, it would be possible to obtain an impact energy of nearly 16 MeV with the Pegasus high voltage platform. Also, the large number of atoms contained in a nanoparticle means that each atom carries only a small fraction of the projectile's kinetic energy. This distributes energy over a larger area and results in a higher energy density at the surface, increasing the sputter yield.[191] A technical advantage of nanoparticle sources also exists. An electrosprayed solution of monodisperse nanoparticles is no longer a mixture of projectiles with a variety of different sizes that must be carefully filtered before analysis.[197] Instead, the nanoparticle beam contains projectiles that differ only in charge state, though regardless of charge state, all projectiles would display a similar mode of interaction. Similarities exist

between this approach and others currently employed, such as desorption electrospray ionization (DESI), but the use of functionalized nanoparticles would allow for greater control of projectile characteristics. Experimental control of these parameters is essential for understanding the mechanics underlying SI emission, as evidenced by this dissertation.

REFERENCES

(1) Williams, P. *Annu. Rev. Mater. Sci.* **1985**, *15*, 517-548.

(2) Boxer, S. G. *Ann. Rev. Biophys.* **2009**, *38*, 53.

(3) Thiel, V., Sjövall, P. *Annu. Rev. Earth Pl. Sc.* **2011**, *39*, 125-156.

(4) Demirev, P. A. *Mass Spectrom. Rev.* **1995**, *14*, 279-308.

(5) Winograd, N., Garrison, B. J. *Annu. Rev. Phys. Chem.* **2010**, *61*, 305-322.

(6) Benninghoven, A. *Phys. Status Solidi B* **1969**, *34*, K169-K171.

(7) Herzog, R. F. K., Viehböck, F. P. *Phys. Rev.* **1949**, *76*, 855-856.

(8) Bernard, V. *Phys. Scripta* **1997**, *1997*, 60.

(9) Sigmund, P. *Phys. Rev.* **1969**, *184*, 383.

(10) García-Rosales, C., Eckstein, W., Roth, J. *J. Nucl. Mater.* **1995**, *218*, 8-17.

(11) Eckstein, W., Preuss, R. *J. Nucl. Mater.* **2003**, *320*, 209-213.

(12) Andersen, H. H., Brunelle, A., Della-Negra, S., Depauw, J., Jacquet, D., et al. *Phys. Rev. Lett.* **1998**, *80*, 5433-5436.

(13) Sigmund, P. *Nucl. Instrum. Meth. B* **1987**, *27*, 1-20.

(14) Macfarlane, R., Torgerson, D. *Science* **1976**, *191*, 920-925.

(15) Nakata, Y., Honda, Y., Ninomiya, S., Seki, T., Aoki, T., et al. *J. Mass Spectrom.* **2009**, *44*, 128-136.

(16) Behrisch, R., Eckstein, W., *Sputtering by Particle Bombardment: Experiments and Computer Calculations from Threshold to MeV Energies*. Springer: **2007**.

(17) Williams, P. *Surf. Sci.* **1979**, *90*, 588-634.

(18) Ziegler, J. F., Biersack, J. P., Ziegler, M. D., *SRIM, the stopping and range of ions in matter*. SRIM: Chester (Maryland), **2008**.

(19) Andersen, H. H., Bay, H. L. *J. Appl. Phys.* **1974**, *45*, 953-4.

(20) Andersen, H. H., Bay, H. L. *J. Appl. Phys.* **1975**, *46*, 2416-2422.

(21) Blain, M. G., Della-Negra, S., Joret, H., Le, B. Y., Schweikert, E. A. *Phys. Rev. Lett.* **1989**, *63*, 1625-8.

(22) Appelhans, A. D., Delmore, J. E. *Anal. Chem.* **1989**, *61*, 1087-93.

(23) Wucher, A. *Appl. Surf. Sci.* **2006**, *252*, 6482-6489.

(24) Novikov, A., Caroff, M., Della-Negra, S., Depauw, J., Fallavier, M., et al. *Rapid Commun. Mass Sp.* **2005**, *19*, 1851-1857.

(25) Gillen, G., Fahey, A. *Appl. Surf. Sci.* **2003**, *203–204*, 209-213.

(26) Van Stipdonk, M. J., Harris, R. D., Schweikert, E. A. *Rapid Commun. Mass Sp.* **1996**, *10*, 1987-1991.

(27) Harris, R. D., Van Stipdonk, M. J., Schweikert, E. A. *Int. J. Mass Spectrom.* **1998**, *174*, 167-177.

(28) Gillen, G., King, R. L., Chmara, F. *J. Vac. Sci. Technol. A* **1999**, *17*, 845-852.

(29) Kruger, D., Iltgen, K., Heinemann, B., Kurps, R., Benninghoven, A. *J. Vac. Sci. Technol. B* **1998**, *16*, 292-297.

(30) Pillatsch, L., Wirtz, T., Migeon, H. N., Scherrer, H. *Surf. Interface Anal.* **2010**, *42*, 645-648.

(31) Swanson, L. W. *Nucl. Instrum. Methods* **1983**, *218*, 347-353.

(32) Benguerba, M., Brunelle, A., Della-Negra, S., Depauw, J., Joret, H., et al. *Nucl. Instrum. Meth. B* **1991**, *62*, 8-22.

(33) Johansson, B. *Surf. Interface Anal.* **2006**, *38*, 1401-1412.

(34) Tempez, A., Schultz, J. A., Della-Negra, S., Depauw, J., Jacquet, D., et al. *Rapid Commun. Mass Sp.* **2004**, *18*, 371-376.

(35) Pinnick, V. Ph.D. Dissertation. Texas A&M University, College Station, Texas, **2009**.

(36) Wagner, M. S. *Anal. Chem.* **2004**, *76*, 1264.

(37) Henkes, P. R. W. *Rev. Sci. Instrum.* **1990**, *61*, 360-362.

(38) Yamada, I., Matsuo, J., Toyoda, N., Kirkpatrick, A. *Mater. Sci. Eng. R Rep.* **2001**, *34*, 231-295.

(39) Matthew, M. W., Beuhler, R. J., Ledbetter, M., Friedman, L. *J. Phys. Chem.-US* **1986**, *90*, 3152-3159.

(40) Yamada, I. *Nucl. Instrum. Meth. B* **1996**, *112*, 242-247.

(41) Beuhler, R. J., Friedman, L. *Int. J. Mass Spectrom.* **1989**, *94*, 25-39.

(42) Mahoney, J. F., Perel, J., Ruatta, S. A., Martino, P. A., Husain, S., et al. *Rapid Commun. Mass Sp.* **1991**, *5*, 441-445.

(43) Beuhler, R. J., Friedman, L. *J. Chem. Phys.* **1982**, *77*, 2549-2557.

(44) Mahoney, J. F., Perel, J., Lee, T. D., Legesse, K. *Int. J. Mass Spectrom.* **1987**, *79*, 249-266.

(45) Kroto, H. W., Heath, J. R., O'Brien, S. C., Curl, R. F., Smalley, R. E. *Nature* **1985**, *318*, 162-163.

(46) Della-Negra, S., Brunelle, A., Le Beyec, Y., Curaudeau, J. M., Mouffron, J. P., et al. *Nucl. Instrum. Meth. B* **1993**, *74*, 453-456.

(47) Baudin, K., Brunelle, A., Della-Negra, S., Jacquet, D., Håkansson, P., et al. *Nucl. Instrum. Meth. B* **1996**, *112*, 59-63.

(48) Diehnelt, C. W., Van Stipdonk, M. J., Schweikert, E. A. *Phys. Rev. A* **1999**, *59*, 4470-4474.

(49) Wong, S. C. C., Hill, R., Blenkinsopp, P., Lockyer, N. P., Weibel, D. E., et al. *Appl. Surf. Sci.* **2003**, *203–204*, 219-222.

(50) Weibel, D., Wong, S., Lockyer, N., Blenkinsopp, P., Hill, R., et al. *Anal. Chem.* **2003**, *75*, 1754-1764.

(51) Winograd, N. *Anal. Chem.* **2005**, *77*, 142 A-149 A.

(52) Lu, C., Wucher, A., Winograd, N. *Anal. Chem.* **2010**, *83*, 351-358.

(53) Matsuo, J., Okubo, C., Seki, T., Aoki, T., Toyoda, N., et al. *Nucl. Instrum. Meth. B* **2004**, *219-220*, 463-467.

(54) Moritani, K., Hashinokuchi, M., Nakagawa, J., Kashiwagi, T., Toyoda, N., et al. *Appl. Surf. Sci.* **2008**, *255*, 948-950.

(55) Lee, J. L. S., Ninomiya, S., Matsuo, J., Gilmore, I. S., Seah, M. P., et al. *Anal. Chem.* **2009**, *82*, 98-105.

(56) Aoki, T., Seki, T., Ninomiya, S., Ichiki, K., Matsuo, J. *Nucl. Instrum. Meth. B* **2009**, *267*, 1424-1427.

(57) Bouneau, S., Della-Negra, S., Depauw, J., Jacquet, D., Le Beyec, Y., et al. *Nucl. Instrum. Meth. B* **2004**, *225*, 579-589.

(58) Anders, C., Urbassek, H. M. *Nucl. Instrum. Meth. B* **2005**, *228*, 57-63.

(59) Anders, C., Urbassek, H. M. *Nucl. Instrum. Meth. B* **2007**, *258*, 497-500.

(60) Anders, C., Urbassek, H. M. *Nucl. Instrum. Meth. B* **2008**, *266*, 44-48.

(61) Delcorte, A., Garrison, B. J., Hamraoui, K. *Anal. Chem.* **2009**, *81*, 6676-6686.

(62) Delcorte, A., Restrepo, O. A., Czerwinski, B., Garrison, B. J. *Surf. Interface Anal.* **2012**, ahead of print.

(63) Baranov, I., Della-Negra, S., Domaratsky, V., Chemezov, A., Novikov, A., et al. *Nucl. Instrum. Meth. B* **2008**, *266*, 1993-2001.

(64) Salonen, E., Nordlund, K., Keinonen, J. *Nucl. Instrum. Meth. B* **2003**, *212*, 286-290.

(65) Anders, C., Urbassek, H. M., Johnson, R. E. *Phys. Rev. B* **2004**, *70*, 155404.

(66) Carroll, S. J., Nellist, P. D., Palmer, R. E., Hobday, S., Smith, R. *Phys. Rev. Lett.* **2000**, *84*, 2654.

(67) Restrepo, O. A., Delcorte, A. *J. Phys. Chem. C* **2011**, *115*, 12751-12759.

(68) Li, Z., Verkhoturov, S. V., Locklear, J. E., Schweikert, E. A. *Int. J. Mass Spectrom.* **2008**, *269*, 112-117.

(69) Li, Z., Verkhoturov, S. V., Schweikert, E. A. *Anal. Chem.* **2006**, *78*, 7410-7416.

(70) Pinnick, V., Rajagopalachary, S., Verkhoturov, S. V., Kaledin, L., Schweikert, E. A. *Anal. Chem.* **2008**, *80*, 9052-9057.

(71) Pinnick, V. T., Verkhoturov, S. V., Kaledin, L., Bisrat, Y., Schweikert, E. A. *Anal. Chem.* **2009**, *81*, 7527-7531.

(72) Rickman, R. D., Verkhoturov, S. V., Hager, G. J., Schweikert, E. A. *Int. J. Mass Spectrom.* **2005**, *245*, 48-52.

(73) Rickman, R. D., Verkhoturov, S. V., Hager, G. J., Schweikert, E. A., Bennett, J. A. *Int. J. Mass Spectrom.* **2005**, *241*, 57-61.

(74) Chen, L.-J., Seo, J. H., Eller, M. J., Verkhoturov, S. V., Shah, S. S., et al. *Anal. Chem.* **2011**, *83*, 7173-7178.

(75) Liang, C. K., Verkhoturov, S. V., Bisrat, Y., Dikler, S., DeBord, J. D., et al. *Surf. Interface Anal.*, ahead of print.

(76) Pinnick, V., Verkhoturov, S. V., Kaledin, L., Schweikert, E. A. *Surf. Interface Anal.* **2011**, *43*, 551-554.

(77) Guillermier, C., Della, N. S., Rickman, R. D., Hager, G. J., Schweikert, E. A. *Int. J. Mass Spectrom.* **2007**, *263*, 298-303.

(78) Guillermier, C., Pinnick, V., Verkhoturov, S. V., Schweikert, E. A. *Appl. Surf. Sci.* **2006**, *252*, 6644-6647.

(79) Rajagopalachary, S., Verkhoturov, S. V., Schweikert, E. A. *Anal. Chem.* **2009**, *81*, 1089-1094.

(80) Rajagopalachary, S., Verkhoturov, S. V., Schweikert, E. A. *Nano Lett.* **2008**, *8*, 1076-1080.

(81) Rajagopalachary, S., Verkhoturov, S. V., Schweikert, E. A. *Surf. Interface Anal.* **2011**, *43*, 547-550.

(82) Della-Negra, S., Depauw, J., Guillermier, C., Schweikert, E. A. *Surf. Interface Anal.* **2011**, *43*, 62-65.

(83) Hager, G. J. Ph.D. Dissertation. Texas A&M University, College Station, Texas, **2007**.

(84) Rickman, R. D. Ph.D. Dissertation. Texas A&M University, College Station, Texas, **2004**.

(85) Della-Negra, S., Arianer, J., Depauw, J., Verkhoturov, S. V., Schweikert, E. A. *Surf. Interface Anal.* **2011**, *43*, 66-69.

(86) Taylor, G. *P. Roy. Soc. Lond. A Mat.* **1964**, *280*, 383-397.

(87) Dedman, C. J., Roberts, E. H., Gibson, S. T., Lewis, B. R. *Rev. Sci. Instrum.* **2001**, *72*, 2915.

(88) Eller, M. J., Verkhoturov, S. V., Della-Negra, S., Rickman, R. D., Schweikert, E. A. *Surf. Interface Anal.* **2010**, *42*.

(89) Eller, M. J., Verkhoturov, S. V., Della-Negra, S., Schweikert, E. A. *J. Phys. Chem. C* **2010**, *114*, 17191-17196.

(90) Eller, M. J., Verkhoturov, S. V., Fernandez-Lima, F. A., DeBord, J. D., Schweikert, E. A., et al. *Surf. Interface Anal.* **2012**, ahead of print.

(91) Verkhoturov, S. V., Eller, M. J., Rickman, R. D., Della-Negra, S., Schweikert, E. A. *J. Phys. Chem. C* **2009**, *114*, 5637-5644.

(92) Eller, M. J. Ph.D. Dissertation. Texas A&M University, College Station, TX, **2012**.

(93) Brunelle, A., Della-Negra, S., Depauw, J., Joret, H., Le Beyec, Y. *Rapid Commun. Mass Sp.* **1991**, *5*, 40-43.

(94) Brenes, D. A., Garrison, B. J., Winograd, N., Postawa, Z., Wucher, A., et al. *J. Phys. Chem. Lett.* **2011**, *2*, 2009-2014.

(95) Le Beyec, Y. *Int. J. Mass Spectrom.* **1998**, *174*, 101-117.

(96) Jacquet, D., Le Beyec, Y. *Nucl. Instrum. Meth. B* **2002**, *193*, 227-239.

(97) Beuhler, R. J., Friedman, L. *J. Phys., Colloq.* **1989**, C2.

(98) Beuhler, R., Friedman, L. *Chem. Rev.* **1986**, *86*, 521-537.

(99) Guillermier, C., Della-Negra, S., Schweikert, E. A., Dunlop, A., Rizza, G. *Int. J. Mass Spectrom.* **2008**, *275*, 86-90.

(100) Dunlop, A., Jaskierowicz, G., Ossi, P. M., Della-Negra, S. *Phys. Rev. B* **2007**, *76*, 155403.

(101) Andersen, H. H., Johansen, A., Olsen, M., Touboltsev, V. *Nucl. Instrum. Meth. B* **2003**, *212*, 56-62.

(102) Shulga, V. I., Sigmund, P. *Nucl. Instrum. Meth. B* **1990**, *47*, 236-242.

(103) Bouneau, S., Brunelle, A., Della-Negra, S., Depauw, J., Jacquet, D., et al. *Nucl. Instrum. Meth. B* **2006**, *251*, 383-389.

(104) Srama, R., Woiwode, W., Postberg, F., Armes, S. P., Fujii, S., et al. *Rapid Commun. Mass Sp.* **2009**, *23*, 3895-3906.

(105) Ledbetter, M. C., Beuhler, R. J., Friedman, L. *Proc. Natl. Acad. Sci. USA* **1987**, *84*, 85-8.

(106) Feld, H., Zurmuehlen, R., Leute, A., Benninghoven, A. *J. Phys. Chem.* **1990**, *94*, 4595-9.

(107) Gnaser, H. *Nucl. Instrum. Meth. B* **1999**, *149*, 38-52.

(108) Fernandéz-Lima, F. A., Ponciano, C. R., da Silveira, E. F., Nascimento, M. A. C. *Chem. Phys. Lett.* **2007**, *445*, 147-151.

(109) Wirtz, T., Migeon, H. N. *Appl. Surf. Sci.* **2004**, *222*, 186-197.

(110) Li, G., Cyriac, J., Gao, L., Graham Cooks, R. *Surf. Interface Anal.* **2011**, *43*, 498-501.

(111) Fitzgerald, J. J. D., Kunnath, P., Walker, A. V. *Anal. Chem.* **2010**, *82*, 4413-4419.

(112) Brewer, T. M., Szakal, C., Gillen, G. *Rapid Commun. Mass Sp.* **2010**, *24*, 593-598.

(113) Mori, K., Asakawa, D., Sunner, J., Hiraoka, K. *Rapid Commun. Mass Sp.* **2006**, *20*, 2596-2602.

(114) Toyoda, N., Matsuo, J., Aoki, T., Yamada, I., Fenner, D. B. *Appl. Surf. Sci.* **2003**, *203-204*, 214-218.

(115) Rickman, R. D., Verkhoturov, S. V., Parilis, E. S., Schweikert, E. A. *Phys. Rev. Lett.* **2004**, *92*, 047601.

(116) Rickman, R. D., Verkhoturov, S. V., Schweikert, E. A. *Appl. Surf. Sci.* **2004**, *231-232*, 54-58.

(117) Baio, J. E., Weidner, T., Samuel, N. T., McCrea, K., Baugh, L., et al. *J. Vac. Sci. Technol. B* **2010**, *28*, C5D1-C5D8.

(118) Chang, C.-J., Chang, H.-Y., You, Y.-W., Liao, H.-Y., Kuo, Y.-T., et al. *Anal. Chim. Acta* **2012**, *718*, 64-69.

(119) Li, G., Cyriac, J., Gao, L., Graham, C. R. *Surf. Interface Anal.* **2011**, *43*, 498-501.

(120) Mochiji, K. *Hyomen Kagaku* **2010**, *31*, 599-603.

(121) Piwowar, A., Fletcher, J., Lockyer, N., Vickerman, J. *Surf. Interface Anal.* **2011**, *43*, 207-210.

(122) Svara, F. N., Kiss, A., Jaskolla, T. W., Karas, M., Heeren, R. M. A. *Anal. Chem.* **2011**, *83*, 8308-8313.

(123) Schilke, K. F., McGuire, J. *J. Colloid Interf. Sci.* **2011**, *358*, 14-24.

(124) Suzuki, N., Gamble, L., Tamerler, C., Sarikaya, M., Castner, D. G., et al. *Surf. Interface Anal.* **2007**, *39*, 419-426.

(125) Roepstorff, P., Fohlman, J. *Biol. Mass Spectrom.* **1984**, *11*, 601-601.

(126) Solé-Domènech, S., Johansson, B., Schalling, M., Malm, J., Sjövall, P. *Anal. Chem.* **2010**, *82*, 1964-1974.

(127) de Meyer, F., Smit, B. *P. Natl. Acad. Sci. USA* **2009**, *106*, 3654-3658.

(128) Brasaemle, D. L. *J. Lipid Res.* **2007**, *48*, 2547-2559.

(129) Brown, H. A., Marnett, L. J. *Chem. Rev.* **2011**, *111*, 5817-5820.

(130) Goto-Inoue, N., Hayasaka, T., Zaima, N., Setou, M. *BBA-Mol. Cell Biol. L.* **2011**, *1811*, 961-969.

(131) Passarelli, M. K., Winograd, N. *BBA-Mol. Cell Biol. L.* **2011**, *1811*, 976-990.

(132) Fernandez-Lima, F. A., Post, J., DeBord, J. D., Eller, M. J., Verkhoturov, S. V., et al. *Anal. Chem.* **2011**, *83*, 8448-8453.

(133) Fernandez-Lima, F. A., DeBord, J. D., Schweikert, E. A., Della-Negra, S., Kellersberger, K. A., et al. *Surf. Interface Anal.* **2012**, in press.

(134) Sud, M., Fahy, E., Cotter, D., Brown, A., Dennis, E. A., et al. *Nucleic Acids Res.* **2007**, *35*, D527-D532.

(135) Brunelle, A., Della-Negra, S., Depauw, J., Jacquet, D., Le Beyec, Y., et al. *Phys. Rev. A* **2001**, *63*, 022902.

(136) Huheey, J. E., Keiter, E. A., Keiter, R. L., *Inorganic Chemistry: Principles of Structure and Reactivity*. Pearson Education: **2000**.

(137) Luxembourg, S. L., Heeren, R. M. A. *Int. J. Mass Spectrom.* **2006**, *253*, 181-192.

(138) Lou, X., van, D. J. L. J., Meijer, E. W. *J. Am. Soc. Mass Spectr.* **2010**, *21*, 1223-1226.

(139) Vékey, K. *J. Mass Spectrom.* **1996**, *31*, 445-463.

(140) Sztaray, J., Memboeuf, A., Drahos, L., Vekey, K. *Mass Spectrom. Rev.* **2011**, *30*, 298-320.

(141) Gabelica, V., De Pauw, E. *Mass Spectrom. Rev.* **2005**, *24*, 566-587.

(142) Nefliu, M., Smith, J. N., Venter, A., Cooks, R. G. *J. Am. Soc. Mass Spectr.* **2008**, *19*, 420-427.

(143) Luo, G., Marginean, I., Vertes, A. *Anal. Chem.* **2002**, *74*, 6185-6190.

(144) Mori, K., Hiraoka, K. *J. Mass Spectrom. Soc. Jpn.* **2008**, *56*, 33-39.

(145) Derwa, F., De, P. E., Natalis, P. *Org. Mass Spectrom.* **1991**, *26*, 117-18.

(146) De Pauw, E., Pelzer, G., Marien, J., Natalis, P. *Springer Proc. Phys.* **1986**, *9*, 103-8.

(147) DeBord, J. D., Fernandez-Lima, F. A., Verkhoturov, S. V., Schweikert, E. A., Della-Negra, S. *Surf. Interface Anal.* **2012**, in press.

(148) Delcorte, A., Garrison, B. J., Hamraoui, K. *Anal. Chem.* **2009**, *81*, 6676-6686.

(149) Della-Negra, S., Depauw, J., Guillermier, C., Schweikert, E. A. *Surf. Interface Anal.* **2011**, *43*, 62-65.

(150) Derwa, F., De Pauw, E., Natalis, P. *Org. Mass Spectrom.* **1991**, *26*, 117-18.

(151) Gabelica, V., De, P. E. *Mass Spectrom. Rev.* **2005**, *24*, 566-587.

(152) Collette, C., Drahos, L., De Pauw, E., Vékey, K. *Rapid Commun. Mass Sp.* **1998**, *12*, 1673-1678.

(153) Nefliu, M., Smith, J. N., Venter, A., Cooks, R. G. *J. Am. Soc. Mass Spectr.* **2008**, *19*, 420-427.

(154) Morsa, D., Gabelica, V., De Pauw, E. *Anal. Chem.* **2011**, *83*, 5775-5782.

(155) Naban-Maillet, J., Lesage, D., Bossee, A., Gimbert, Y., Sztaray, J., et al. *J. Mass Spectrom.* **2005**, *40*, 1-8.

(156) Marcus, R. A. *J. Chem. Phys.* **1952**, *20*, 359-64.

(157) Marcus, R. A., Rice, O. K. *J. Phys. Colloid Chem.* **1951**, *55*, 894-908.

(158) Gaussian 09, Revision B.01, Frisch, M. J., Trucks, G. W., Schlegel, H. B., Scuseria, G. E., Robb, M. A., et al., Gaussian, Inc.: Wallingford CT, **2009**.

(159) Parr, R. G., Yang, W., *Density-Functional Theory of Atoms and Molecules*. Oxford University Press: New York, **1994**.

(160) Becke, A. D. *J. Chem. Phys.* **1993**, *98*, 5648-5652.

(161) Lee, C., Yang, W., Parr, R. G. *Phys. Rev. B* **1988**, *37*, 785-9.

(162) Frisch, M. J., Pople, J. A., Binkley, J. S. *J. Chem. Phys.* **1984**, *80*, 3265-3269.

(163) Krishnan, R., Binkley, J. S., Seeger, R., Pople, J. A. *J. Chem. Phys.* **1980**, *72*, 650-4.

(164) Moller, C., Plesset, M. S. *Phys. Rev.* **1934**, *46*, 618-22.

(165) Dewar, M. J. S., Storch, D. M. *J. Am. Chem. Soc.* **1985**, *107*, 3898-3902.

(166) Roothaan, C. C. J. *Rev. Mod. Phys.* **1951**, *23*, 69-89.

(167) Gabelica, V., De Pauw, E., Karas, M. *Int. J. Mass Spectrom.* **2004**, *231*, 189-195.

(168) Dzhemilev, N. K., Goldenberg, A. M., Veriovkin, I. V., Verkhoturov, S. V. *Int. J. Mass Spectrom.* **1995**, *141*, 209-215.

(169) Drahos, L., Vekey, K. *J. Mass Spectrom.* **2001**, *36*, 237-263.

(170) Robinson, P. J., Holbrook, K. A., *Unimolecular Reactions*. Wiley-Interscience: New York, **1972**; p 371.

(171) Wucher, A., Dzhemilev, N. K., Veryovkin, I. V., Verkhoturov, S. V. *Nucl. Instrum. Meth. B* **1999**, *149*, 285-293.

(172) Zhou, J., Takahashi, L. K., Wilson, K. R., Leone, S. R., Ahmed, M. *Anal. Chem.* **2010**, *82*, 3905-3913.

(173) Garrison, B. J., Postawa, Z., Ryan, K. E., Vickerman, J. C., Webb, R. P., et al. *Anal. Chem.* **2009**, *81*, 2260-2267.

(174) Delcorte, A., Bertrand, P. *Anal. Chem.* **2005**, *77*, 2107-2115.

(175) Delcorte, A., Medard, N., Bertrand, P. *Anal. Chem.* **2002**, *74*, 4955-4968.

(176) Adriaensen, L., Vangaever, F., Gijbels, R. *Appl. Surf. Sci.* **2004**, *231–232*, 256-260.

(177) Delcorte, A., Yunus, S., Wehbe, N., Nieuwjaer, N., Poleunis, C., et al. *Anal. Chem.* **2007**, *79*, 3673-3689.

(178) Conrad, R., Harsdorff, M. *Int. J. Electron.* **1990**, *69*, 153-67.

(179) Travaly, Y., Zhang, L., Zhao, Y., Pfeffer, R., Uhrich, K., et al. *J. Mater. Res.* **1999**, *14*, 3673-3683.

(180) Delcorte, A., Garrison, B. J. *Nucl. Instrum. Meth. B* **2007**, *255*, 223-228.

(181) Chen, L.-J., Shah, S. S., Silangcruz, J., Eller, M. J., Verkhoturov, S. V., et al. *Int. J. Mass Spectrom.* **2011**, *303*, 97-102.

(182) Chen, L.-J., Shah, S. S., Verkhoturov, S. V., Revzin, A., Schweikert, E. A. *Surf. Interface Anal.* **2011**, *43*, 555-558.

(183) Lub, J., Benninghoven, A. *Org. Mass Spectrom.* **1989**, *24*, 164-168.

(184) Schweikert, E. A., James, W. D. *Rugged Miniaturized Mass Sensors for Use in Plutonium Conversion Processes*; Amarillo National Resource Center for Plutonium: Amarillo, 1999.

(185) Woodyard, J. D., Burgess, C. E., Rainwater, K. A. *Mechanisms of Formation of Trace Decomposition Products in Complex High Explosive Mixtures*; Amarillo National Resource Center for Plutonium: Amarillo, 1999.

(186) Pospíšil, J. *Polym. Degrad. Stabil.* **1988**, *20*, 181-202.

(187) Stapel, D., Benninghoven, A. *Appl. Surf. Sci.* **2001**, *174*, 261-270.

(188) Adriaensen, L., Vangaever, F., Gijbels, R. *Anal. Chem.* **2004**, *76*, 6777-6785.

(189) Kéki, S., Nagy, L., Deák, G., Zsuga, M. *J. Am. Soc. Mass Spectr.* **2004**, *15*, 1455-1461.

(190) DeBord, J. D., Della-Negra, S., Fernandez-Lima, F. A., Verkhoturov, S. V., Schweikert, E. A. *J. Phys. Chem. C* **2012**, *116*, 8138-8144.

(191) Garrison, B. J., Postawa, Z. *Mass Spectrom. Rev.* **2008**, *27*, 289-315.

(192) Green, F. M., Gilmore, I. S., Seah, M. P. *Anal. Chem.* **2011**, *83*, 3239-3243.

(193) Bolton, E. E., Wang, Y., Thiessen, P. A., Bryant, S. H., *Annual Reports in Computational Chemistry*, **2008**, *4*, 217-241.

(194) Fernandez-Lima, F. A., Eller, M. J., Verkhoturov, S. V., Della-Negra, S., Schweikert, E. A. *J. Phys. Chem. Lett.* **2010**, *1*, 3510-3513.

(195) Fernandez-Lima, F. A., Pinnick, V. T., Della-Negra, S., Schweikert, E. A. *Surf. Interface Anal.* **2011**, *43*, 53-57.

(196) Fernandez-Lima, F. A., Eller, M. J., DeBord, J. D., Levy, M. J., Verkhoturov, S. V., et al. *J. Phys. Chem. Lett.* **2012**, 337-341.

(197) Suh, J., Han, B., Okuyama, K., Choi, M. *J. Colloid Interf. Sci.* **2005**, *287*, 135-140.

APPENDIX A

OPERATIONAL PROCEDURES FOR

THE PEGASUS ION SOURCE PLATFORM

Startup Procedure

1. Insure vacuum in platform chamber and main chamber are < $5x10^{-6}$ torr.
2. Turn on fiber optic control panel
3. Set extraction voltage to 10 kV.
4. Set acceleration voltage to 20 KV.
5. Slowly increase source current following the schedule below:
    a. For new source:
        i. Turn up current by 0.25 A every 10 min until 1.5 A is reached.
        ii. Turn up current by 0.05 A every 10 min until source emits or 2.2 A is reached
        iii. If source does not emit, replace with new source.
        iv. If source emits, monitor emission voltage stability. If unstable increase current by 0.05 A until stable.
    b. For used source
        i. Turn up current by 0.5 A every 5 min until 1.5 A is reached.
        ii. Set current to stable emission current from last operation.
        iii. If source is unstable or does not emit, increase current by 0.05 A every 5 min until stable emission.
        iv. If source still does not emit stably, replace with new source.
6. Perform beam optimization using Faraday cup measurement of beam current and the following optimization loop:
    a. Optimize X,Y positioning.
    b. Optimize Einzel lens.
    c. Optimize horizontal and vertical deflection.
    d. If necessary, select projectile using Wien filter.
        i. To turn on Wien filter, set the current to 1.20 A
        ii. The necessary Wien filter voltage can be determined using the equation $V_{\pm} = \frac{2076}{\sqrt{m}}$ where m is the m/q of the desired projectile in amu.
    e. Repeat steps a-d until optimal beam current is obtained.
7. Close and lock cage door.
    a. Remove key and place in control panel.
    b. Insure that grounding pole is detached from the platform and is placed on storage hook interlock.

c. Insure that the cage gate is closed.

8. Increase floating voltage on platform to desired voltage (100 kV max).
    a. Slowly increase floating voltage, pausing momentarily every 5 kV to avoid sparking.
9. Insure beam current is still acceptable at high voltage.
10. Open gate valve in beam line and introduce beam to analysis chamber.

Experiment can now be performed using selected Au_n^{+q} projectiles.

Shutdown procedure

1. Close gate valve to main chamber.
2. Reduce platform floating voltage to 0 kV.
    a. Slowly reduce platform floating voltage, pausing momentarily every 5 kV to avoid sparking.
3. Reduce horizontal and vertical deflectors to 0 V.
4. Reduce Wien filter values to 0.
5. Reduce Einzel lens to 0 kV.
6. Reduce source current to 0 A.
7. Reduce acceleration voltage to 0 kV.
8. Reduce extraction voltage to 0 kV.
9. Turn off fiber optic control panel.
10. Remove key from control panel and open cage door.
11. Ground the platform using grounding rod.

Notes:

A. Sparking:
    a. No action needs to be taken for isolated sparking (Rate of 1 spark/hour).
    b. In case of frequent sparking on platform, reduce floating voltage to 0 kV and troubleshoot source of discharge.
B. Maintenance:
    a. Instrument room should be kept free of dust.
        i. Clean dusty items before bringing them into the room.
        ii. Floor should be swept once per week.
        iii. Lab bench and tables should be cleaned as needed.
        iv. Air filters in ceiling should be changed monthly.
        v. All platform insulators should be cleaned with ethanol and Kimwipes monthly.

Emergency Shutdown Procedure

1. Turn off the power breaker

POWER BREAKER

CONTROL PANEL

2. Remove key from control panel
   And open cage door

KEY

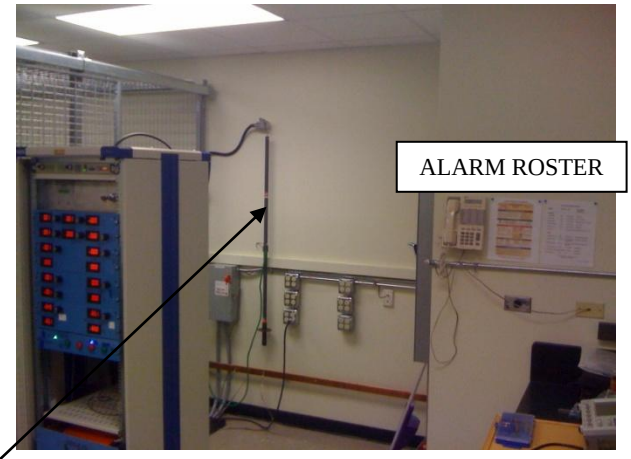

ALARM ROSTER

3. Ground the platform using
   Grounding rod.

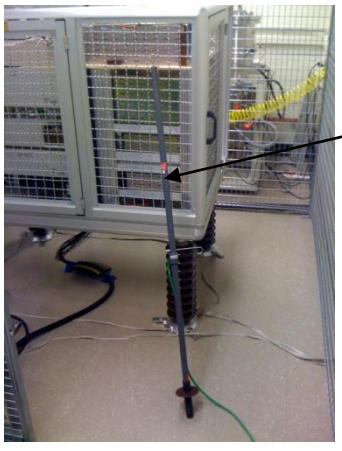

GROUNDING ROD

4. Call for assistance (see phone numbers on the CCCA Fire Alarm Roster)